

**MICRO-SCALE CHARACTERIZATION OF BREAST CANCER USING MEMS
AND ROBOTICS**

A Dissertation
Presented to
The Academic Faculty

By

Kihan Park

In Partial Fulfillment
of the Requirements for the Degree
Doctor of Philosophy in
Robotics

Georgia Institute of Technology

August 2019

Copyright © Kihan Park 2019

MICRO-SCALE CHARACTERIZATION OF BREAST CANCER USING MEMS AND ROBOTICS

Approved by:

Dr. Jaydev P. Desai
Wallace H. Coulter Department of
Biomedical Engineering
Georgia Institute of Technology

Dr. Jun Ueda
George W. Woodruff School of
Mechanical Engineering
Georgia Institute of Technology

Dr. Frank L. Hammond III
Wallace H. Coulter Department of
Biomedical Engineering
Georgia Institute of Technology

Dr. Peter J. Hesketh
George W. Woodruff School of
Mechanical Engineering
Georgia Institute of Technology

Dr. David J. Foran
Robert Wood Johnson Medical
School
*Rutgers, The State University of
New Jersey*

Date Approved: June 26, 2019

ACKNOWLEDGEMENTS

I would like to express the deepest appreciation to my advisor, Professor Jaydev P. Desai, for giving me the opportunity to do research and providing invaluable guidance throughout this research. He has continually and convincingly conveyed a spirit of adventure in regard to research and scholarship, and an excitement in regard to teaching. His vision, sincerity and motivation have deeply inspired me how to be a good mentor and it was a great privilege and honor to work and study under his guidance. I would also like to thank the rest of my dissertation committee members, Professors David J. Foran, Jun Ueda, Peter J. Hesketh, and Frank L. Hammond, for their great support and invaluable advice. I offer my sincere appreciation for the learning opportunities provided by the committee.

The research reported in this dissertation was mainly supported by the National Cancer Institute of the National Institutes of Health under Award Number R01CA161375. The content is solely the responsibility of the author and does not necessarily represent the official views of the National Institutes of Health. This work was performed in part at the Georgia Tech Institute for Electronics and Nanotechnology, a member of the National Nanotechnology Coordinated Infrastructure, which is supported by the National Science Foundation (Grant ECCS-1542174). I also acknowledge the support of Biospecimen Repository Service and Histopathology Shared Resources of the Rutgers Cancer Institute of New Jersey (P30CA072720) for tissue archive and specimen preparation.

I would like to thank my lab members and collaborators for their continued support. I would like to acknowledge Dr. Hardik J. Pandya currently at Indian Institute of Science, Carolyn M. Davis, Dr. Wenjin Chen, Lei Cong, Lucyann Franciosa from Rutgers Cancer Institute of New Jersey, and Dr. Marina A. Chekmareva, Dr. Lauri A. Goodell from Rutgers Robert Wood Johnson Medical School for collaborating in the design of the MEMS-based sensors, the fabrication of the micromanipulator, the biological tissue sample selection, and pathological analysis, respectively. Moreover, I am also grateful to my research colleagues

in the RoboMed Lab, Jun, Bernard, Yeongjin, Xuefeng, Chad, Nahian, Seokhwan, Yash, Phillip, and Nancy for their constant encouragement.

Last but not least, I would like to express my deepest gratitude to my family. This dissertation would not have been possible without their warm love, continued patience, and endless support. I am extremely thankful to my mother and my sister for their love, caring, and sacrifices for educating and preparing me for my future. I am also very much thankful to my wife, Jiyeon, and my daughter, Gia, for their love, understanding, encouragement, and continuing support to complete this research work. My heartfelt thanks.

TABLE OF CONTENTS

Acknowledgments	iii
List of Tables	x
List of Figures	xi
List of Abbreviationsxviii
Summary	xxi
Chapter 1: Introduction and Background	1
1.1 Motivation	1
1.2 Related Works	3
1.2.1 MEMS-based Sensors for Characterization of Biological Tissues and Cells	3
1.2.2 Micro-manipulation Systems	6
1.2.3 Signatures and Diagnosis of Breast Cancer	10
Chapter 2: MEMS-based Sensors for Characterization of Cancerous Breast Tis- sues	13
2.1 Introduction	13
2.2 Flexible MEMS-based Electro-mechanical Sensor	15
2.2.1 Design and Fabrication	15

2.2.2	Strain Detection Mechanism for Mechanical Sensors	18
2.2.3	Linear Regression Model	21
2.2.4	Spring Constant Measurement	23
2.2.5	Tissue Preparation and Annotation	23
2.2.6	Sensitivity Measurement and Sensor Performance of the Breast Tissue	26
2.3	Electro-mechanical Characterization of Human Breast Tissues	31
2.3.1	Experimental Setup	31
2.3.2	Study Design	33
2.3.3	Sample Preparation	34
2.3.4	Immunohistochemical (IHC) Staining	34
2.3.5	Electro-mechanical Signatures of Breast Biopsies	36
2.4	Towards Lateral Tissue Scanning	51
2.4.1	Design and Fabrication of Capacitive Microcantilever for Multi- directional Sensing	51
2.4.2	Lateral Measurement Experiment	55
2.5	Conclusion	56
Chapter 3: Microscope Compatible Underactuated Micro-manipulation Platform		58
3.1	Introduction	58
3.2	System Design	60
3.2.1	Requirements	60
3.2.2	Key Design Decisions	61
3.2.3	Considerations for Manufacturing	66
3.3	Underactuated Planar Mechanism	67

3.4	Kinematic Analysis	69
3.4.1	Geometric Constraints	69
3.4.2	Kinematic Modeling	72
3.4.3	Controllability	78
3.5	Point-to-point Control Strategy	81
3.5.1	Step 1: Rotation and finding the desired sliding line in XY plane under $\dot{\theta} = 0$ condition	81
3.5.2	Step 2: Reaching the sliding line	83
3.5.3	Step 3: Translation to the desired position along the sliding line	84
3.5.4	Simulation	85
3.6	Experiments and Discussion	87
3.6.1	Breast Tissue Core Study	87
3.6.2	Point-to-point Micropositioning	89
3.7	Conclusion	97
Chapter 4: Machine Learning Approach for Breast Cancer Localization		99
4.1	Introduction	99
4.2	Materials and Methods	100
4.2.1	Force-Indentation Model	100
4.2.2	Support Vector Machine (SVM) Algorithm	101
4.2.3	Breast Tissue Sample Preparation	103
4.2.4	Experimental Setup	103
4.3	Results and Discussion	104
4.4	Conclusion	110

Chapter 5: Portable Cancer Diagnostic Tool Using a Disposable MEMS-based Biochip	111
5.1 Introduction	111
5.2 Biochip Towards a Portable Cancer Diagnostic Tool	112
5.2.1 Biochip Fabrication	112
5.2.2 Breast Tissue Preparation	113
5.2.3 Experimental Setup	117
5.2.4 Experimental Results and Discussion	120
5.3 Electromechanical Coupling Factor as a Biomarker for Breast Cancer	126
5.3.1 Portable Diagnostic Tool	127
5.3.2 Piezoelectric Model	128
5.3.3 Breast Tissue Sample Preparation	130
5.3.4 Histological Staining Protocols	130
5.3.5 Pre-conditioning	133
5.3.6 Experiments and Results	133
5.4 Conclusion	141
Chapter 6: Toward <i>in situ</i> and <i>in vivo</i> Breast Cancer Diagnosis	143
6.1 Introduction	143
6.2 MWCNT/PDMS-based Flexible Sensor	145
6.2.1 Dispersion of MWCNTs	145
6.2.2 Characterization of MWCNT/PDMS Elastomer	147
6.2.3 Sensor Fabrication	149
6.2.4 Strain Sensor in a Mock-up Needle for <i>In Situ</i> Tissue Characterization	150

6.3 Conclusion	152
Chapter 7: Conclusion and Future Work	155
7.1 Conclusion	155
7.2 Contributions	156
7.3 Future Work	157
Appendix A: Nomenclature for Chapter 3	160
Appendix B: Use of Copyrighted Materials and Permissions	164
References	165

LIST OF TABLES

1.1	Comparison of commercially available micro-positioning systems	7
2.1	Individual electrical (change in tissue resistance, mean \pm SD) and mechanical (elasticity E, mean \pm SD) analysis of breast tissue samples.	46
2.2	Double tailed t -test between diseased groups from electromechanical characterization.	48
3.1	Friction coefficients for Teflon on layer 1 materials	65
3.2	Experimental result for the stage motion	89
3.3	Observation of the state variables	91
3.4	Experimental results of point-to-point control	94
4.1	Features of the micropositioning platform	106
4.2	Summary for the experimental conditions	107
4.3	Quantitative experimental results of 10 tests	107
5.1	Experimental results	138
5.2	p -value of the two-sample t -test	139

LIST OF FIGURES

2.1	Tissue preparation: Hematoxylin and eosin (H&E) stained surface section of patient tissue block.	14
2.2	Flexible MEMS device: (a) Schematic diagram, (b) Magnified schematic of sensor array top view, and (c) Angled view.	15
2.3	Process flow for flexible electro-mechanical sensor array.	16
2.4	Sensor fabrication SEM images: (a) Strain gauge array, (b) Single strain gauge, (c) Array of devices showing gold pads/SiO ₂ /strain gauge, (d) Magnified image of single device, (e) Array of gold coated SU-8 pillars/gold pads/SiO ₂ /strain gauges, and (f) Magnified images of SU-8 pillars on gold pads (inset shows gold coated SU-8 pillars on gold pads).	19
2.5	SEM image of the device.	20
2.6	Photos of flexible MEMS-based device.	20
2.7	Strain sensing mechanism for PEDOT:PSS based sensor.	20
2.8	Measuring electrical output from single strain sensor: (a) Schematics and (b) Experimental setup.	21
2.9	Schematic diagram of the AFM configuration used for spring constant measurement of PEDOT:PSS strain gauge using reference cantilever method: 2D representation of (a) AFM cantilever in contact with SU-8 pillar/strain gauge, (b) AFM cantilever pressed against the SU-8 pillar/strain gauge to a preset force value, and (c) 3D representation of spring constant measurement.	24
2.10	AFM force curve on the SU-8 pillar/strain gauge/PDMS.	24
2.11	Spring constant measurement of sensor.	25
2.12	SEM image of (a) Micro-grid, (b) Crumpled micro-grid, and (c) Breast tissue core placed on micro-grid.	25

2.13 Breast tissue core: (a) and (b) H&E image and optical image of benign sample, (c) and (d) H&E image and optical image of cancerous sample. . .	26
2.14 Device mounted on cone shape holder for mechanical and electrical characterization: (a) Schematic and (b) Actual photograph.	27
2.15 Sensitivity measurement of fabricated sensor array.	28
2.16 (a) Mechanical characterization: response of device on benign and cancerous breast tissue and (b) Force curves obtained from normal and cancerous breast tissue.	29
2.17 Electrical characterization: response of device on benign and cancerous breast tissue.	30
2.18 Flexible electro-mechanical device: (a) Schematic process for the fabrication of electro-mechanical device incorporating PDMS and SU-8 polymers, (b) Flat and curved schematic of the device, (c) Cross-sectional SEM images of 1) Array of strain gauges, 2) Circular pads over strain gauges, and 3) Array of gold coated SU-8 pillars on gold pads (Scale bar = 100 μm), and (d) Photographs of the final device.	32
2.19 Experimental set-up for measuring electrical and mechanical properties of the breast tissue: (a) The inverted microscope facilitates in directing the flexible sensor array on to the region-of-interest in the breast tissue core, (b) The flexible sensor array mounted on a 3D-printed cone, and (c) Bottom electrodes with micro-grids for holding tissue cores. The scale bar is 200 μm	33
2.20 Electronic module for displaying voltage as a function of the indentation of breast tissue.	37
2.21 Electronic module for measuring electrical resistance of the breast tissue. . .	37
2.22 Spring constant measurement.	38
2.23 Sensitivity measurement of the fabricated sensor array.	39
2.24 Field-emission scanning electron microscopy revealing microstructure of breast tissue cores.	39

2.25	Electro-mechanical signatures of human breast tissue and corresponding immunohistochemistry: (a, b) Elasticity map and (c, d) Change in electrical signals for epithelial and stromal regions of normal (P3A-28480) and invasive ductal carcinoma (P13A-29689) tissue cores respectively. (e, f) Staining of normal (P3A-28480) and invasive ductal carcinoma (P13A-29689) cores. Scale bar for all images is 50 μm	41
2.26	Electro-mechanical signatures of human breast tissue with tumor progression: (a)-(d) Elasticity map and (e)-(h) Change in electrical signals for epithelial and stromal regions of ductal carcinoma <i>in situ</i> (DCIS) (P6A-11809), lobular carcinoma <i>in situ</i> (LCIS) (P10A-27928), invasive ductal carcinoma (IDC) (P14A-26249) and invasive lobular carcinoma (ILC) (P19A-26763). .	42
2.27	Immunohistochemistry of breast tissue cores: (a) Ductal carcinoma <i>in situ</i> (DCIS) (P6A-11809), (b) Lobular carcinoma <i>in situ</i> (LCIS) (P10A-27928), (c) Invasive Lobular carcinoma (ILC) (P19A-26763) breast tissue cores. Staining with 1) H&E; 2) Red: E-cadherin, Brown: Estrogen receptor (ER); 3) Red: Smooth muscle actin (SMA), Brown: P63; and 4) Red: CD31, Brown: Ki67. The scale bar in each case is 50 μm	44
2.28	Statistical analysis: Elastic modulus and electrical resistance of tumors from ductal and lobular groups relative to normal breast tissue.	47
2.29	A group-wise electro-mechanical analysis of the breast tissue cores.	49
2.30	Force curves from the breast tissue cores. Force curves obtained from epithelial and stromal region of (a) Normal, (b) Ductal carcinoma <i>in situ</i> (DCIS), (c) Lobular carcinoma <i>in situ</i> (LCIS), (d) Invasive ductal carcinoma (IDC), and (e) Invasive lobular carcinoma (ILC) breast tissues.	50
2.31	Schematic of capacitive microcantilever and its comb-drive structure.	52
2.32	Fabrication process of capacitive microcantilever.	53
2.33	SEM images of fabricated capacitive microcantilevers: (a) Angled contact (45°), (b) Normal contact (90°), and (c) Comb-drive structure.	54
2.34	Assembled comb-drive sensor with PCB: (a) Capacitive microcantilever on PCB and (b) Wire bondings	54
2.35	Differential capacitive readout mechanism.	55
2.36	Calibration of the comb-drive sensor: (a) Calibration method, (b) Calibration result in the shear direction, and (c) Calibration result in the normal direction.	56

2.37	Experimental setup for lateral measurement: (a) microscopic view of a breast tissue sample and (b) schematic of a tissue sample at the sideview.	56
3.1	Tissue microarray (TMA).	60
3.2	Micro-positioning stage mounted on inverted microscope, Nikon TE-2000U.	62
3.3	Experimental set-up for friction data collection.	64
3.4	(a) Schematic of the underactuated planar mechanism (scaled drawing) and (b) The manufactured platform.	68
3.5	Schematic of the geometric relations and the coordinate system of the stage (scaled drawing). $\{W\}$, $\{B\}$, \mathbf{u}_1^W and \mathbf{u}_2^W is the world frame (fixed frame), the body frame (moving frame), and the input velocity vector of linear actuators in x^W and y^W direction, respectively. The parameters denoted by * represent the known values due to the structure or measurements.	70
3.6	Experimental setup for finding instantaneous COR of the stage: (a) Schematic of geometrically defined COR and (b) The experimental setup.	71
3.7	Results of the vision tracking experiment to find the instantaneous COR: (a) The coordinates of instantaneous COR, $[x_A^W, y_A^W]^T$ and (b) Comparison of the measured angle of the stage with the calculated angle from instantaneous COR.	72
3.8	Schematic of the angular momentum of the stage (scaled drawing).	75
3.9	Examples of the contour plot for $J_c = \frac{y_O^W}{x_O^W}$ under the motion constraint of $\dot{\theta} = 0$: (a) With $\theta = 0^\circ$ and (b) With $\theta = 10^\circ$	83
3.10	Simulation results of proposed point-to-point control strategy for $[(x_O^W)_d, (y_O^W)_d, \theta_d]^T = [1 \text{ mm}, 2 \text{ mm}, 1^\circ]^T$: (a) The state variables and the inputs, (b) The tracking errors (i.e. e_x , e_y , and e_θ), and (c) The trace of the coordinates (x_O^W, y_O^W)	86
3.11	Experiment for breast tissue core study: (a) Profiles of the commanded control inputs and observed displacements of the actuators, (b) Experimental setup, (c) Tissue core image at initial configuration, and (d) Tissue core image at final configuration.	88
3.12	Fiber-optic sensor calibration result.	90

3.13	Experimental setup for point-to-point control.	91
3.14	Tissue core images at the initial and final position (x,y) and orientation θ : (a) Experiment (1): $[x_d, y_d, \theta_d]^T = [-100\mu m, 100\mu m, 0^\circ]^T$, (b) Experiment (2): $[x_d, y_d, \theta_d]^T = [100\mu m, 100\mu m, 10^\circ]^T$, and (c) Experiment (3): $[x_d, y_d, \theta_d]^T = [100\mu m, 100\mu m, -10^\circ]^T$. Red and blue dotted lines represent the central lines of the stage at the initial and final state, respectively. Note: α_d is determined from the desired position and orientation using Eq. (3.11).	92
3.15	Trace of the tissue core sample: (a) Experiment (1): $[x_d, y_d, \theta_d]^T = [-100\mu m, 100\mu m, 0^\circ]^T$, (b) Experiment (2): $[x_d, y_d, \theta_d]^T = [100\mu m, 100\mu m, 10^\circ]^T$, and (c) Experiment (3): $[x_d, y_d, \theta_d]^T = [100\mu m, 100\mu m, -10^\circ]^T$. Note: α_d is determined from the desired position and orientation using Eq. (3.11).	93
3.16	Tracking errors and control inputs: (a) Experiment (1): $[x_d, y_d, \theta_d]^T = [-100\mu m, 100\mu m, 0^\circ]^T$, (b) Experiment (2): $[x_d, y_d, \theta_d]^T = [100\mu m, 100\mu m, 10^\circ]^T$, and (c) Experiment (3): $[x_d, y_d, \theta_d]^T = [100\mu m, 100\mu m, -10^\circ]^T$. Note: α_d is determined from the desired position and orientation using Eq. (3.11).	95
4.1	Schematic diagram of sample indentation with a spherical tip.	100
4.2	Micro force sensor with a $25 \mu m$ radius spherical tip (FT-S1000-LAT-TP, FemtoTools AG, Switzerland) used for the indentation experiment.	101
4.3	Schematic of support vector machine (SVM).	102
4.4	Breast tissue preparation: (a) Schematic of tissue microarray (TMA) and (b) A hematoxylin and eosin (H&E) image with annotated cancerous re- gions by a certified pathologist.	104
4.5	Experimental setup for microindentation.	105
4.6	Breast tissue indentation: (a) Indentation points as defined on a virtual grid and (b) A microscopic image of breast tissue during indentation.	106
4.7	Experimental result for the local tissue elasticity: (a) Elasticity map for one of the breast tissue samples, (b) Distribution of the measured elasticity values for the 5,000 indentation points (500 indentation points for each specimen; total of 10 specimens) of the cancerous breast tissue samples, and (c) Quantitative classification result for each sample.	108

4.8	Classification result for 10 cancerous breast tissue samples. A region in blue and red color represents a region classified as 'Normal' and 'Cancerous', respectively, while a dotted blue line on the H&E image encloses a cancerous region which is determined by a certified pathologist.	109
4.9	Quantitative classification result for each sample.	110
5.1	(a) Schematic diagram of biochip and (b) Process flow for fabricating the biochip.	112
5.2	Dimensions of the biochip and integrated elements. All dimensions are in microns. Drawings are not to scale.	114
5.3	SEM images of: (a) Microheater, (b) Cr/Au interdigitated electrodes over microheater, (c) Sensing layer, (d) Gold coated SU-8 pillars over Cr/Au electrode over silicon dioxide over sensing layer, and (e) Backside of silicon diaphragm. (f) A photograph of the biochip.	115
5.4	(a) Schematic diagram of breast tissue core preparation, (b) and (c) Photographs of paraffinized tissue and deparaffinized breast tissue.	116
5.5	SEM images of (a) Normal (27959), (b) Invasive ductal carcinoma (24353) breast tissue cores, (c) and (d) H&E images of normal and invasive ductal carcinoma breast tissue cores, respectively.	118
5.6	(a) Schematic diagram of the experimental setup and (b) Blown-up schematic diagram of the packaging system.	119
5.7	Wheatstone bridge circuit for electrical characterization of tissues.	120
5.8	Experimental results for electrical characterization of tissues.	122
5.9	(a) Force calibration curve of the fabricated sensor and (b) Force curves obtained from indenting normal and cancerous (IDC) breast tissues.	124
5.10	(a) Calibration plot of the microheater and (b) Temperature and thermal conductivity measurement of normal and cancerous (IDC) breast tissues. . .	125
5.11	Schematic of collagen structure.	126
5.12	Schematic of the portable diagnostic tool.	127

5.13	Compliance of breast tissue for two different electrical circuits for obtaining the electromechanical coupling factor (k_z) of the tissue along the Z-axis using tissue indentation tests.	129
5.14	Breast tissue sample preparation. (Legend A: Adjacent sections for IHC staining and special staining. Legend B: H&E stained "before/pre" section. Legend C: Cylinder sample to be indented. Legend D: H&E stained "after/post" section.	131
5.15	Example histological and immunohistological images of normal (#27955) and IDC (#36015) breast tissue: (a) H&E after sampling (b) H&E before sampling (c) Trichrome, (d) SMA, and (e) Fibronectin. Scale bar on each image indicates 500 μm	134
5.16	Experimental setup: (a) Overall view of the diagnostic tool and (b) Fabricated biochip in the package.	135
5.17	Stress-strain curves of the breast tissues under compression 25°C: (a) With electrically opened and (b) With electrically shorted.	136
5.18	Experimental result of breast tissue signatures in Z-axis at 25°C: (a) Tangent stiffness and (b) Electromechanical coupling factor.	137
6.1	SEM images of the MWCNT/PDMS elastomers fabricated by: (a) The shear mixing protocol with 10 wt% of MWCNT, (b) The shear mixing protocol with 5 wt% of MWCNT, (c) The IPA dispersion protocol with 10 wt% of MWCNT, and (d) The IPA dispersion protocol with 5 wt% of MWCNT.	147
6.2	Electrical and mechanical characteristics of MWCNT/PDMS elastomers in the dimension of 1(W) \times 25(L) \times 0.3(H) mm (effective length for the elongation test: 15 mm) without pure PDMS encapsulation.	148
6.3	MWCNT/PDMS-based flexible sensor fabrication process.	149
6.4	Proof-of-concept mock-up needle sensorized with the MWCNT/PDMS-based flexible sensor: (a) Exploded view of apparatus (b) Assembled sensor base and slide as upscaled rendering (left) and to-scale picture (right), and (c) Fully assembled to-scale sensor apparatus.	151
6.5	Calibration result of the MWCNT/PDMS-based flexible sensor in the mock-up needle.	153

LIST OF ABBREVIATIONS

3-RRR Three sets of RRR.

AFM Atomic Force Microscopy.

ANN Artificial Neural Network.

COM Center of Mass.

COR Center of Rotation.

DAQ Data Acquisition.

DC Direct Current.

DCIS Ductal Carcinoma *in situ*.

DOF Degree-of-freedom.

DRIE Deep Reactive Ion Etching.

ECM Extra-cellular Matrix.

EIT Electrical Impedance Tomography.

ER Estrogen Receptor.

ETM Electro-thermo-mechanical.

FE-SEM Field Emission Scanning Electron Microscopy.

FFPE Formalin-fixed Paraffin-embedded.

H&E Hematoxylin and Eosin.

IC Integrated Circuit.

IDC Invasive Ductal Carcinoma.

IHC Immunohistochemical.

ILC Invasive Lobular Carcinoma.

IPA Isopropyl Alcohol.

LCIS Lobular Carcinoma *in situ*.

MCS Modular Control System.

MEMS Micro-electro-mechanical Systems.

MWCNT Multi-walled Carbon Nanotube.

OC Open Circuit.

OD Outside Diameter.

Pap test Papanicolaou test.

PBS Phosphate-buffered Saline.

PCB Printed Circuit Board.

PDMS Polydimethylsiloxane.

PECVD Plasma Enhanced Chemical Vapor Deposition.

PEDOT:PSS poly(3,4-ethylenedioxythiophene) poly(styrenesulfonate).

PM Permanent Magnet.

PPR Two prismatic actuator and one rotational actuator.

PR Progesterone Receptor.

RH Relative Humidity.

RIE Reactive Ion Etching.

ROI Region of Interest.

ROM Range of Motion.

RRR Three rotational actuators.

SC Short Circuit.

SD Standard Deviation.

SEM Scanning Electron Microscopy.

SMA Smooth-muscle Actin.

SOI Silicon-on-insulator.

SVM Support Vector Machine.

TMA Tissue Microarray.

TS Tangent Stiffness.

UV Ultraviolet.

wt% Percentage by Weight.

SUMMARY

According to the cancer statistics from the American Cancer Society, breast cancer is the most common type of cancer in females and continues to be the second leading cause of cancer-related female deaths in the US. As breast cancer progresses, the microenvironment around cancerous breast tissues undergoes a physical reconfiguration to be tumor-permissive. The capability to monitor the signatures of cancer progression in breast tissue is important for improving the accuracy of diagnosis and early detection, which is critical factors for successful treatment and recovery of the patient. The goal of this project is to develop experimental and computational tools to characterize the onset and progression of cancer in human breast tissue at the micro-scale as additional diagnostic methods. More specifically, the proposal consists of following three research areas: 1) design, development, and control of micro-manipulators capable of *ex vivo* tissue indentation, 2) design and fabrication of micro-electromechanical system (MEMS) based sensors, which are a subsystem of the indentation system, for measuring various physical properties of human breast tissues, and 3) analysis and validation of the properties as biomarkers for breast cancer. The *ex vivo* experimental results show that the proposed system can capture various physical properties of human breast tissues reliably and distinguish cancerous tissues from normal breast tissues.

As an engineering approach to the goal, development of a multi-parameter characterization technique for benign and cancerous breast tissue in a high throughput manner is investigated in the dissertation. Much of the difficulty in rendering consistent evaluation of pathological tissue specimens arises from the qualitative impressions of observers. Hence, a quantitative phenotype to automatically characterize the type and stage of cancer based upon an objective measure of its morphology and mechanical properties could provide insight regarding the changes that occur in the tissue environment during the course of disease onset and progression. A myofibroblastic-derived, collagen-rich extra-cellular matrix

is one of the distinctive signatures on breast cancer progression and these changes of the cellular structure cause differences in physical properties of breast tissue. To characterize the spatial distribution of the physical properties of benign and cancerous breast tissue specimens and increase characterization throughput across specimens larger than the travel range of commercial micromanipulators, a customized microscope compatible microindentation system capable of aligning the tissue specimens has been developed. In addition, MEMS-based sensors have also been developed for measuring various type of tissue characteristics such as mechanical, electrical, and thermal properties at the micro-scale and the data acquired has been analyzed by machine learning algorithms to achieve automated cancer diagnostic process.

CHAPTER 1

INTRODUCTION AND BACKGROUND

1.1 Motivation

According to the cancer statistics from the American Cancer Society, 271,270 new cases (268,600 females and 2,670 males) and 42,260 deaths (41,760 females and 500 males) are expected to be reported as new breast cancer patients in the US alone during 2019 [1]. As breast cancer progresses, the microenvironment around cancerous breast tissues undergoes a physical reconfiguration to be tumor-permissive [2, 3]. A myofibroblastic-derived, collagen-rich extra-cellular matrix (ECM) is one of the distinctive signatures on breast cancer progression and these changes of the cellular structure cause differences in physical properties of breast tissue [4–7]. The capability to monitor the signatures of cancer progression in breast tissue is important for improving the accuracy of diagnosis and early detection, which is critical factors for successful treatment and recovery of the patient. Early detection of breast cancer is one of the key factors for increasing survival rates and improving patients’ quality of life [8]. Given the importance of early detection of breast cancer, investigators throughout the clinical and research communities are working to develop new biomarkers for facilitating more accurate breast cancer diagnosis.

Palpable lumps are often the first patient-reported symptoms of breast cancer [9]. Other physical properties, such as dense appearance on mammogram as well as hypo-reflectivity in ultrasound, establish the first line of screening and diagnosis of breast disease [10]. These gross manifestations are undoubtedly rooted in the underlying changes that occur in microscopic components of the tissue. Stroma stiffness as well as cytoskeletal tension is generally considered the main contributors of the overall rigidity of cancer tissue. The desmoplastic change that is often found around tumors is characterized by increased prolif-

eration of fibroblasts and high numbers of extracellular fibers. Fibroblast cells may undergo transformation into a myofibroblastic phenotype to be stained positively for smooth-muscle actin (SMA). It is believed that in case of breast cancer, in an effort to repair the damaged tissue caused by carcinoma cell invasion, the normal tissue stroma responds with excess collagen deposition [11, 12]. Accumulation of collagen in the benign tissue located proximal to the tumor leads to coagulation which may be associated with increasing tumor grade. This process causes changes in tissue properties such as elasticity and electrical impedance. The changes in elasticity and electrical conductivity of these tissues are related to the degree of malignancy [13, 14]. In addition, biophysical and electrophysiology studies reveal that the conductivity and elasticity of the cells and tissue changes during the course of progression of the disease [15–20]. A reliable method to quantify physical properties in normal and cancerous breast tissues could serve to support early detection of breast cancer and more accurate staging of specimens.

A breast cancer is classified as lobular carcinoma if it develops in lobules or ductal carcinoma if it develops in ducts [21]. The inner lining of milk ducts or the lobules that supply the ducts with milk are the areas for starting off for the occurrence of breast cancer [21]. A disruption of normal tissue homeostasis occurs during the growth of tumor and progression in the encompassing healthy tissues [21]. In the case of the breast cancer, an excess of collagen is deposited by the normal tissue stroma in an effort to repair the damaged tissue caused by carcinoma cell invasion [4, 5]. This accumulation of collagen in the benign tissue located proximal to the tumor leads to coagulation and causes changes in tissue elasticity [4, 5]. Breast cancer can be diagnosis by any unusual symptoms, although sometimes screening tests such as a mammogram and the Papanicolaou test (Pap test) are used for diagnosing breast cancer [22]. In most of the cases, these tests alone cannot determine the malignancy and biopsy is used to obtain definitive diagnosis results [22]. The life of an individual can be prolonged and the quality of life would be improved by early detection and treatment of the breast cancer. The importance of early cancer detection and accurate

staging of disease for improved treatment has prompted considerable research interest in quantifying the state and progression of cancer. The morphological signature in the tumor environment changes as cancer progresses [16, 18]. Literature reveals that the electrical and mechanical properties of the cells and tissue changes during the course of progression of the disease [14, 15, 20]. Therefore, micro-scale devices can provide a pathway to gain further insight into mechanical, electrical, histological, and immunohistochemical profile changes from onset through disease progression and can be used to demarcate the specific stages of cancer in epithelial and stromal regions providing quantitative indicators facilitating the diagnosis of breast cancer.

1.2 Related Works

1.2.1 MEMS-based Sensors for Characterization of Biological Tissues and Cells

The need for miniaturization of diagnostic and therapeutic devices has resulted in tremendous growth in the research on micro-electromechanical systems (MEMS) devices. MEMS devices are small in size and can be batch fabricated at low cost, thereby having a competitive advantage over other devices. The capability of analyzing and manipulating the biological materials at micro- and nano-scale and the possibility of incorporating it into portable lab-on-a-chip devices makes the MEMS sensor a potential candidate for diagnostic capabilities. Mechanical and electrical phenotyping have been demonstrated as promising techniques to study the progression of the breast cancer [18, 23, 24]. To use the MEMS devices for biomedical application, however, there are fabrication challenges apart from integrating it with electronics, signal processing, calibration and device packaging [25].

It is believed that in case of breast cancer, in an effort to repair the damaged tissue caused by carcinoma cell invasion, the normal tissue stroma responds with excess collagen deposition [11]. Accumulation of collagen in the benign tissue located proximal to the tumor leads to coagulation which may be associated with increasing tumor grade. This process causes changes in tissue elasticity [11]. The changes in elasticity and electrical

conductivity of these tissues are related to the degree of malignancy [13, 14, 16, 18, 19, 26–28]. Biophysical and electrophysiology studies reveal that the conductivity and elasticity of the cells and tissue changes during the course of progression of the disease [14–16, 18–20, 26]. A reliable method to quantify both mechanical and electrical properties in normal and diseased tissues could serve to support early detection and more accurate staging of specimens. Palpable lumps are often the first patient-reported symptoms of breast cancer [9]. Other physical properties, such as dense appearance on mammogram as well as hyporeflexivity in ultrasound, establish the first line of screening and diagnosis of breast disease [10]. These gross manifestations are undoubtedly rooted in the underlying changes that occur in microscopic components of the tissue. Stroma stiffness as well as cytoskeletal tension is generally considered the main contributors of the overall rigidity of cancer tissue. The desmoplastic change that is often found around tumors is characterized by increased proliferation of fibroblasts and high numbers of extracellular fibers. Fibroblast cells may undergo transformation into a myofibroblastic phenotype to be stained positively for SMA.

On the contrary, the breast cancer cells, which are the actual origin and carrier of disease, have been shown to be more pliable when examined at the microscopic scale, in both *in vitro* and *ex vivo* environments. Recent development of mechanical property measurement techniques at the micro- and nano-scale facilitates the study of cancer biomechanics [9, 10, 16, 18, 19, 29]. To study the nanomechanical properties associated inherent to metastatic adenocarcinoma cells conventional atomic force microscopy (AFM) and scanning-force microscopy techniques were used [16, 18, 19, 29]. When probed with AFM, breast cancer cells lines and tissues were shown to be less stiff than their benign counterparts in culture [9, 10, 16, 18, 19, 29]. In recent AFM experiment performed on human breast core biopsy, sampling regions near center of the tumors also displayed less stiffness whereas the peripheral region were stiff [18]. Various quantitative mechanical and physical assays has been studied to extract the elastic and viscoelastic deformability of cancer cells. A detailed study has also been carried out on mechanistic discussions of the changes in cell

deformability, cytoadherence, migration, invasion and tumor metastasis [19]. Our research group (RoboMed Lab. at Georgia Institute of Technology) has applied a range of different biophysical and biomechanical sensors on formalin-fixed paraffin-embedded (FFPE) specimen of breast cancer and observed that epithelial and stromal tissue exhibit different measurable characteristics which follow a distinctive vicissitudes from benign to cancerous state [29, 30].

For the mechanical characterization of breast tissue, nanoindentation is a common technique [18] and the device should be sensitive to measuring forces in the range of nano- to micro-Newton. The ability to micro-fabricate a cantilever relatively cheaply has made it possible to analyze and manipulate biological materials with high force and spatial resolution. The chief among these measurement techniques is the AFM. AFM has become the quintessential tool in the biophysics community for high-resolution imaging and manipulation of biological specimens across the length scale [18, 31]. Conceptually, the AFM is a simple apparatus, operating on the principle of measuring the interaction forces between a cantilever probe and a sample. The AFM consists of a tip attached (or micro-fabricated) at the end of a microfabricated cantilever, which is raster scanned on the surface of the specimen. The cantilever deflection (attractive/repulsive depending on the tip-sample distance) due to interactions with the specimen are measured optically using a photodetector. Although AFM has been considered as a reliable and accurate method for the mechanical characterization of breast tissues due to its high precision capabilities and minimal sample preparation [18], this method has inherent drawbacks of dependency on complex electronics, hefty optics and fragility of AFM cantilevers [32–36]. Piezoresistive sensing which translates the force to resistance overcomes the drawback of AFM. The piezoresistive sensors fabricated from silicon-on-insulator (SOI) has been used to study biomechanical property of the tissue [32, 33]. However, the piezoresistive sensors fabricated using silicon is fragile in nature. In addition, it has a high Young's modulus and thus for achieving large deflections the mechanical structures needs to be thin which deteriorates the mechanical

strength of the device. A conductive polymer, namely poly(3,4-ethylenedioxythiophene) poly(styrenesulfonate) (PEDOT:PSS) has a high sheet resistance than other conductive polymer, strong mechanical bending and ease of use which makes it a viable option to fabricate strain gauge sensors instead of silicon-based sensors [37, 38]. Polydimethylsiloxane (PDMS) being able to use in rapid prototyping with soft lithography and acting as a compliant polymer having moduli on the order of 1 *MPa* is explored for development of microfluidics [39, 40]. Combining the advantage of the flexibility of PDMS and conductivity of PEDOT:PSS, an array of the mechanical sensor can be fabricated.

There currently is no commercially available device that is capable of measuring electro-mechanical characteristics of tissue core samples simultaneously in a high throughput manner. This chapter presents the fabrication and application of a novel MEMS-based flexible sensor array for performing simultaneous, objective, reproducible measurements of the electro-mechanical properties of epithelial and stromal regions of normal and cancerous breast tissue cores.

1.2.2 Micro-manipulation Systems

Today, there exist numerous positioning stages on the market. Some of these stages are designed and tested by researchers to fit their specific applications and others are commercially available through Physik Instrumente, ThorLabs, Zaber, and Mad City Labs [41–44]. Each stage is designed or selected taking into consideration design constraints such as stage dimensions, actuated degrees-of-freedom, resolution, travel range, microscope focal lengths, etc. Table 1.1 lists the specifications for applicable one, two and three-DOF micro-positioning stages that are commercially available. Newport, SmarAct, Olympus, and Nikon products were also researched through online catalogs but did not offer multi-axis stages compatible with microscopy [45–48]. Newport offers 1-DOF linear micro-positioning systems with the potential for creating stacked actuator positioners [45]. SmarAct offers a variety of piezoactuated 1-DOF linear actuators (which can also be stacked)

as well as rotary positioners [46]. Both Newport and SmarAct offer 6-DOF stages called Hexapods and SmarPods respectively; however, these 6-DOF stages are not compatible with inverted microscopes and are more expensive than stages with fewer DOFs. These 6-DOF designs feature actuators mounted below the stage platform such that objective lenses cannot fit below the specimen [45, 46].

Table 1.1: Comparison of commercially available micro-positioning systems

DOF	Product Code	Actuation	Travel Range	Step Size	Resolution	Ref.
1 (Z)	MZS500-E	Piezoelectric	500 μm	0.25 μm	25 nm	[42]
2 (XY)	MLS203	DC Linear	110 \times 75 mm ²	0.1 μm	3 μm	[42]
2 (XY)	M-687.UN	Piezoelectric	135 \times 85 mm ²	–	0.1 μm	[41]
2 (XY)	ASR-E Series	Stepper	100 \times 120 mm ²	10 μm	0.15 μm	[43]
3 (XY θ)	M-880	Piezoelectric	20 \times 20 mm ² , 8°	0.75 μm	–	[41]

Current micro-positioning stages are limited in their ability to manipulate a target specimen. There are three main drawbacks associated with current stages when applied to tissue characterization tasks: Firstly, most stages allow for two or three-DOF motion but lack the ability to rotate the specimen [41–46]. This becomes a problem when the desired region of interest (ROI) is not a rectangular region aligned parallel to the slide or the wafer edge. The rotational capability would allow researchers to indent or otherwise characterize a smaller region than previously needed to ensure complete analysis of the ROI, thus increasing efficiency. Secondly, many microscope stages are manually adjusted or operate under open-loop control, thus failing to guarantee the correct position of the ROI [47, 48]. Closed-loop control schemes can help to minimize errors that arise from sources such as vibration during step movements, backlash between actuator gears, hysteresis, and dead reckoning. Thirdly, most stages accomplish either a large travel range or sub-micron resolution manipulation, but not both. Small travel ranges prevent efficient analysis of tissue microarrays (TMAs) and other material samples that have multiple or large ROIs. The multi-DOF micro-positioning stage developed in this work seeks to address these three drawbacks and allow for accurate and efficient material characterization at a lower cost than an average commercial stage.

In order for the microfabricated devices to make contact with the ROI, the stage must lower the sensing device to make contact with the specimen. This movement is achieved by high-resolution linear actuators, better than $0.1\ \mu\text{m}$ resolution for breast tissue indentation [29, 49]. The following are some of the most commonly used methods for linear actuation: Permanent magnet (PM) direct current (DC) motors, stepper motors, PM DC servomotors, linear motors, magnetic actuators, hydraulic actuators, pneumatic actuators, shape memory alloys, and piezoelectric actuators [50–56]. The literature suggests that 4-DOF micro-positioning can be best achieved by electromagnetic motors or piezoelectric actuators [55, 56].

The main advantage of using piezoelectrics over electromagnetic alternatives is the ease of miniaturization, high energy density (one tenth the volume and weight of electromagnetic materials with equivalent energy storage), high energy efficiency (in power range below $30\ \text{W}$), safety, and high resolution motion. Additionally, these actuators provide nearly frictionless motion and certain materials show little change in performance over a large temperature range. Piezoelectric actuators can achieve high resolution linear motion, up to approximately $1\ \text{nm}$ for displacements in the hundreds of microns, without bulky equipment or safety hazards, which are all significant advantages for design of a micro-positioning stage. Disadvantages of any piezoelectric actuator include output force limitations, tendency to vibrate during actuation, and limited travel range [50, 54–56].

The concept of piezoelectricity was first discovered in the 1880s, when the Curie brothers found that certain crystalline materials became electrically polarized when subjected to mechanical stress [54]. They quickly discovered that the reverse was also true— the material would change shape under the application of an electric field [54]. However, it was not until 1921 with the invention of the quartz crystal controlled oscillator that scientists recognized its potential advantages over current methods of actuation, namely relays and electromagnetic motors [54, 55]. Since then additional materials including barium titanate, lead zirconate titanate, PZT, and ZnO have been harnessed for their piezoelectric properties

and used in applications such as inkjet printers, diesel injection valves, and cooling pumps for electronic systems [54, 55].

ThorLabs recommends the integration of their MZS500-E Z-Axis Stage and MLS203 XY Scanning Stage to accomplish 3-DOF motion [42]. This design achieves large in-plane travel ranges but does not have the resolution desired for this application [42]. Resolution in the X and Y directions is limited by the actuation method, a brushless DC linear motor with precision linear bearings for stage guidance [42]. The company claims that there is zero error from backlash as the stage does not have a leadscrew [42]. The main contributor to positioning error appears to be the perpendicularity of the X and Y axes (called flatness by ThorLabs). ThorLabs cites a $\pm 1 \mu\text{m}$ error per 10 *mm* travel for each axis [42]. Although this stage is conveniently designed for use with Nikon, Olympus, and Zeiss microscopes, the ThorLabs stage places the rectangular frame-shaped Z-axis stage above the specimen and flush with the XY stage such that devices for material characterization cannot easily access the sample [42]. Additionally, the Z stage cites only a 500 μm travel range, insufficient movement for most material characterization devices to access the specimen while also staying clear of the overhead light source required for imaging [42, 48].

Physik Instrumente presents its M-687 PILine XY stage as an inverted microscope-compatible solution for 2-DOF motion [41]. The M-687 is compatible with both Nikon and Olympus microscopes and provides a large travel range with high resolution [41]. This resolution is expected for a piezoactuated stage [56]. According to the datasheet provided by Physik Instrumente, this stage is a viable option for 2-DOF motion, but does not allow for easy integration with other positioners to increase its positioning power from 2- to 4-DOF [41]. The specimen would need to be mounted on a rotary positioner, which would inherently increase the distance between objective lens and material sample. Should out-of-plane motion be required for material characterization devices, a Z-axis positioner would have to be mounted to the existing stacked actuator design. This could be challenging as $160 \times 110 \text{ mm}^2$ of the stage's surface area is used for a clear aperture and the remaining

material contains linear rails for the stacked design [41].

An alternative to the PI stage is offered by Zaber Inc. [43]. Their ASR-E Series XY Stage uses 2-phase stepper motors to provide precise motion in an crossed-roller guideway design [43]. This design is less desirable than its PI counterpart as it is limited to $10\text{ }\mu\text{m}$ step sizes and its resolution (cited as $0.15\text{ }\mu\text{m}$) does not incorporate the approximately $4\text{ }\mu\text{m}$ backlash caused by the use of leadscrews [41, 43]. It is difficult to predict how the stage will perform as the system's repeatability is only $2\text{ }\mu\text{m}$ [43].

Finally, the M-880, a Physik Instrumente stage, offers 3-DOF positioning but does not meet engineering requirements for the average microscope (such as stage dimensions) [41]. The parallel kinematic control scheme and piezoelectric actuation, however, are valuable features to consider [41]. Other designs such as those used in the work of Yang *et al.* and Ryu *et al.* utilize more complex joint configurations with flexure piezoactuators to achieve 3-DOF micro-positioning (adding out-of-plane motion or rotation respectively) [57, 58]. Stage designs using piezoelectric cylinders and metal flexures can also be used for high resolution linear motion as seen in Cai *et al.*, a XYZ micro-positioning stage for scanning probe microscopy [59]. Work by Tan *et al.* reinforces the importance of proper alignment of actuators and other components such as linear guideways to prevent positioning errors [60].

Knowledge of available products and challenges seen by current and past micro-positioning stages were taken into account, especially during the final selection of the joint scheme, actuators, and manufacturing and assembly of components. The next chapter will discuss the stage design and analysis, including geometric constraints and controllability followed by experimental results.

1.2.3 Signatures and Diagnosis of Breast Cancer

The mechanical properties (stiffness or elasticity) of the breast tissue change with the progression of the disease and act as a biomarker for detecting and studying cancerous breast

tissues. The change in stiffness can be directly linked to cancer progression [23]. The mechanical property that is known to be linked to the tumor formation is due to the modified structure of extracellular matrix (ECM) proteins which are found near breast cancer cells [24, 61]. Based on several studies using Atomic Force Microscopy (AFM) and micro-sensors, it is known that the stiffness of the epithelial and stromal layer in cancerous tissue significantly differs from the normal breast tissue [62]. An important current area of cancer research is to study the electro-thermo-mechanical (ETM) properties of the breast tissue simultaneously and provide more accurate diagnostic information about the breast cancer. In addition, interest also lies in developing a portable device for quick and accurate analysis of the breast cancer. However, no significant effort has been made towards the development of a portable device that is capable of measuring ETM properties of the breast tissue simultaneously.

One of the single largest risk factors for breast cancer is high density breast tissue [63–65]. It is known that breast tissue gets stiffer due to increased collagen during the process of transforming from benign to malignant [12, 66], however the reason why breast tissue with dense collagen increases the risk of breast cancer is not yet clearly understood at the molecular level [4, 67]. Provenzano et al. has visualized increased collagen on cancerous breast tissue as well as difference of collagen fibril organization on normal and cancerous breast tissue using nonlinear microscopy techniques such as multiphoton laser-scanning microscopy (MPLSM) and second harmonic generation (SHG) which provide powerful tools to image cellular autofluorescence and extracellular matrix (ECM) structure [4]. Though these imaging techniques do not measure the absolute amount of collagen, the results clearly show increased collagen in a tumor through a collagen distribution map based on the intensity of the fluorescent signal. As ECM undergoes changes with the progression of breast cancer, the electrical properties of breast tissue are also changing. Based on these property changes in cancerous breast tissue, researchers in the engineering community including our group have used mechanical and electrical characterization to

discriminate breast tissue as normal or cancerous. Elasticity and electric impedance have both been used as representative biomarkers of breast cancer [17, 68–75]. With the help of nanotechnology, phenotyping breast cancer at the cellular level has been recognized as one of the main research areas. However, the investigation of breast cancer at the cellular scale requires not only a bulky system but also a skilled operator. To translate the outcome from laboratory to clinical use, development of a portable and easy-to-use device is critical for clinical application.

Many research groups have investigated methods of finding quantitative biomarkers of breast cancer caused by the structural changes in breast tissue during cancer progression such as mechanical stiffness, electrical impedance, or thermal conductivity [63, 71, 73–77]. The change in mechanical stiffness of breast tissue is a well-known signature of breast cancer and it has been reported in a number of clinical research papers as a qualified diagnostic measure [62, 78, 79]. Due to inherent uncertainties in biological samples and the reported results in different experimental conditions, however, more elaborate experimental protocols and data analysis methodologies are required for the standardization to be used as a clinical diagnostic procedure.

Some researchers envision that machine learning will be a significant tool in many fields including medicine [80]. In fact, several machine learning techniques such as Bayesian classifier, artificial neural network (ANN), and support vector machine (SVM) have been studied for breast cancer diagnosis [81–84]. However, those studies focus on manipulating big data efficiently from medical history, symptoms, and other examination results, not on localizing the tumor, though there is a report regarding a localization of inclusion in phantom tissue via machine learning [85].

CHAPTER 2

MEMS-BASED SENSORS FOR CHARACTERIZATION OF CANCEROUS BREAST TISSUES

2.1 Introduction

Cancer has been recognized as a human ailment for thousands of years and yet the underlying mechanisms of its progression are still not fully understood [13, 14, 20, 86]. Breast cancer is the most prevalent type of cancer and second most frequent cause of cancer deaths in females [1]. A disruption of normal tissue homeostasis occurs during the growth of tumor and progression in the encompassing healthy tissue [11].

The use of flexible micro-electromechanical systems (MEMS) based device provides a unique opportunity in biomedical robotics such as characterization of normal and malignant tissues. This chapter reports on design and development of a flexible MEMS-based sensor array integrating mechanical and electrical sensors on the same platform to enable the study of the change in electro-mechanical properties of the benign and cancerous breast tissues. The analysis for the electrical characterization of the tissue specimens will be presented with demonstration of the feasibility of using the sensor for mechanical characterization of the tissue specimens.

The experimental design focuses on sensing differences and distinct changes of disparate tissue components of the breast tissue specimens and the corresponding tumor marker signatures of those components. This is achieved by careful preparation and configuration of tissue specimens as well as use of digital pathology methodology (Fig. 2.1). Tissue components revealed by histologic staining were highlighted by board-certified pathologist. These annotations were used to direct the MEMS-based flexible sensor array to the corresponding microscopic region-of-interest on the unstained serial slice of tissue.

Biomarker expression of the same regions was further revealed by immunohistochemical (IHC) staining of a stack of adjacent tissue slices. This design establishes unique tissue mechanical-electrical-histological-immunohistochemical profile of distinct tissue regions.

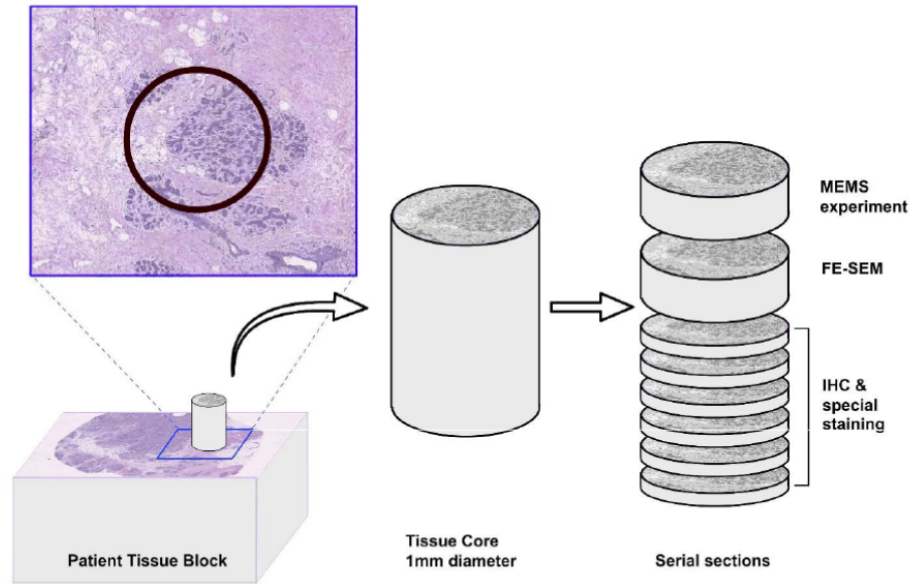


Figure 2.1: Tissue preparation: Hematoxylin and eosin (H&E) stained surface section of patient tissue block.

The device designed with an integrated array of strain gauges and electrically conducting SU-8 pillars is fabricated on polydimethylsiloxane (PDMS) material. Serial sections of tissue specimen were stained with related cancer markers to confirm the region saliency. It is widely accepted that a carcinoma *in situ*, which is enclosed in an intact lining of basement membrane, may progress into an invasive tumor and disseminate into surrounding tissue upon breaking this enclosure [87, 88]. As breast tumors are often heterogeneous in their composition, coexistence of *in situ* and invasive histologic type is often seen in the morphological presentation of cases. The pathological staging of tumor based on the existence and co-existence of these components reflects the aggressiveness of the disease and can provide valuable insight regarding the clinical management of the disease [89]. An absolute majority, 75-80%, of breast cancer cases are of ductal origin [49]. Lobular carcinoma of breast originates from the lobular and terminal duct epithelium and represents

another 5-10% of cases [90]. The experiments are for the *in situ* and invasive pathological groups of these subtypes to better understand the biomechanical and electrical change of breast cancer tissue during disease progression.

2.2 Flexible MEMS-based Electro-mechanical Sensor

2.2.1 Design and Fabrication

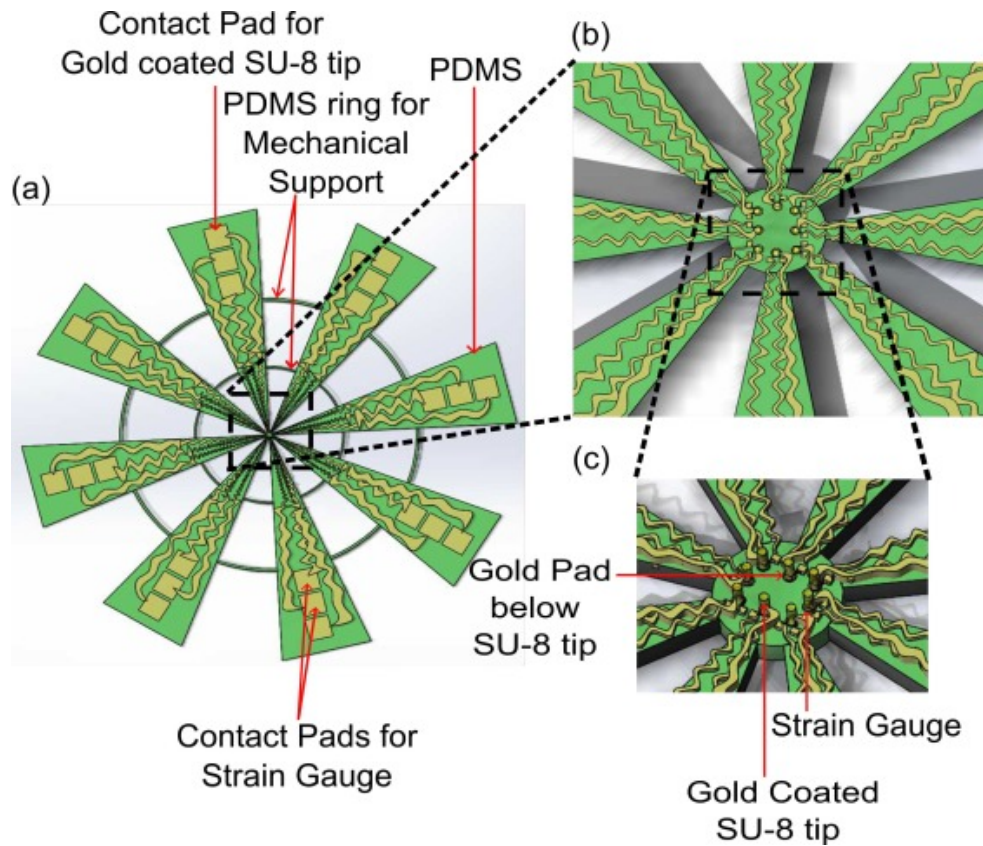


Figure 2.2: Flexible MEMS device: (a) Schematic diagram, (b) Magnified schematic of sensor array top view, and (c) Angled view.

The electro-mechanical sensor array is fabricated on the PDMS polymer substrate. PDMS (SYLGARD 184 from Sigma Aldrich) is coated on a 4-inch silicon (Si) wafer and the sensing layers are built one on another subsequently. The Si provides structural support during the fabrication. The process flow for the device is shown in Fig. 2.3. Six mask processes were used to fabricate the flexible electro-mechanical device. The fabrication pro-

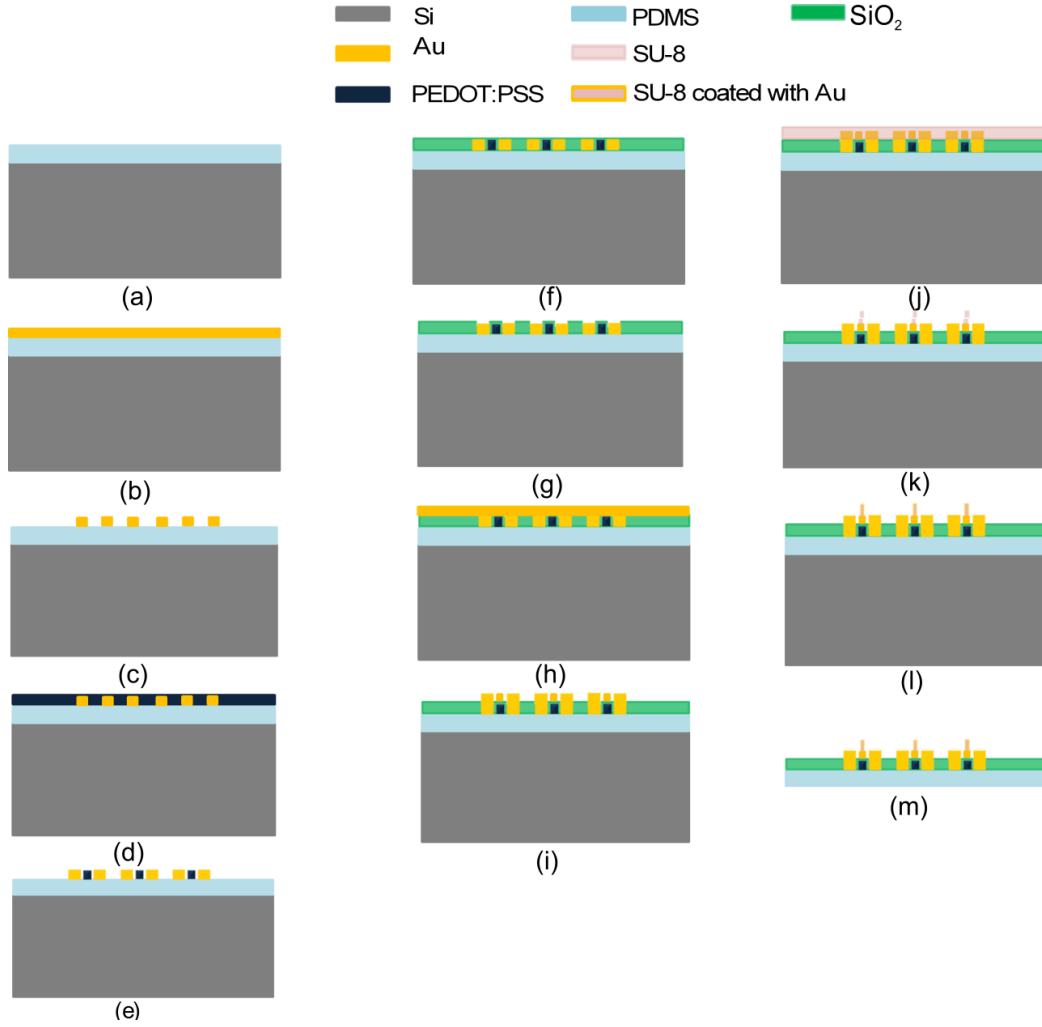


Figure 2.3: Process flow for flexible electro-mechanical sensor array.

cess is as follows: (a) PDMS (140 μm) was spin coated on Si wafers followed by curing at 90°C for 12 hours in furnace, (b) Chrome/gold (Cr/Au) (20 nm/500 nm) was deposited by using e-beam evaporator. As the PDMS and the metal deposited on PDMS cracked when the photoresist is prebaked at 90°C, an alternate approach was used in which the positive photoresist on metal coated PDMS was settled down for 6 minutes followed by baking in oven for 1 minute at 60°C before ultraviolet (UV) light exposure. This method keeps the PDMS and metal film intact, (c) Cr/Au was patterned to form electrodes for mechanical sensors (strain gauges), (d,e) PEDOT:PSS was spin coated and patterned to form array of strain gauges (0.6 μm thick), (f,g) Silicon dioxide (SiO₂ 0.8 μm) was deposited using low

temperature (80°C) plasma enhanced chemical vapor deposition (PECVD) and patterned to open contact pads for electrical connection, (h,i) Cr/Au (20 nm/500 nm) was deposited using e-beam evaporator and patterned to form electrode for electrical sensors, (j,k) SU-8 2025 was spin coated and patterned to form pillars of 30 μm diameter and 50 μm height, (l) SU-8 pillars were coated with Cr/Au using e-beam evaporation and lift-off technique to make it electrically conductive. The angle between the wafer and the gold evaporation source was kept at 45°. The final part of the process was to release the complete device from Si wafer to facilitate sensor array mounting. (m) The PDMS was peeled off from Si wafer to realize the device. The electro-mechanical sensor array covers 180 $\mu m \times 180 \mu m$ area while the complete device is 20 mm in diameter. The goal of the device is to measure the changes in the benign and cancerous breast tissue core and the dimensions of the active region (sensor array) was selected accordingly. The region of interest in breast tissue core is 180 $\mu m \times 180 \mu m$ in the present case. The diameter of the device was selected so as to facilitate the attachment of the device with the holder for experimental measurements. The length of the device could be changed depending on the holder design, but the active region dimensions need to be kept fixed.

The scanning electron microscopy (SEM) image of the mechanical sensor array and single strain gauge sensor is shown in Fig. 2.4(a) and 2.4(b). The strain gauge made from PEDOT:PSS polymer can withstand much larger strain due to its flexibility [91] while maintaining its conductivity which is not the case in metal based strain gauges [92]. Each strain gauge was 50 $\mu m \times 70 \mu m$ in size. Fig. 2.4(c) shows an array of Cr/Au electrodes/SiO₂/strain gauges. The circular Cr/Au pad (50 μm diameter) was used as the base for electrical contact to the SU-8 pillar (see Fig. 2.4(d)). Figure 2.4(e) shows the array of conducting SU-8 pillars integrated on the gold pads and Fig. 2.4(f) shows the magnified image of SU-8 pillars with top surface shining due to metal coating. It is to be noted that the top and only one side of SU-8 pillar was coated and not entire pillar, since it is necessary to obtain an electrical contact from the tip of the SU-8 pillar to the base to enable the

measurement of the electrical property of the tissue. These pillars serve a dual purpose in the device design namely: (a) transferring the force to strain gauge and (b) acting as the conductive probe for electrical characterization (Electrode E1).

The SU-8 pillar diameter was kept at $30\ \mu m$ as it has two advantages: (a) Ease of alignment at the center of the gold pad, which is $50\ \mu m$ in diameter, and (b) metal coating using lift-off technique is easy if the pillar size is less than the gold pad. The spacing between the pillars was chosen to facilitate the metal coating on SU-8 pillars. The SEM image of realized device is shown in Fig. 2.5, while Fig. 2.6 shows the photo of the flexible electro-mechanical device. The connection from the electro-mechanical sensor array to the contact pads ($1\ mm \times 1\ mm$) is through gold serpentine geometry to enable a compact footprint for routing the measured signal to the electrical circuit.

2.2.2 Strain Detection Mechanism for Mechanical Sensors

Due to the piezoresistive effect, the electrical resistance of the film is proportional to the strain of the film [93]. The schematic diagram of strain sensing mechanism is shown in Fig. 2.7.

The known force value using AFM cantilever is applied on the SU-8 pillar resulting in bending of the strain sensor and corresponding change in resistance is measured. The gauge factor G is given by following relationship:

$$G\varepsilon = \frac{\Delta R}{R_i} = \frac{R_s - R_i}{R_i} \quad (2.1)$$

where, ε , R_i and R_s are the strain, initial resistance of the sensor, and sensor resistance on curved surface, respectively.

The gauge factor calculation determines the strain from the change in resistance. When the strain gauge integrated on flexible substrate is deformed to form curved surface, it

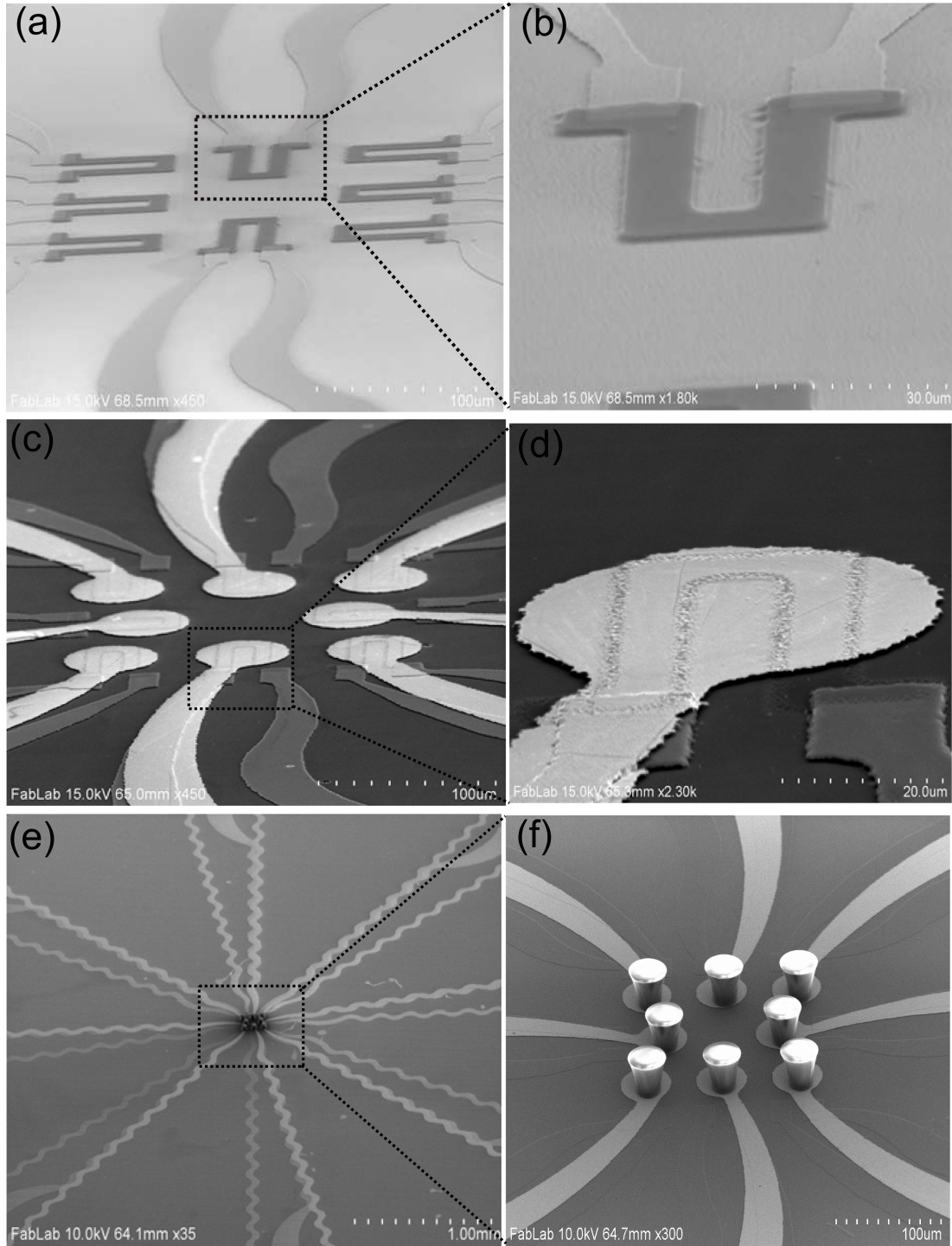


Figure 2.4: Sensor fabrication SEM images: (a) Strain gauge array, (b) Single strain gauge, (c) Array of devices showing gold pads/SiO₂/strain gauge, (d) Magnified image of single device, (e) Array of gold coated SU-8 pillars/gold pads/SiO₂/strain gauges, and (f) Magnified images of SU-8 pillars on gold pads (inset shows gold coated SU-8 pillars on gold pads).

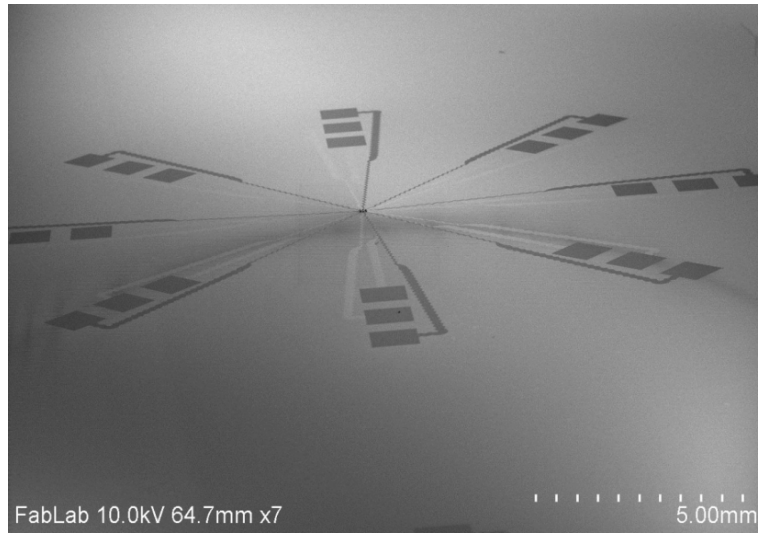


Figure 2.5: SEM image of the device.

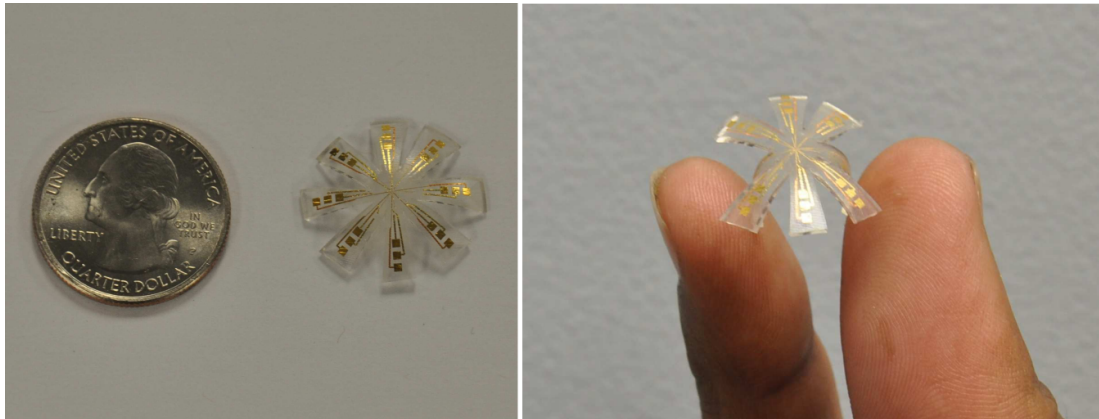


Figure 2.6: Photos of flexible MEMS-based device.

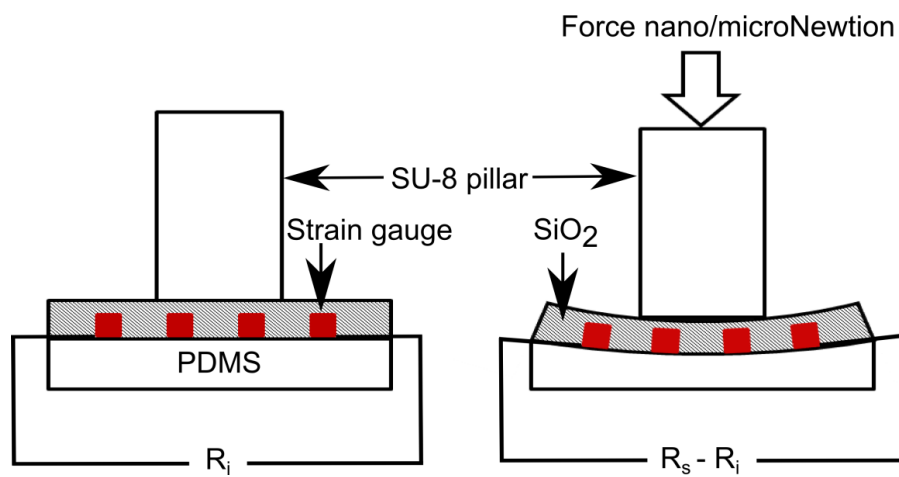


Figure 2.7: Strain sensing mechanism for PEDOT:PSS based sensor.

results in surface strain ϵ given by:

$$\epsilon = \frac{t}{2r} \quad (2.2)$$

where, r is the radius of curvature and t is the substrate thickness. The substrate (PDMS) thickness was $140 \mu m$ in the present study. To measure the gauge factor of the strain gauges, the flexible device was placed on the curved surface of cylinders with different radii. The schematic representation and photo of actual measurement setup for measuring the gauge factor is shown in Fig. 2.8.

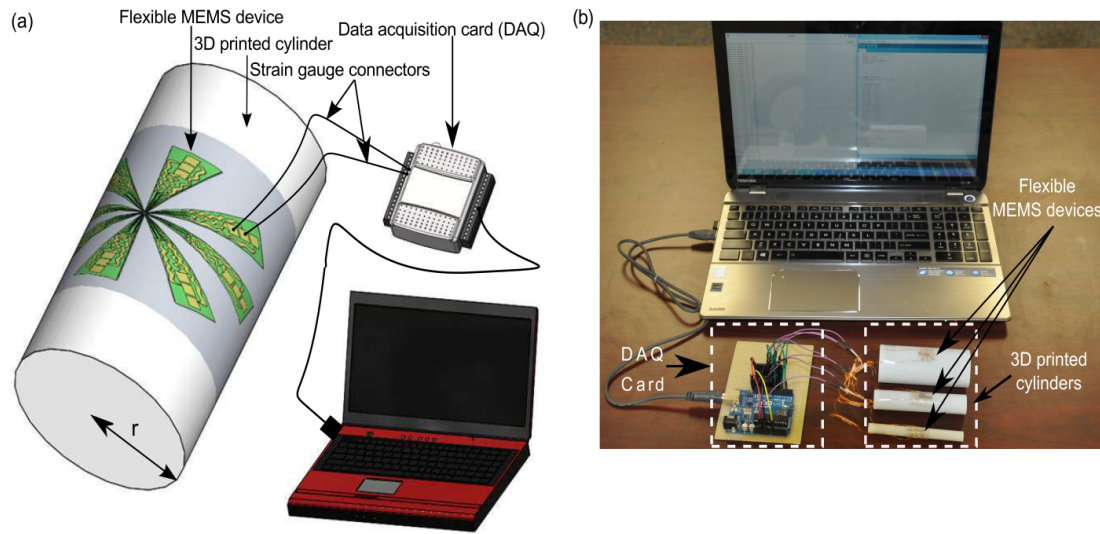


Figure 2.8: Measuring electrical output from single strain sensor: (a) Schematics and (b) Experimental setup.

The change in resistance ΔR , strain ϵ and gauge factor G are then calculated. The resistance of the strain gauges was measured to be $1.2 \pm 0.1 k\Omega$ in its undeformed configuration. The induced strains in the sensor were found to be 1.4, 0.7 and 0.35 when placed on the cylinder with radii of 5 mm, 10 mm, and 20 mm, respectively. Using Eq. 2.1, the measured gauge factor of the sensor was determined to be 4.0 ± 0.1 .

2.2.3 Linear Regression Model

For accurate estimation of material properties of the tissue, researchers have studied contact models that describe tissue behaviors [94] and algorithms finding contact point between

a sensor and tissue [29]. Since most of the tissue contact models are based on force-indentation relationship, piezoresistive type sensors that have resistance as an output should be calibrated in terms of force to be applied to conventional contact models. For n number of data sets in calibration, output resistance R_s , and contact F have a linear relationship to the sensor deformation δ_s , when contact occurs at the k^{th} index. Thus:

$$(R_s)_i = \begin{cases} \alpha_{11} + \alpha_{12}(\delta_s)_i + \varepsilon_1, & \text{if } i \leq k. \\ \alpha_{21} + \alpha_{22}(\delta_s)_i + \varepsilon_2, & \text{if } k + 1 \leq i \leq n. \end{cases} \quad (2.3)$$

$$F_i = k_s \delta_s = \begin{cases} k_s \left[\frac{(R_s)_i - \alpha_{11} + \varepsilon_1}{\alpha_{12}} \right], & \text{if } i \leq k. \\ k_s \left[\frac{(R_s)_i - \alpha_{21} + \varepsilon_2}{\alpha_{22}} \right], & \text{if } k + 1 \leq i \leq n. \end{cases} \quad (2.4)$$

where the values $\alpha_j = [\alpha_{j1}(\Omega) \ \alpha_{j2}(\Omega/\mu m)]$; ($j=1,2$) are linearly regressed parameters in the non-contact and contact regime, respectively, k_s is the calibrated spring constant of the sensor and ε_j ; ($j=1,2$) are the errors that typically have different distribution depending on the material interaction with the sensor [95]. In this model, ε_1 is caused by the viscous interaction between the sensor and phosphate-buffered saline (PBS) solution covering the tissue, while ε_2 are primarily results from sensor-tissue friction. Material properties in conventional contact models vary with the determination of contact point within the same data set. The contact point can be determined by a variety of methods such as estimating the location of a threshold slope [96], curve fitting [97], and statistical modeling [29]. One of the advantages of the sensor that has been developed is that it allows current flow on contact and hence it acts as a switch to detect when the contact has occurred.

In AFM studies for tissue indentation [29], the deformation depth of tissue $\hat{\delta}_t$ can be calculated in the contact region ($k + 1 \leq i \leq n$) as the difference of sensor deflection with respect to sensor position in the Z direction as shown in Eq. 2.5. Thus:

$$(\hat{\delta}_t)_i = \Delta Z_s - \delta_s = (Z_s)_i - (Z_s)_k - \frac{(R_s)_i - \alpha_{21} + \varepsilon_2}{\alpha_{22}} \quad (2.5)$$

By using the tissue deformation and force data, elastic modulus of tissue can be estimated by Zhang's contact model of a cylindrical tip that requires geometric information (of the tissue and the indenter), reaction force, and tissue deformation depth [98].

2.2.4 Spring Constant Measurement

To measure the spring constant of the strain gauge sensor, an AFM probe (pre-calibrated) was used as a reference cantilever and pressed it on the SU-8 pillar with a known force (see Fig. 2.9). The spring constant k_{ref} of the AFM probe was calibrated using the thermal method [99]. The AFM force curve is obtained from the end of test cantilever upon pressing the SU-8 pillar. The measured transmitted force is given by:

$$F_{AFM} = k_{ref}(def_1 - def_0) \quad (2.6)$$

where, def_0 and def_1 are the initial and final deflection of the AFM cantilever which is sensed by the photodiode (see Fig. 2.9 and Fig. 2.10). The deflection in the sensor, δ_s , is given by the difference in the net deflection of the test cantilever and Z-travel. Figure 2.11 shows the deflection of the sensor δ_s for increasing force values. The spring constant of the fabricated sensor was $0.42 \text{ nN}/\mu\text{m}$. The goodness of fit (R^2 -value) was found to be 0.9870, which shows that the sensor has a linear response.

2.2.5 Tissue Preparation and Annotation

To facilitate the electro-mechanical characterization of the tissue, a gold pad having micro-grids (Electrode E2) was fabricated on glass wafer to hold the tissue. Cr/Au (20 nm/800 nm) was deposited using e-beam evaporation and patterned to form micro-grids. Figure 2.12(a) and (c) show the SEM images of the gold pad having micro-grid and tissue placed on micro-grid, respectively.

The glass wafer needs to be moisture free to enhance the adhesion of Cr/Au. Failure to

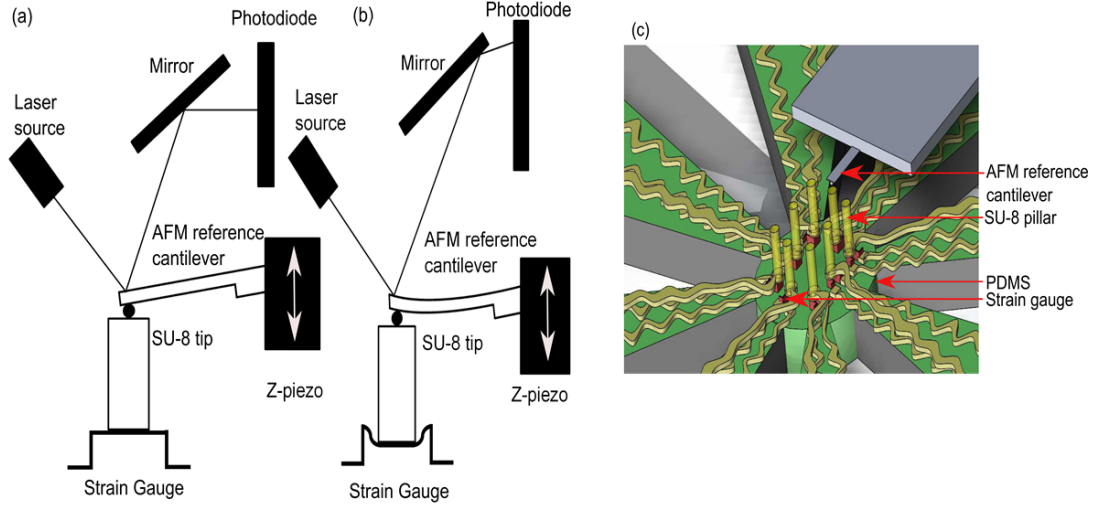


Figure 2.9: Schematic diagram of the AFM configuration used for spring constant measurement of PEDOT:PSS strain gauge using reference cantilever method: 2D representation of (a) AFM cantilever in contact with SU-8 pillar/strain gauge, (b) AFM cantilever pressed against the SU-8 pillar/strain gauge to a preset force value, and (c) 3D representation of spring constant measurement.

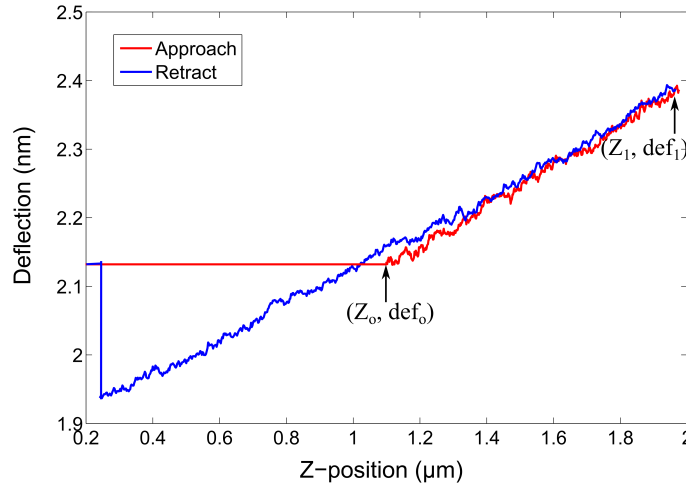


Figure 2.10: AFM force curve on the SU-8 pillar/strain gauge/PDMS.

which resulted in the crumpled micro-grid as shown in Fig. 2.12(b). The inverted microscope was used for observing the tissue samples and thus a grid was used instead of using a thick pad. The tissue is placed on the conducting micro-grid. Formalin-fixed paraffin-embedded tumor and normal breast tissue blocks were carefully identified from Biospecimen Repository at Rutgers Cancer Institute of New Jersey. With guidance of an annotated

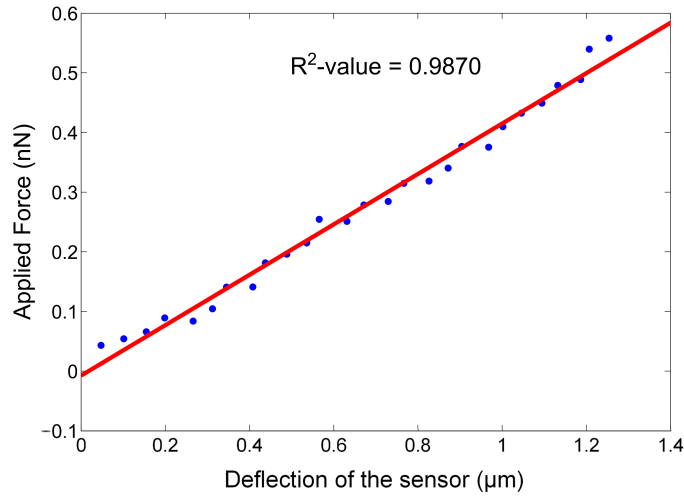


Figure 2.11: Spring constant measurement of sensor.

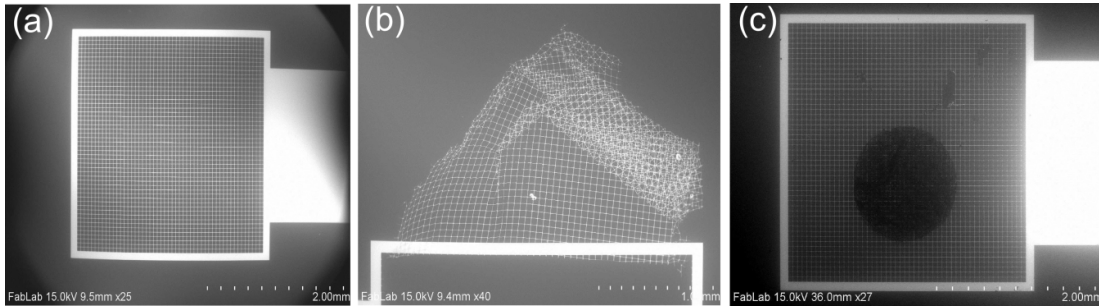


Figure 2.12: SEM image of (a) Micro-grid, (b) Crumpled micro-grid, and (c) Breast tissue core placed on micro-grid.

adjacent hematoxylin and eosin (H&E) slice, one sample of tissue core (1 *mm* diameter) was extracted from each tissue block and inserted into an individual pre-punctured paraffin blocks to make a mini-tissue microarray (TMA) using tissue microarrayer Breecher ATA-27. The mini-TMAs were sectioned at 8 μm thickness and carefully placed at the center of the gold pad containing micro-grids in 42-44°C water bath. The TMAs placed on the grids were de-paraffinized and stored in PBS until the experiment. An adjacent 5 *mm* section of each mini-TMA was stained, digitized into whole slide image, as well as quality controlled and annotated by a certified pathologist. The whole slide images, with designated tissue regions highlighted as tissue annotation were stored at the Rutgers Cancer Institute of New Jersey whole slide image web service. Figure 2.13 shows the H&E and optical image of be-

nign and cancerous breast tissue used in present work. Green and red areas are the regions of interest.

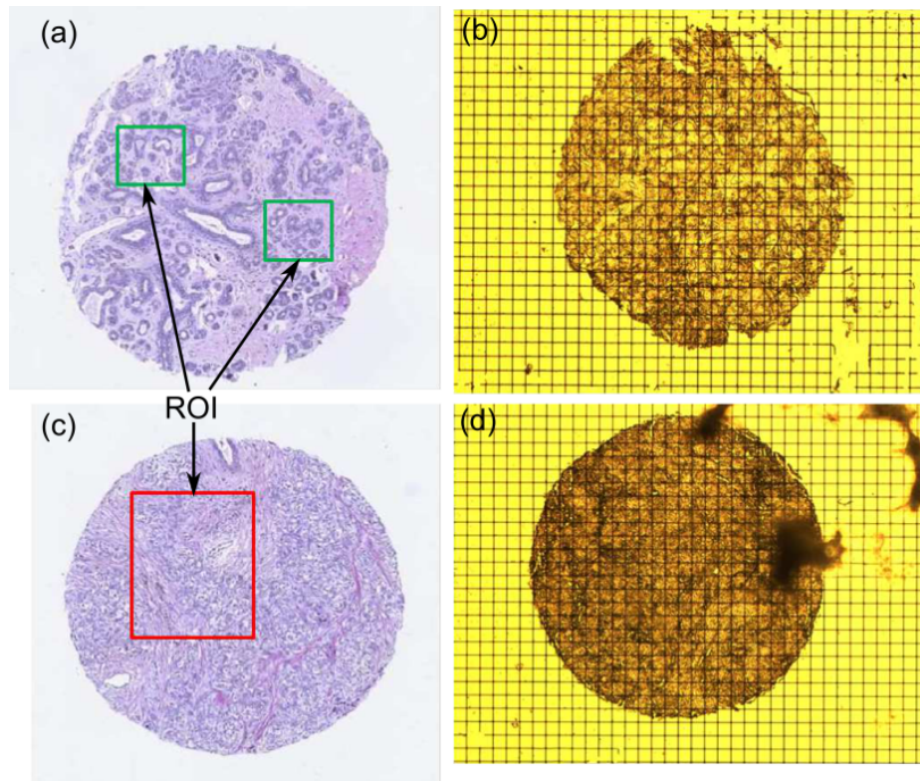


Figure 2.13: Breast tissue core: (a) and (b) H&E image and optical image of benign sample, (c) and (d) H&E image and optical image of cancerous sample.

2.2.6 Sensitivity Measurement and Sensor Performance of the Breast Tissue

The strain gauges used for mechanical characterization change their resistance on applying strain and these strain values are measured to voltage by an electronic module consisting of multiplexer and data acquisition card. To measure the sensitivity of the sensor array, the device was mounted on a 3D-printed cone shaped holder (see Fig. 2.14) which was attached to the micromanipulator MP-285 (Sutter Instrument Company, CA, USA). Using MP-285, the device was pressed down on a glass substrate to measure its sensitivity. For ease of approaching, right angle (90°) contact was assumed only during the measurement since the sensor output caused by bending of the pillar from inclined indentation are not distinguished from the output of z-direction compression of the pillar intended.

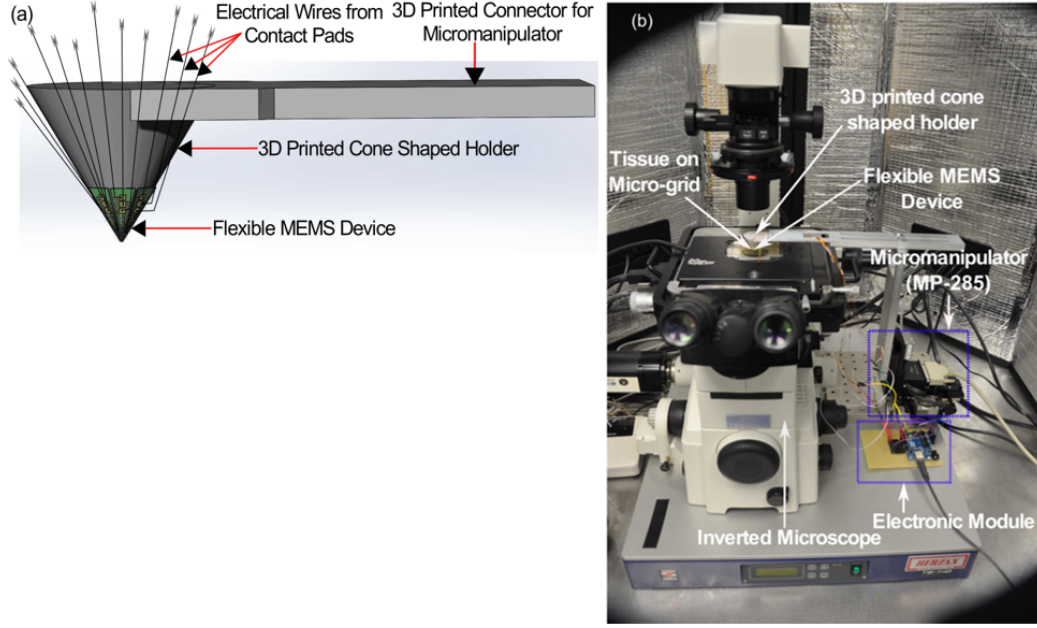


Figure 2.14: Device mounted on cone shape holder for mechanical and electrical characterization: (a) Schematic and (b) Actual photograph.

To avoid inclined contact, the area of the sensor where the pillars are located was mounted on the flat tip of the cone shape holder and maximum height of the profile (i.e. difference between maximum peak height and maximum valley depth) of the tissue was under $0.5 \mu m$, which was much smaller compared to the dimension of the pillars.

A linear regression model was used to find the correlation between the changes in the sensor reading to the sensor displacement (see Fig. 2.15). Figure 2.15 is the output voltage obtained from the sensor array and is a linear fit when pressed on the glass substrate. The data obtained is used to calculate the force from each sensor using linear regression model. The average goodness of fit (R^2 -value) was found to be 0.9966, which shows that the sensor has a linear response. The average sensitivity of the eight sensors was found to be $4.2308 \times 10^{-4} V/\mu m$.

The sensor was pressed down on benign and cancerous tissue for $7 \mu m$. A clear demarcation between benign and cancerous breast tissue cores was obtained. It was further observed that, for the same z-displacement, the change in voltage for benign core was higher than that for the cancerous breast tissue core (see Fig. 2.16(a)). The force vs. Z-

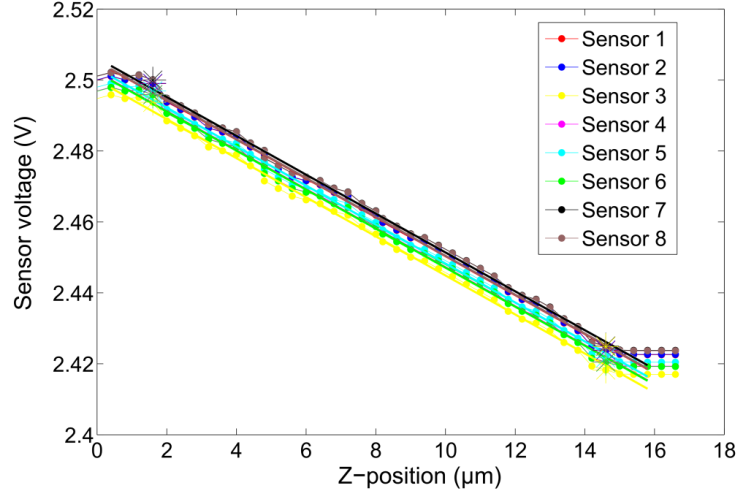


Figure 2.15: Sensitivity measurement of fabricated sensor array.

position obtained from the benign and cancerous breast tissue by pressing the sensor array on the tissue for $7 \mu m$ depth is shown in Fig. 2.16(b). The tissue elasticity, E is estimated by using Zhang's contact model [98] with a cylindrical tip and is given by:

$$E = \frac{F(1 - \nu^2)}{2r\kappa\delta_t} = \frac{k_s\delta_s(1 - \nu^2)}{2r\kappa(\Delta Z - \delta_s)} \quad (2.7)$$

where, F is contact force, ν is Poisson's ratio, r is the radius of indenter, δ_t is the tissue deformation, and κ value is a unitless coefficient determined by the geometry of the indenter.

The spring constant of the sensor and sensor deflection were obtained from the measured spring constant (from the section 2.2.4) and linear regression model (from the section 2.2.3), respectively. Multiplication of these two values yields contact force and δ_t is determined by the difference between Z-position of the manipulator and sensor deflection. By using the table of κ -values, assuming that the tissue is incompressible [98], the elasticity of the tissue can be determined.

The values of tissue elasticity estimated from the observed reaction force (see Fig. 2.16(b)) when the sensor is pressed down to $7 \mu m$ on benign and cancerous tissue are

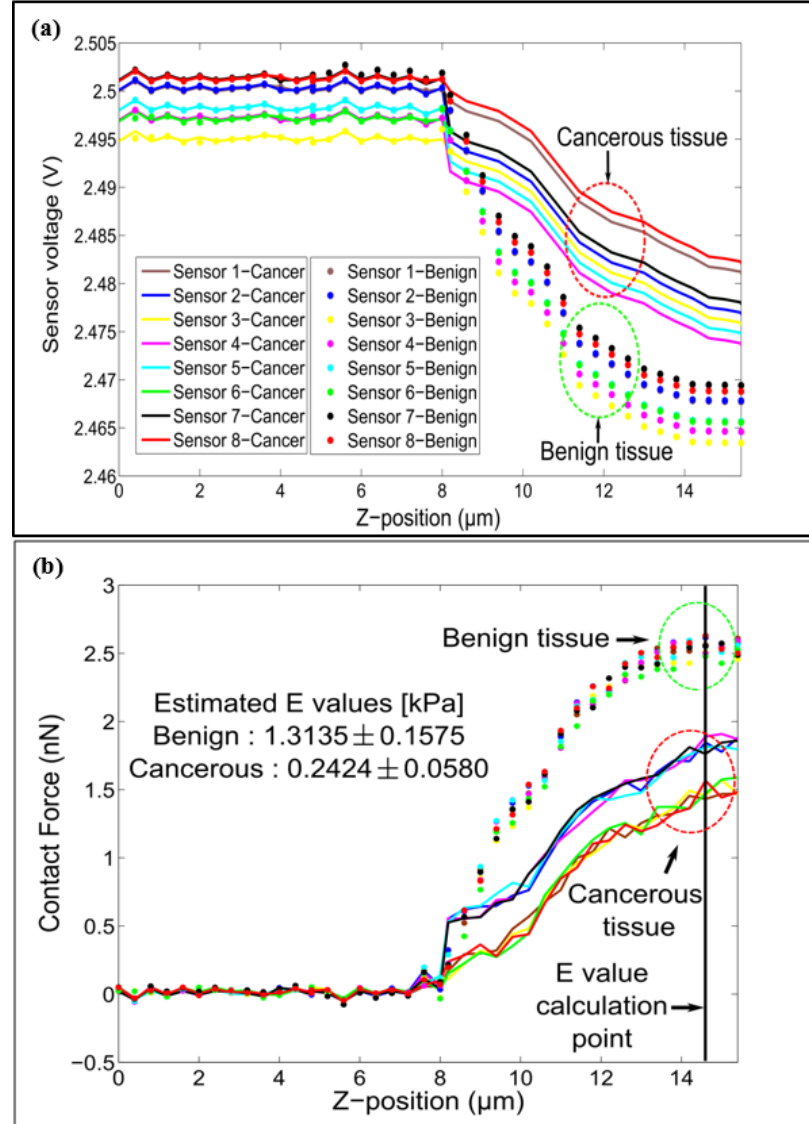


Figure 2.16: (a) Mechanical characterization: response of device on benign and cancerous breast tissue and (b) Force curves obtained from normal and cancerous breast tissue.

1.3135 ± 0.1575 [kPa] and 0.2424 ± 0.0580 [kPa], respectively. It is important to note that since the sensor is also inherently flexible, not all of the $7 \mu\text{m}$ motion of the tissue after contacting the tissue is translated to the deformation of the tissue. The sensor motion of $7 \mu\text{m}$ constant was kept in all trials for consistency.

For the micron size breast tissue, the stiffness of normal tissues is higher than cancerous tissue cores. For the micron size breast tissue core ($8 \mu\text{m}$ thick in the present case), the electrically conductive SU-8 pillars (E1) provides an easy way to complete the electrically

conducting path. The height of the SU-8 pillars was kept at $50\text{ }\mu\text{m}$ as it facilitated in electrical measurements without breaking. Increasing the height of pillars to $100\text{ }\mu\text{m}$ caused breakage of pillars while decreasing the size to $20\text{-}30\text{ }\mu\text{m}$ made electrical measurements difficult. To measure the electrical resistance of the breast tissue, a constant voltage is applied between electrode E1 and electrode E2. When the electrode (E1) touches the tissue sample, the current passes through the top electrode (E1) through the breast tissue to the bottom electrode (E2). Depending on the resistance of the breast tissue, the current passing through the tissue would be different and that is reflected in the measured voltage. Figure 16 shows the voltage values obtained from the sensor when pressed down (about $4\text{ }\mu\text{m}$) on the tissue core. From Fig. 2.17, there is a difference in the conductivity of the breast tissue between benign and cancerous tissue cores. It is important to note that a variety of other electrical signals of varying frequency can be passed through the tissue and that the tissue resistance is not the only electrical parameter for characterizing the tissue electrical properties. Another important parameter of the electrical property of the tissue could be the electrical impedance of the tissue itself.

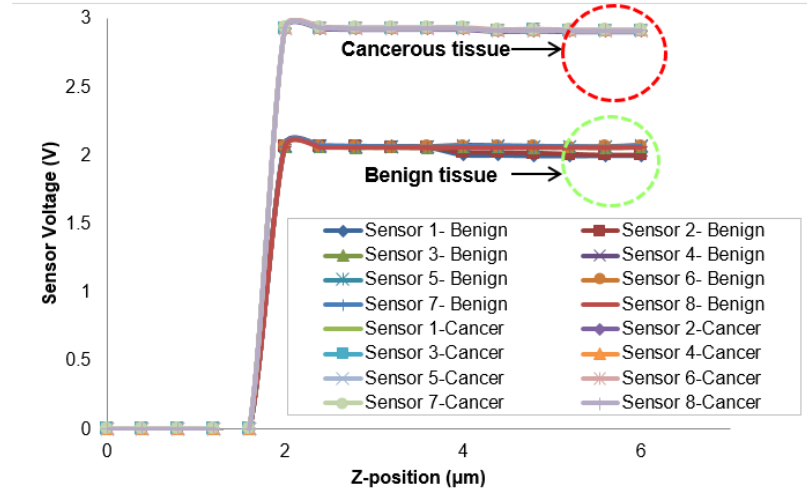


Figure 2.17: Electrical characterization: response of device on benign and cancerous breast tissue.

The goal of the present work was to fabricate flexible sensor array and to explore it as a possible candidate for electro-mechanical measurements of micron size tissue cores. Thus,

only one sample of each type (benign and cancer) is used for measurement. More extensive studies of benign and diseased breast tissue cores are required for a stronger claim of the capability of a device to delineate the type of tissue core.

2.3 Electro-mechanical Characterization of Human Breast Tissues

2.3.1 Experimental Setup

The process flow for fabricating flexible micro-electro-mechanical sensor array is shown in Fig. 2.18(a). Due to the known issue of a mismatch of the coefficient of thermal expansion (CTE) between the photoresist and PDMS, an alternate approach is used for patterning metal on PDMS, in which, instead of prebaking photoresist at high temperature, it was allowed to settle for about 10 minutes before UV exposure. This method keeps the PDMS and metal film intact. The advantages of PEDOT:PSS conducting polymer are: easy to use, strong mechanical bending and higher sheet resistance than other conducting polymer which makes it a feasible material for fabricating the strain gauges [37, 38].

The SU-8 pillars in the design are coated with gold to enable transmission of current from the SU-8 pillar to the base plate through the tissue specimen. Thus, the novelty of the design is that the SU-8 pillars act as both a mechanical force transmission component (by transmitting the indentation force to the strain gauges) as well as electrically conducting probes to measure the tissue resistance. Figure 2.18(b) shows the flat and curved schematic diagrams of the device. The SEM images of the array of strain gauge, array of gold pads over strain gauge separated by insulating layer, and array of SU-8 pillars (acting as top electrodes E1) can be seen from Fig. 2.18(c). The photograph of the device is shown in Fig. 2.18(d). Figure 2.19(a) shows the overall experimental system comprising of the inverted microscope, MP-285 micromanipulator, and sensor electronics. The flexible sensor array was mounted on 3D-printed cone shaped holder (Fig. 2.19(b)). The breast tissue cores were placed on the bottom electrodes (E2) which consists of metallic grids (5 μm width and 20 μm spacing) (Fig. 2.19(c)). In the present work, an inverted microscope which

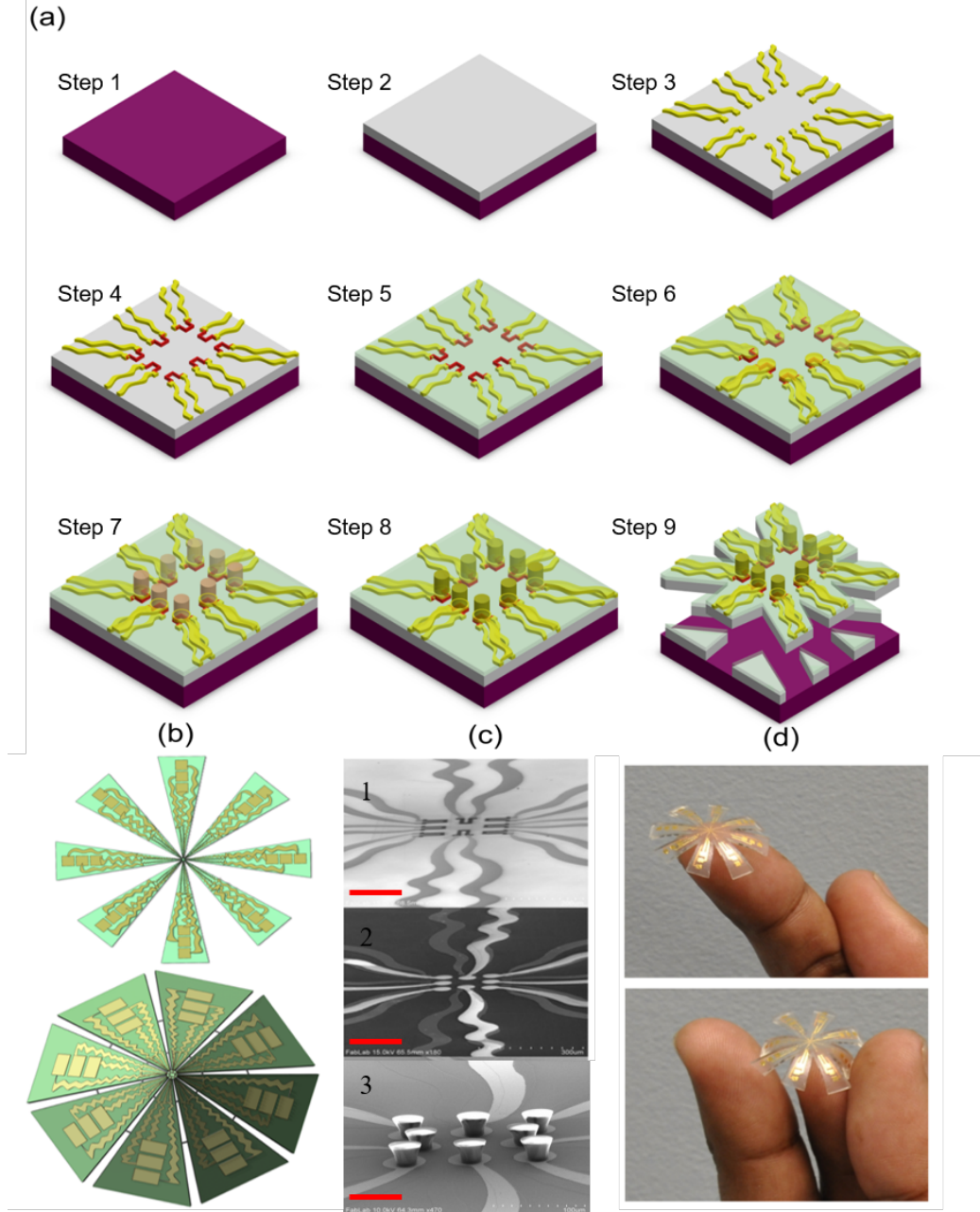


Figure 2.18: Flexible electro-mechanical device: (a) Schematic process for the fabrication of electro-mechanical device incorporating PDMS and SU-8 polymers, (b) Flat and curved schematic of the device, (c) Cross-sectional SEM images of 1) Array of strain gauges, 2) Circular pads over strain gauges, and 3) Array of gold coated SU-8 pillars on gold pads (Scale bar = 100 μm), and (d) Photographs of the final device.

enforces the use of grid pattern in the bottom electrodes instead of metallic pad was used.

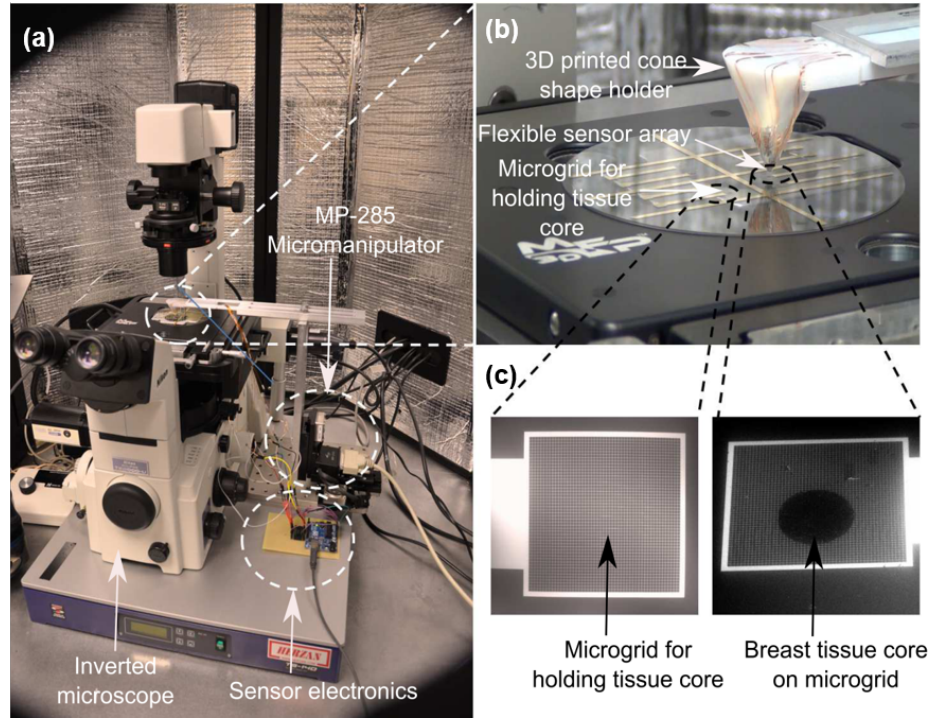


Figure 2.19: Experimental set-up for measuring electrical and mechanical properties of the breast tissue: (a) The inverted microscope facilitates in directing the flexible sensor array on to the region-of-interest in the breast tissue core, (b) The flexible sensor array mounted on a 3D-printed cone, and (c) Bottom electrodes with micro-grids for holding tissue cores. The scale bar is 200 μm .

2.3.2 Study Design

This is a retrospective study based on banked tumor tissue specimen obtained from Biospecimen Repository Service at Rutgers Cancer Institute of New Jersey. Usage of de-identified human specimen in this study was approved by Institutional Review Board of Rutgers Cancer Institute of New Jersey, Rutgers University, The State University of New Jersey. Disease group of tissue specimen was first determined from deidentified pathology description associated with each specimen, and subsequently verified by board-certified pathologist by examining specimen morphology under the microscope. (Disease groups of ductal hyperplasia and lobular hyperplasia were not included in the reported data as there was not enough representative specimens identified and constructed from these groups.)

2.3.3 Sample Preparation

Candidate breast tissue blocks with different histologic types were acquired from the Biospecimen Repository Core Facility at Rutgers Cancer Institute of New Jersey according to IRB protocols which have been approved by Rutgers University. H&E sections of these donor blocks were examined by board-certified pathologist to highlight regions corresponding to the desired histologic groups. Tissue cores of 1 *mm* diameter were extracted and placed into a recipient paraffin block. One additional 0.6 *mm* diameter tissue core of different origin was placed at distance of 4 *mm* from the breast tissue cores as orientation aid in subsequent experiment steps. The board-certified pathologist quality-controlled the H&E stained section of the two-core TMAs and highlighted regions-of-interests (ROIs) of the desired morphology. The H&E section was digitized by Trestle MedMicroscopy system at 20 \times equipment setting. The resulting whole slide images were hosted for online access at Rutgers Cancer Institute Imaging Shared Resource with the ROIs digitally annotated.

The first 10 μ m section was carefully transferred to the device by positioning the 1 *mm* breast tissue core at center of the microgrid. Another 10 μ m section was mounted on cover glass and deparaffinized for field-emission-scanning-electron-microscopy (FE-SEM) imaging. The rest of the tissue block was serial-sectioned at 4 μ m thickness for immunohistochemical stains.

All the designed tissue cores were assembled onto a device, the device was deparaffinized and kept in PBS before performing the experiment.

2.3.4 Immunohistochemical (IHC) Staining

- General Protocol

All IHC were performed using Ventana Discovery XT automated IHC/ISH slide staining system. Slides were cut at 4-5 μ m. Deparaffinization and antigen retrieval were performed using CC1 (Cell Conditioning I, Ventana Medical Systems, Cat# 950-124). All primary antibodies were incubated at 37°C for 1 hour. Universal Sec-

ondary Antibody (Ventana Medical Systems, Cat# 760-4205) was incubated for 12 minutes followed by chromogenic detection kit DAB Map (Ventana Medical Systems, Cat# 760-124) or Red Map (Ventana Medical Systems, Cat# 760-123). Slides were counterstained with Hematoxylin, then dehydrated and cleared before cover slipping from Xylene.

- Estrogen Receptor (ER)

Paraffin slides were cut at 4-5 μm . Deparaffinization and antigen retrieval was performed using CC1 (Cell Conditioning Solution, Ventana Medical Systems, Cat# 950-124). Anti-ER (Ventana Medical Systems, Cat# 790-4324, rabbit monoclonal antibody) was applied and slides were incubated at 37°C for 1 hour. Universal Secondary antibody (Ventana Medical Systems, Cat# 760-4205) was incubated for 12 minutes followed by chromogenic detection kit DABMap (Ventana Medical Systems, Cat# 760-124). Slides were counterstained with Hematoxylin, then dehydrated and cleared before cover slipping from Xylene.

- Progesterone Receptor (PR)

Paraffin slides were cut at 4-5 μm . Deparaffinization and antigen retrieval were performed using CC1 (Cell Conditioning Solution, Ventana Medical Systems, Cat# 950-124). Anti-PR (Ventana Medical Systems, Cat# 790-2223, rabbit monoclonal antibody) was applied and slides were incubated at 37°C for 1 hour. Universal Secondary antibody (Ventana Medical Systems, Cat# 760-4205) was incubated for 12 minutes followed by chromogenic detection kit DABMap (Ventana Medical Systems, Cat# 760-124). Slides were counterstained with Hematoxylin, then dehydrated and cleared before cover slipping from Xylene.

- Dual IHC staining: P63 + Smooth Muscle Actin (SMA)

Paraffin slides were cut at 4-5 μm . Deparaffinization and antigen retrieval were performed using CC1 (Cell Conditioning Solution, Ventana Medical Systems, Cat# 950-

124). Anti-P63 (Ventana Medical Systems, Cat# 790-4509, mouse monoclonal antibody) was applied and slides were incubated at 37°C for 1 hour. Universal Secondary antibody (Ventana Medical Systems, Cat# 760-4205) was incubated for 12 minutes followed by chromogenic detection kit DABMap (Ventana Medical Systems, Cat# 760-124).

Slides were well-rinsed and re-labeled with proper protocols. Anti-SMA antibody (Ventana Medical Systems, Cat# 760-2833, mouse monoclonal antibody) was applied and slides are incubated at 37°C for 1 hour. Universal Secondary antibody (Ventana Medical Systems, Cat # 760-4205) was incubated for 12 minutes followed by chromogenic detection kit RedMap (Ventana Medical Systems, Cat# 760-123). Slides were counterstained with Hematoxylin, then dehydrated and cleared before cover slipping from Xylene.

- Imaging and Biomarker Evaluation

Stained specimens were imaged using a Trestle whole slide scanner under 20× objective. The images had a scale of 0.33 $\mu\text{m}/\text{pixel}$ and were displayed on image servers at Rutgers Cancer Institute of New Jersey. Board-certified pathologist visually evaluated the immunohistochemical specimens using the TMA-Miner software developed in house, grading each tissue core with strategically designed evaluation qualifiers.

2.3.5 Electro-mechanical Signatures of Breast Biopsies

The mechanical signatures of the breast tissue cores are obtained by indenting it using flexible sensor array attached to the micro-manipulator with the sensor electronics capturing the data from individual strain gauge (Fig. 2.20). Since tissues consist of cells and extracellular medium, their electrical properties can be measured. The cell's electrical characteristics depend on the microscopic structures and proteins which are presented in intracellular material and which charges and moves in response to the applied fields [100]. To measure the electrical properties of the tissue cores, a constant voltage is applied between the electrodes

E1 and E2 (Fig. 2.21). When the SU-8 pillars come in contact with the tissue cores, the current passes through SU-8 pillars (E1) to the bottom electrodes (E2) through the intermediate tissue layer sandwiched between the two electrodes. The SU-8 pillars are partially coated as it is enough to complete electrical path from top of pillar to electrode (E2) which comprises of metallic grid pad to hold the tissue. This configuration is connected with a resistor in series and the potential difference caused due to tissue resistance is measured.

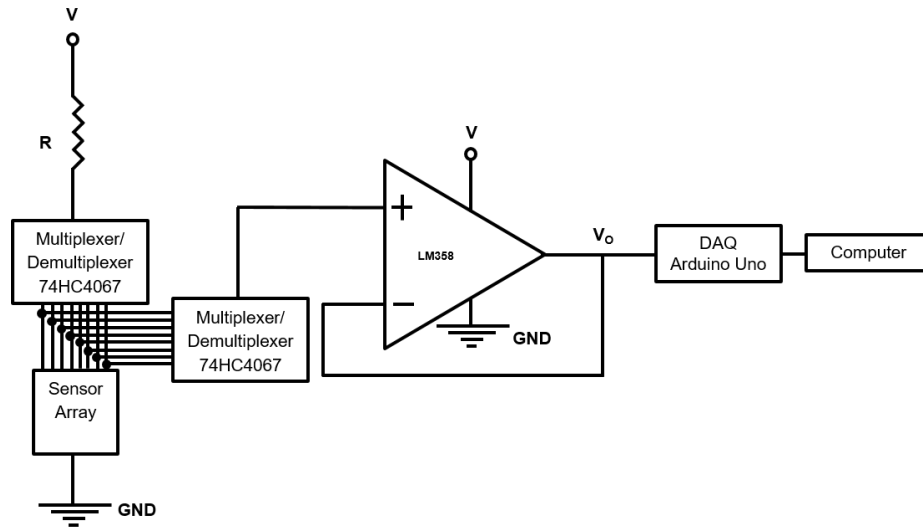


Figure 2.20: Electronic module for displaying voltage as a function of the indentation of breast tissue.

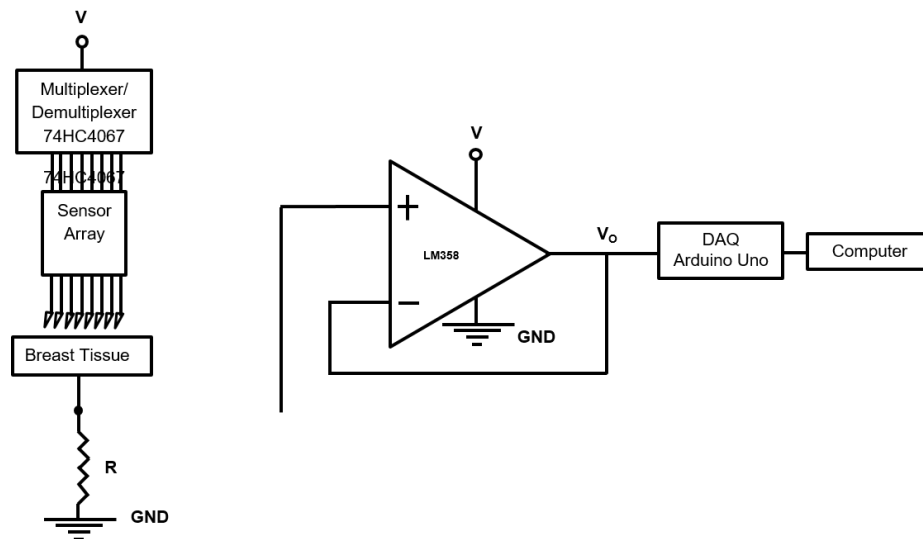


Figure 2.21: Electronic module for measuring electrical resistance of the breast tissue.

One can reasonably hypothesize that the conductivity of the breast tissue changes throughout the course of disease progression in cancer and thus so does the corresponding measured voltage. This change in voltage is correlated with the change in tissue resistance which is plotted as the electrical signature of the breast tissue. The sensor calibration and sensitivity measurement is shown in Fig. 2.22 and Fig. 2.23, respectively.

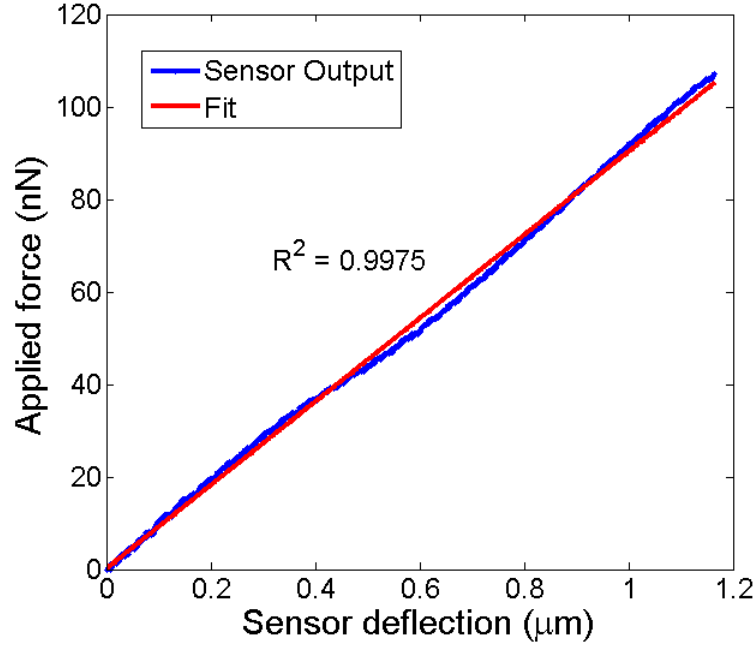


Figure 2.22: Spring constant measurement.

The fabricated sensors are calibrated in two stages before using it as a force sensing device to measure the mechanical properties of the breast tissue. In the first stage, the spring constant of each pillar in sensor array is determined using reference cantilever method and the relation between the sensor deflection and sensor output is determined. The AFM system (MFP-3D-BIOTM, Asylum Research, Inc.) is used for measuring spring constant. Figure 2.22 represents the force versus deflection curve of a pillar on the sensor array. The amount of sensor deflection is calculated as the difference between Z-direction movement and deflection of AFM tip. The mean value and standard deviation of spring constant for eight pillars is measured as $90.74 \pm 3.90 \text{ nN}/\mu\text{m}$, while the average R^2 -value is found to be 0.9975 ± 0.0021 .

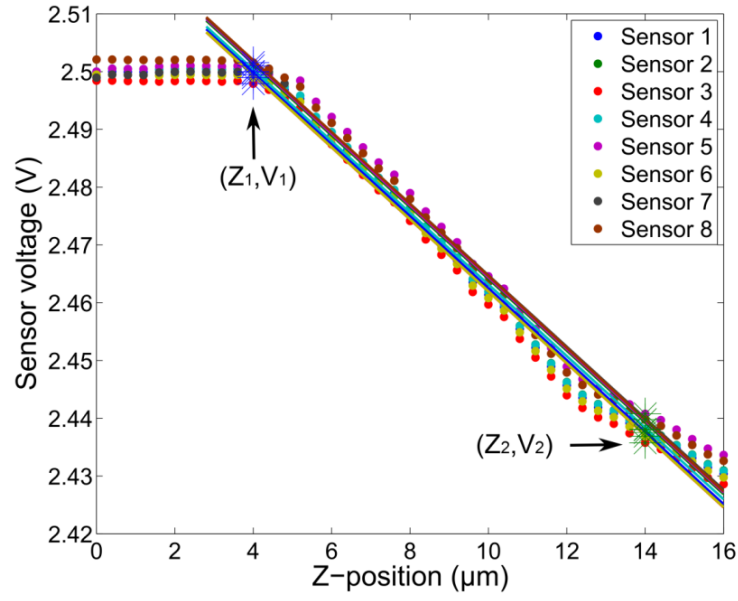


Figure 2.23: Sensitivity measurement of the fabricated sensor array.

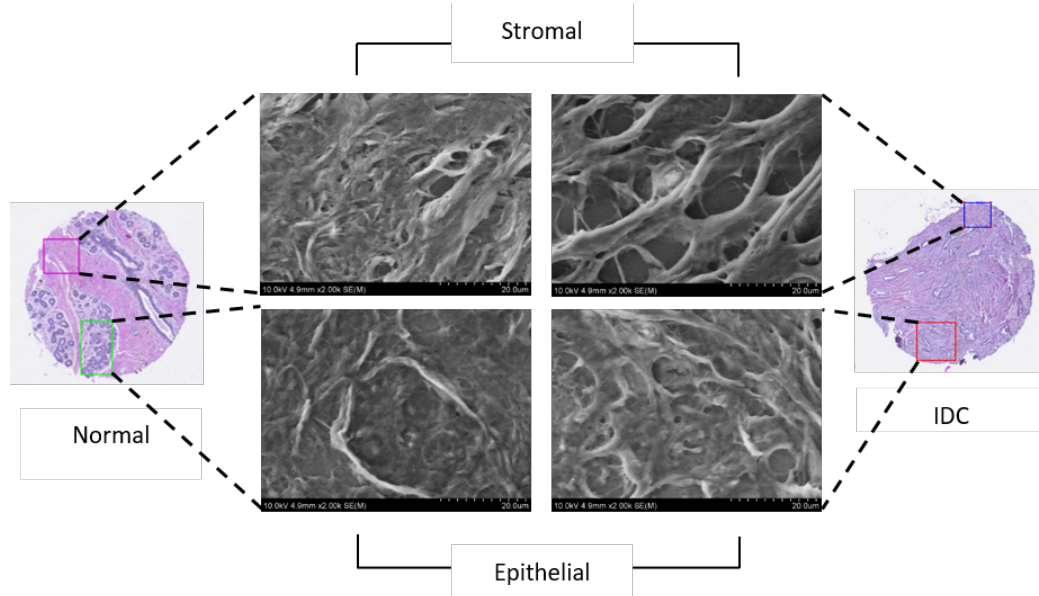


Figure 2.24: Field-emission scanning electron microscopy revealing microstructure of breast tissue cores.

The elasticity and resistance of the breast tissue cores are measured when the sensor array is displaced down by $6 \mu m$. To explicate and correlate the electro-mechanical profiles of the breast tissue with the progression of cancer, the breast tissue cores are stained using various staining methods. FE-SEM is used to observe the micro-structural changes in breast

tissue core (Fig. 2.24). The FE-SEM images confirm the architectural changes in the breast tissue. The normal epithelial region shows an organized glandular structure with intact base membrane, while a delicate network of fibers can be seen in stromal region. In case of cancer, the stromal region was composed thick fiber bundles with increased fenestration and epithelial region shows a ruptured layer compared to normal epithelial region. The stiffness value of the breast tissue from each sensor is obtained by indenting the sensor array for $6\ \mu m$ and is plotted for normal and diseased tissue (Figs. 2.25 and 2.26).

The average value of elasticity obtained from sensor array is $43.79 \pm 4.60\ kPa$ for normal epithelial region of breast tissue core (Fig. 2.25(a)). The histology images (Fig. 2.25(e)) show that the normal tissue demonstrated well defined lobules and terminal ducts, surrounded by loose intralobular stroma and dense interlobular stroma. The measurement at denser interlobular stromal region had higher value of elasticity ($79.18 \pm 7.82\ kPa$) (Fig. 2.25(a)). Epithelial cells were of two types, the majority is columnar lining the lumen with myoepithelial cells lying between the epithelial layer and basal lamina. Myoepithelials demonstrated nuclear reactivity to P63 and staining of SMA.

Mitotic activity as displayed by Ki67 was not brisk. Scattered cells showed immunoreactivity with estrogen receptor. Delicate vascular network was highlighted by CD31, especially in inter-lobular distribution. The electrical resistance of epithelial and stromal region of breast tissue cores is $334.95 \pm 7.43\ k\Omega$ and $387.38 \pm 0.93\ k\Omega$ respectively (Fig. 2.25(c)). For invasive ductal carcinoma (IDC), the resistance values for epithelial and stromal regions increased to $699.69 \pm 2.07\ k\Omega$ and $733.37 \pm 1.49\ k\Omega$ (Fig. 2.25(d)). The reason for lower electrical resistance for normal tissue compared to cancer could be attributed to the organized glandular structure with intact basement membrane, while the stroma formed delicate network of fibers (Fig. 2.24). In carcinoma, on the other hand, the stroma was composed of loose but thickened fiber bundles and the tumor region not only lost their normal architecture but also presented increased fenestration (Fig. 2.24) resulting in higher resistance and lower conductivity. It has been shown that there is a significant difference between the

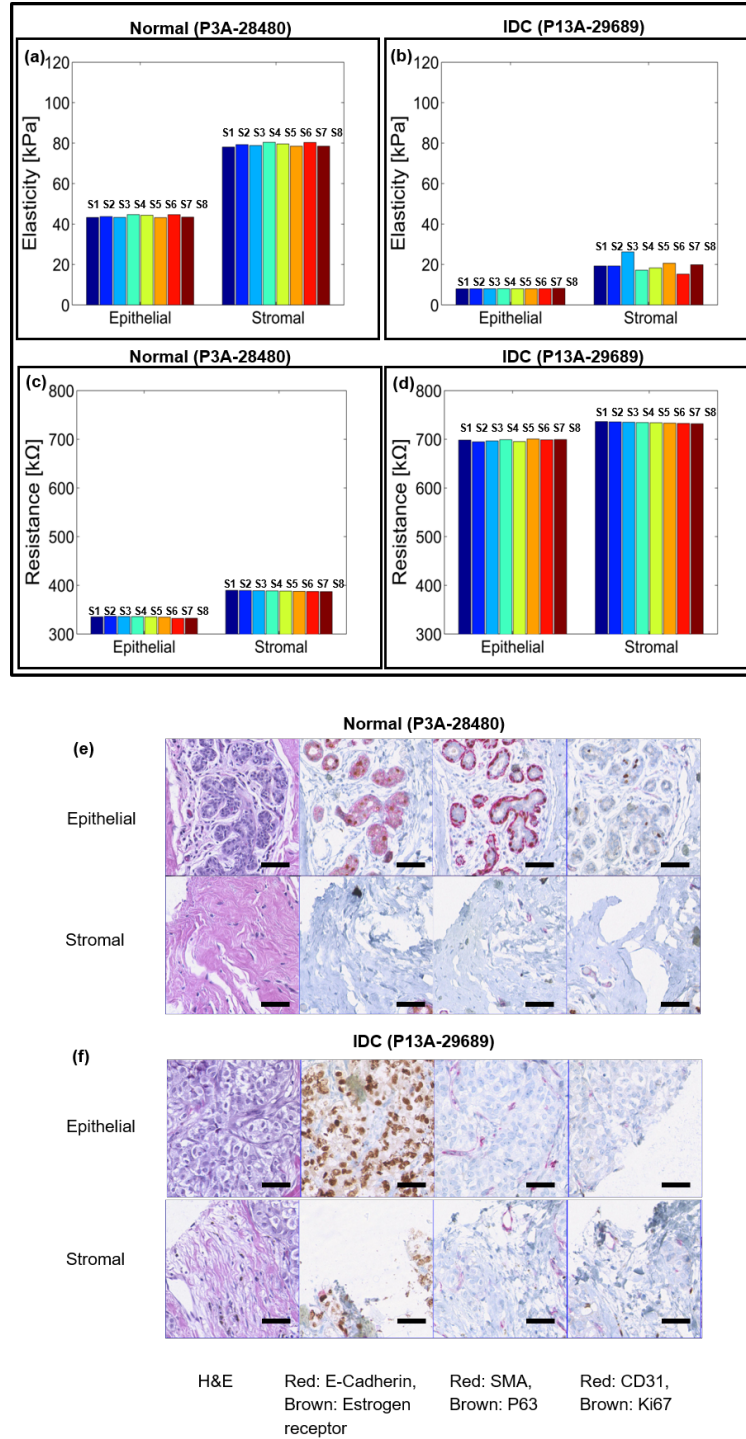


Figure 2.25: Electro-mechanical signatures of human breast tissue and corresponding immunohistochemistry: (a, b) Elasticity map and (c, d) Change in electrical signals for epithelial and stromal regions of normal (P3A-28480) and invasive ductal carcinoma (P13A-29689) tissue cores respectively. (e, f) Staining of normal (P3A-28480) and invasive ductal carcinoma (P13A-29689) cores. Scale bar for all images is 50 μm .

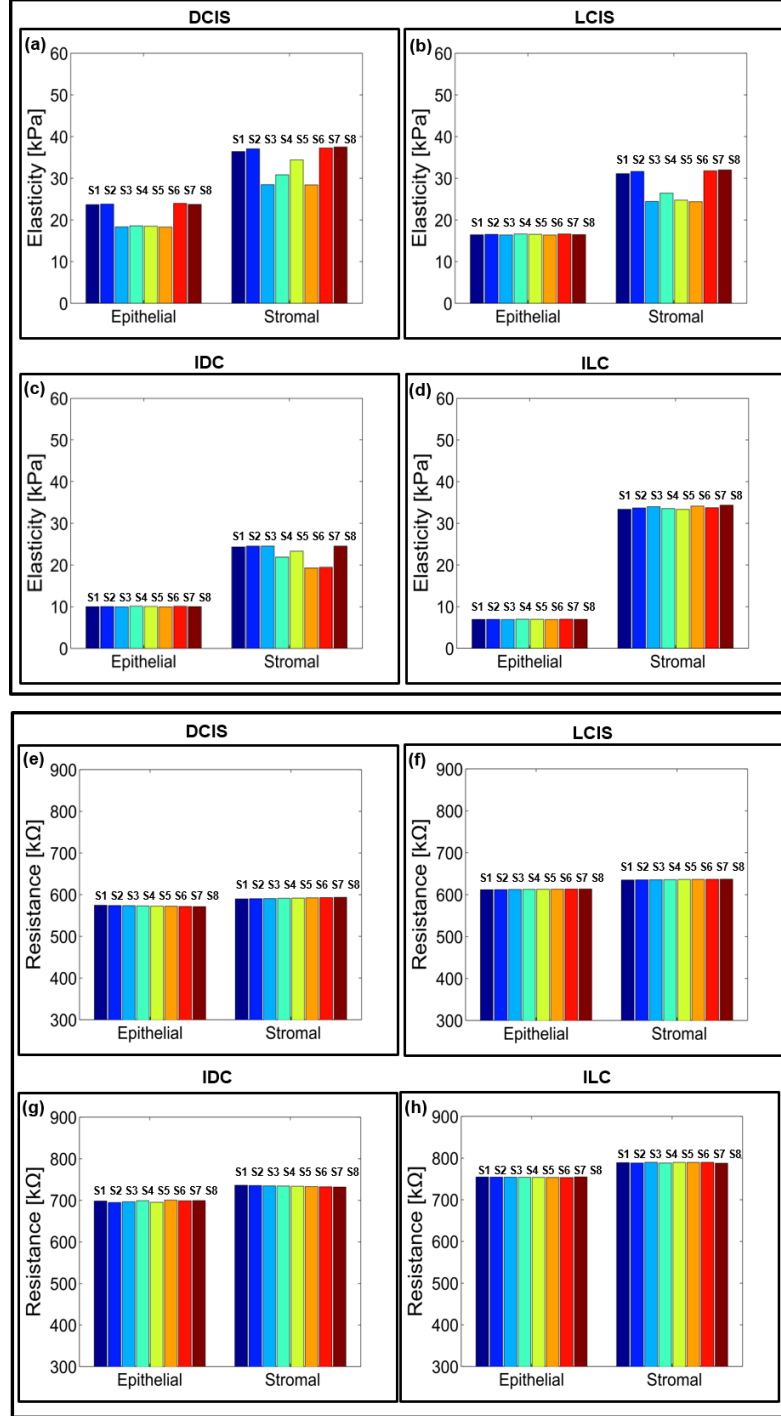


Figure 2.26: Electro-mechanical signatures of human breast tissue with tumor progression: (a)-(d) Elasticity map and (e)-(h) Change in electrical signals for epithelial and stromal regions of ductal carcinoma *in situ* (DCIS) (P6A-11809), lobular carcinoma *in situ* (LCIS) (P10A-27928), invasive ductal carcinoma (IDC) (P14A-26249) and invasive lobular carcinoma (ILC) (P19A-26763).

resistivity of normal living tissue and that of dead tissue [100]. The conductivity changes as a function of time after death because the permeability of the cell membrane changes within hours of cell death. Thus, *in vitro* experiments of normal living tissue could give a different set of electrical readings than the result shown in the present study [100]. The elasticity of the epithelial and stromal region for IDC was found to be $8.03 \pm 0.97 \text{ kPa}$ and $19.49 \pm 3.02 \text{ kPa}$, respectively (Fig. 2.25(b)). The immunohistochemistry for invasive carcinoma demonstrated solid growth pattern (Fig. 2.25(f)). Loss of myoepithelial layer was demonstrated by the absence of staining with SMA and P63. The ductal carcinoma was strongly ER positive. Proliferation index was low by Ki67. A more edematous area was observed possibly due to fluid build-up in the tissue resulting in softening of tissue as measured by the sensor array.

To study the intermediate stages of the breast cancer, the breast tissue cores from ductal carcinoma *in situ* (DCIS), lobular carcinoma *in situ* (LCIS), invasive ductal carcinoma (IDC) and invasive lobular carcinoma (ILC) were indented and the electro-mechanical response was measured (Fig. 2.26). The DCIS was characterized by proliferation of neoplastic cells without breaking the myoepithelial layer (As demonstrated by SMA and P63) (Fig. 2.27(a)). This particular sample of DCIS was of high grade, comedo type displaying luminal necrosis, high index of proliferation by Ki67 and negative for estrogen receptor. In case of LCIS, the lobules are distended and distorted by proliferation of neoplastic cells monotonous (low nuclear grade) in appearance. The basement membrane and myoepithelial layer were intact. Neoplastic cells were ER positive with low proliferation index (Fig. 2.27(b)). The technology of immunohistochemistry staining involved additional rigorous processing to the specimen and as a result some tissue cores may fall off the glass slide or show tearing artifacts. The corresponding tissue cores with CD31 and Ki67 staining did suffer from this artifact as shown in Fig. 2.27(b).

This results in soft and moderately stiff areas resulting in different peaks for each sensor (Figs. 2.26(a) and (b)). A fried egg appearance with central-located nuclei and pale cyto-

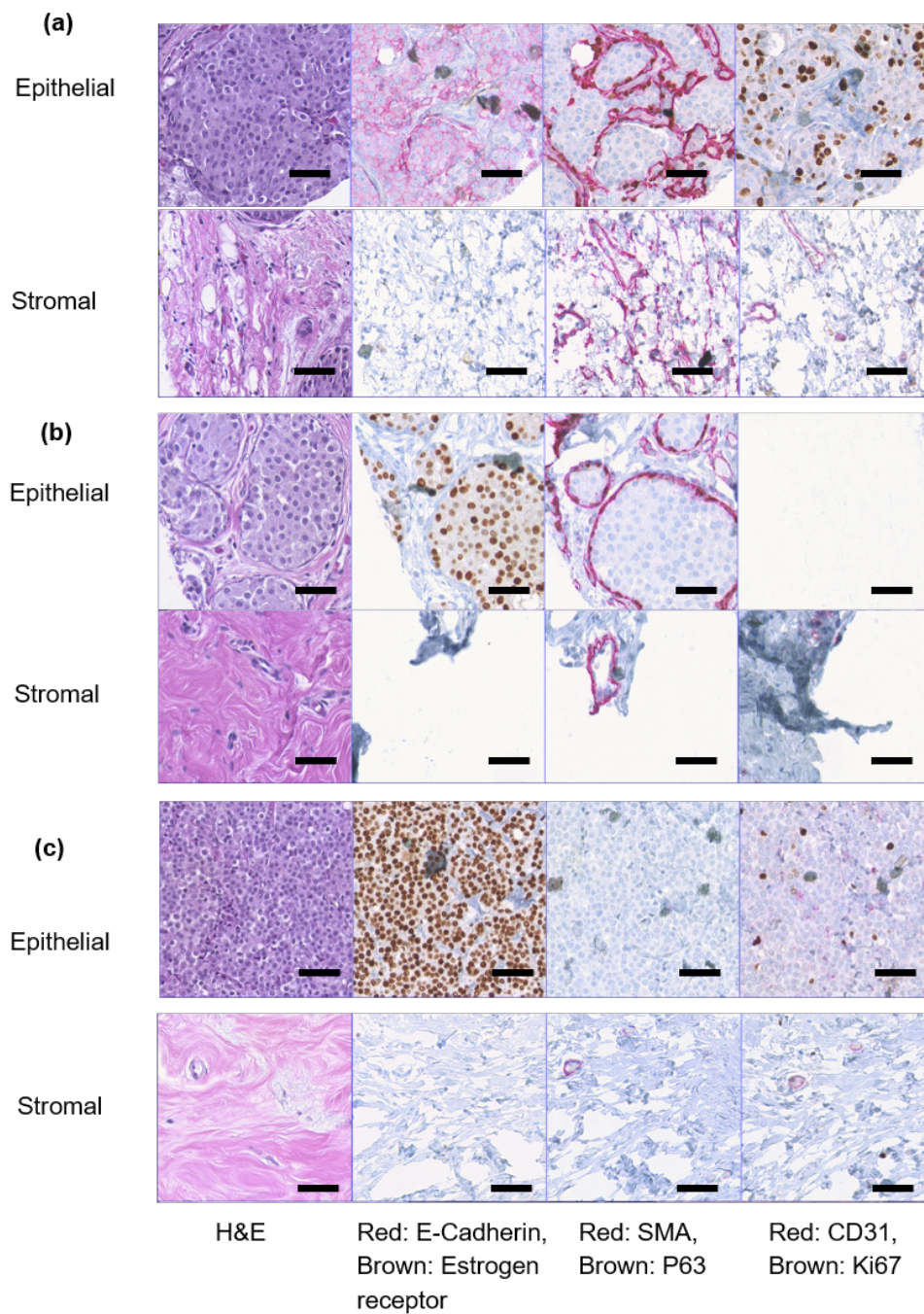


Figure 2.27: Immunohistochemistry of breast tissue cores: (a) Ductal carcinoma *in situ* (DCIS) (P6A-11809), (b) Lobular carcinoma *in situ* (LCIS) (P10A-27928), (c) Invasive Lobular carcinoma (ILC) (P19A-26763) breast tissue cores. Staining with 1) H&E; 2) Red: E-cadherin, Brown: Estrogen receptor (ER); 3) Red: Smooth muscle actin (SMA), Brown: P63; and 4) Red: CD31, Brown: Ki67. The scale bar in each case is 50 μm .

plasm was displayed by the ILC tissue core (Fig. 2.27(c)). Neoplastic cells broke through the basement membrane and filled out the surrounding stroma. The immunoreactivity for P63 is absent, the cells are strongly and diffusely ER positive, with mild increase in proliferating activity. Lobular carcinoma diagnosis has been on the rise, possibly caused by hormonal treatment for postmenstrual managements. Lobular carcinoma cases often do not display pathologic response to chemotherapy [101] but has low rate of recurrence [102]. Most prominent molecular traits of lobular carcinoma include loss of E-cadherin expression and down regulation of an adhesion protein CDH1 [103], which may be the reason that lobular carcinoma displays less desmoplastic fibroblastic proliferation, instead, ILC invades surrounding tissue in its distinct single file pattern and shows a signature 'targetoid' morphology surrounding ducts and lobules [49]. This lack of stroma disturbance was reflected in the observation by withholding more elasticity in stroma than IDC. Compared with epithelial and stromal region from normal specimen, *in situ* and invasive carcinoma from both ductal and lobular origin displayed remarkable loss of elasticity (Figs. 2.26(a)-(d)). Both invasive tumors displayed a magnitude of reduction in elastic modulus from normal breast tissue, which agreed with previous *in vitro* studies [18, 29]. Interestingly *in situ* forms of breast cancer displayed intermediate level of firmness before they break open the basement membrane and disseminate into surrounding tissue. It can be further observed that the electrical properties of the breast tissue cores changes with progression of disease and thus the measurement of the electrical resistance of each core could act as distinct signature for the disease stage (Figs. 2.26(e)-(h)). The electro-mechanical properties of breast tissue cores for 20 patients (5 normal, 4 DCIS, 3 LCIS, 4 IDC and 4 ILC) are summarized in Table 2.1.

In the case of normal tissue, the elasticity range was being $39.94 \pm 4.20 \text{ kPa}$ to $43.80 \pm 4.54 \text{ kPa}$ and the electrical resistance of the tissue was $331.78 \pm 1.49 \text{ k}\Omega$ to $346.25 \pm 7.63 \text{ k}\Omega$ for epithelial region indicating stiffer phenotype. As cancer progresses, the tissue becomes softer and the resistance of the tissue also changes ($6.83 \pm 0.86 \text{ kPa}$ to 6.98 ± 0.72

Table 2.1: Individual electrical (change in tissue resistance, mean \pm SD) and mechanical (elasticity E, mean \pm SD) analysis of breast tissue samples.

No.	BRS No.	Age/Sex	Year	Type	E [<i>kPa</i>]	R [<i>k</i> Ω]	Status
P1	30365	39/F	2014	Epi.	37.86 \pm 3.49	346.25 \pm 7.63	Normal
P2	28363	-/F	2013	Epi. Str.	43.79 \pm 4.60 79.18 \pm 7.82	334.95 \pm 7.43 387.38 \pm 0.93	Normal
P3	28480	31/F	2013	Epi. Str.	34.94 \pm 4.20 103.19 \pm 9.21	334.75 \pm 1.63 388.32 \pm 0.96	Normal
P4	28152	-/F	2013	Epi.	41.25 \pm 3.26	331.78 \pm 1.49	Normal
P5	31872	26/F	2014	Epi. Str.	43.80 \pm 4.54 79.19 \pm 8.12	335.89 \pm 7.26 387.47 \pm 0.93	Normal
P6	11809	78/F	2008	Epi. Str.	21.11 \pm 2.12 33.80 \pm 3.21	572.99 \pm 1.13 591.80 \pm 1.38	DCIS
P7	29688	52/F	2013	Epi. Str.	22.22 \pm 2.03 34.74 \pm 3.12	573.22 \pm 1.23 589.42 \pm 1.16	DCIS
P8	28453	47/F	2013	Epi. Str.	21.67 \pm 1.84 36.58 \pm 3.24	573.68 \pm 1.18 589.99 \pm 1.32	DCIS
P9	25043	89/F	2012	Epi. Str.	21.14 \pm 1.71 34.59 \pm 3.56	573.13 \pm 1.19 589.45 \pm 1.41	DCIS
P10	27928	46/F	2013	Epi. Str.	16.52 \pm 1.19 28.32 \pm 1.94	612.77 \pm 0.61 636.00 \pm 0.63	LCIS
P11	11223	65/F	2007	Epi. Str.	15.19 \pm 1.03 28.73 \pm 2.04	612.37 \pm 0.41 636.21 \pm 0.33	LCIS
P12	25350	70/F	2012	Epi. Str.	15.46 \pm 1.06 28.07 \pm 2.13	615.85 \pm 0.21 635.90 \pm 0.83	LCIS
P13	29689	52/F	2013	Epi. Str.	8.03 \pm 0.97 19.49 \pm 3.02	699.69 \pm 2.07 733.37 \pm 1.49	IDC
P14	26249	67/F	2012	Epi. Str.	10.02 \pm 1.14 22.74 \pm 2.14	697.85 \pm 2.17 734.12 \pm 1.89	IDC
P15	17316	51/F	2010	Epi. Str.	9.40 \pm 1.03 22.04 \pm 2.91	700.32 \pm 2.32 731.71 \pm 4.03	IDC
P16	27952	31/F	-	Epi. Str.	9.72 \pm 0.94 25.28 \pm 2.28	699.74 \pm 2.37 731.65 \pm 3.03	IDC
P17	19306	78/F	2010	Epi.	6.98 \pm 0.72	753.84 \pm 0.46	ILC
P18	11223	65/F	2007	Epi. Str.	6.83 \pm 0.86 38.25 \pm 3.60	754.09 \pm 0.34 790.40 \pm 0.82	ILC
P19	26763	-/F	2012	Epi. Str.	6.95 \pm 0.79 33.77 \pm 3.36	754.13 \pm 0.67 789.07 \pm 0.64	ILC
P20	25350	70/F	2012	Epi.	6.85 \pm 0.83	754.26 \pm 0.47	ILC

kPa and 753.84 \pm 0.46 *k* Ω to 754.26 \pm 0.47 *k* Ω in case of ILC). The results obtained for nanomechanical phenotyping representing the loss of tissue stiffness with progression of

cancer matches with the existing literature [18]. It was found that the stromal region of cancerous breast tissue loses stiffness compared to normal breast tissue core. The reason for this phenomenon is not clear. The elemental reasoning is that the mechanical heterogeneity changes depending on the region from which tissue is extracted from. In some cases adjacent neoplastic change affects properties of the stroma resulting in softening of tissue core in stromal region. Statistical significance was consistently found (Fig. 2.28) demonstrating the gradual reduction of elasticity and increase in resistance for both origins; with p -values from double tailed t -test between diseased groups listed in Table 2.2.

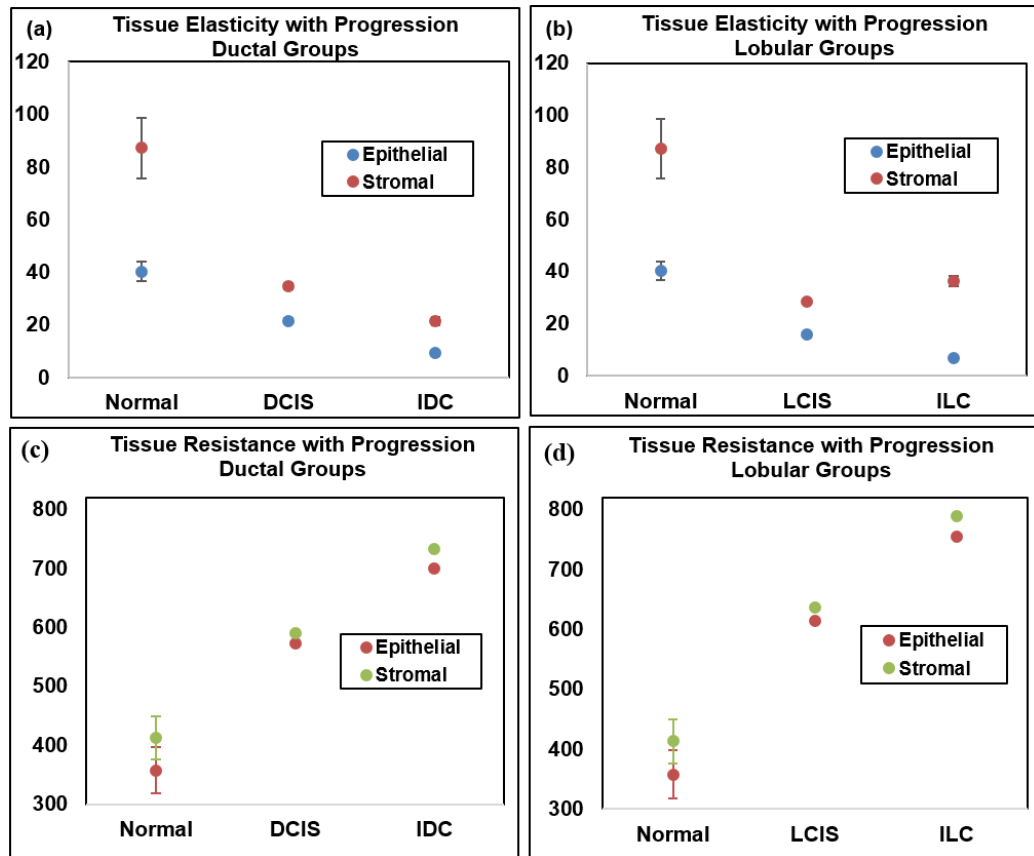


Figure 2.28: Statistical analysis: Elastic modulus and electrical resistance of tumors from ductal and lobular groups relative to normal breast tissue.

Although previous studies demonstrated certain consistency in genetic portraits of *in situ* and invasive carcinomas of breast [88], the gradual elastic change detected in this experiment hinted a progression change in the mechanical environment. Figure 2.29 shows

Table 2.2: Double tailed t -test between diseased groups from electromechanical characterization.

		Between normal and <i>in situ</i>	Between <i>in situ</i> and invasive
Elasticity	Ductal Origin	3.3×10^{-4} ($n=9$)	4.6×10^{-4} ($n=7$)
	Lubular Origin	8.3×10^{-5} ($n=8$)	2.0×10^{-4} ($n=7$)
Resistance	Ductal Origin	3.7×10^{-4} ($n=9$)	1.7×10^{-5} ($n=7$)
	Lubular Origin	1.8×10^{-4} ($n=8$)	5.5×10^{-5} ($n=7$)

the group-wise distribution of data from normal to cancer.

The mechanical signature of the epithelial region in case of normal breast tissue is delineated by elasticity value ranging from 34.94 ± 1.49 kPa to 43.80 ± 4.54 kPa . The force curve obtained by indenting breast tissue cores is shown in Fig. 2.30. From Fig. 2.25 it could be observed that the normal region shows well organized ductal and glandular structure. An intact layer of myoepithelial cells that outlined the glands are highlighted by P63 and SMA. The tumor specimen, on the contrary, displays strong positivity for estrogen receptor as well as evidence of angiogenesis as shown in sporadic CD31 staining. Myoepithelial cell layer is destroyed and SMA appeared in stroma with a different pattern, which is considered a sign of desmoplastic change (Fig. 2.27). The elasticity and resistance values obtained from each group (Normal, DCIS, LCIS, IDC, ILC) are plotted in Fig. 2.29. The cancerous epithelial regions are demonstrated by elasticity ranging from 6.83 ± 0.86 kPa to 6.98 ± 0.72 kPa . The normal stromal and cancerous stromal regions in the breast tissue can also be identified in similar way. The electrical signatures of the epithelial region of normal breast tissue is given by resistance ranging from 331.78 ± 1.49 $k\Omega$ to 346.25 ± 7.63 $k\Omega$, in case of cancerous epithelial region the range is 572.99 ± 1.13 $k\Omega$ to 753.84 ± 0.46 $k\Omega$. The resistance range of normal stromal and cancer stromal is from 387.38 ± 0.93 $k\Omega$ to 388.32 ± 0.96 $k\Omega$ and 589.42 ± 1.16 $k\Omega$ to 790.40 ± 0.82 $k\Omega$, respectively. It is unclear whether the additional tension in *in situ* tumor was a result of the encasement from basement membrane or, very likely, disseminated tumor cells incur even more cytoskeletal relaxation in the process of migrating through the connective tissue.

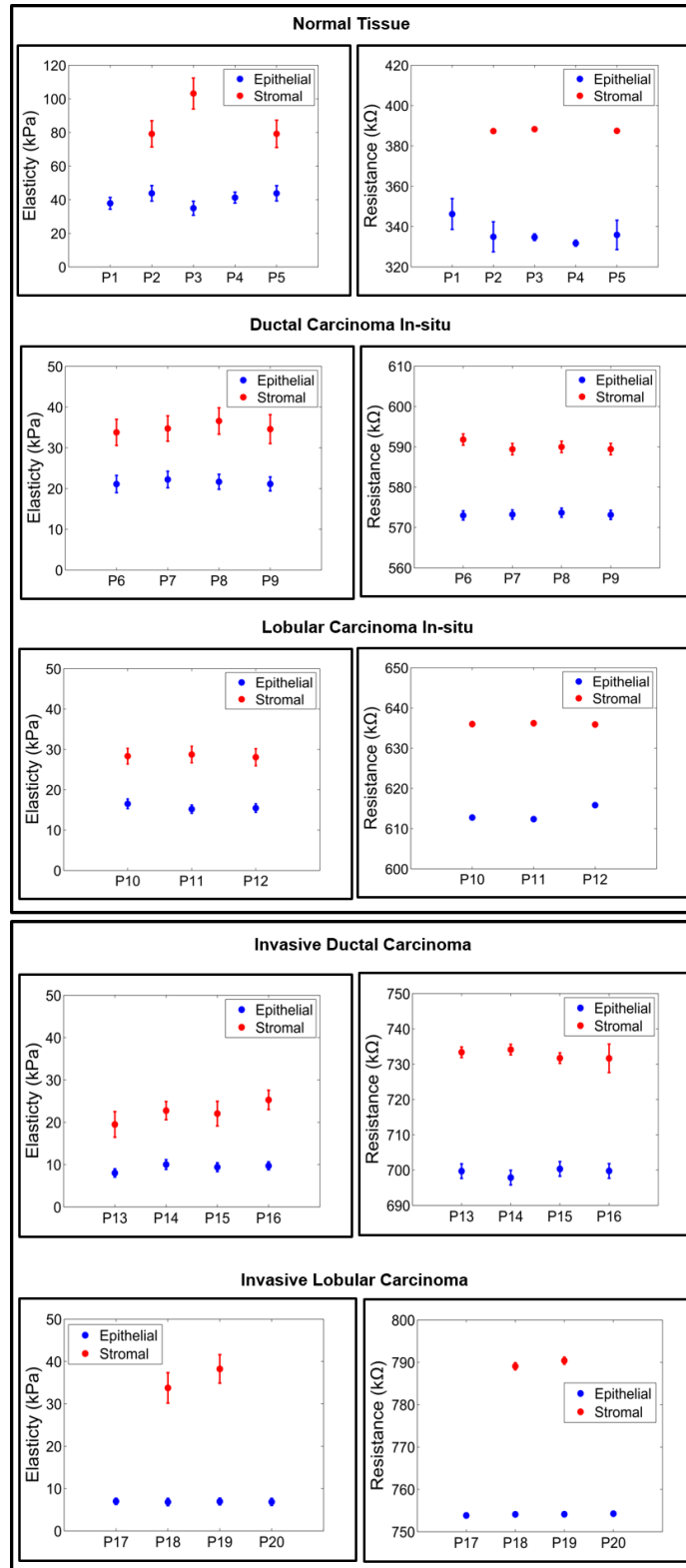


Figure 2.29: A group-wise electro-mechanical analysis of the breast tissue cores.

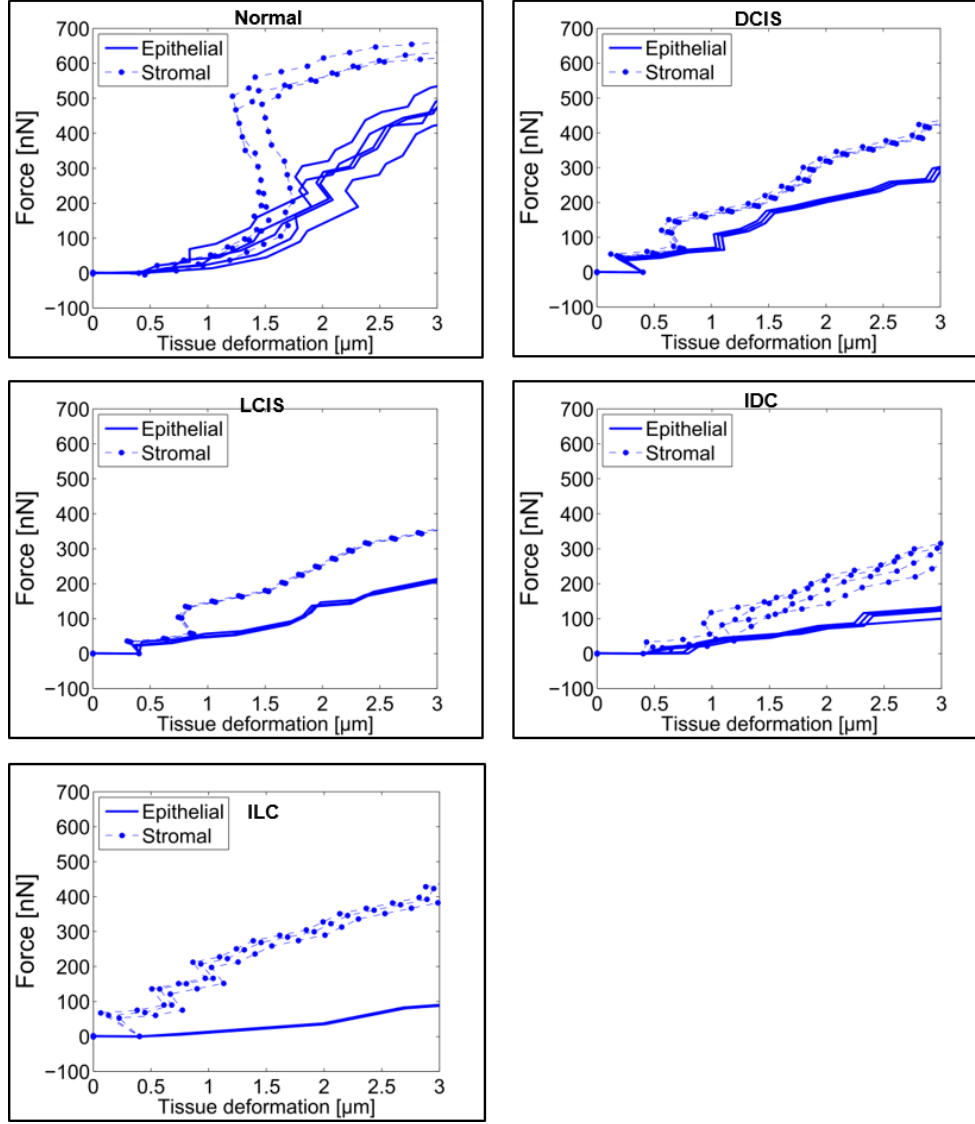


Figure 2.30: Force curves from the breast tissue cores. Force curves obtained from epithelial and stromal region of (a) Normal, (b) Ductal carcinoma *in situ* (DCIS), (c) Lobular carcinoma *in situ* (LCIS), (d) Invasive ductal carcinoma (IDC), and (e) Invasive lobular carcinoma (ILC) breast tissues.

It is worth noting that banked normal breast tissue samples mainly originated from mammary reduction procedure and patients undergoing such procedure usually belongs to younger age group (as shown in the Supplementary Table 2.1). There may be certain changes between younger and older breast tissue that were not captured in current experimental design. On the other hand, it is commonly accepted that breast tissue goes through changes during menstrual cycle and that in breast tissue; the density varies amongst normal

women. The results clearly reflected such variation amongst subjects in the normal group. The tumor microenvironment, on the contrary, displayed much similarity within disease groups signaling common changes which may be captured in devices such as those demonstrated in this study. The ultimate goal of this research is to detect the biophysical changes, which reflect underlying biochemical or genetic alterations and help in clinical decision-making. In this era when smaller and smaller lesions are detected by imaging studies, and with more diagnostic tests awaiting to be performed, with a small device and small amount of tissue specimen, it will be able to generate combinations of biophysical readings that will be helpful for diagnosis and/or prognosis.

2.4 Towards Lateral Tissue Scanning

2.4.1 Design and Fabrication of Capacitive Microcantilever for Multi-directional Sensing

It was demonstrated that both mechanical and electrical property of breast tissue can be measured simultaneously as biomarkers for breast cancer throughout the extensive experiments in the previous sections. However, there are a few limitations of the flexible sensor that need to be improved. The sensor in the previous section examines a sample in a single axis via indentation without any microscopic view and there needs to be improved on its packaging and installation method to make the experiment easier. In addition, reducing the experimental duration is essential for the samples to keep themselves from environmental disturbances such as changes in temperature and humidity.

To overcome those limitations, a cantilever type of new cantilever sensor capable of a lateral measurement for faster scanning has been designed as shown in Fig. 2.31. The comb-drive structure consists of moving and fixed combs and the change in capacitance between the two combs is proportional to the distance between two combs which are determined by the amount of force applied at the tip. Investigating a sample line-by-line will allow much faster scanning than indenting a sample point-by-point. A MEMS-based sensor capable of measuring shear and normal contact force and electrical resistance has been

designed. To achieve higher sensitivity than the previous sensor in measuring contact force, a comb-drive structure has been implemented as a capacitance type of force sensor. Two electrodes (one at the sensor tip and the other under the tissue sample) are implemented as a similar manner of electrical characterization in the previous approach. A breast tissue sample is placed on a transparent electrode and microheater so that the mechanical and electrical properties of breast tissue can be characterized at various temperatures.

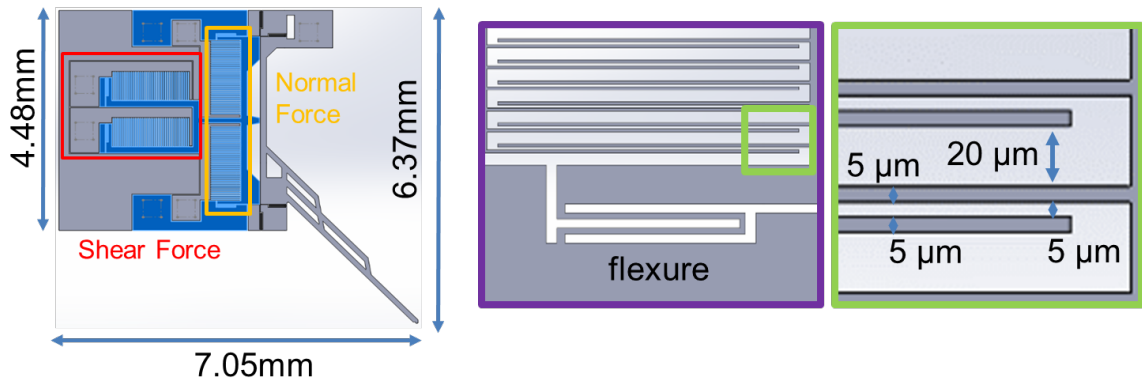


Figure 2.31: Schematic of capacitive microcantilever and its comb-drive structure.

Based on the previous tissue indentation experiments, the following target requirements have been established: 1) Force sensing directions: Normal and shear direction (2-DOF), 2) Maximum force sensing range: 1 mN (Normal direction) and 1 mN (Shear direction, tentative), 3) Force sensing resolution: 5 μN in both directions, and 4) Maximum deflection: 5 μm in both directions.

The dimensions of the comb-drive structure have been selected to ensure the target resolution to be satisfied based on the literature reviews [104, 105]. A single pair of combs consists of moving and fixed comb and two pairs of combs are in charge of measuring forces in a single direction. When a force applied to the sensor, a capacitance from one pair of combs decreases while the other increases by placing the fixed combs in opposite direction and the difference between the two pairs of combs is the final sensor output to be measured. This actually doubles the sensitivity of the sensor and is called a differential mechanism. To achieve the target force and deflection range, compliant flexures and me-

chanical stoppers are included in the design and the center of mass (COM) of the moving structure is located on a point minimizing the moment arm of the structure against applied forces at the tip.

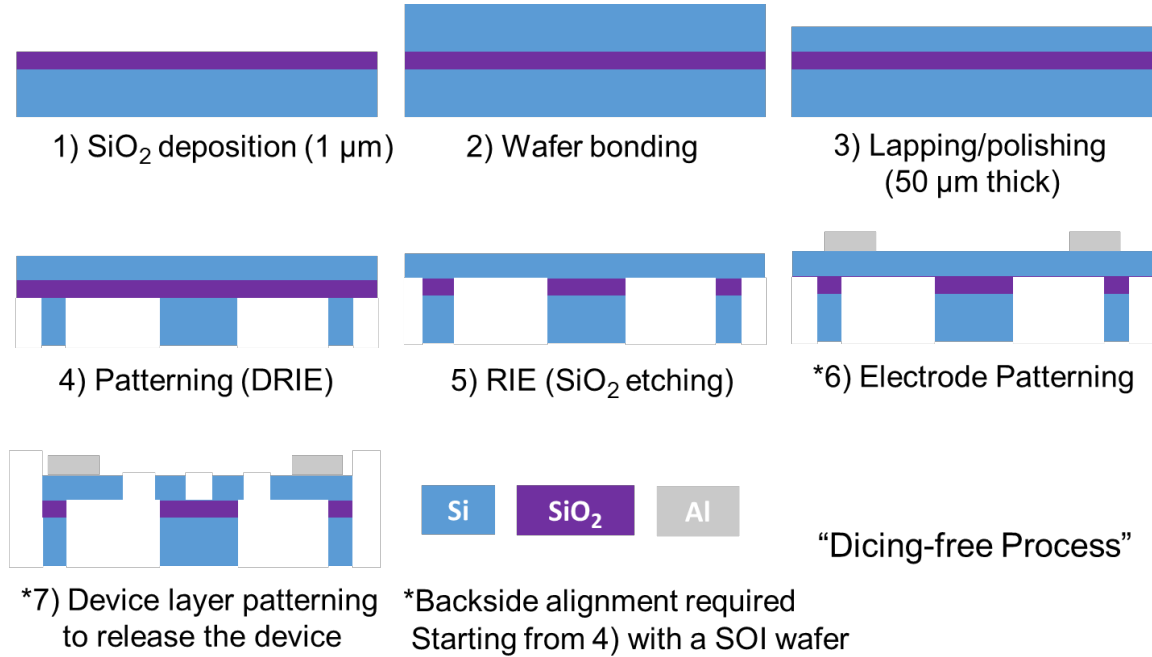


Figure 2.32: Fabrication process of capacitive microcantilever.

Figure 2.32 shows the fabrication process of the comb-drive sensor. The three-mask process utilizes basic MEMS fabrication techniques on a 4-inch silicon-on-insulator (SOI) wafer (Orientation: $\langle 1-0-0 \rangle$, Type/Dopant: P/Boron, Resistivity: $1-10 \Omega\text{-cm}$, and Thickness: 50, 1, and $380 \mu\text{m}$ for device layer, buried thermal oxide, and handle wafer, respectively) such as photolithography, reactive ion etching (RIE), deep reactive ion etching (DRIE), lift-off technique, and backside alignment. The detailed fabrication process is as follows: 1) Deposit SiO₂ ($1 \mu\text{m}$) on a polished silicon wafer using PECVD, 2) Fusion bond the wafer with another polished wafer, 3) Lap and polish the device layer into $50 \mu\text{m}$ thickness (the processes 1-3 can be replaced with purchasing a SOI wafer), 4) Spin-coat/pattern/bake a photoresist (Microposit SPR220-7.0) suit for DRIE over $10 \mu\text{m}$ thickness on the backside of the wafer and etch the backside with DRIE using the standard Bosch process (the buried oxide acts as an etching stop), 5) Etch the buried oxide with

RIE (the device layer made of silicon acts as an etching stop) and remove the photoresist

6) Pattern aluminum (500 nm, the minimum thickness ensuring reliable wire bonding on an aluminum pad [106]) deposited by an electron-beam evaporator using backside alignment and the bi-layer lift-off technique [107], and 7) Spin-coat/pattern/bake a photoresist (Microposit SPR220-7.0) suit for DRIE over 3 μm thickness on the device layer and etch the device layer with DRIE using the standard Bosch process to release the sensor, then remove the photoresist.

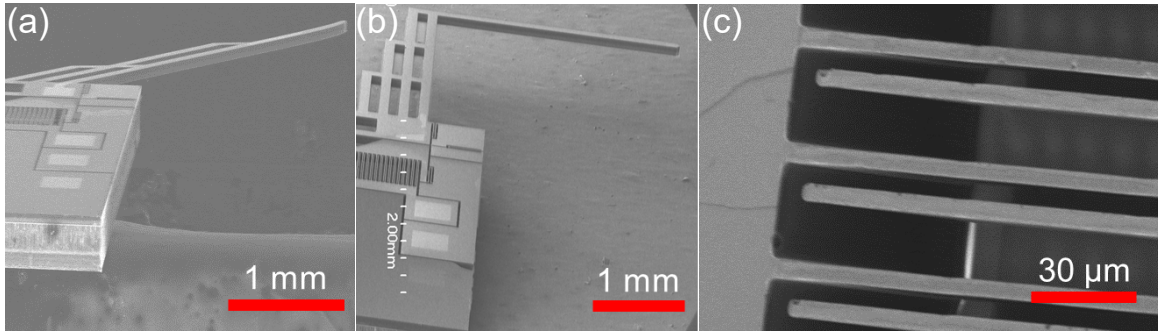


Figure 2.33: SEM images of fabricated capacitive microcantilevers: (a) Angled contact (45°), (b) Normal contact (90°), and (c) Comb-drive structure.

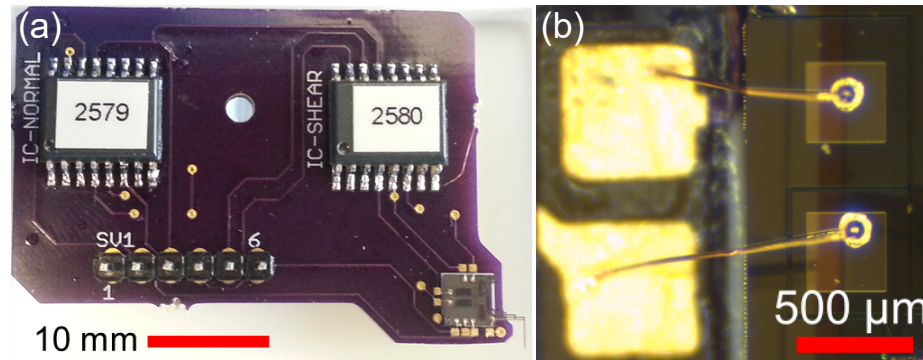


Figure 2.34: Assembled comb-drive sensor with PCB: (a) Capacitive microcantilever on PCB and (b) Wire bondings

Since MEMS-based sensors, especially for this kind of cantilever type of sensors are really vulnerable and easily break when they get impacted during dicing or handling, this dicing-free process with a thick handling layer on the bottom enables to bring the sensor to the experiment without any damage. Two different types of tip for angled contact in 45°

and normal contact (90°) have been fabricated as shown in Fig. 2.33. Then, the sensor was bonded and electrically connected to PCB by wire bonding (see Fig. 2.34). Two universal capacitive readout integrated circuit (IC) chips (MS3110P, Microsensors, Inc., USA. Datasheet available online on [108]) with a resolution of $4.0 [aF/rtHz]$ were used to convert capacitance change into voltage change using the differential measurement mode. The chip yielding a single output is powered by a single supply of DC +5 [V] from an external input through the connector pins on the PCB (see Fig. 2.34(a)). When we assume the moving structure of the sensor moves along the desired direction only, the distance between the combs determines the capacitance of the pair of combs. By the design, the direction of capacitance change from two pairs of combs is opposite to maximize the sensitivity and the output from the chip in the differential mode is strictly proportional to the difference in capacitance between the two combs, C_1 and C_2 in the Fig. 2.35.

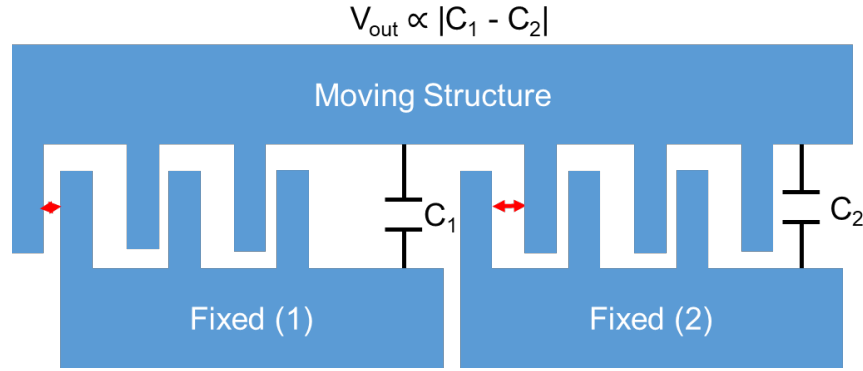


Figure 2.35: Differential capacitive readout mechanism.

2.4.2 Lateral Measurement Experiment

The fabricated sensor was calibrated with contact force in each normal and shear direction by using a commercially available microindenter (TriboIndenter, Hysitron, USA). Although the sensor outputs in normal and shear direction are not perfectly independent, the output in one direction is sensitive enough to the other direction and they look quite linear against the contact force as shown in Fig. 2.36(b)-(c).

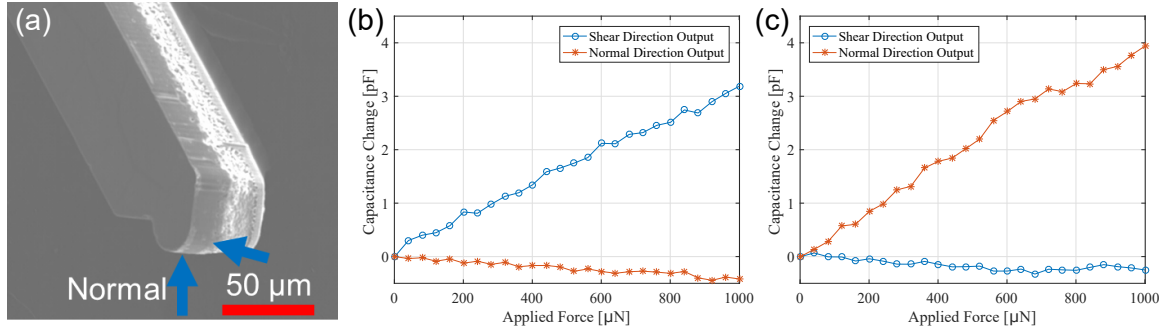


Figure 2.36: Calibration of the comb-drive sensor: (a) Calibration method, (b) Calibration result in the shear direction, and (c) Calibration result in the normal direction.

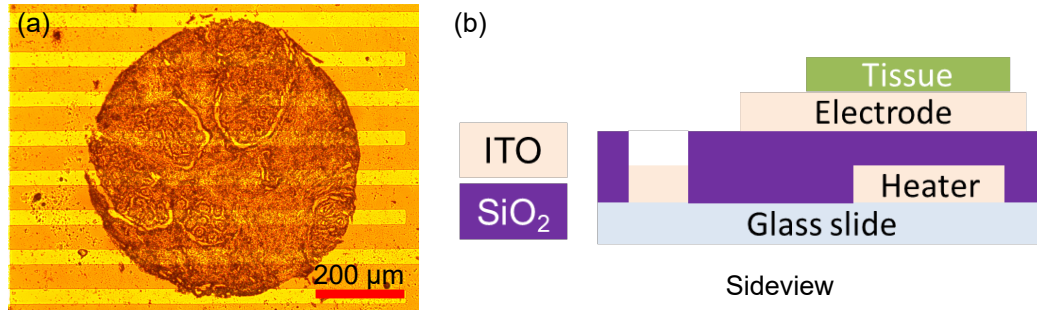


Figure 2.37: Experimental setup for lateral measurement: (a) microscopic view of a breast tissue sample and (b) schematic of a tissue sample at the sideview.

Figure 2.37(a) shows a microscopic view of a tissue sample for the lateral measurement experiment, while Figure 2.37(b) represents the schematic of a tissue sample for the experiment. However, the lateral measurement experiments with the fabricated sensors from this batch were not successful mainly due to two failure modes: 1) weak adhesion between the electrode and the tissue sample and 2) the underestimated shear force range in the design. During the lateral movements, it happened either peeled the tissue sample off at the shallow sweeping or the sensor broke at the deep sweeping.

2.5 Conclusion

This section represents the fabrication and characterization of the flexible MEMS-based device with the possibility of simultaneous electro-mechanical analysis of tissue. The results obtained from the initial experiments shows a flexible MEMS device that can be used

to delineate the breast cancer tissue from the benign tissue based on mechanical and electrical measurements. The device is not only simple but also small enough to report tissue changes at the microscopic level. In future work, simultaneous electro-mechanical phenotyping of breast tissue to determine the malignancy in tissues as well as the stage of disease progression from the onset of the disease is envisaged. The present MEMS-based device is not only a potential candidate for breast cancer diagnosis but for other diseases in which the biomechanical changes occur in the tissue from the onset to progression.

The pathological change in cells and tissue microstructures causes measurable changes in the electro-mechanical properties and thus providing a diagnostic tool in studying the carcinogenic tissues. It has been demonstrated for a method for simultaneous electro-mechanical phenotyping of the breast cancer using a novel MEMS-based flexible sensor array, whereby simultaneous mechanical and electrical properties of the breast tissue can be measured. A flexible sensor array is fabricated from low cost polymer (PDMS) as a substrate, conducting polymer (PEDOT:PSS) as piezoresistive sensor and a viscous polymer (SU-8) as conducting pillars. A notable observation is the change in electrical resistance and softening (lower mechanical stiffness) of the tissue regions with the progression of cancer. A microcantilever for multi-directional electro-mechanical characterization of breast tissue has been also presented with the higher sensitivity than the previous piezoresistive sensor to examine tissue samples much faster by the lateral measurement under a microscopic view, although the sensor needs to be improved throughout the design modification and the adhesion improvement between the electrode and the tissue sample via a chemical treatment [109]. The work presented in this chapter can serve as an alternative technique for observing the underlying architectural changes that occur during the course the progression of breast cancer. There still remains intriguing questions on how the technology can be used to make a portable device capable of performing out of lab experiments to detect breast cancer.

CHAPTER 3

MICROSCOPE COMPATIBLE UNDERACTUATED MICRO-MANIPULATION PLATFORM

3.1 Introduction

Since micropositioning techniques are essential for various scientific and engineering studies dealing with manipulation at the micro-scale (such as precise manufacturing or optical/chemical/biological applications), highly precise planar stages have been widely researched and developed in both academia and industry [110, 111]. Though several micropositioning stages exist, they have several drawbacks. Many of current stages are manually operated or incompatible with a microscope, while others allow translational motions only without rotational capability [112–114]. The rotational capability enables to phenotype a tissue sample more accurately by matching the coordinates of the sample through the microscopic image to the pathological region of interest. Most automated micropositioning stages have adopted piezoelectric actuator due to its advantages of high spatial resolution and high energy density that allows the system to be miniaturized [56]. A small range of motion (ROM) and slow movement speed, which are inherent of piezoelectric actuators, are other drawbacks of current micropositioning stages [110, 111]. For example, one of the representative and commercially available $XY\theta$ micropositioning stages, M-880 3-degrees of freedom (DOF) planar precision positioning system (Physik Instramente, Germany), has the ROM of $\pm 10\text{ mm}$ in the X and Y axis with minimum incremental motion of $0.75\text{ }\mu\text{m}$ and $\pm 4^\circ$ in the rotation [41]. The ROM of stages for ultra-precision application is even smaller mainly due to a trade-off between ROM and resolution. In the work of [115], "large travel ultra-precision $XY\theta$ stage" has the ROM of $3\text{ mm} \times 3\text{ mm}$ for XY motion and less than 1° rotational motion, while its spatial resolution is less than 10 nm . Nowadays,

however, piezoelectric actuators with large ROM are commercially available by increasing the ROM of the actuators [116, 117]. Since, current micropositioning stages are not suitable for the targeted application, which is automated tissue indentation, this research is motivated by the need for developing a customized micropositioning stage which has large ROM along with rotational capability.

Current micropositioning stages can be grouped by actuation type as another way of classification: PPR (two prismatic actuator and one rotational actuator), RRR (three rotational actuators), or 3-RRR (three sets of RRR). Though the mechanisms applied to current stages look different in morphological, they have fully actuated mechanism in common that has equal number of actuators to the number of kinematic chains.

An underactuated mechanism enables not only to make a system more compact and efficient, but it also helps to reduce the cost for building such a system by eliminating some actuators and several parts for the assembly [118]. However, the control problem for an underactuated system is challenging, since there is no general law applicable to any arbitrary underactuated system [119]. Lynch [120] has shown that underactuated planar body with unilateral thrusters is controllable based on Sussmann's sufficient condition of local controllability [121]. Similarly, Li has shown that the dynamic model of a planar body is also small-time locally controllable by two pushing inputs [122].

Control for an underactuated system along a desired trajectory is realized by either modifying path planners for fully actuated systems such as the time-scaling algorithm [123], the decoupled approach to trajectory planning [124], passive velocity field control [125], or applying a customized control law for the specific system [126, 127]. Lynch and Bullo developed the path planner between two zero velocity states using decoupling velocity vector fields for kinematically controllable underactuated systems [128, 129]. Narikiyo proposed control strategies for several underactuated systems based on passive velocity field control [130]. However, the studies based on decoupling velocity vector fields are not applicable to all underactuated systems and often require cumbersome computation.

3.2 System Design

3.2.1 Requirements

One of the main goal of this micro-positioning stage is to perform automated micro/nano-indentation of TMA with increased accuracy and sampling throughput. Consequently, there are engineering requirements that the micro-positioning stage must meet while also being a versatile platform for future work. These engineering requirements stem from the the need to integrate with pre-existing equipment, the TMA, and the current and future indentation devices for tissue characterization.

First, the stage must fit and function within the confines of an inverted microscope, and its attached overhead lamp. Especially pertinent specifications include objective lens focal lengths and ranges of motion, the 310 mm distance between eyepiece apparatus and lamp neck, and overhead lamp range of motion. Second, the dimensions of the material sample determine the resolution required and basic dimensions for the slide holder design. The micro-positioning stage must accommodate a standard glass slide with a TMA. The standard slide is around $75 \times 25 \times 1\text{ mm}^3$. Although the TMA does not cover the slide's entire surface, the stage should enable viewing and indentation of all parts of the array.

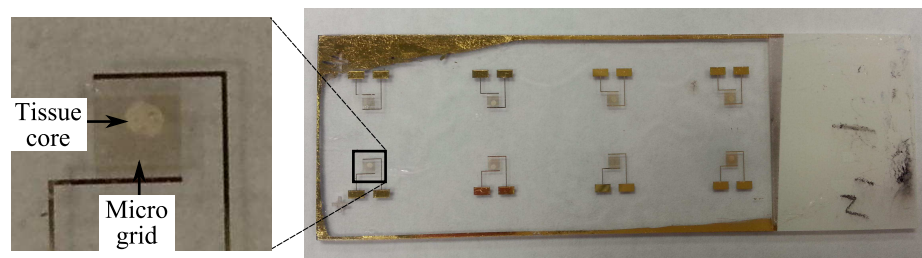


Figure 3.1: Tissue microarray (TMA).

The TMA is a two-dimensional array of $600\text{ }\mu\text{m}$ diameter of tissue cores placed on a single slide (see Fig. 3.1). Within each tissue core there may be multiple regions for analysis that must be performed separately and at a high resolution. Additionally, the system is required to perform high-resolution micro/nano-indentation across the individual

tissue cores, where the center-to-center space between the adjacent indentation points could be as small as $2\text{ }\mu\text{m}$. Thus, the system requires sub-micron resolution and repeatability. Finally, the stage must be able to mount and manipulate indentation devices for tissue characterization. As a result, the stage was designed to move the sensing device in the vertical direction (Z-axis) with step sizes of less than 100 nm . The system requirements are as follows:

1. Travel range greater than $50\times 50\text{ mm}^2$.
2. Sub-micron resolution and repeatability
3. Closed-loop position control with integrated position sensors
4. Low-profile design ($\sim 25\text{ mm}$ thickness) such that it can replace the manual positioning stage currently paired with the inverted microscope (Nikon TE-2000U) and allowing the test slide to remain in focus.
5. Total of 4 degrees-of-freedom: $XY\theta$ micro-positioning stage for linear and rotational manipulation and Z-axis linear positioner for manipulation of the indenting device

3.2.2 Key Design Decisions

Fig. 3.2 below depicts the complete assembly of the final design based on the previously described joint scheme and the selection of the SmarAct SLC-2490-S and Modular Control System (MCS).

For ease of discussion, the assembly can be separated into the following "layers":

1. *Layer 1* is the baseplate which serves as the support for layers 2 and 3, attaching all parts to the microscope's support ledges and raising the stage above the objective lenses so that they can rotate freely.
2. *Layer 2* is the stage, sometimes referred to as the slide holder. This layer is the square plate on which the tissue sample is mounted. This stage is manipulated to situate the

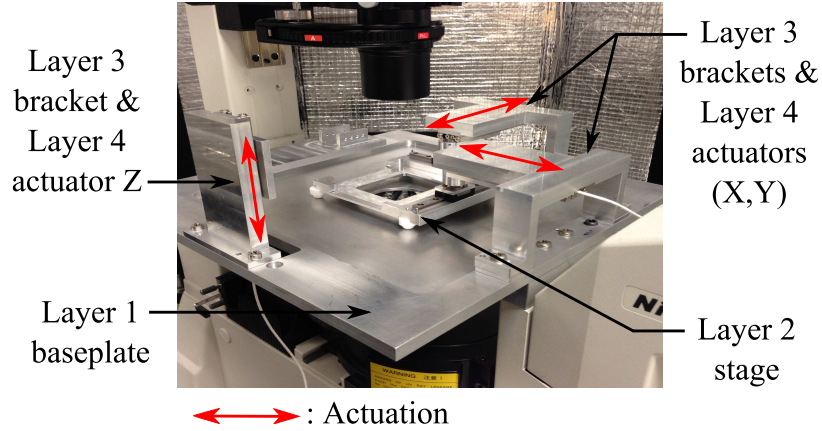


Figure 3.2: Micro-positioning stage mounted on inverted microscope, Nikon TE-2000U.

ROI directly over the objective lens in use. It also houses the two perpendicular rails and carriages to which the revolute joints are mounted. Layer 2 moves within the cut out in layer 1.

3. *Layer 3* includes all three brackets that fix the actuators to layer 1 and ensure their perpendicularity.
4. *Layer 4* includes all three linear actuators, as well as the two actuator tips (connections between prismatic and revolute joints) for the XY-axes and the indentation device holder for the Z-axis.

Much of the layer 1 design was determined by the need to fit within the microscope's workspace, raising layer 2 above the objective lenses but still within the focal length of each lens. Specifications for the microscope were not readily available, so an experiment was conducted to determine the focal length and vertical range of each of the three objective lenses. Using a manually adjusted microscope stage, a tissue sample was raised in 1 *mm* increments until the image went out of focus. From this experiment it was determined that each lens has a vertical range of approximately 10 *mm*. The limiting focal length was 13 *mm*.

Material thicknesses for layer 1 were selected to position layer 2 within the focal lengths of each lens and allow the user to switch objective lenses without removing the stage.

Thicknesses of 23 *mm* and 9.5 *mm* were selected for the support blocks and main baseplate surface, respectively. Aside from the physical dimensions of layer 1, careful consideration was put into the material selection of the baseplate. The main surface of the baseplate is 307.5×305.0 *mm*² but 241×241 *mm*² of that surface makes up the cavity in which layer 2 is situated. This cavity is a mere 3 *mm* thick and could warp during the manufacturing process. Material selection charts support the use of metals and alloys over other materials due to the need for a high Young's Modulus, low thermal expansion coefficient, and low cost [131]. Aluminum was selected over high alloy steels due to its lower cost and wide range of alloys available. Finally, a variety of aluminum alloys were compared and MIC-6 was selected. MIC-6 is a continuously cast aluminum specifically designed for quick removal of material. According to MatWeb, its cast granular structure and stress relieving properties allow high-speed metal removal with little to no distortion commonly seen in long-grained wrought, flat-rolled metals [132]. The metal sheet size and time required for accurate manufacturing of the baseplate reinforced the value of ordering MIC-6 plate to prevent having to re-start the baseplate should standard aluminum warp.

For Layer 2, the overall dimensions were chosen to allow room for both the tissue specimen (mounted on a silicon wafer or standard glass slide) and the two perpendicular rails. The 112×112 *mm*² plate allows for an 80×80 *mm*² slide or wafer. Material thicknesses were selected to position the specimen within the objective lens' focal lengths while also providing enough material strength to prevent warping and allow other components to attach via small screws.

One key decision in the stage design was determining how to support layer 2 while still maintaining a low-friction interface between layers 1 and 2. Four combinations were considered for sliding motion between layers 1 and 2: Aluminum and aluminum, aluminum and Teflon, Teflon-coated aluminum and Teflon, and aluminum and graphite. After some initial research, graphite was disqualified due to its low hardness, 1.0-2.0 on the Mohs scale [133]. An experiment to determine the actual coefficient of sliding friction was conducted

using the experimental set-up shown in Fig. 3.3. The aluminum surface was belt sanded and then meticulously hand sanded to produce a smooth surface resembling that of the machined MIC-6 cavity of layer 1. Any imperfections were circled with a permanent marker and avoided during each trial. The edges of the Teflon disc were rounded using an exacto knife and inspected using magnifying glasses to ensure rounded edges. A truly spherical Teflon piece could not be used as it would not support the 500 g mass used as a normal force. Five trials were completed for the Teflon on aluminum case. A force sensor was calibrated and attached to the micromanipulator. Next, the micromanipulator and accompanying C++ code were used to move the force sensor and push the layer 2 material and 500 g mass across the layer 1 material. Voltage measurements collected by the force sensor were averaged and used to calculate a coefficient of friction for each trial. This process was repeated for the Teflon on Teflon-coated aluminum case. A Teflon coating was applied to the aluminum surface using two layers of DuPont Teflon non-stick dry-film lubricant (as directed on the aerosol can). Results of the experiment are depicted in Table 3.1.

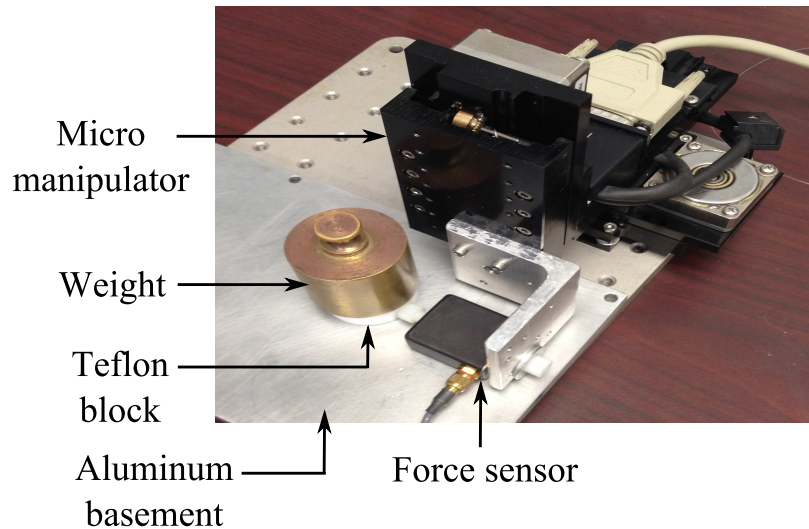


Figure 3.3: Experimental set-up for friction data collection.

The friction data collected suggests that an aluminum baseplate and Teflon feet attached to the stage would result in the lowest coefficient of sliding friction. Differences between the theoretical and experimental values may have been caused by different aluminum sur-

Table 3.1: Friction coefficients for Teflon on layer 1 materials

Teflon on Al	Teflon on Teflon-coated Al
0.100 ± 0.006	0.158 ± 0.024

faces as well as the use of Teflon-coated aluminum vice solid Teflon in the baseplate cavity. Another trade-off that was considered was the diameter of the Teflon feet. There is a delicate balance between having a smaller contact and having such a small contact that any surface imperfections in the aluminum are magnified. In essence, larger diameter feet would be more forgiving of any small surface imperfections in the MIC-6 caused by the circular motion of the CNC machine and hand sanding during manufacturing.

Layer 3 consists of the three brackets for mounting the piezoelectric actuators. The main design decisions for layer 3 were determining the overall bracket dimensions and ensuring that their placement maximized the travel range for each actuator despite the limited workspace. According to the actuator specifications, each actuator can move up to 31.5 mm in either direction for a total travel range of 63 mm . The linear rails embedded in the stage limit the travel range to approximately 60 mm . During one iteration of the XY-bracket design, the actuators were mounted on the top face of rectangular brackets. This design limited the actuator's ability to retract as the layer 4 actuator tips (connections between the actuators and revolute joints) would run into the actuator after pulling back the length of the actuator tip. Additionally, this design took up valuable space that could be used to enlarge the layer 1 cavity, increasing the range of motion of layer 2. The final iteration uses inverted XY-brackets that allow actuators and actuator tips (layer 4) to extend and retract freely. Rather than consuming a full 90 mm of the 305 mm length between the view finder and overhead lamp of the microscope, the inverted brackets use only 23.5 mm for attaching brackets to layer 1. The bracket extends over the layer 1 cavity while leaving room for adjustment of the overhead lamp and a variety of indentation device attachments. Moreover, manually attachable/detachable dowel pins are implemented on each rotational joint for applications that need translational motion only.

Design of the Z-bracket was relatively straightforward as workspace in the vertical direction is not as limited as it is in the XY-plane. The Z-bracket was designed to adequately support and align the Z-direction actuator with its X and Y-direction counterparts. The key design decisions for the layer 3 (Z-bracket) involved its compatibility with layers 1 and 4. The Z-bracket must position the actuator for indentation over the through hole in layer 1 to allow the actuator to extend below the stage's top face, utilizing its full 63 *mm* range of motion. With respect to layer 4, the Z-bracket must have the material strength to support the weight of the actuator, indentation device assembly as well as any moments caused by indenting.

Layer 4 includes the piezoelectric actuators, actuator tips, and indentation device holder. Design of layer 4 presented two main concerns: 1) ensuring correct dimensions for the actuator tips such that they would fit into the revolute joint assembly with tight tolerances, 2) building actuator tips that allow for tool access for attaching each actuator tip to both the piezoelectric actuator and layer 2. The indentation device holder was designed to hold indenter such as microcantilevers or other future devices that screwed directly into the Z-direction actuator and can be adjusted vertically depending on the screw holes used. The sensing device can be adjusted horizontally within the holder's four pairs of screw holes, if needed.

3.2.3 Considerations for Manufacturing

Throughout the design, manufacturing, and assembly process, it was necessary to investigate multiple manufacturing and assembly methods to ensure the tightest of tolerances and least play possible in the final stage assembly. First, it was important to ensure perpendicularity among the X, Y, and Z-brackets and their respective actuators and actuator tips. Similarly, the linear rails and carriages in layer 2 needed to be perpendicular to one another. This was accomplished by using the CNC for initial cuts and then gradually removing 0.001 inches of material in the stage and brackets to press fit each rail and actuator.

Rounded pockets were made in the aluminum to allow tools to pass around rail and actuator corners but press fits were designed to keep the maximum surface contact between the rails or actuators and their aluminum mounts. After the rails and actuators were mounted, the brackets were aligned using carefully placed dowel pins protruding from the layer 1 baseplate. These were installed to maintain bracket alignment during future use and disassembly and also to differentiate between the X and Y brackets. Second, the revolute joint assembly required special attention. While press fitting was the simple solution, press fitting the bearings onto the stage and also into the actuator tips would place unnecessary pressure on the bearings. Instead, the bearings were press fit only into the actuator tips. Next, each bearing was slip fit onto a graduated post attached to each carriage. Finally, a small screw was tightened via a hole in the actuator tip to expand the diameter of the graduated post and fix the inner ring of the bearing to the post. These manufacturing methods were essential to the resolution of the micro-positioning stage and the perpendicularity of the rails and actuators.

3.3 Underactuated Planar Mechanism

Although there are three types of planar mechanisms (serial, parallel, and hybrid) for micropositioning stages, parallel mechanisms are widely used due to several advantages, namely: 1) high accuracy (errors are not accumulated through the kinematic chain), 2) high structural stiffness, and 3) low inertia [134, 135]). As a result, the system has been designed as a parallel mechanism as shown in Fig. 3.4(a). The key feature of the mechanism is passive rotational joints added to orthogonal linear XY stage at idealized points of contact of PZT actuators with the stage. If the net line of force exerted on the body does not pass through the center of mass, the net force generates linear and rotational motion of the body simultaneously. In addition to this basic physics, motion constraints are imposed by two linear guides orthogonal each other and passive rotational joints on the actuation points allowing the body to move and rotate only along the guides.

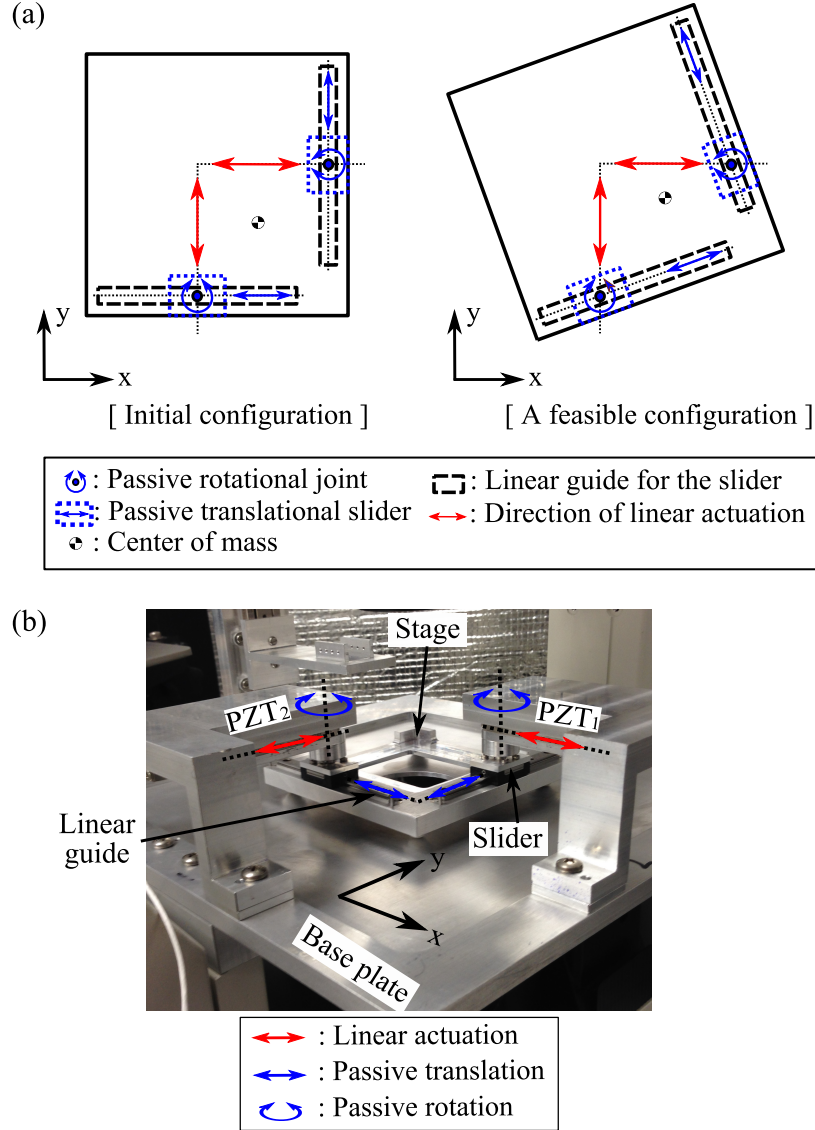


Figure 3.4: (a) Schematic of the underactuated planar mechanism (scaled drawing) and (b) The manufactured platform.

The platform consists of three major layers in the longitudinal direction: 1) base plate, 2) moving stage, and 3) brackets with actuators. The base plate is fixed to a microscope and provides a planar working space for the moving stage. The moving stage has two linear guides that are perpendicular to each other, and is actuated by two piezoelectric linear actuators (SLC-2490-S, SmarAct, Germany) combined with 1 *nm* resolution position sensor. The slider on each linear guide is attached to the actuator. The rotational bearing between the slider and the actuator allows passive rotation of the stage relative to the fixed

base plate.

The manufactured platform is shown in Fig. 3.4(b). Actual size of the stage is $112 \times 112 \text{ mm}^2$ with 85 mm length of the linear guide. The linear actuator is capable of 63 mm stroke, which is determined as the target ROM to scan a whole standard glass slide. There is a hole at the center of the stage and the base plate for light to pass through, to obtain microscopic images. Low profile design is also important in a microscope compatible platform, due to the limited focal length of the microscope [136].

3.4 Kinematic Analysis

3.4.1 Geometric Constraints

Since the rotational motion of the stage is constrained by two linear guides, the center of rotation (COR) of the stage does not necessarily coincide with its geometric center or the center of mass (COM). Moreover, it can be observed that the stage rotates with different radii in different configurations. Hence, the COR is not a fixed point when the stage moves. The geometric relations for the stage including the COR are shown in Fig. 3.5. The circle with the diameter of \overline{PQ} , which is the distance between two actuator tips, can be defined at every configuration as drawn by red dotted line in Fig. 3.5. The point O and the origin of body frame $\{B\}$, is on the circle due to the right angle of $\angle POQ$. Similarly, the two points, S and T , which is the intersection point of the extension lines from each actuator in parallel with the world frame coordinates and the body frame coordinates, respectively, are on the circle as well. Since the angle subtended at the center is twice the angle at the circumference, $\angle SMA$ (or $\angle AMT$) must be the same as the stage angle θ .

When a rigid body rotates about a fixed point, the COR is geometrically determined by the intersection point between two perpendicular bisectors of two points on the body as shown in Fig. 3.6(a). Therefore, one can find the COR of the stage as the point A , which is the intersection point between the angular bisector of $\angle SMT$ and the circle with diameter \overline{PQ} , and the COR moves along the circle when the stage rotates. To visualize

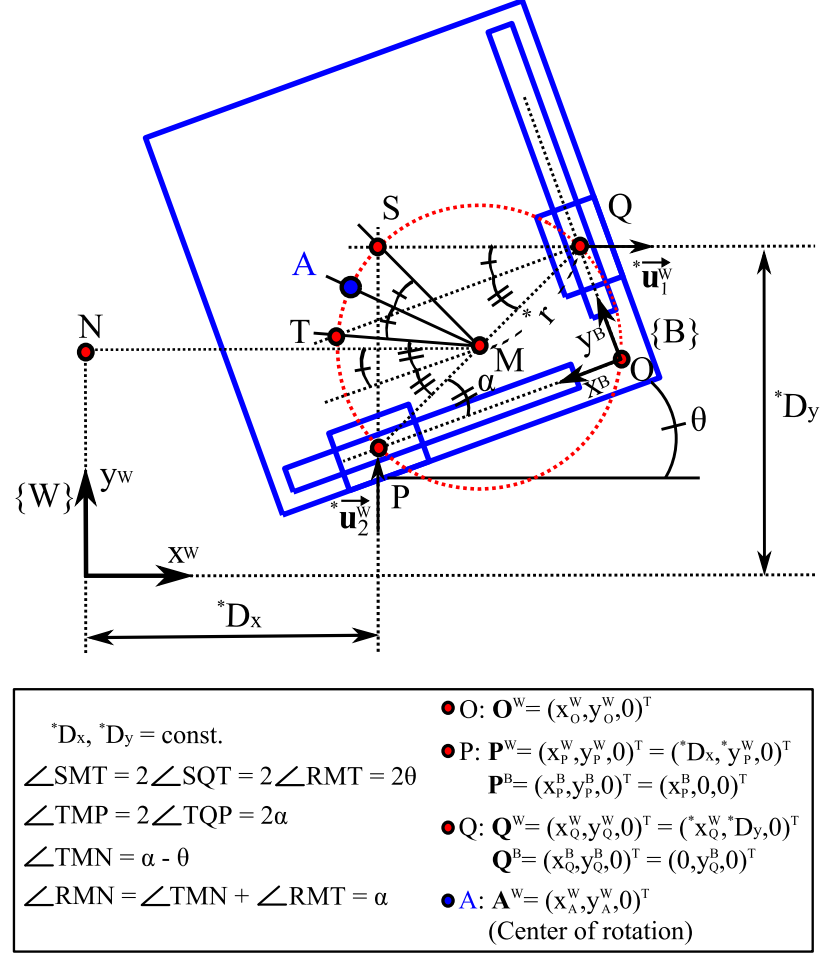


Figure 3.5: Schematic of the geometric relations and the coordinate system of the stage (scaled drawing). $\{W\}$, $\{B\}$, \mathbf{u}_1^W and \mathbf{u}_2^W is the world frame (fixed frame), the body frame (moving frame), and the input velocity vector of linear actuators in x^W and y^W direction, respectively. The parameters denoted by $*$ represent the known values due to the structure or measurements.

and verify instantaneous COR of the stage, a vision tracking experiment was conducted with four markers as shown in Fig. 3.6(b). Two markers on the stage are for calculating the instantaneous COR points while the stage is manually rotated with fixed actuators. The other two markers on the base plate are for a reference line so that one can calculate the rotational angle of the stage. Calculated COR coordinates in $\{W\}$ frame obtained from the vision tracking data are shown in Fig. 3.7(a) along with the simulated COR trajectory, which is the circle with diameter, \overline{PQ} . In this plot, the origin of the $\{W\}$ frame is placed on the point M , which is the midpoint of \overline{PQ} , for ease of understanding. Therefore,

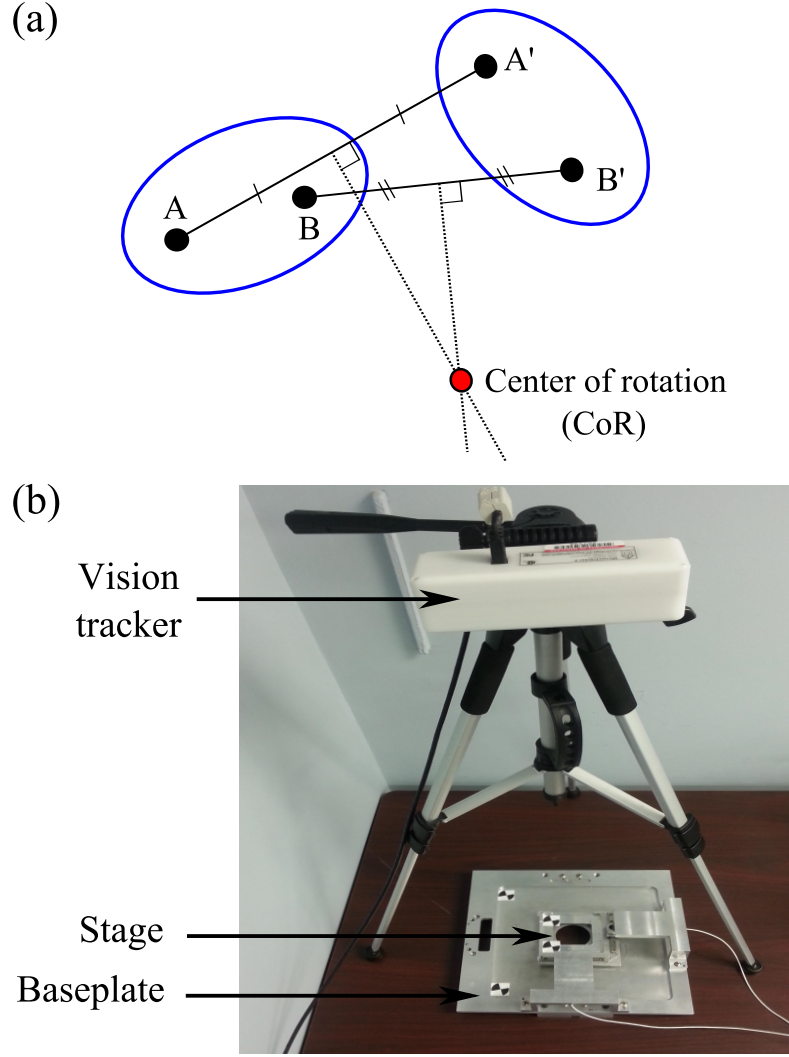


Figure 3.6: Experimental setup for finding instantaneous COR of the stage: (a) Schematic of geometrically defined COR and (b) The experimental setup.

the simulation result represents the equation of: $(x_A^W)^2 + (y_A^W)^2 = \overline{PQ}^2/4$. Unless angle θ is close to zero, the COR of the stage moves along the circle made by the geometric constraints as predicted. The instability near zero degrees is due to the low resolution of the vision tracker and singularity in the analytical model. Figure 3.7(b) shows the similarity between the rotational angle calculated from instantaneous COR and the measured angle from the markers with root-mean-square-error of 0.189° . Moreover, the angular ROM of the stage can be found to be $[-28.5^\circ, 28.5^\circ]$.

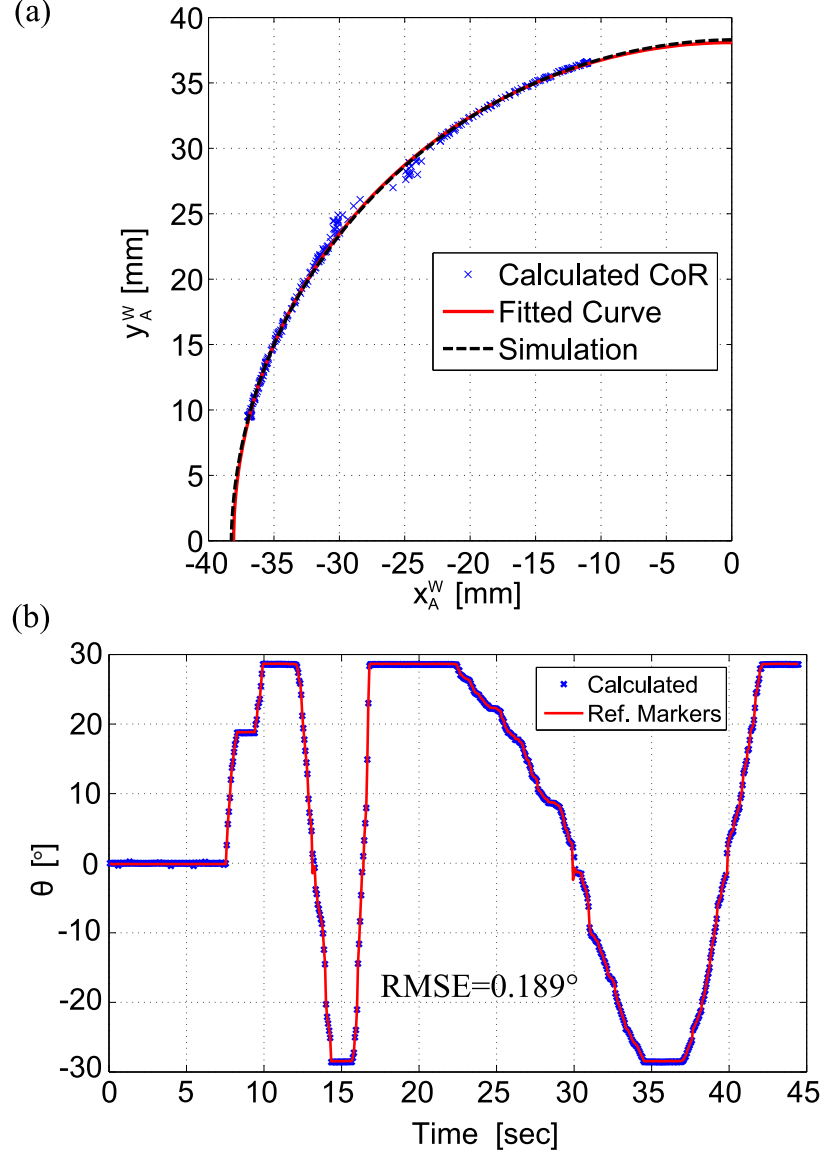


Figure 3.7: Results of the vision tracking experiment to find the instantaneous COR: (a) The coordinates of instantaneous COR, $[x_A^W, y_A^W]^T$ and (b) Comparison of the measured angle of the stage with the calculated angle from instantaneous COR.

3.4.2 Kinematic Modeling

To derive the kinematic model of the stage, the two coordinate systems, namely, the world frame, $\{W\}$ (fixed frame), and the body frame, $\{B\}$ (moving frame), are defined and shown in Fig. 3.5. The origin of the body frame $\{B\}$ is placed at the intersection point of two linear guides. The direction of x^B -axis is opposite to the direction of x^W -axis at the initial

configuration so that all variables in $\{B\}$ can be defined as positive values. Since the coordinate system of the microscopic image is fixed, the kinematic model should be interpreted in the fixed frame $\{W\}$ for ease of matching these two coordinate systems. The rotation matrix from the body frame $\{B\}$ to the world frame $\{W\}$, \mathbf{R}_B^W , and its time derivative, $\dot{\mathbf{R}}_B^W$, can be expressed as:

$$\mathbf{R}_B^W = \begin{bmatrix} -C_\theta & -S_\theta & 0 \\ -S_\theta & C_\theta & 0 \\ 0 & 0 & -1 \end{bmatrix}, \quad \dot{\mathbf{R}}_B^W = \begin{bmatrix} S_\theta & -C_\theta & 0 \\ -C_\theta & -S_\theta & 0 \\ 0 & 0 & 0 \end{bmatrix} \dot{\theta} \quad (3.1)$$

where, $S_\theta = \sin\theta$ and $C_\theta = \cos\theta$.

Since the linear actuators are aligned along the respective axes in $\{W\}$, the velocity input vector of each linear actuator has only one non-zero component. Thus:

$$\mathbf{u}_1^W = \begin{bmatrix} u_1 \\ 0 \\ 0 \end{bmatrix} = \begin{bmatrix} \dot{x}_Q^W \\ 0 \\ 0 \end{bmatrix}, \quad \mathbf{u}_2^W = \begin{bmatrix} 0 \\ u_2 \\ 0 \end{bmatrix} = \begin{bmatrix} 0 \\ \dot{y}_P^W \\ 0 \end{bmatrix} \quad (3.2)$$

The velocity of point Q is \mathbf{u}_1^W and that of point P is \mathbf{u}_2^W . The position and velocity of point Q in $\{W\}$ can be written as:

$$\mathbf{Q}^W = \begin{bmatrix} x_Q^W \\ y_Q^W \\ z_Q^W \end{bmatrix} = \mathbf{R}_B^W \mathbf{Q}^B + \mathbf{O}^W = \begin{bmatrix} -y_Q^B S_\theta + x_O^W \\ y_Q^B C_\theta + y_O^W \\ 0 \end{bmatrix} = \begin{bmatrix} x_Q^W \\ D_y \\ 0 \end{bmatrix} \quad (3.3)$$

$$\begin{aligned}
\dot{\mathbf{Q}}^W &= \begin{bmatrix} \dot{x}_Q^W \\ \dot{y}_Q^W \\ \dot{z}_Q^W \end{bmatrix} = \dot{\mathbf{R}}_B^W \mathbf{Q}^B + \mathbf{R}_B^W \dot{\mathbf{Q}}^B + \dot{\mathbf{O}}^W \\
&= \begin{bmatrix} \dot{x}_O^W - \dot{y}_Q^B S_\theta - y_Q^B C_\theta \dot{\theta} \\ \dot{y}_O^W + \dot{y}_Q^B C_\theta - y_Q^B S_\theta \dot{\theta} \\ 0 \end{bmatrix} = \begin{bmatrix} \dot{x}_Q^W \\ 0 \\ 0 \end{bmatrix} = \begin{bmatrix} u_1 \\ 0 \\ 0 \end{bmatrix}
\end{aligned} \tag{3.4}$$

Since the stage is a rigid body, the position and velocity at any point on the stage can be described in the same way. By re-arranging the equations of position and velocity of the point P and Q , the velocity of point O in $\{W\}$ can be described as:

$$\begin{aligned}
\dot{\mathbf{O}}^W &= \begin{bmatrix} \dot{x}_O^W \\ \dot{y}_O^W \\ \dot{z}_O^W \end{bmatrix} = \begin{bmatrix} C_\theta^2 u_1 - S_\theta C_\theta u_2 + \dot{\theta}(-X_O T_\theta + Y_O) \\ S_\theta C_\theta u_1 + C_\theta^2 u_2 + \dot{\theta}(X_O + Y_O T_\theta) \\ 0 \end{bmatrix} \\
&= f(x_O^W, y_O^W, \theta, \dot{\theta}, u_1, u_2)
\end{aligned} \tag{3.5}$$

where, $X_O = x_O^W - D_x$, $Y_O = D_y - y_O^W$, and $T_\theta = \tan\theta$, while D_x and D_y are the distance of point P along x^W -axis and the distance of point Q along the y^W -axis from the origin of $\{W\}$, respectively.

Now, angular momentum conservation of the stage is applied to derive the state differential equation of the stage by formulating an independent equation for $\dot{\theta}$ as a function of the state variables and the control inputs only. As long as the rotational axis is parallel to the principal Z -axis of the moment of inertia, angular momentum of the body in XY plane can be treated as a scalar. Figure 3.8 represents a schematic diagram for calculating angular

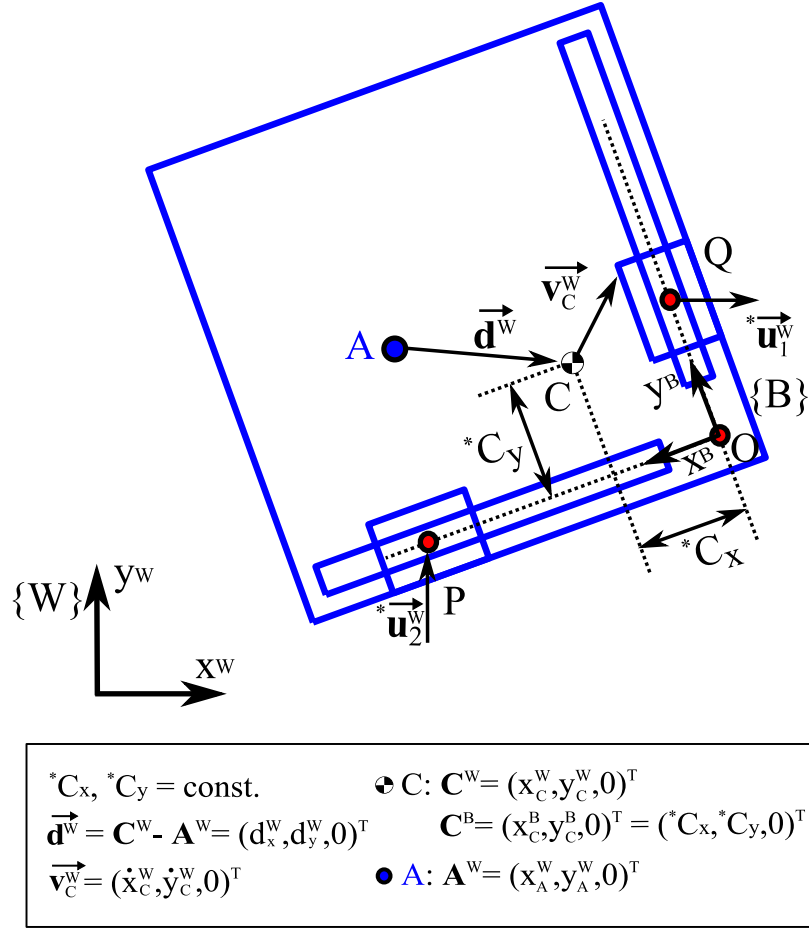


Figure 3.8: Schematic of the angular momentum of the stage (scaled drawing).

momentum of the stage. \mathbf{L} , the angular momentum of the stage is given by:

$$\begin{aligned}
 \mathbf{L} &= \begin{bmatrix} L_x \\ L_y \\ L_z \end{bmatrix} = \mathbf{d}^W \times m \mathbf{v}_C^W = \begin{bmatrix} d_x^W \\ d_y^W \\ 0 \end{bmatrix} \times m \begin{bmatrix} \dot{x}_C^W \\ \dot{y}_C^W \\ 0 \end{bmatrix} \\
 &= \begin{bmatrix} 0 \\ 0 \\ m(d_x^W \dot{y}_C^W - d_y^W \dot{x}_C^W) \end{bmatrix} = \begin{bmatrix} 0 \\ 0 \\ (I_C + m(\mathbf{d}^W \cdot \mathbf{d}^W))\dot{\theta} \end{bmatrix}
 \end{aligned} \tag{3.6}$$

where, \mathbf{d}^W is the moment arm vector, m is the mass of the stage, \mathbf{v}_C^W the linear velocity

vector at the COM, and I_C is the moment of inertia at the COM.

To solve for $\dot{\theta}$ from the angular momentum equation, \mathbf{d}^W and \mathbf{v}_C^W need to be expressed as functions of the state variables, $\dot{\theta}$, and the control inputs explicitly. Since the COM is also on the stage, its position \mathbf{C}^W and velocity $\dot{\mathbf{C}}^W$ in $\{W\}$ can be expressed as:

$$\mathbf{C}^W = \begin{bmatrix} x_C^W \\ y_C^W \\ z_C^W \end{bmatrix} = \mathbf{R}_B^W \mathbf{C}^B + \mathbf{O}^W = \begin{bmatrix} x_O^W - C_x C_\theta - C_y S_\theta \\ y_O^W - C_x S_\theta + C_y C_\theta \\ 0 \end{bmatrix} \quad (3.7)$$

where, $\mathbf{C}^B = [C_x, C_y, 0]^T$.

$$\begin{aligned} \dot{\mathbf{C}}^W = \mathbf{v}_C^W &= \begin{bmatrix} \dot{x}_C^W \\ \dot{y}_C^W \\ \dot{z}_C^W \end{bmatrix} = \dot{\mathbf{R}}_B^W \mathbf{C}^B + \mathbf{R}_B^W \dot{\mathbf{C}}^B + \dot{\mathbf{O}}^W \\ &= \begin{bmatrix} C_\theta^2 u_1 - S_\theta C_\theta u_2 + \dot{\theta}(C_x S_\theta - C_y C_\theta - X_O T_\theta + Y_O) \\ S_\theta C_\theta u_1 + C_\theta^2 u_2 - \dot{\theta}(C_x C_\theta + C_y S_\theta - X_O - Y_O T_\theta) \\ 0 \end{bmatrix} \\ &= f(x_O^W, y_O^W, \theta, \dot{\theta}, u_1, u_2) \end{aligned} \quad (3.8)$$

From the geometric constraint of $\angle AMN = \alpha$, the expression for the COR position

contains α as well. Consequently, the moment arm vector, \mathbf{d}^W , is derived as:

$$\begin{aligned}\mathbf{d}^W &= \begin{bmatrix} d_x^W \\ d_y^W \\ d_z^W \end{bmatrix} = \mathbf{C}^W - \mathbf{A}^W \\ &= \frac{1}{2} \begin{bmatrix} X_O + Y_O T_\theta - 2C_x C_\theta - 2C_y S_\theta + \frac{\sqrt{X_O^2 + Y_O^2} C_\alpha}{C_\theta} \\ X_O T_\theta - Y_O - 2C_x S_\theta + 2C_y C_\theta - \frac{\sqrt{X_O^2 + Y_O^2} S_\alpha}{C_\theta} \\ 0 \end{bmatrix} \\ &= f(x_O^W, y_O^W, \theta, \alpha)\end{aligned}\tag{3.9}$$

where, $\mathbf{A}^W = [x_A^W, y_A^W, 0]^T = \mathbf{M}^W + [-r C_\alpha, r S_\alpha, 0]^T$, $\mathbf{M}^W = [x_M^W, y_M^W, 0]^T = \mathbf{R}_B^W \mathbf{M}^B + \mathbf{O}^W$, $S_\alpha = \sin \alpha$, $C_\alpha = \cos \alpha$, and $r = \frac{1}{2} \overline{PQ} = \frac{\sqrt{(x_P^B)^2 + (y_Q^B)^2}}{2} = \frac{\sqrt{X_O^2 + Y_O^2}}{2C_\theta}$.

By substituting \mathbf{d}^W and \mathbf{v}_C^W into Eq. (3.6), $\dot{\theta}$ can be expressed as:

$$\dot{\theta} = \frac{C_\theta}{H} (u_1 K_1 + u_2 K_2) = f(x_O^W, y_O^W, \theta, \alpha, u_1, u_2)\tag{3.10}$$

where, $H = \frac{2I_C C_\theta}{m} + C_x (X_O - C_{(\alpha+\theta)} \sqrt{X_O^2 + Y_O^2}) + C_y (Y_O - S_{(\alpha+\theta)} \sqrt{X_O^2 + Y_O^2})$, $K_1 = Y_O - 2C_y C_\theta + S_{(\alpha+\theta)} \sqrt{X_O^2 + Y_O^2}$, $K_2 = X_O - 2C_x C_\theta + C_{(\alpha+\theta)} \sqrt{X_O^2 + Y_O^2}$, $S_{(\alpha+\theta)} = \sin(\alpha + \theta)$, and $C_{(\alpha+\theta)} = \cos(\alpha + \theta)$.

Since $\dot{\theta}$ is a function of α as well, it is required to express $\dot{\alpha}$ as a function of the state variables and control inputs. From geometry, one can derive:

$$\tan \alpha = \frac{y_Q^B}{x_P^B} = \frac{\frac{D_y - y_O^W}{C_\theta}}{\frac{x_O^W - D_x}{C_\theta}} = \frac{Y_O}{X_O}\tag{3.11}$$

By differentiating Eq. (3.11):

$$\begin{aligned}
\dot{\alpha} &= \frac{\dot{y}_Q^B x_P^B - y_Q^B \dot{x}_P^B}{(x_P^B)^2 + (y_Q^B)^2} = \frac{-\dot{y}_O^W X_O - \dot{x}_O^W Y_O}{X_O^2 + Y_O^2} \\
&= -\dot{\theta} + \frac{u_1(-X_O S_\theta C_\theta - Y_O C_\theta^2) + u_2(-X_O C_\theta^2 + Y_O S_\theta C_\theta)}{X_O^2 + Y_O^2} \\
&= f(x_O^W, y_O^W, \theta, \alpha, u_1, u_2)
\end{aligned} \tag{3.12}$$

The state differential equation of the stage with the state vector $\mathbf{X} = [x_O^W, y_O^W, \theta, \alpha]^T$ can be expressed as:

$$\begin{aligned}
\dot{x}_O^W &= u_1 C_\theta^2 - u_2 S_\theta C_\theta + \frac{C_\theta}{H} (u_1 K_1 + u_2 K_2) (-X_O T_\theta + Y_O) \\
\dot{y}_O^W &= u_1 S_\theta C_\theta + u_2 C_\theta^2 + \frac{C_\theta}{H} (u_1 K_1 + u_2 K_2) (X_O + Y_O T_\theta) \\
\dot{\theta} &= \frac{C_\theta}{H} (u_1 K_1 + u_2 K_2) \\
\dot{\alpha} &= -\frac{C_\theta}{H} (u_1 K_1 + u_2 K_2) + \frac{C_\theta^2}{X_O^2 + Y_O^2} [u_1 (-X_O T_\theta - Y_O) + u_2 (-X_O + Y_O T_\theta)]
\end{aligned} \tag{3.13}$$

3.4.3 Controllability

When one considers a nonlinear system, Φ , without drift, the general model of the system is given by:

$$\Phi : \dot{\mathbf{X}} = \mathbf{g}_1(\mathbf{X})u_1 + \cdots + \mathbf{g}_m(\mathbf{X})u_m \tag{3.14}$$

where, $\mathbf{X} \in \mathbb{R}^n$ is the n -dimensional state vector of the system, $\mathbf{u} = [u_1, \dots, u_m]^T \in \mathbb{R}^m$ is the m -dimensional system input vector, and \mathbf{g}_j ($j = 1, \dots, m$) are smooth, linearly independent vector fields on \mathbb{R}^n defined for all time, t [137].

Chow's theorem [137] states that the system S is controllable if $\bar{\Delta} = \mathbb{R}^n$ for all $X \in U$, where $\bar{\Delta}$ is the involutive closure of the given distribution $\Delta = span\{\mathbf{g}_1, \dots, \mathbf{g}_m\}$ under the

Lie bracket [138]. The Lie bracket between two vector fields \mathbf{f} and \mathbf{g} is defined as:

$$[\mathbf{f}, \mathbf{g}] = \frac{\partial \mathbf{g}}{\partial \mathbf{X}} \mathbf{f} - \frac{\partial \mathbf{f}}{\partial \mathbf{X}} \mathbf{g} \quad (3.15)$$

Using Chow's theorem [137], the rank of the involutive closure of $\Delta = \text{span} \{ \mathbf{g}_1, \dots, \mathbf{g}_m \}$ is investigated. The involutive closure can be constructed by taking the Lie bracket between two vector fields in Δ [139]. The construction rule is given by:

$$G_i = G_{i-1} + [G_1, G_{i-1}] \quad (3.16)$$

where, $[G_1, G_{i-1}] = \text{span} \{ [\mathbf{f}, \mathbf{g}] : \mathbf{f} \in G_1, \mathbf{g} \in G_{i-1} \}$. If $\text{rank}[G_{i+1}] = \text{rank}[G_i]$, G_i becomes the involutive closure.

To check controllability of the stage, the state differential equation is rearranged as:

$$\dot{\mathbf{X}} = \begin{bmatrix} \dot{x}_O^W \\ \dot{y}_O^W \\ \dot{\theta} \\ \dot{\alpha} \end{bmatrix} = \mathbf{g}_1(\mathbf{X})u_1 + \mathbf{g}_2(\mathbf{X})u_2 \quad (3.17)$$

where,

$$\mathbf{g}_1 = \sum_{i=1}^4 \frac{\partial \dot{X}_i}{\partial u_1} \frac{\partial}{\partial X_i} = \begin{bmatrix} C_\theta^2 + \frac{C_\theta K_1(-X_O T_\theta + Y_O)}{H} \\ S_\theta C_\theta + \frac{C_\theta K_1(X_O + Y_O T_\theta)}{H} \\ \frac{C_\theta K_1}{H} \\ -\frac{C_\theta K_1}{H} - \frac{C_\theta^2(X_O T_\theta + Y_O)}{X_O^2 + Y_O^2} \end{bmatrix},$$

$$\mathbf{g}_2 = \sum_{i=1}^4 \frac{\partial \dot{X}_i}{\partial u_2} \frac{\partial}{\partial X_i} = \begin{bmatrix} -S_\theta C_\theta + \frac{C_\theta K_2(-X_O T_\theta + Y_O)}{H} \\ C_\theta^2 + \frac{C_\theta K_2(X_O + Y_O T_\theta)}{H} \\ \frac{C_\theta K_2}{H} \\ -\frac{C_\theta K_2}{H} - \frac{C_\theta^2(X_O - Y_O T_\theta)}{X_O^2 + Y_O^2} \end{bmatrix}$$

Using $G_1 = \text{span}\{\mathbf{g}_1, \mathbf{g}_2\}$ as the initial distribution, the construction rule is applied until the resultant distribution does not gain any additional dimension. Thus, it yields:

$$\begin{aligned} G_1 &= \text{span}\{\mathbf{g}_1, \mathbf{g}_2\}, & \text{rank}(G_1) &= 2 \\ G_2 &= \text{span}\{\mathbf{g}_1, \mathbf{g}_2, \mathbf{g}_3\}, & \text{rank}(G_2) &= 3 \\ G_3 &= \text{span}\{\mathbf{g}_1, \mathbf{g}_2, \mathbf{g}_3, \mathbf{g}_4, \mathbf{g}_5\}, & \text{rank}(G_3) &= 4 \\ \text{rank}(G_i) &= \text{rank}(G_3) & \text{for integer } i &\geq 3 \end{aligned} \tag{3.18}$$

where, $\mathbf{g}_3 = [\mathbf{g}_1, \mathbf{g}_2]$, $\mathbf{g}_4 = [\mathbf{g}_1, [\mathbf{g}_1, \mathbf{g}_2]] = [\mathbf{g}_1, \mathbf{g}_3]$, and $\mathbf{g}_5 = [\mathbf{g}_2, [\mathbf{g}_1, \mathbf{g}_2]] = [\mathbf{g}_2, \mathbf{g}_3]$.

The involutive closure has the same dimension as the dimension of the state space. Therefore, the underactuated stage using two linear actuators with passive revolute joints is locally controllable by Chow's theorem. It is important to note that when $H = 0$, \mathbf{g}_1 and \mathbf{g}_2 are undefined (note: $X_O^2 + Y_O^2 > 0$, $\because X_O > 0$ and $Y_O > 0$ by the structure). Theoretically, $H = 0$ occurs when the moment of inertia at the COR coincides with the coefficient of $\dot{\theta}$ from the angular momentum equation calculated by the linear momentum of the stage.

This implies that the system is locally controllable at all times unless when $H = 0$. In the system, H cannot be equal to zero under the bounded parameters of C_x , C_y , and θ . Since the stage is symmetric about the line, $y_O^B = x_O^B$ in $\{B\}$, the COM lies on the line and the relation, $C_x = C_y$ holds. When the conditions are applied, $C_\theta > 0$ ($\because -28.5^\circ \leq \theta \leq 28.5^\circ$, as shown in the "Geometric constraints" section), $C_x = C_y$, and they are both greater than zero, H is always greater than zero as shown below:

$$\begin{aligned}
H &= \frac{2I_C C_\theta}{m} + C_x \left[X_O + Y_O - (C_{(\alpha+\theta)} + S_{(\alpha+\theta)}) \sqrt{X_O^2 + Y_O^2} \right] \\
&= \frac{2I_C C_\theta}{m} + C_x \left[X_O + Y_O - \sqrt{2} S_{(\alpha+\theta+45^\circ)} \sqrt{X_O^2 + Y_O^2} \right] \\
&\geq \frac{2I_C C_\theta}{m} + C_x (\sqrt{X_O} - \sqrt{Y_O})^2 > 0
\end{aligned} \tag{3.19}$$

Since all the designed parameters of I_C , m , C_x , C_θ , X_O , and Y_O are positive numbers, the denominator H is positive definite. Therefore, the current stage is locally controllable at all times.

3.5 Point-to-point Control Strategy

3.5.1 Step 1: Rotation and finding the desired sliding line in XY plane under $\dot{\theta} = 0$ condition

For a single variable dynamic system with a state vector $\mathbf{x} = [x, \dot{x}, \ddot{x}, \dots, x^{(n-1)}]^T \in \mathbb{R}^n$, the original n^{th} -order tracking problem is replaced into a 1^{st} -order stabilization problem in s by defining a time-varying sliding surface s as [140]:

$$s(\mathbf{x}; t) = \left(\frac{d}{dt} + \lambda \right)^{(n-1)} \tilde{x} = 0 \tag{3.20}$$

where $\tilde{x} = x_d - x$ is the tracking error and λ is a strictly positive constant.

When $n = 1$, the sliding surface for the rotation can be defined as $s_1 = e_\theta$. Based on

$\dot{s}_1 = 0$, the input vector for the rotation, \mathbf{u}_{rot} can be defined as:

$$\mathbf{u}_{rot} = (\mathbf{G}_\theta^T \mathbf{G}_\theta)^{-1} \mathbf{G}_\theta^T \dot{\theta}_d + k_{rot} [1, 1]^T \text{sgn}(s_1) \quad (3.21)$$

where k_{rot} is a strictly positive control gain for the rotation, $\text{sgn}(s_1)$ is the signum function of a real number s_1 , and $\mathbf{G}_\theta = [\frac{C_\theta K_1}{H}, \frac{C_\theta K_2}{H}]$.

The tracking error of rotation converges to 0 as $t \rightarrow \infty$ (i.e. globally asymptotically stable) by Lyapunov stability theorem with a choice of positive definite Lyapunov function, $V_1 = \frac{1}{2}s_1^2$ as shown below:

$$\begin{aligned} \dot{V}_1 &= s_1 \dot{s}_1 = s_1 (\dot{\theta}_d - \dot{\theta}) = s_1 \left(\dot{\theta}_d - \frac{C_\theta K_1}{H} u_1 - \frac{C_\theta K_2}{H} u_2 \right) \\ &= s_1 (-2k_{rot} \text{sgn}(s_1)) \\ &= -2k_{rot} |s_1| < 0 \quad \forall s_1 \neq 0 \quad \text{and} \quad \dot{V}_1(s_1 = 0) = 0 \end{aligned} \quad (3.22)$$

Once the stage reaches the desired orientation, the motion constraint $\dot{\theta} = 0$ is imposed, allowing the two inputs to be related by $u_2 = -\frac{K_1}{K_2} u_1$. Thus, the stage always keeps its desired orientation until it reaches the desired position. The trajectory of point O under the motion constraint of $\dot{\theta} = 0$ is determined by the ratio of \dot{y}_O^W to \dot{x}_O^W as:

$$J_c = \frac{\dot{y}_O^W}{\dot{x}_O^W} = \frac{S_\theta C_\theta K_2 - C_\theta^2 K_1}{C_\theta^2 K_2 + S_\theta C_\theta K_1} \quad (3.23)$$

Due to the imposed motion constraint of $\dot{\theta} = 0$, J_c should be a straight line and the slope of the line is determined by (x_O^W, y_O^W) and θ as shown in Fig. 3.9. This implies that pure translational motion of the stage can be achieved between two points having the same

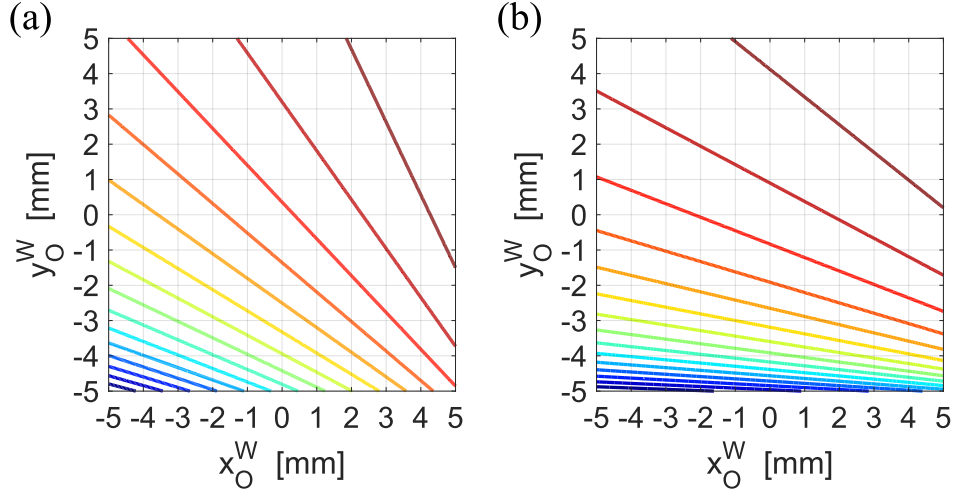


Figure 3.9: Examples of the contour plot for $J_c = \frac{y_O^W}{x_O^W}$ under the motion constraint of $\dot{\theta} = 0$: (a) With $\theta = 0^\circ$ and (b) With $\theta = 10^\circ$.

value of J_c . Without loss of generality, one can find J_d , which is J_c at the desired state, as:

$$J_d = \left(\frac{\dot{y}_O^W}{\dot{x}_O^W} \right)_{\mathbf{x}=\mathbf{x}_d, \dot{\theta}=0} = \frac{S_{\theta_d} C_{\theta_d} (K_2)_d - C_{\theta_d}^2 (K_1)_d}{C_{\theta_d}^2 (K_2)_d + S_{\theta_d} C_{\theta_d} (K_1)_d} \quad (3.24)$$

where $(K_i)_d = (K_i)_{\mathbf{x}=\mathbf{x}_d}$ for $i = 1, 2$.

The desired sliding line in XY plane that consists of a set of points $\{(x, y)\} = \{(x_O^W, y_O^W) \mid J_c = J_d\}$ can be defined as:

$$y = a(x - (x_O^W)_d) + (y_O^W)_d \quad (3.25)$$

where a is the slope of the sliding line.

3.5.2 Step 2: Reaching the sliding line

Let $s_2 = a(x_O^W - (x_O^W)_d) + (y_O^W)_d - y_O^W = -ae_x + e_y$ be the sliding surface to reach the desired line found in Step 1). By setting $\dot{s}_2 = 0$, one can define the inputs for reaching the desired

sliding line as:

$$\mathbf{u}_{sld} = \begin{bmatrix} u_{sld1} \\ u_{sld2} \end{bmatrix} = \begin{bmatrix} \frac{N_{sld}}{H(J_d - J_c)(C_\theta^2 K_2 + S_\theta C_\theta K_1)} + k_{sld} \text{sgn}(s_2) \\ -\frac{K_1}{K_2} u_{sld1} + k_{rot} \text{sgn}(s_1) \end{bmatrix} \quad (3.26)$$

where k_{sld} is a strictly positive control gain for reaching the sliding line and $N_{sld} = HK_2 \times (-J_d(\dot{x}_O^W)_d + (\dot{y}_O^W)_d) + C_\theta K_2^2 k_{rot} \text{sgn}(s_2)(-X_O T_\theta + Y_O)$.

While u_{sld1} is attracting the states towards the desired sliding line, u_{sld2} tries to keep its orientation from uncertainties such as unmodeled dynamics and kinematic modeling errors. \mathbf{u}_{sld} satisfies globally asymptotically stable condition of Lyapunov stability theorem with a positive definite Lyapunov function, $V_2 = \frac{1}{2}s_2^2$, under the motion constraint of $\dot{\theta} = 0$. \dot{V}_2 can be expressed as:

$$\begin{aligned} \dot{V}_2 &= s_2 \dot{s}_2 = s_2 [-J_d((\dot{x}_O^W)_d - \dot{x}_O^W) + (\dot{y}_O^W)_d - \dot{y}_O^W] \\ &= s_2 [-J_d(\dot{x}_O^W)_d + (\dot{y}_O^W)_d - (J_d - J_c)\dot{x}_O^W] \\ &= s_2 [(-J_d(\dot{x}_O^W)_d + (\dot{y}_O^W)_d - (J_d - J_c) \left(C_\theta^2 + S_\theta C_\theta \frac{K_1}{K_2} \right) u_1 \\ &\quad + \frac{C_\theta K_2}{H} k_{rot} \text{sgn}(s_1)(-X_O T_\theta + Y_O)] \\ &= s_2 [-k_{sld} \text{sgn}(s_2)] \\ &= -k_{sld} |s_2| < 0 \quad \forall s_2 \neq 0 \text{ and } \dot{V}_2(s_2 = 0) = 0 \end{aligned} \quad (3.27)$$

3.5.3 Step 3: Translation to the desired position along the sliding line

To reach the desired position along the sliding line, let $s_3 = e_x = (x_O^W)_d - x_O^W$ be the sliding surface. When $\dot{s}_3 = 0$, it satisfies globally asymptotically stable condition of Lyapunov

theorem by defining the inputs as:

$$\mathbf{u}_{trl} = \begin{bmatrix} u_{trl1} \\ u_{trl2} \end{bmatrix} = \begin{bmatrix} \frac{N_{trl}}{H(C_\theta^2 K_2 + S_\theta C_\theta K_1)} + k_{trl} \text{sgn}(s_3) \\ -\frac{K_1}{K_2} u_{trl1} + k_{rot} \text{sgn}(s_1) + k_{slid} \text{sgn}(s_2) \end{bmatrix} \quad (3.28)$$

where k_{trl} is a strictly positive control gain for the translational motion along the sliding line and $N_{trl} = HK_2(\dot{x}_O^W)_d - C_\theta^2 K_2^2(k_{rot} \text{sgn}(s_1) + k_{slid} \text{sgn}(s_2))(-X_O T_\theta + Y_O)$.

u_{trl2} maintains the orientation and keeps adjusting the states to stay on the sliding line while u_{trl1} tracks the desired x coordinate. The control inputs guarantees the stability of the system and the convergence of s_3 to zero with a positive definite Lyapunov function, $V_3 = \frac{1}{2}s_3^2$. \dot{V}_3 can be expressed as:

$$\begin{aligned} \dot{V}_3 &= s_3 \dot{s}_3 = s_3[(\dot{x}_O^W)_d - \dot{x}_O^W] \\ &= s_3[(\dot{x}_O^W)_d - \left(C_\theta^2 + S_\theta C_\theta \frac{K_1}{K_2}\right) u_1 \\ &\quad - \frac{C_\theta K_2}{H}(k_{rot} \text{sgn}(s_1) + k_{slid} \text{sgn}(s_2))(-X_O T_\theta + Y_O)] \\ &= s_3[-k_{trl} \text{sgn}(s_3)] \\ &= -k_{trl}|s_3| < 0 \quad \forall s_3 \neq 0 \quad \text{and} \quad \dot{V}_3(s_3 = 0) = 0 \end{aligned} \quad (3.29)$$

3.5.4 Simulation

Since α is computed at every time step from the state differential equation (Eq. (3.13)) and α is not directly controlled, let $[(x_O^W)_0, (y_O^W)_0, \theta_0]^T = [0 \text{ mm}, 0 \text{ mm}, 0^\circ]^T$ and $[(x_O^W)_d, (y_O^W)_d, \theta_d]^T = [1 \text{ mm}, 2 \text{ mm}, 1^\circ]^T$ be the initial and desired position and orientation of the stage for the simulation, respectively. Initially, the origin of the fixed frame, $\{W\}$, coincides with the origin of the moving frame, $\{B\}$ and α_0 is determined as 45° by substituting $(x_O^W)_0, (y_O^W)_0, D_x = -47.5 \text{ mm}$, and $D_y = 47.5 \text{ mm}$ in Eq. (3.11). The moment of inertia at COM and the coordinates of COM point in $\{B\}$ were determined by 3D modeling as $I_c = 297.57 \text{ kg mm}^2$ and $\mathbf{C}^B = [C_x, C_y, 0]^T = [39.21 \text{ mm}, 39.21 \text{ mm}, 0]^T$, respectively. The

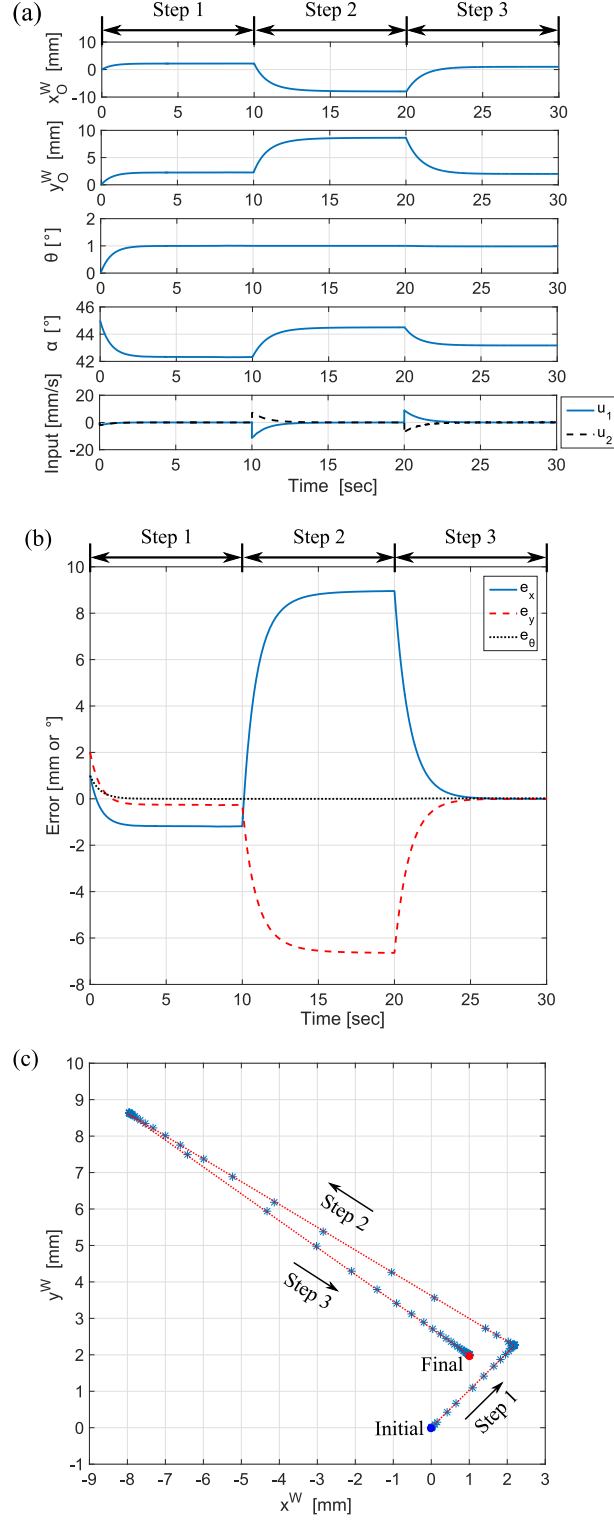


Figure 3.10: Simulation results of proposed point-to-point control strategy for $[(x_O^W)_d, (y_O^W)_d, \theta_d]^T = [1 \text{ mm}, 2 \text{ mm}, 1^\circ]^T$: (a) The state variables and the inputs, (b) The tracking errors (i.e. e_x , e_y , and e_θ), and (c) The trace of the coordinates (x_O^W, y_O^W) .

slope of the sliding line was determined as $a = -0.7414$ from the contour plot for J_c . The control gains, $(k_{rot}, k_{sld}, k_{trl}) = (0.001 + 120|s_1|, 0.001 + 10|s_2|, 0.001 + |s_3|)$, were used in the simulation. Since the stage is controlled by velocity inputs, reducing inherent chattering effect and smoothing the inputs are important for stable manipulation. Instead of using constant control gains, each control gain was determined by the summation of a small positive constant gain and a gain proportional to the absolute error. Using this approach, it is able to smoothly control and achieve good control performance at both millimeter-scale and micro-scale. The maximum speed and maximum stroke of the actuator did not violate the physical limitations during the simulation by choosing proper control gains.

Figure 3.10(a) shows the state variables and the input during the simulation. By applying the control strategy, the errors of position and orientation of the stage converge to zero as shown in Fig. 3.10(b). The trace of the coordinates (x_O^W, y_O^W) during the simulation is shown in Fig. 3.10(c), where one can track how the stage has moved according to each step of the control strategy.

3.6 Experiments and Discussion

3.6.1 Breast Tissue Core Study

To check the feasibility of the system as an automated tissue indentation system, a single breast tissue core was studied with the condition of $\dot{\theta} = 0$. This case study yields how accurately the system can manipulate the tissue sample to perform tissue characterization studies at a specified target location. When $\dot{\theta} = 0$ condition with the initial angle, $\theta = 0$ is applied, the moving stage is expected to move along -45° line without rotation based on the kinematic model. It is important to note that with these constraints on θ and $\dot{\theta}$, there is a relationship between the two control inputs. (See Fig. 3.11(a)).

For the experiment, multiple tissue cores of diameter $600 \mu m$ on a glass slide were prepared (one of the tissue core is seen in Fig. 3.11(b)), and then commanded the control inputs so that the desired displacement of $\Delta x = -75 \mu m$ and $\Delta y = 75 \mu m$ is achieved.

Though the linear sensors of PZT actuators with resolution of 1 nm can read actuators' position accurately, additional sensor is required to measure the stage angle θ as explained in observability section. To measure the stage angle θ , the imaging system on the microscope is used as an additional measurement method. Two points on the tissue core are tracked for measuring the angle of the moving stage and one of them is used for calculation of displacements by comparing before and after images of the tissue core, to observe how the state variables, x, y , and θ , change when the control inputs are applied (Fig. 3.11(c) and Fig. 3.11(d)). Table 3.2 compares the measurement results from linear position sensors of the PZT actuators and the captured images from the microscope imaging system after five trials. The results show that the stage has sub-micron accuracy and repeatability for positioning of the tissue core under the constraints, $\dot{\theta} = 0$ and initial stage angle $\theta = 0$.

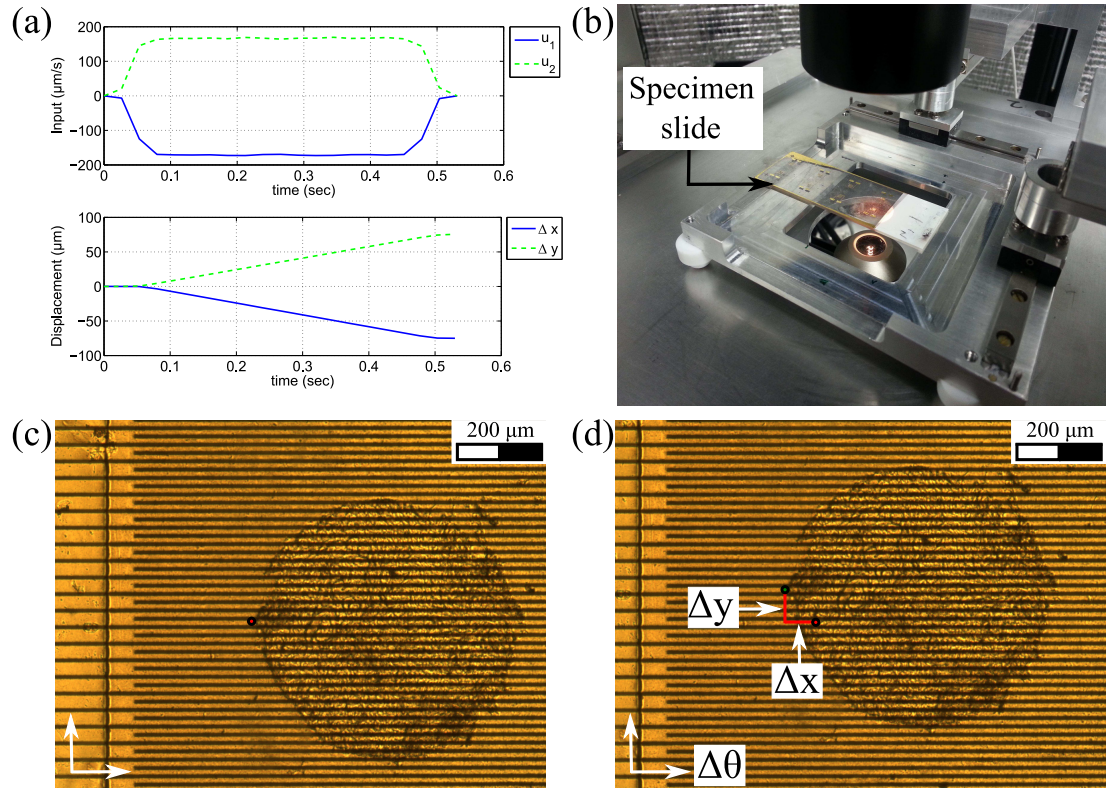


Figure 3.11: Experiment for breast tissue core study: (a) Profiles of the commanded control inputs and observed displacements of the actuators, (b) Experimental setup, (c) Tissue core image at initial configuration, and (d) Tissue core image at final configuration.

Table 3.2: Experimental result for the stage motion

	$\Delta x (\mu m)$	$\Delta y (\mu m)$	$\Delta \theta (^\circ)$
Desired	-75.000	75.000	0
PZT position sensor	-74.991 ± 0.005	74.998 ± 0.004	N/A
Captured images	-74.595 ± 0.293	74.765 ± 0.341	0.005 ± 0.004

3.6.2 Point-to-point Micropositioning

In practical application with a microscope, the position and orientation of a sample (which can be arbitrary within the range of motion of the system) should be tracked, instead of the point \mathbf{O}^W . Since the stage is a rigid body, the coordinates of a sample on the stage can be represented in the fixed frame $\{W\}$ once the coordinates of the sample are given in the moving frame $\{B\}$ as:

$$\begin{bmatrix} x^W \\ y^W \\ 0 \end{bmatrix} = \mathbf{R}_B^W \begin{bmatrix} x^B \\ y^B \\ 0 \end{bmatrix} + \mathbf{O}^W \quad (3.30)$$

where $[x^W, y^W, 0]^T$ and $[x^B, y^B, 0]^T$ are the coordinates of a sample on the stage represented in the fixed frame $\{W\}$ and the moving frame $\{B\}$, respectively.

$$\mathbf{X}^W = \mathbf{R}_B^W \mathbf{X}^B + \mathbf{O}^W \quad (3.31)$$

Measuring the orientation for the stage is challenging for two reasons; 1) the position of the stage cannot be obtained unless the orientation is known and 2) the relative angle between the base plate and the moving stage should be measured under the limited space. An encoder, one of the most common sensors for measuring the angle, is not applicable to the stage due to varying center of rotation and an external vision system with markers has too low resolution and requires wider space as shown in the previous section. Since

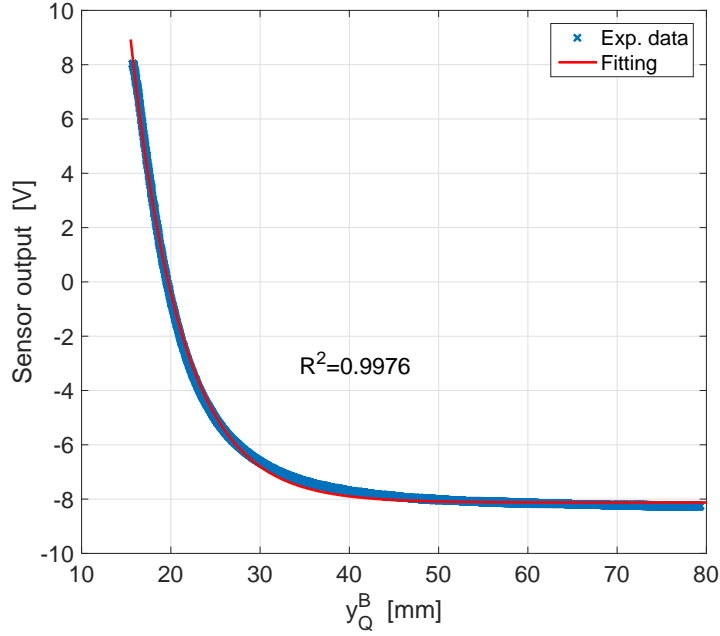


Figure 3.12: Fiber-optic sensor calibration result.

the orientation of the stage can be obtained by measuring either \overline{OP} or \overline{OQ} from the geometry (See Table 3.3), a fiber-optic sensor was chosen as a feasible option. Through the comparison of two cases, which are measuring both \overline{OP} and \overline{OQ} directly by two fiber-optic sensors and using the trigonometry, $(\overline{OP})^2 + (\overline{OQ})^2 = (\overline{PQ})^2$, with measuring \overline{OQ} , the latter showed better control performance mainly due to much higher precision on the measurement of \overline{PQ} by the nanometer resolution PZT positioner. To realize a feedback control system, an additional fiber-optic sensor (FU-77, Keyence, Japan) with amplifier (FS-V31, Keyence, Japan) was implemented on the stage to measure y_Q^B , the distance, \overline{OQ} . Figure 3.12 shows the calibration result of the fiber-optic sensor and the exponential curve fitting ($y = p_1 e^{(p_2 x + p_3)} + p_4$, where $[p_1, p_2, p_3, p_4]^T = [204.2, -0.1763, 0.25, -8.126]^T$) with R^2 -value of 0.9978. Instead of using the one-to-one exponential function, a lookup table consisting of the calibration data was used for the actual experiments to achieve higher accuracy. The PZT₂ sweeps the full range of motion at a speed of $10 \mu\text{m/s}$, while the passive rotational joints are locked to prevent the stage from rotating. By measuring the positions of the two actuators (i.e. y_P^W and x_Q^W) and y_Q^B , the stage becomes a fully observable system

by determining all the state variables of $\mathbf{X} = [x_O^W, y_O^W, \theta, \alpha]^T$ as shown in Table 3.3.

Table 3.3: Observation of the state variables

Variables	Definition
r	$\overline{PQ}/2 = \sqrt{(x_Q^W - D_x)^2 + (D_y - y_P^W)^2}/2$
x_P^B	$\sqrt{4r^2 - (y_Q^B)^2}$
α	$\tan^{-1}(y_Q^B/x_P^B)$
θ	$\tan^{-1}\left((D_y - y_P^W)/(x_Q^W - D_x)\right) - \alpha$
$\mathbf{O}^W = [x_O^W, y_O^W, 0]^T$	$[D_x + x_P^B \cos\theta, y_P^W + x_P^B \sin\theta, 0]^T$

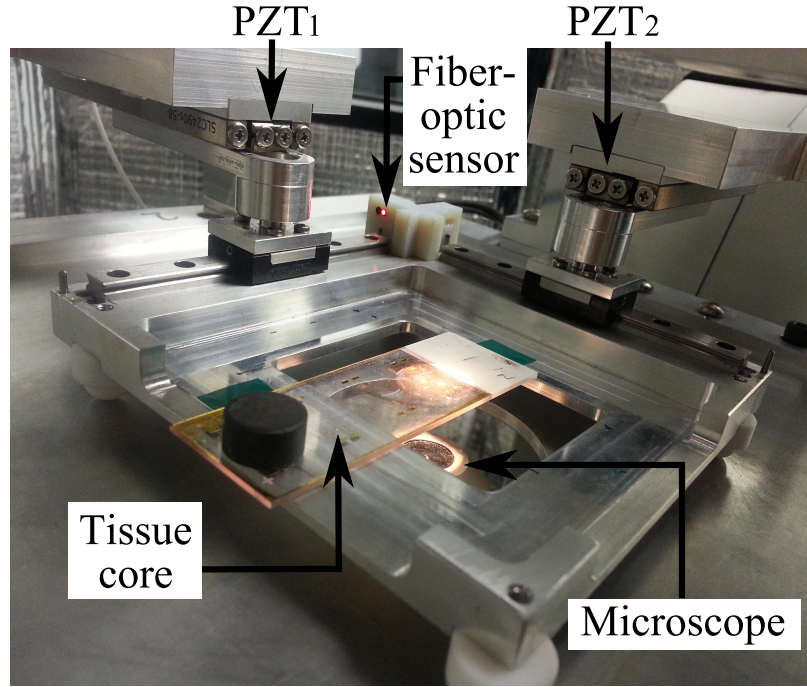


Figure 3.13: Experimental setup for point-to-point control.

Figure 3.13 shows the experimental setup for tracking a tissue core sample of $600 \mu m$ diameter on a glass slide. Current control hardware system includes the Modular Control System (MCS, SmarAct, Germany) as the controller specialized for the PZT actuators and data acquisition board (Model 626, Sensoray, USA) which contains 16-bits analog-to-digital converter for reading the output of the fiber-optic sensor. C++ language is used as a compiler for implementation of the control algorithm and update rate of the control action

is set to 100 Hz, which comes from the maximum reliable update rate of the PZT position sensors.

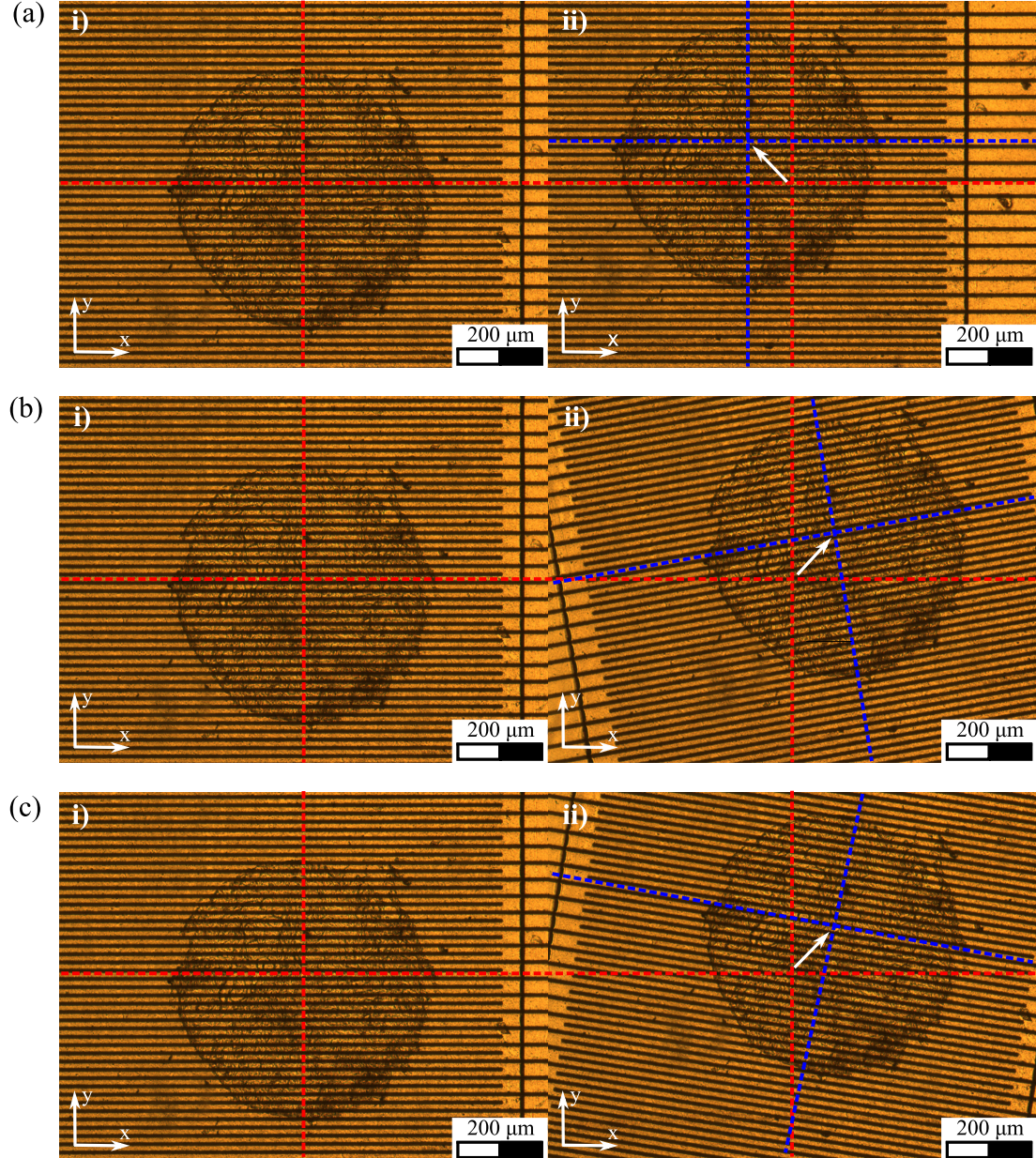


Figure 3.14: Tissue core images at the initial and final position (x,y) and orientation θ : (a) Experiment (1): $[x_d, y_d, \theta_d]^T = [-100\mu m, 100\mu m, 0^\circ]^T$, (b) Experiment (2): $[x_d, y_d, \theta_d]^T = [100\mu m, 100\mu m, 10^\circ]^T$, and (c) Experiment (3): $[x_d, y_d, \theta_d]^T = [100\mu m, 100\mu m, -10^\circ]^T$. Red and blue dotted lines represent the central lines of the stage at the initial and final state, respectively. Note: α_d is determined from the desired position and orientation using Eq. (3.11).

The target task of this experiment is to move the tissue core from the initial position and

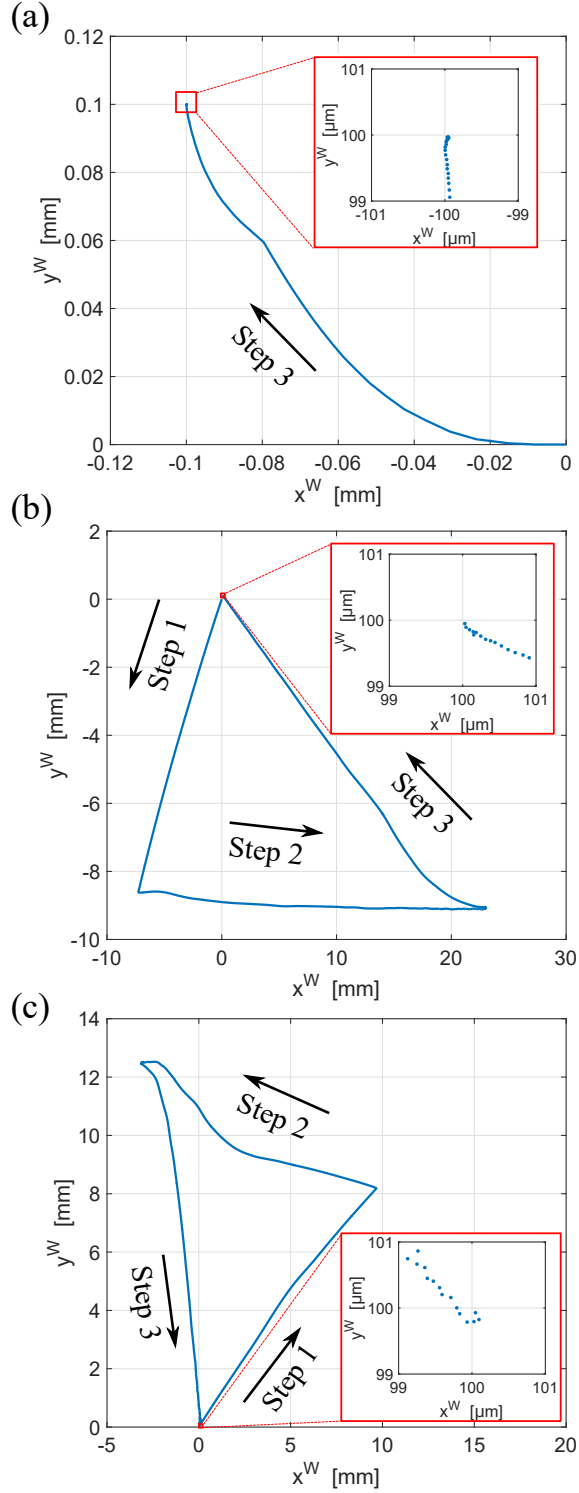


Figure 3.15: Trace of the tissue core sample: (a) Experiment (1): $[x_d, y_d, \theta_d]^T = [-100\mu\text{m}, 100\mu\text{m}, 0^\circ]^T$, (b) Experiment (2): $[x_d, y_d, \theta_d]^T = [100\mu\text{m}, 100\mu\text{m}, 10^\circ]^T$, and (c) Experiment (3): $[x_d, y_d, \theta_d]^T = [100\mu\text{m}, 100\mu\text{m}, -10^\circ]^T$. Note: α_d is determined from the desired position and orientation using Eq. (3.11).

orientation to desired position and orientation by the proposed control scheme. Comparison of microscopic images before and after the task is used as an auxiliary tool to evaluate the control performance. The center point of the stage is tracked throughout the experiments. At the initial state, it corresponds to the center of the microscopic image. Three test cases were conducted to verify the control performance of the system:

- Experiment (1): $[x_d, y_d, \theta_d]^T = [-100\mu m, 100\mu m, 0^\circ]^T$ (translation)
- Experiment (2): $[x_d, y_d, \theta_d]^T = [100\mu m, 100\mu m, 10^\circ]^T$ (maximum rotation in counter-clockwise direction with the desired position and orientation)
- Experiment (3): $[x_d, y_d, \theta_d]^T = [100\mu m, 100\mu m, -10^\circ]^T$ (maximum rotation in clockwise direction with the desired position and orientation)

Table 3.4: Experimental results of point-to-point control

		$x (\mu m)$	$y (\mu m)$	$\theta (^\circ)$
Exp. (1)	D	-100.00	100.00	0.00
	M	-99.91 ± 0.23	99.97 ± 0.29	0.01 ± 0.01
	I	-100.22 ± 0.42	100.16 ± 0.48	0.01 ± 0.01
Exp. (2)	D	100.00	100.00	10.00
	M	100.21 ± 0.43	100.37 ± 0.39	10.01 ± 0.02
	I	101.09 ± 0.82	100.97 ± 0.80	9.98 ± 0.07
Exp. (3)	D	100.00	100.00	-10.00
	M	99.88 ± 0.53	100.33 ± 0.43	-10.01 ± 0.01
	I	100.92 ± 0.79	100.38 ± 0.77	-10.04 ± 0.05

D: Desired, M: Measured, I: Image analysis

The desired position and orientation of Experiment (1) can be achieved by applying only 'Step 3' of the control strategy, since the initial position of the stage lies on the desired sliding line with the desired orientation already, while Experiment (2) and Experiment (3) require all steps of the control strategy.

The experimental results of the proposed point-to-point control after 5 trials of each case are presented in Table 3.4. The micropositioning platform shows sub-micron accuracy and repeatability both in measurement and image analysis. Tissue core images at the initial

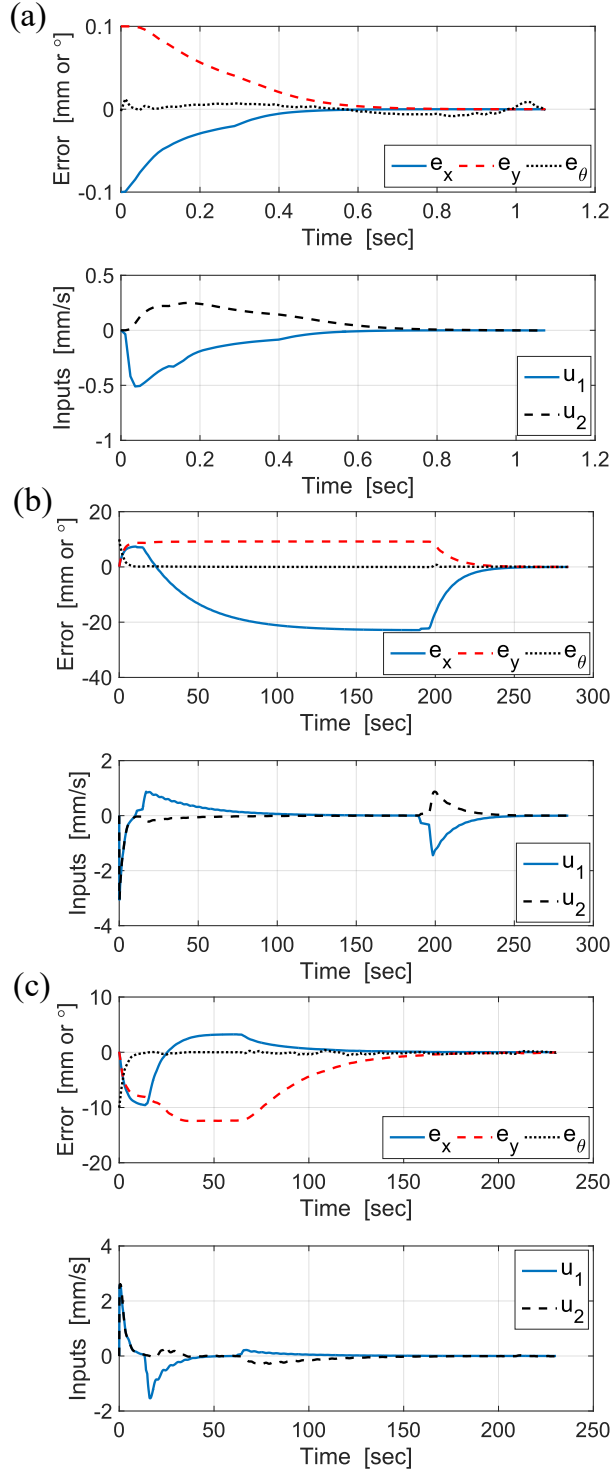


Figure 3.16: Tracking errors and control inputs: (a) Experiment (1): $[x_d, y_d, \theta_d]^T = [-100\mu m, 100\mu m, 0^\circ]^T$, (b) Experiment (2): $[x_d, y_d, \theta_d]^T = [100\mu m, 100\mu m, 10^\circ]^T$, and (c) Experiment (3): $[x_d, y_d, \theta_d]^T = [100\mu m, 100\mu m, -10^\circ]^T$. Note: α_d is determined from the desired position and orientation using Eq. (3.11).

and final state of each case are shown in Fig. 3.14. Figure 3.15 shows the actual trace of the tissue sample for each case. Since the control law is based on the kinematic model of the system, rotation occurs during the motion under the constraint $\dot{\theta} = 0$ due to the inherent dynamics of the actuators and friction between the stage and the base plate. However, the corrective control actions compensate the errors and ensure that the state converges to the desired state. The errors of the state variables and the control inputs during the experiments are shown in Fig. 3.16.

The workspace of the stage in XY plane varies with the desired angle. Theoretically, the stage can sweep $63 \times 63 \text{ mm}^2$, whole range of actuators' stroke at the zero degrees. However, ROM in the XY plane at $\pm 10^\circ$, the maximum/minimum angle in the current design, shrinks to $32 \times 32 \text{ mm}^2$. Therefore, the practical workspace of the stage can be determined conservatively as $(x, y, \theta) = (32 \text{ mm}, 32 \text{ mm}, 20^\circ)$. However, the stage cannot reach angles greater than $\pm 10^\circ$ in the current design. The theoretical range of angle, $[-28.5^\circ, 28.5^\circ]$, was measured under the condition that the stage is manually rotated by an external force, not by the system inputs, to verify the geometric constraints. In the theoretical case, the entire range of linear guide can be utilized for rotational motion only, while the linear PZT actuations contribute to the linear and rotational motion of the stage simultaneously. Moreover, the proposed control law requires a longer travel distance to reach the sliding line for the larger desired angle. Therefore, the slider on the linear guide reaches at the end of the linear guide before reaching maximum theoretical angle when the stage is rotated by the linear PZT actuators under the proposed control scheme. It is also important to note that the cables of the fiber-optic sensor introduce disturbances into the system that the controller cannot compensate by physically touching the brackets (the structure fixing the PZT actuator). At larger angles, the cables bounce back due to interference with the motion of the stage. The maximum angle of the stage can be increased by implementing a more elaborate control law with optimal path planning and solving the cable routing problem.

3.7 Conclusion

The design and control of an underactuated 4-DOF micropositioning stage for automated tissue indentation at the micro-scale was presented along with the analysis of its geometric constraints and the point-to-point control strategy. Although the path of the stage from one state to the next is less intuitive than that of a fully-actuated system, the model and experiments described herein verify that the stage can be controlled. Moreover, the stage design presented offers additional degrees of freedom, low-profile design, and other key features not currently available at low cost. Through the breast tissue core study, it was demonstrated that the moving stage can achieve a desired position and orientation with sub-micron accuracy. By adding one more fiber optic sensor on the rail, the system can be fully observable which enables feedback control to move the stage from an arbitrary position and orientation to another arbitrary position and orientation. In future work, stage dynamics, defining range of motion, path generation for automated indentation, and closed loop control with fully observable states for rapid tissue phenotyping, including rotational capability will be investigated.

Though the control law proposed is based on the kinematic model of the stage, the system appears to be robust from dynamic uncertainties in the experiments. The underactuated stage has to undergo larger travel distance along with a less intuitive path to reach the desired state than a fully-actuated stage. However, the simulation and experiments with the proposed control strategy have shown promising results to be implemented in biomedical applications that require microscope compatible micropositioning platform. Besides several advantages of an underactuated system, enlarging ROM for a micropositioning stage with sub-micron accuracy is a meaningful result for the automation of phenotyping multiple biological samples. As the next step, automated tissue indentation experiments with a 4-DOF indentation system (the $XY\theta$ stage with additional Z-directional indenter) will be performed to verify the feasibility of the automated tissue indentation process at the

micro-scale.

CHAPTER 4

MACHINE LEARNING APPROACH FOR BREAST CANCER LOCALIZATION

4.1 Introduction

As breast cancer progresses, the microenvironment around cancerous breast tissues undergoes a physical reconfiguration to be tumor-permissive [2, 3]. A myofibroblastic-derived, collagen-rich extra-cellular matrix (ECM) is one of the distinctive signatures on breast cancer progression and these changes of the cellular structure cause differences in physical properties of breast tissue [4–7]. The capability to monitor the signatures of cancer progression in breast tissue is important for improving the accuracy of diagnosis and early detection, which is critical factors for successful treatment and recovery of the patient. Based on the literature and the previous experimental results regarding the feasibility of mechanical stiffness as a biomarker for breast cancer diagnosis, machine learning approach is applied not only to discern between normal and cancerous breast tissues but also find a region of interest (ROI) on each tissue sample as pathologists do for breast cancer diagnosis.

The goal in this section is to predict ROIs accurately on the tissue sample for localization of tumor via machine learning. In this chapter, a feasible breast cancer diagnostic procedure via machine learning is proposed. Local tissue elasticity from the indentation experiment is the basis for machine learning and being able to localize a particular region as normal or cancerous. In section 4.2, basic materials for the approach such as a force-indentation contact model, SVM, breast tissue preparation, and experimental setup are introduced. A motorized microindentation system which consists of a microscope compatible micromanipulation stage and micro indenter is used for acquiring the contact force data. SVM, a machine learning algorithm, utilizes the tissue elasticity values determined by a nonlinear contact model. The experimental results are presented in section 4.3 followed

by concluding remarks in section 4.4.

4.2 Materials and Methods

4.2.1 Force-Indentation Model

A schematic of tissue indentation with a spherical tip is shown in Fig. 4.1 and a commercially available micro force sensor with a $25\ \mu\text{m}$ radius spherical tip (FT-S1000-LAT-TP, FemtoTools AG, Switzerland) is used for the indentation experiment (Fig. 4.2).

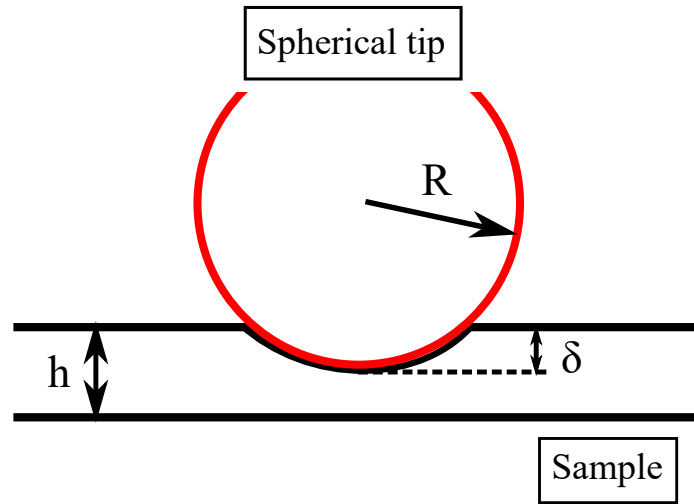


Figure 4.1: Schematic diagram of sample indentation with a spherical tip.

A contact model developed by Long et al. is a suitable force-indentation model for soft tissue indentation which accounts for nonlinearities of an incompressible neo-Hookean material during indentation with a spherical tip [141]. According to the contact model, the contact force, F , is given by:

$$F = \frac{16E\sqrt{R}}{9} \left[\frac{\delta^{1.5} + 1.15\sqrt{\gamma}\delta^2 + \alpha_1\gamma\sqrt{\gamma}\delta^3 + \alpha_2\gamma^3\delta^{4.5}}{1 + 2.3\gamma\sqrt{\gamma}\delta^{1.5}} \right] \quad (4.1)$$

where, E is Young's modulus of the sample, R is the radius of the spherical tip, δ is the indentation depth, h is the thickness of the sample, and the remaining parameters are defined

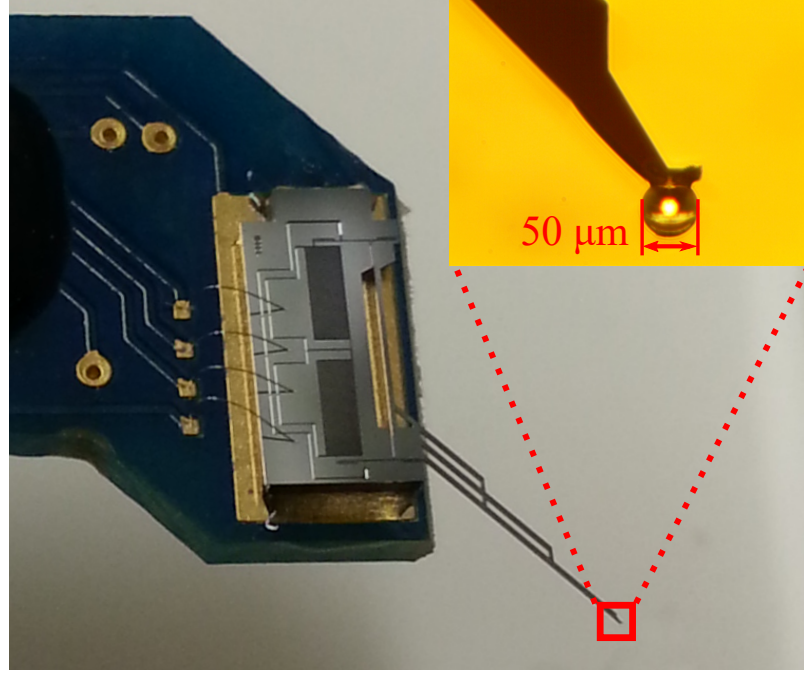


Figure 4.2: Micro force sensor with a $25 \mu\text{m}$ radius spherical tip (FT-S1000-LAT-TP, FemtoTools AG, Switzerland) used for the indentation experiment.

as:

$$\alpha_1 = 10.05 - 0.63 \sqrt{\frac{h}{R}} \left(3.10 + \frac{h^2}{R^2} \right)$$

$$\alpha_2 = 4.8 - 4.23 \frac{h^2}{R^2}$$

$$\gamma = \frac{R}{h^2}$$

4.2.2 Support Vector Machine (SVM) Algorithm

Determining a certain indentation point as 'Normal' or 'Cancerous' based on the mechanical characterization of breast tissue can be defined as a binary classification task. Support vector machine (SVM), known as one of the useful classifiers in machine learning area, is used for the classification task. For a given training data set of n points, $(\mathbf{x}_1, y_1), \dots, (\mathbf{x}_n, y_n)$ where \mathbf{x}_i is a real vector and y_i ($i = 1, \dots, n$) is either -1 or +1, which indicates the class of the tissue as 'Normal' and 'Cancerous' respectively, a SVM algorithm separates

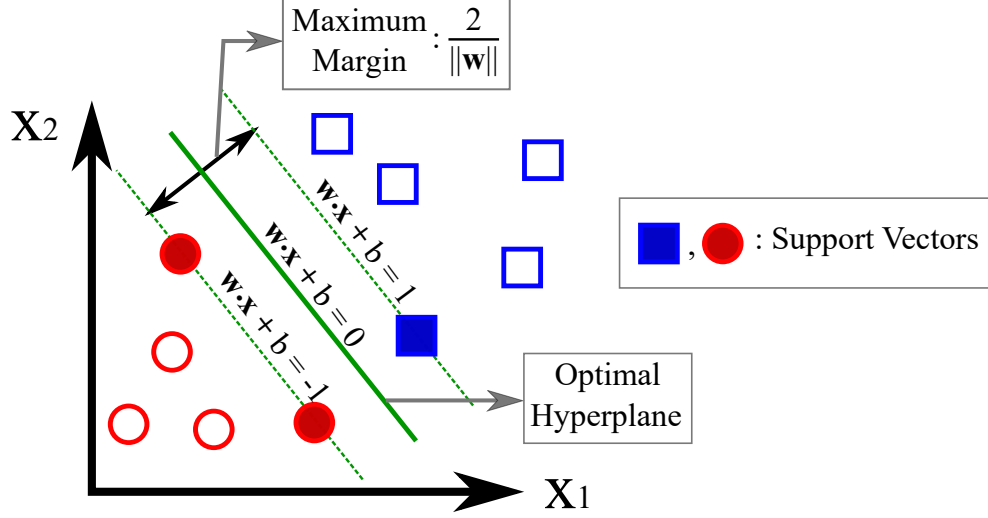


Figure 4.3: Schematic of support vector machine (SVM).

the given training data into two classes by finding an optimal hyperplane which maximizes the hard-margin, $\frac{2}{\|\mathbf{w}\|}$, where \mathbf{w} is the normal vector to the hyperplane and b is the bias, as shown in Fig. 4.3. To extend SVM for cases that the given data are not linearly separable, soft-margin SVM is introduced with a slack variable, ξ_i , which accounts for an upper bound on the training classification errors. To get an optimal hyperplane from linearly non-separable data, the total penalties for misclassified data should be minimized with respect to the optimal hyperplane. Hence, the soft-margin SVM algorithm can be expressed as [142]:

$$\min_{\mathbf{w}, b, C} \left[\frac{1}{2} \|\mathbf{w}\|^2 + C \sum_{i=1}^n \xi_i \right] \quad (4.3)$$

$$\forall (\mathbf{x}_i, y_i) \quad s.t. \quad y_i(\mathbf{w} \cdot \mathbf{x}_i + b) \geq 1 - \xi_i, \quad \xi_i \geq 0$$

where C is the regularization parameter that determines the trade-off between increasing the geometric margin and decreasing the number of wrong classifications.

4.2.3 Breast Tissue Sample Preparation

Formalin-fixed paraffin-embedded (FFPE) normal and cancerous breast tissue samples were carefully identified from Biospecimen Repository at Rutgers Cancer Institute of New Jersey. Extracted tissue cores from biopsy were inserted individually into a pre-punctured paraffin block to make a tissue microarray (TMA) using a tissue microarrayer (ATA-27, Beecher Instruments Inc., USA). The paraffin block with tissues was sectioned twice at $8\ \mu\text{m}$ thickness for pathological annotation and indentation experiment, respectively as shown in Fig. 4.4(a). A certified pathologist annotated cancerous regions with blue color for the first slice based on hematoxylin and eosin (H&E) stained image as shown in Fig. 4.4(b). The second slice placed on a glass slide was de-paraffinized and stored in phosphate-buffered saline (PBS) solution until the indentation experiment was conducted.

4.2.4 Experimental Setup

A microindentation system has been built and customized for a specific inverted microscope (Eclipse TE-2000U, Nikon, Japan). The system consists of a micromanipulation stage for planar positioning of the sample and a microindenter with a micro force sensor as shown in Fig. 4.5. All motions of the system are driven by piezoelectric linear actuators (SLC-2490-S, SmarAct, Germany) with $1\ \text{nm}$ resolution position sensors and the corresponding controller (MCS-3C-USB-TAB, SmarAct, Germany) for the actuators. Details about the stage construction and its kinematics can be found in the prior chapters or publications[136, 143]. A brief summary of the features of the micropositioning platform is presented in Table 4.1.

For each tissue sample, 500 indentation points were selected along a grid with $20\ \mu\text{m}$ spacing in the horizontal and vertical direction as shown in Fig. 4.6(a). The regions near the circumferential edge were excluded from the examination to avoid geometric bias during the experiment. It was assumed that the difference between two consecutive slices from the same tissue block is negligible and labeled every indentation point as either 'Normal'

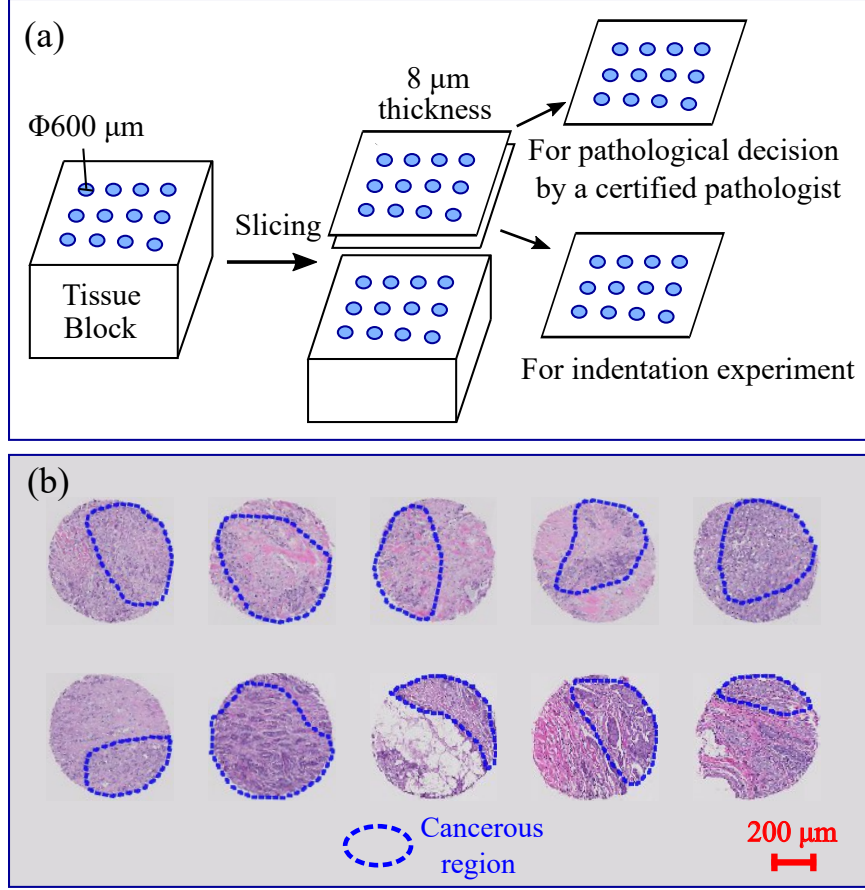


Figure 4.4: Breast tissue preparation: (a) Schematic of tissue microarray (TMA) and (b) A hematoxylin and eosin (H&E) image with annotated cancerous regions by a certified pathologist.

or 'Cancerous' based on the annotated H&E images by a certified pathologist. Using the microindentation system, the contact force and indentation depth data were collected via a data acquisition board (Model 826, Sensoray, USA) under the experimental conditions as summarized in Table 4.2. Fig. 4.6(b) shows a microscopic image for the microindentation experiment with the breast tissue.

4.3 Results and Discussion

The local elasticity value at each indentation point is determined by the contact model (Eq. 4.1) using the measured contact force and indentation depth. Figs. 4.7(a) and 4.7(b) show the experimental result of the elasticity map for a particular sample and distribution of the

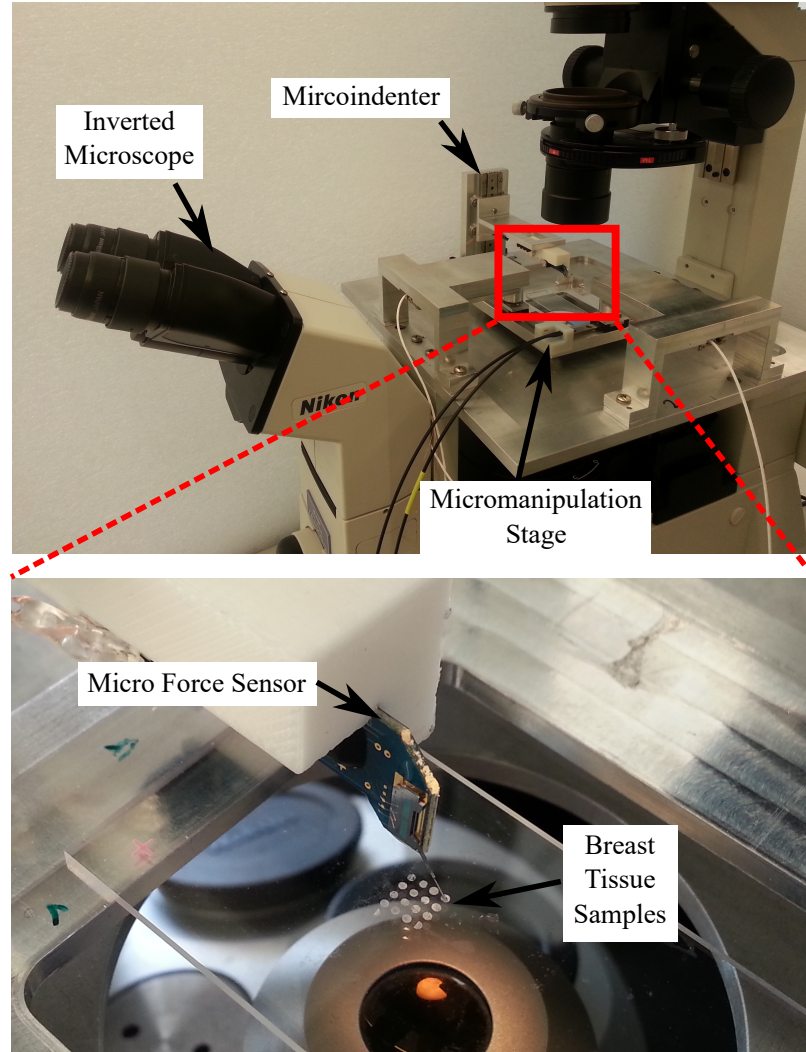


Figure 4.5: Experimental setup for microindentation.

measured elasticity for all the indentation points for the cancerous breast tissue specimens, respectively. Though the measured elasticity values for the normal and cancerous regions are not linearly separable, the optimal hyperplane can be determined by the soft-margin SVM algorithm (Eq. 4.3) while the regularization parameter, C , is set to $\frac{1}{n}$, a factor that generally works well for linear SVM cases[142].

Using a similar approach as the 10-fold cross-validation, the elasticity data from each of the breast tissue samples were used for the test while the soft-margin SVM was trained with the data from other remaining 9 samples. In 10-fold cross-validation, by definition, a given data set is partitioned 'randomly' into 10 equal sized subsets and a single subset is

Table 4.1: Features of the micropositioning platform

Maximum Linear Travel Range	63 mm in X, Y, and Z
Maximum Angular Motion about Z axis	$\pm 10^\circ$
Motion Sensor Resolution	1 nm
Actuator Motion Repeatability	$\pm 90 \text{ nm}^2$
Stage Size	112 x 112 mm ²
Force Sensing Range	$\pm 1000 \mu\text{N}$
Force Sensor Sensitivity	125 $\mu\text{N}/\text{V}$ after conditioning

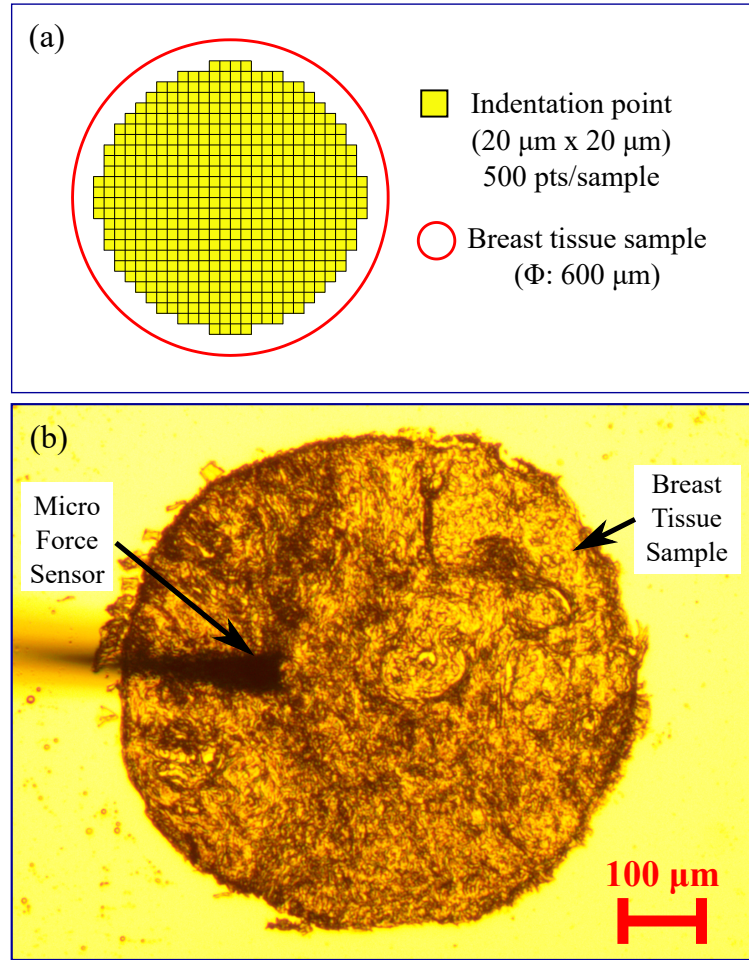


Figure 4.6: Breast tissue indentation: (a) Indentation points as defined on a virtual grid and (b) A microscopic image of breast tissue during indentation.

validated for the test, while the remaining subsets are used as the training data [142]. In this validation, each subset contains 500 elasticity values from each breast tissue sample, respectively, which is not randomly assigned. Fig. 4.8 shows the classification result for

Table 4.2: Summary for the experimental conditions

# of breast tissue samples	10 (cancerous)
# of labels as cancerous	3,181 (out of 5,000)
Indentation Depth	2 μm (25% of the sample thickness)
Indentation Speed	2 $\mu m/s$
Data Sampling Time	15 ms
Environmental Temperature	23 \pm 2°C
Environmental Humidity	32 \pm 5% (RH)

10 cancerous breast tissue samples. The soft-margin SVM returns either 'Normal' or 'Cancerous' for each indentation point based on the obtained optimal hyperplane for each test. The labels, 'Normal' and 'Cancerous', for each indentation point, are represented as blue and red in the classification result (see Fig. 4.8). Qualitatively, the regions classified as 'Cancerous' can be recognized with blurred boundaries for over half of the samples.

Accuracy, precision and recall were calculated as quantitative measures for each sample as:

$$\begin{aligned}
 Accuracy &= \frac{T_p + T_n}{T_p + T_n + F_p + F_n} \\
 Precision &= \frac{T_p}{T_p + F_p} \\
 Recall &= \frac{T_p}{T_p + F_n}
 \end{aligned} \tag{4.4}$$

where, T_p is the number of true positives, T_n is the number of true negatives, F_p is the number of false positives, and F_n is the number of false negatives.

Table 4.3: Quantitative experimental results of 10 tests

Item	mean \pm SD [%]	Max. [%]	Min. [%]
Accuracy	76.20 \pm 9.28	86.20	56.80
Precision	84.35 \pm 12.90	95.78	57.14
Recall	89.94 \pm 5.96	98.95	78.47

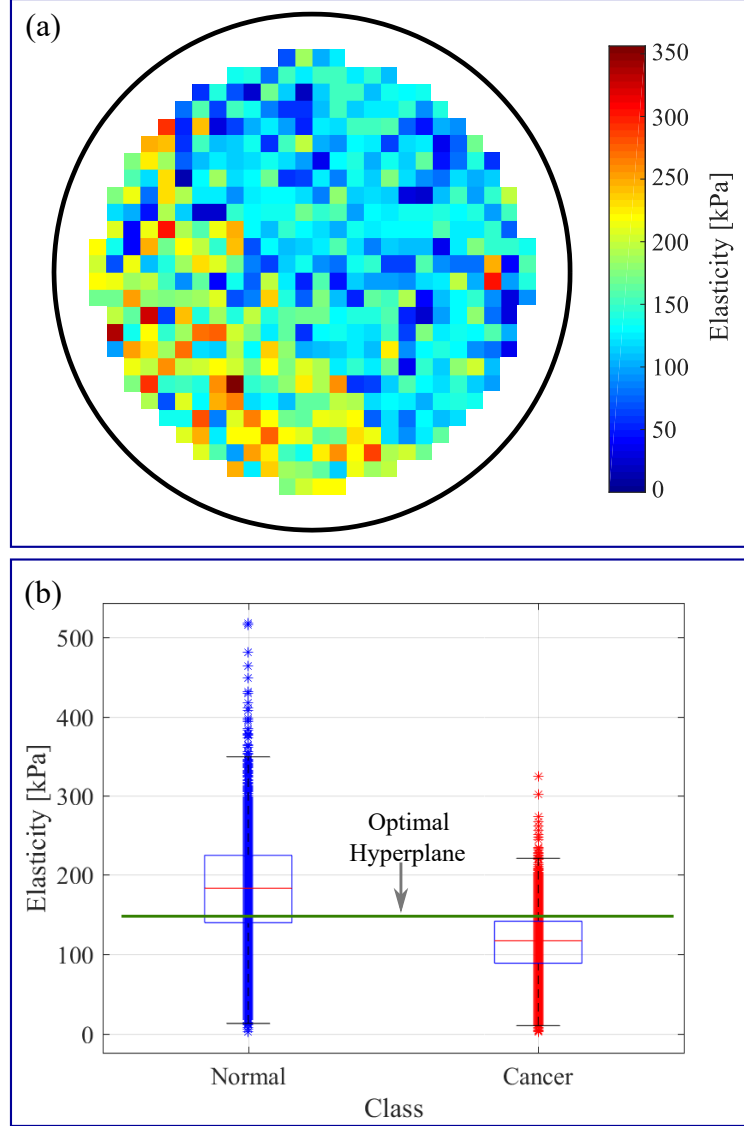


Figure 4.7: Experimental result for the local tissue elasticity: (a) Elasticity map for one of the breast tissue samples, (b) Distribution of the measured elasticity values for the 5,000 indentation points (500 indentation points for each specimen; total of 10 specimens) of the cancerous breast tissue samples, and (c) Quantitative classification result for each sample.

Table 4.3 and Fig. 4.9 show the quantitative result of 10 tests for classification. When making allowance for classification with a single parameter, the classification accuracy of $76.20 \pm 9.28 \%$ can be regarded as a promising approach to determine whether machine learning for breast cancer localization based on tissue characterization is a feasible approach or not. However, there is room for improvement as well. Besides the variation between biological samples, it is suspected that the type of the tissue sample and the inherent

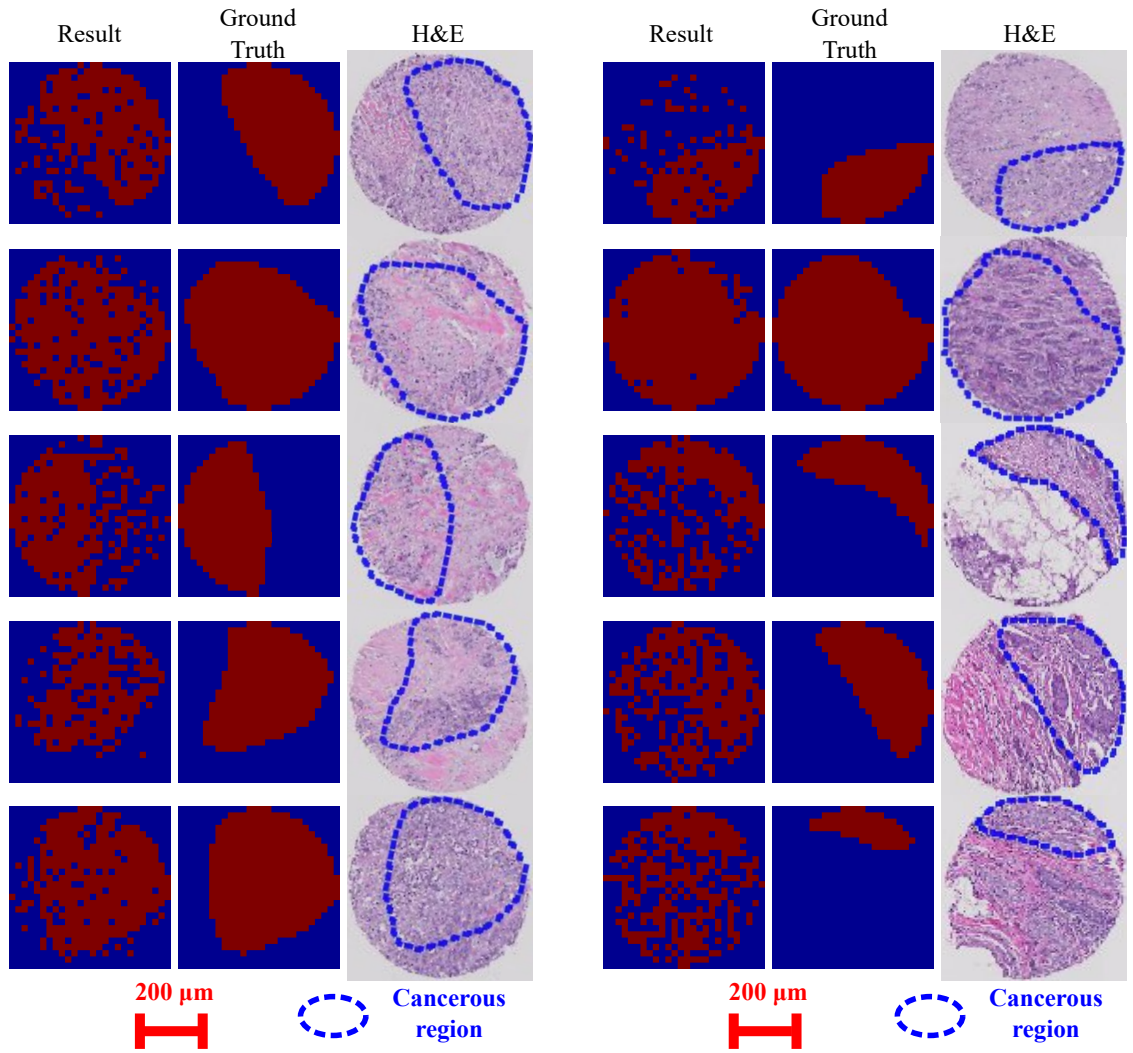


Figure 4.8: Classification result for 10 cancerous breast tissue samples. A region in blue and red color represents a region classified as 'Normal' and 'Cancerous', respectively, while a dotted blue line on the H&E image encloses a cancerous region which is determined by a certified pathologist.

heterogeneity of the tissue structure within a sample are the major causes of classification errors. In Fig. 4.8, the three lowermost samples of the right column, which consist of primarily epithelial tissues, show worse results compared to other samples, which are mostly composed of stromal tissues. Since it is known that epithelial breast tissues are less stiff than stromal breast tissues and cancerous breast tissues are also less stiff than normal breast tissue in micro-scale [17, 74], this combination could affect the performance of the classifier. Therefore, prior knowledge about the type of tissue could help to increase the

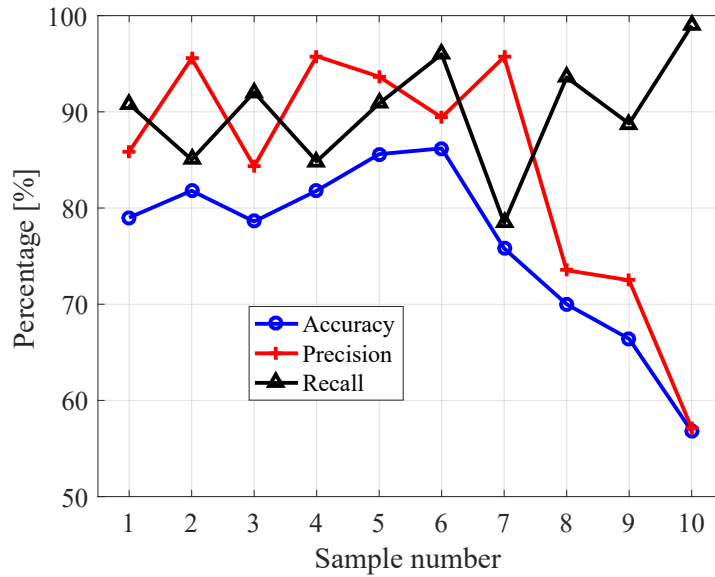


Figure 4.9: Quantitative classification result for each sample.

classification accuracy for specific tissue types such as normal epithelial, normal stromal, cancer epithelial, and cancer stromal.

4.4 Conclusion

Breast cancer localization using SVM based on tissue elasticity value was investigated with a preliminary result for 10 cancerous breast tissue samples. Though a medical decision should be made through a comprehensive understanding of various related parameters, the experimental results show that tissue elasticity can be a feasible factor for breast cancer localization with the help of machine learning. For future work, it is being planned to investigate other physical parameters of breast tissue to find additional informative factors of breast cancer such as electrical or thermal property and enrich the data set of machine learning with multiple parameters from a number of breast tissue samples to improve the accuracy of cancer localization.

CHAPTER 5

PORTABLE CANCER DIAGNOSTIC TOOL USING A DISPOSABLE MEMS-BASED BIOCHIP

5.1 Introduction

Although various diagnostic methods for breast cancer have been developed, current techniques including mammography and visual inspection of the tissue specimen taken by needle biopsy are largely qualitative approaches. Elastography, an imaging technique using the mechanical characterization of breast tissue has also been widely used for breast cancer diagnosis in the clinic. However, it is often difficult to differentiate benign and malignant tissue through elastography, mainly due to the high variability of lesions [144–146]. As an extension of previous chapters, which was the development of a microelectromechanical systems (MEMS) based sensor that enables simultaneous electrical and mechanical property measurement of breast tissue, ETM properties and electromechanical coupling factor of breast tissue is introduced as biomarkers of breast cancer. This research aims to develop a portable diagnostic tool, which provides an automated diagnostic procedure with one-click operation so that involvement in the procedure by the operator can be minimized. Knowledge of available diagnostic methods for breast cancer and challenges encountered by current and past techniques were taken into account during the developing of a prototype. This chapter will discuss the design of a portable diagnostic tool with the disposable 3D-printed package including a biochip, a piezoelectric model of breast tissue, histological staining techniques, and experimental results to demonstrate the feasibility of EMT properties and electromechanical coupling factor of human breast tissues as biomarkers for breast cancer.

5.2 Biochip Towards a Portable Cancer Diagnostic Tool

5.2.1 Biochip Fabrication

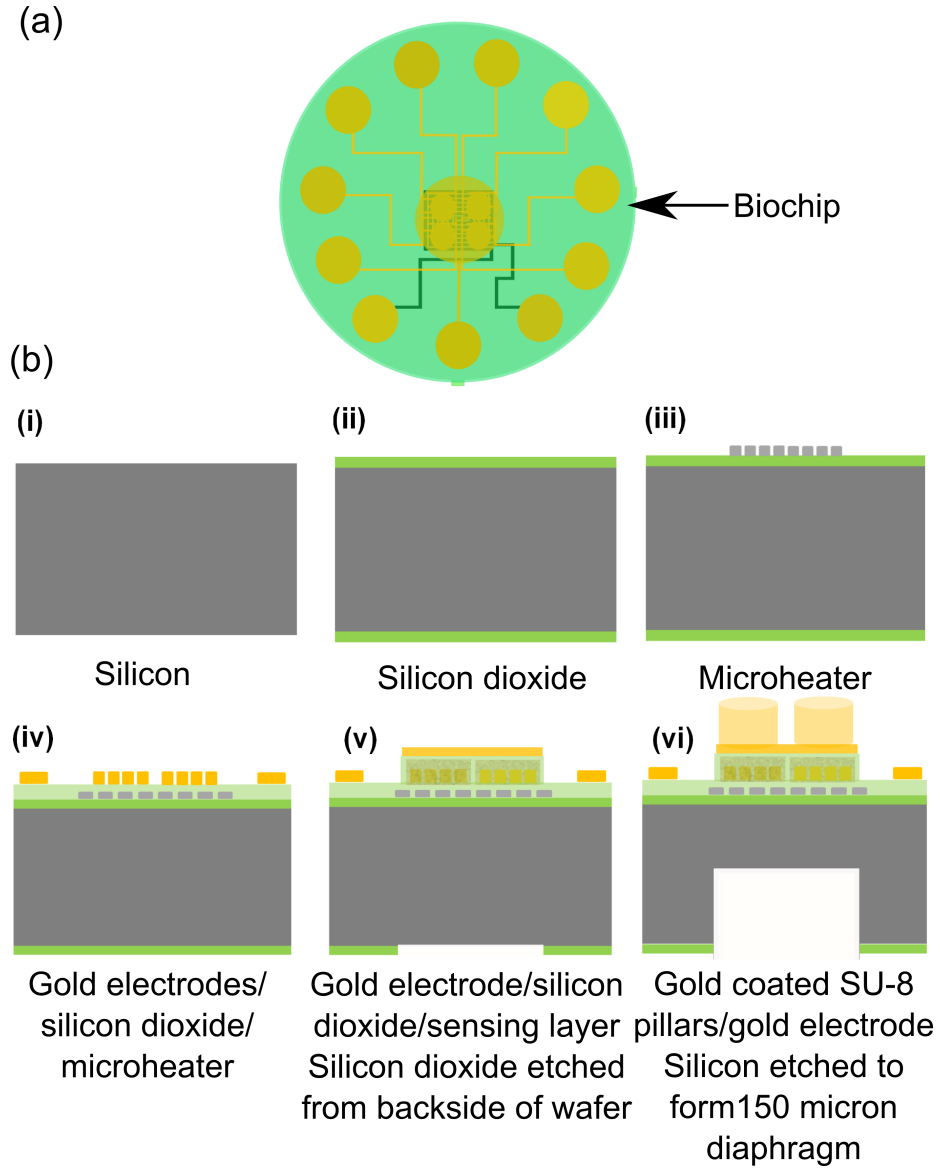


Figure 5.1: (a) Schematic diagram of biochip and (b) Process flow for fabricating the biochip.

The biochip integrated with microheater and piezoresistive sensor array is fabricated on oxidized silicon substrate using a seven mask process. The sensor array covers $2\text{ mm} \times 2\text{ mm}$ area while the complete device is 10 mm in diameter. The fabrication process is as follows

(see Fig. 5.1(b)): (i) a 4-inch, (100) orientation silicon (Si) wafer ($500\ \mu\text{m}$ thick) is used as a substrate, (ii) $1\ \mu\text{m}$ silicon dioxide (SiO_2) is grown using thermal evaporation, (iii) a microheater is fabricated on oxidized silicon substrate by patterning sputtered deposited nichrome (NiCr) ($0.3\ \mu\text{m}$ thick). (iv) SiO_2 ($0.5\ \mu\text{m}$) is deposited using plasma enhanced chemical vapor deposition (PECVD) over microheater. SiO_2 is etched from the contact area of the microheater and Cr/Au ($20\ \text{nm}/500\ \text{nm}$) is deposited using e-beam evaporation and patterned to form interdigitated electrodes, (v) Germanium ($1.5\ \mu\text{m}$) is deposited over Cr/Au electrodes using e-beam evaporation and patterned using lift off technique to form sensing layer. SiO_2 ($1.8\ \mu\text{m}$) is deposited using PECVD over the sensing layer and etched from the contact pads. Cr/Au ($20\ \text{nm}/500\ \text{nm}$) film is deposited and patterned to form the contact pad for the electrical connection to the tissue. (vi) SU-8 pillars ($750\ \mu\text{m}$ diameter and $100\ \mu\text{m}$ height) are patterned over this contact pad and coated with metal to make them electrically conductive. These pillars serve a dual purpose: (a) they act as the force transmitters to the breast tissue during tissue indentation and (b) they are electrically conductive electrodes (E2). (vii) Front-to-Back alignment is used to open the window from the backside of silicon wafer and SiO_2 layer is etched followed by silicon etching ($350\ \mu\text{m}$) to form $150\ \mu\text{m}$ diaphragm. The fabricated biochip is realized by dicing it from silicon wafer using a dicing saw from MicroAutomation. Figure 5.2 shows the dimensions of the elements used in fabricating the biochip.

The SEM images of microheater, interdigitated electrodes, sensing layer, gold electrode for electrical contact, SU-8 pillars over gold electrode, and diaphragm is shown in Fig. 5.3(a) to (e). Figure 5.3(f) shows the photograph of the biochip.

5.2.2 Breast Tissue Preparation

Invasive ductal carcinoma (IDC) and normal tissue blocks are selected from cancer tissue bank in Biospecimen Repository Service at Rutgers Cancer Institute of New Jersey. Guided by a hematoxylin and eosin (H&E) stained tissue section, the technician carefully extracted

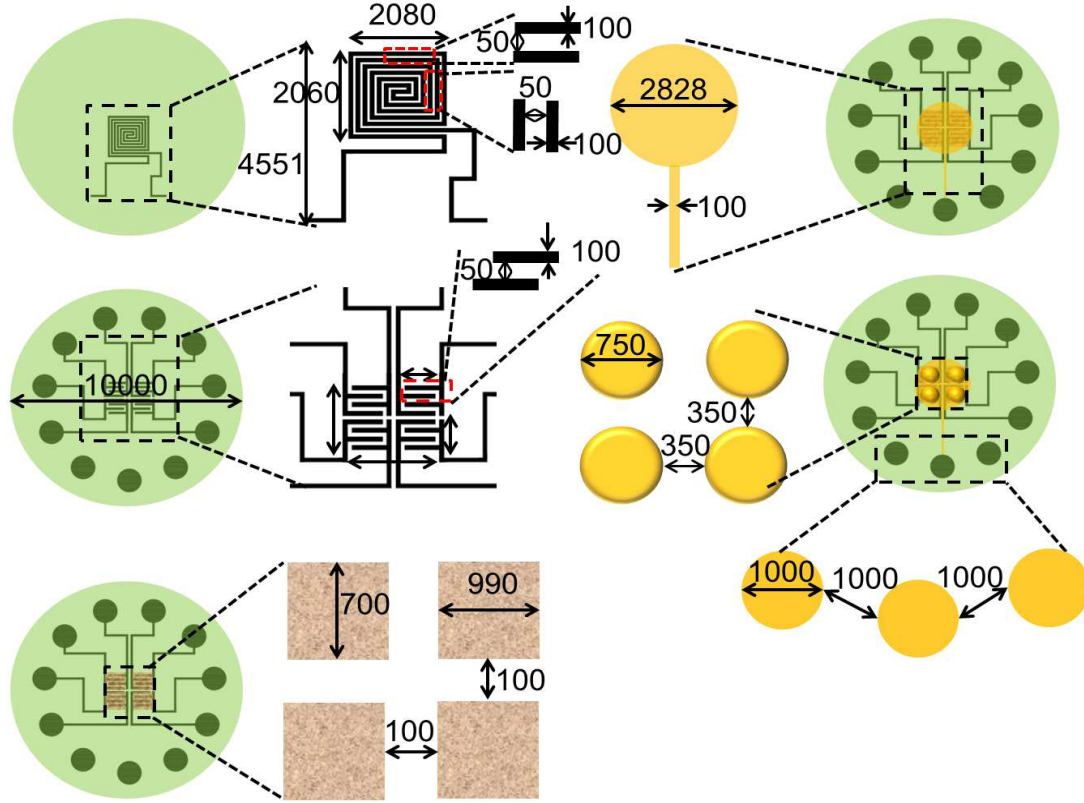


Figure 5.2: Dimensions of the biochip and integrated elements. All dimensions are in microns. Drawings are not to scale.

each tissue cylinder by inserting a needle with 2 mm inner diameter into the selected region of the tissue block using a Manual Tissue Arrayer (Beecher Instruments). The tissue cylinders, which are visually confirmed to contain enough length of embedded tissue, are placed into color-coded Eppendorf tube and deparaffinized (xylene 5 min. \times 3, 100% alcohol 5 min. \times 3, 95 % alcohol 5 min. \times 1, 75 % alcohol 3 min. \times 1, keep in PBS) before the experiment. Compared to the previous works [17, 72, 75], the tissue specimens used in this study are larger in size (2 mm diameter and 3-3.8 mm thickness). The reasons for using larger tissues are: 1) to make it a possible candidate for diagnostic device since larger sampling area helps in reducing the potential repetition of sampling needed for generating reliable results, 2) larger tissue sample facilitates the use of multiple sensors simultaneously, 3) although AFM measurements on tissue specimens often displayed variation over even a small sampling area on the surface of the specimen [19], the experimental data on

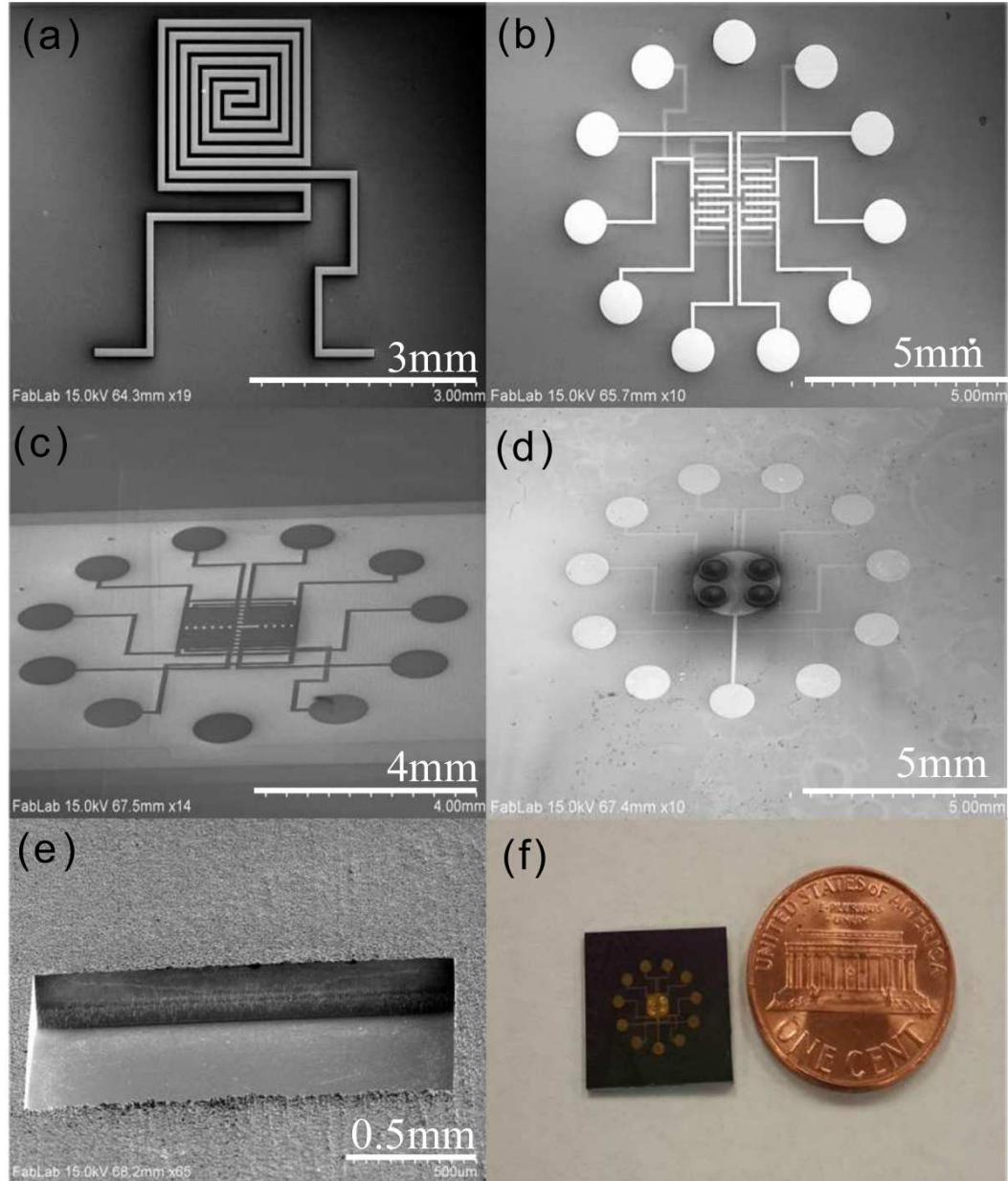


Figure 5.3: SEM images of: (a) Microheater, (b) Cr/Au interdigitated electrodes over microheater, (c) Sensing layer, (d) Gold coated SU-8 pillars over Cr/Au electrode over silicon dioxide over sensing layer, and (e) Backside of silicon diaphragm. (f) A photograph of the biochip.

piezo-resistive assessment of tissue sample had been relatively stable, both over the small spatial area and across specimens of same disease group [72]. Therefore, it is appropriate to increase the sampling distance between the sensors while maintaining signal sensitivity, and 4) having larger tissue specimen may better mimic the scenario of detecting tumor

or tumor margin on the surgical surface. Figure 5.4(a) shows the schematic diagram of the breast tissue core preparation, while Figs. 5.4(b) and (c) show the photographs of the paraffinized and deparaffinized breast tissue cores respectively.

(a)

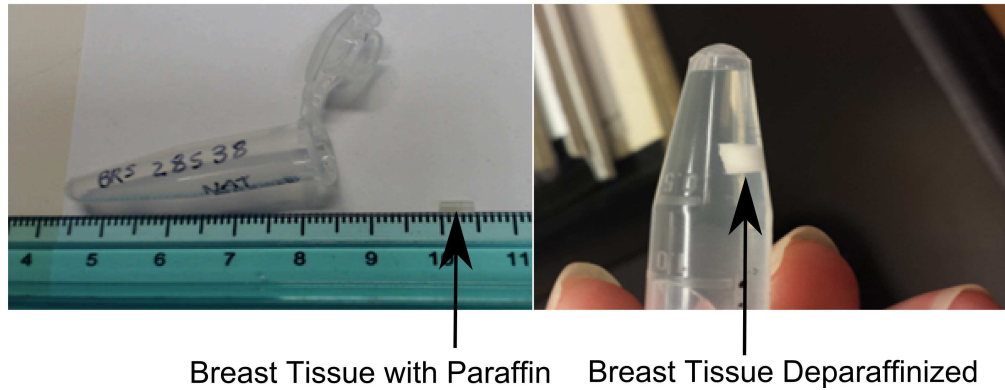
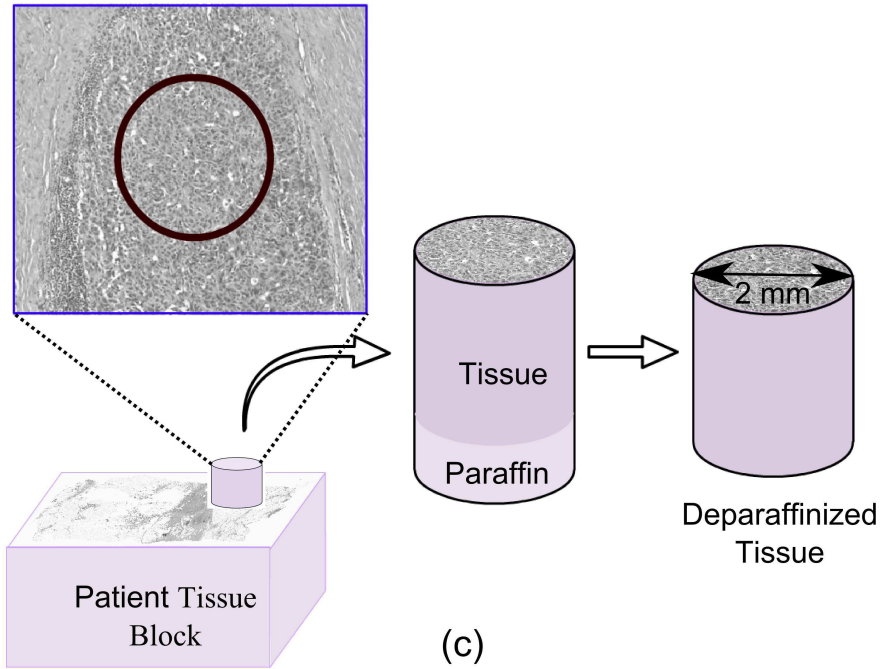


Figure 5.4: (a) Schematic diagram of breast tissue core preparation, (b) and (c) Photographs of paraffinized tissue and deparaffinized breast tissue.

The scanning electron microscopy (SEM) images of the normal and IDC breast tissue is shown in Fig. 5.5. Figure 5.5(a) and (b) shows top view and magnified view of the surface of normal and IDC tissue, respectively. The tumor specimen appeared rough and coarse whereas normal tissue displayed a refined and delicate structure. Figure 5.5(c) and

(d) shows the H&E images of normal and IDC breast tissue cores. Tissue sections were digitized from the FFPE blocks before and after extracting the experimental piece to closely monitor tissue histology on the exact tissue pieces that were examined to include only the most typical histology to represent the disease group where the actual location of sampling is highlighted in yellow. The normal specimen captured a typical terminal ductal lobular unit, which is the basic functional and histological unit of the breast. A segment of terminal duct was shown to branch and form organized clusters of small ductules, where each cluster was called a lobule. The ductules displayed a typical two-layered structure with myoepithelial cells as the outer layer. Intra-lobule connective tissue and inter-lobule connective tissue is also captured in this specimen. The tumor specimen contained large groups of infiltrating tumor cells separated by thin layers of desmoplastic connective tissue and lymphocytes. The breast tumor cells lost the normal structure and displayed mitotic figures.

5.2.3 Experimental Setup

Figure 5.6(a) shows the schematic diagram of a portable cancer diagnosis tool. The tool consists of a MP-285 micromanipulator attached with an indenter and a disposable sensor module integrated with the biochip for measuring electro-thermo-mechanical (ETM) properties of the breast tissue. Figure 5.6(b) shows the blown up schematic diagram of the disposable sensor module. The system is a combination of microfabrication technology, 3D printing technology, reliable packaging, and multi-functional tissue characterization techniques. The sensor module consists of a room for placing tissue sample, a biochip, and connecting pins facilitating the incorporation of the biochip output to the data acquisition card. The tissue sample is placed in the cylindrical space inside the sensor module. The indenter connected to MP-285 micromanipulator also works as an electrically conducting electrode (E1) when it comes in contact with the tissue. A temperature sensor is attached to the end of the indenter to measure the temperature at the top surface of the tissue. With the assumption that the sample tissues are regarded as uniform structures, the measured

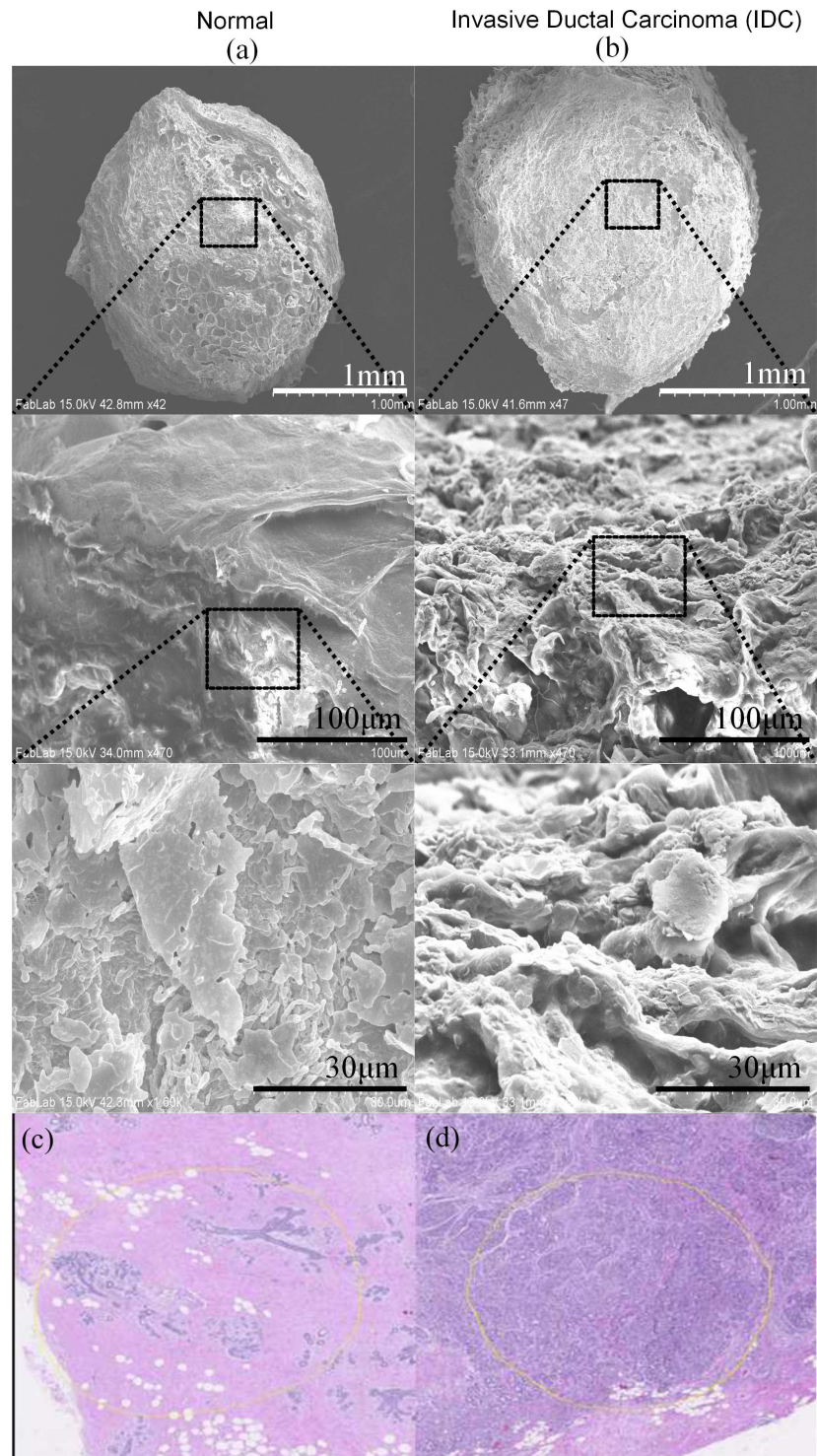


Figure 5.5: SEM images of (a) Normal (27959), (b) Invasive ductal carcinoma (24353) breast tissue cores, (c) and (d) H&E images of normal and invasive ductal carcinoma breast tissue cores, respectively.

temperature values are converted to thermal conductivity using:

$$q = \frac{kA\Delta T}{L_t} \quad (5.1)$$

where, q [W] is the rate of heat transfer through the tissue along the length of the tissue, k [W/mK] is the thermal conductivity, A [m²] is the cross-sectional area of the tissue, ΔT [K] is the temperature difference between bottom and top surface of the tissue, and L_t [m] is the thickness of the tissue.

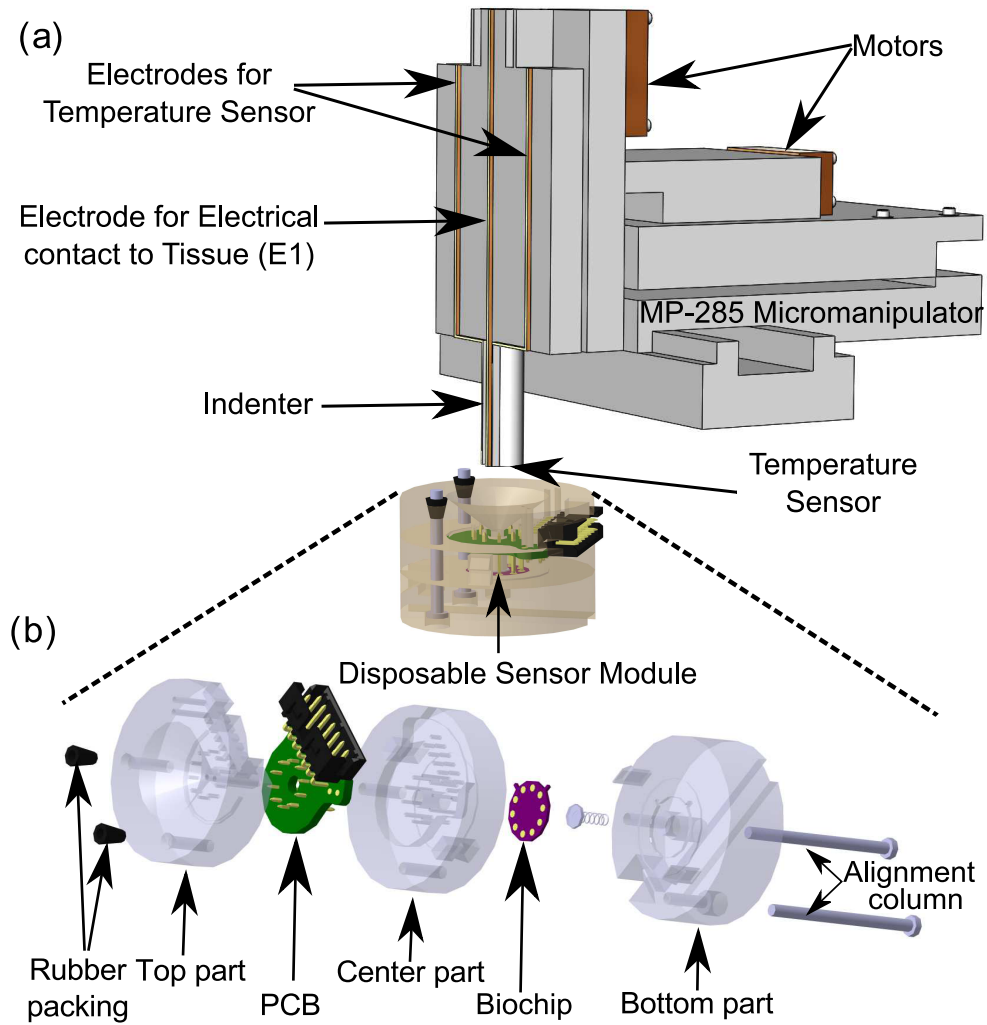


Figure 5.6: (a) Schematic diagram of the experimental setup and (b) Blown-up schematic diagram of the packaging system.

5.2.4 Experimental Results and Discussion

To measure the electrical conductivity of the tissue, a constant voltage is applied between the top electrode (E1) and the bottom electrode (E2) on the sensor chip. The electrical path is complete when the electrode E1 touches the tissue sample and current passes through the top electrode E1 through the tissue to the bottom electrode E2. The output voltage from the Wheatston bridge varies with respect to the resistivity of the tissue (see Fig. 5.7), which correspondingly depends on the type of the tissue (normal or cancerous (IDC)), as the following equation:

$$\rho_t = R_{ref} \frac{(V_{in} - 2V_{out})A}{(V_{in} + 2V_{out})(L_t - d)} \quad (5.2)$$

where, ρ_t is the electrical resistivity of the tissue sample along the length of the tissue, R_{ref} is the resistance of reference resistors in the Wheatstone bridge, V_{in} is the constant input voltage to the Wheatstone bridge, V_{out} is the output voltage from the Wheatstone bridge, and d is the indentation depth. Since the Wheatstone bridge demonstrates the highest sensitivity at the balance, R_{ref} was selected as 3.3 [k Ω], which is close to the mean resistance value of the breast tissue samples in the experiment.

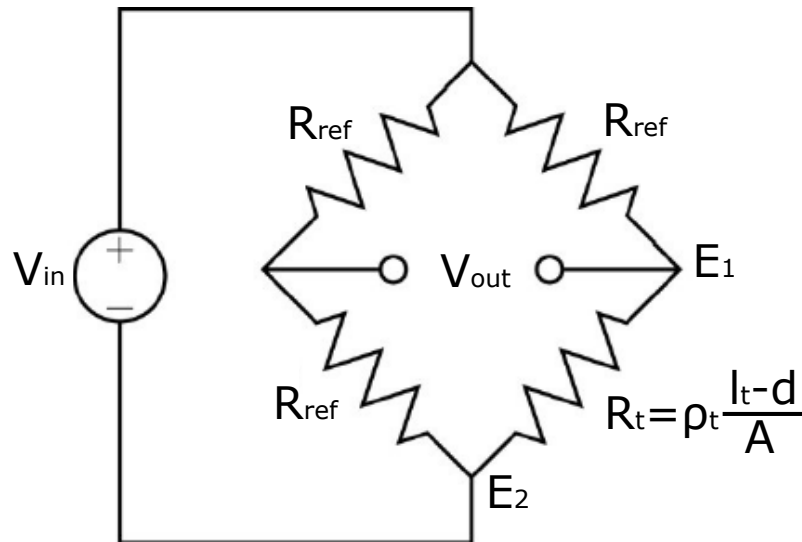


Figure 5.7: Wheatstone bridge circuit for electrical characterization of tissues.

Before the flat electrode E1 at the tip of the indenter touches the tissue sample, the V_{out}

yields zero output and the output becomes non-zero values when the E1 contacts the tissue sample on the flat bottom electrode, E2. Therefore, the electrical measurement circuit assumes that the tissue sample as a single resistor and measures its electrical resistivity, which is independent of the geometry of the tissue sample, instead of electrical resistance while the tissue sample is being indented.

From the scanning electron microscopic image, it is observed that the normal tissues show a smooth topography compared to cancerous tissues, which show ruptured structures [61]. One can reasonably hypothesize: (i) when the current passes through the tissue, the resistance fluctuates depending on the composition of the tissue, (ii) the cancerous tissues being coarse in nature provides a higher resistance path for current to flow compared to smooth structures of the normal tissues. Figure 5.8 shows the electrical resistivity plot of the breast tissues (three normal and three IDC). Cancerous tissue (IDC) shows higher resistivity during indentation compared to normal tissue. The resistivity values obtained from both tissue cores agree with the resistivity of human breast tissues which ranges from 149-463 $\Omega\text{-cm}$ [147]. Breast tissues can be categorized as gland tissue, connective tissue, and subcutaneous fatty tissue according to the morphology of the breast. It is known that there is a significant difference in electrical resistivity among them (For example, fatty tissue has a couple of times higher electrical resistivity than gland tissue). The range (149-463 $\Omega\text{-cm}$) includes the results from all kind of breast tissues. Since breast cancer is detected in gland tissue most frequently, gland tissues were used in the experiment. Therefore, it should vary within smaller range than entire range of resistivity. Of course, narrowing down the range does not guarantee successful differentiation. The literature about electrical resistivity of cancerous breast tissue shows statistical difference between normal and cancer tissue groups instead of suggesting a specific threshold due to overlapping data.

A number of related experiments in the literature show higher resistivity of breast cancer tissue compared to normal mammary glands or normal cases. Morimoto *et al.* [148] reported the resistance value of breast tissues as $1445 \pm 586 \Omega$ for cancerous tissue ($n =$

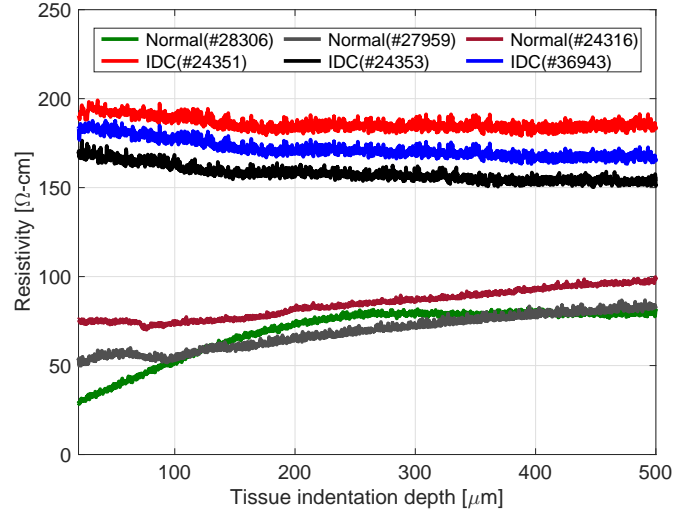


Figure 5.8: Experimental results for electrical characterization of tissues.

31) and $780 \pm 148 \, \Omega$ for normal tissue. Malecka-Massalska *et al.* [149] also reported that cancerous breast tissue ($684.06 \pm 15.83 \, \Omega$ ($n = 34$)) showed higher resistance value than normal breast tissue ($580.42 \pm 12.71 \, \Omega$ ($n = 34$)). Jossinet [150] showed that the electrical resistance of cancerous breast tissue ($n = 23$) is higher than mammary gland ($n = 28$) normal breast tissue. This observation is confirmed by the previous study as well [17, 75]. The localized measurements were related to the disturbance in tissue structure and loss of inter-cellular junctions between cancer cells. Though the experiments had limited number of samples, it was able to find the result consistent with the earlier studies. To measure the mechanical properties of the tissue, the tissue placed inside the sensor module is pressed on the SU-8 pillars using an indenter. These pillars are used to transfer the force to the sensing layer. The output signal from the sensor array depends on the magnitude of force sensed. The amount of force sensed by the sensor depends on the elasticity of the tissue. Thus, the change in signal from the sensor corresponds to the elasticity of the tissue. Figure 5.9(a) shows the calibration result with the commercial load cell (MDB-2.5, Transducer Techniques, USA). The change in resistance values of the sensing layer are measured by the Wheatston bridge. On applying the compressive load normal to the sensor, the output

voltage changes linearly with R^2 -value of 0.9830. Fig. 5.9(b) shows the compressive force measured during the tissue indentation experiment with $100 \mu m/s$ indentation speed. It is known that resistance of p-type piezoresistive material decreases when compression force is applied on it [151, 152]. The fabricated sensor is connected in the Wheatston bridge circuit. As resistance of the sensor decreases due to the applied compressional force, the output voltage from the Wheatston bridge also decreases. The difference between normal and IDC tissues is small for indentations upto $200 \mu m$, however, the difference gets larger on indenting the tissue above $200 \mu m$. This trend corresponds with the published result [78, 147], which shows that the difference in the elasticity values between normal and cancerous breast tissues are higher for larger value of the strains compared to the smaller strain values. Cancerous tissue shows higher elasticity value, since it contains harder inclusion. At small strain, viscoelastic characteristics of biological tissue hide the effect of inclusion (i.e. tissue can be deformed slightly with very small reaction force whether it contains harder inclusion or not). Based on the experiment, the optimal indention depth is around $400 \mu m$ which is the point that gives maximum value from the objective function:

$$Y = |D_E| + |D_R| \quad (5.3)$$

where, D_E and D_R is the difference of mean elasticity [kPa] and mean resistivity [$\Omega\text{-cm}$] between the two groups, respectively.

To measure the response of the microheater, a DC voltage from 0-1.8 V with increment of 0.2 V step is applied and the temperature is measured. The steady state values of the temperature at each voltage is measured and plotted (Fig. 5.10(a)). The best fit R^2 -value obtained is 0.9966. It is observed that the difference between the surface temperature of the tissue and the measured temperature at the top of the tissue is very small (Fig. 5.10(a)). In order to understand the plot more clearly, the measured temperature values from the top surface of the tissue are converted to thermal conductivity values as shown in Fig. 5.10(b).

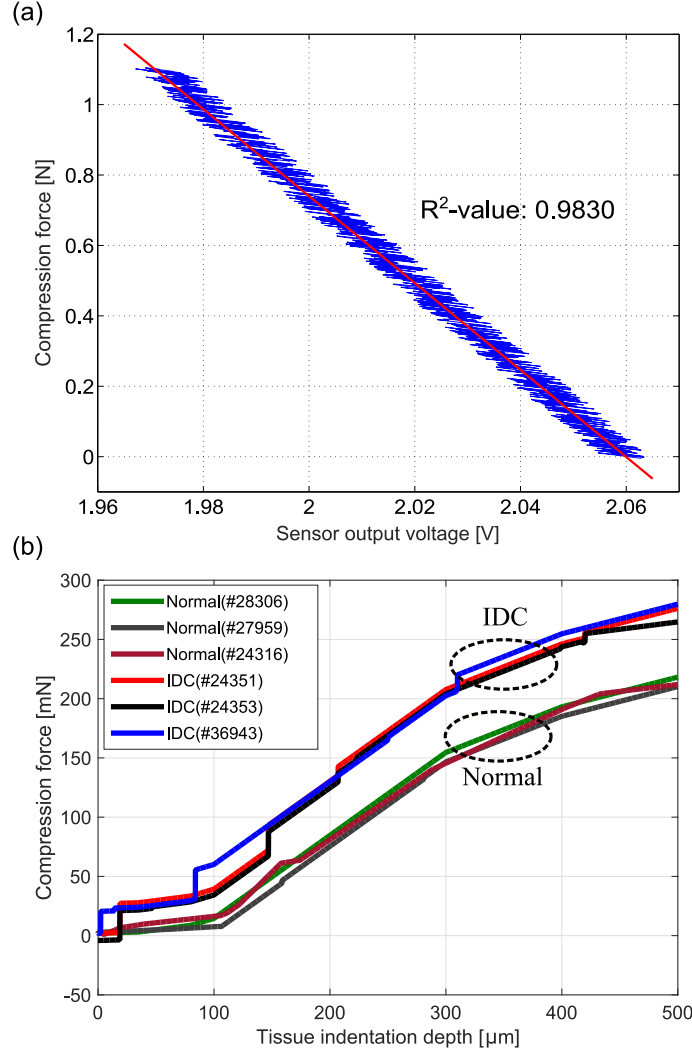


Figure 5.9: (a) Force calibration curve of the fabricated sensor and (b) Force curves obtained from indenting normal and cancerous (IDC) breast tissues.

The breast tissue placed on the biochip is heated from 25°C to 50°C with 5°C step increment using the integrated microheater and the thermal conductivity of the normal and IDC tissues is measured using heat conduction equation (using Eq. 5.1). The thermal conductivity of normal and IDC breast tissues is plotted by measuring the temperature at the top end of tissue using the thermistor placed on the indenter (Fig. 5.10(b)). The two-sample *t*-test for the thermal conductivity data of normal and IDC groups was conducted to analyze data statistically. Apart from the first temperature range (20-25°C), rest of the data falls within *p*-value of 0.05. The *p*-value for the entire data set was calculated as

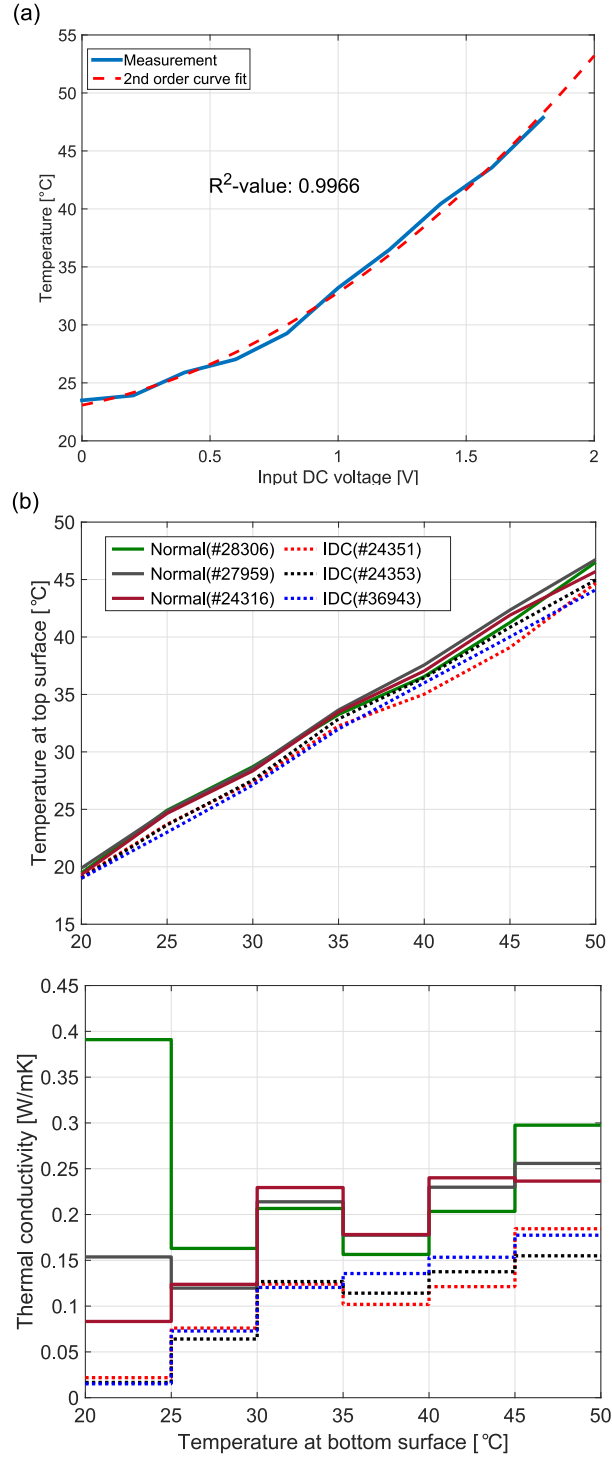


Figure 5.10: (a) Calibration plot of the microheater and (b) Temperature and thermal conductivity measurement of normal and cancerous (IDC) breast tissues.

0.000027 which shows statistically significant difference in thermal conductivity between normal and cancer tissue groups. This implies the thermal conductivity of breast tissue

can be used as a biomarker to differentiate normal tissue from cancerous breast tissue with an enough number of measurement points. In the case of cancerous tissue, the thermal conductivity of the tissue increases with increase in temperature while in normal tissues, the change in the thermal conductivity does not show a particular trend. However, from the t -test it is observed that the thermal conductivity values obtained are statistically different.

The device fabricated for the present study uses 4-inch silicon wafer with the combination of microtechnology and low-cost rapid prototyping. The estimated cost of the device including micro-fabrication, additive manufacturing, testing and evaluation would be around 500 USD. However, the cost can be reduced by fabricating biochips on 12-inch silicon wafer presently used in industry instead of using 4-inch wafer.

5.3 Electromechanical Coupling Factor as a Biomarker for Breast Cancer

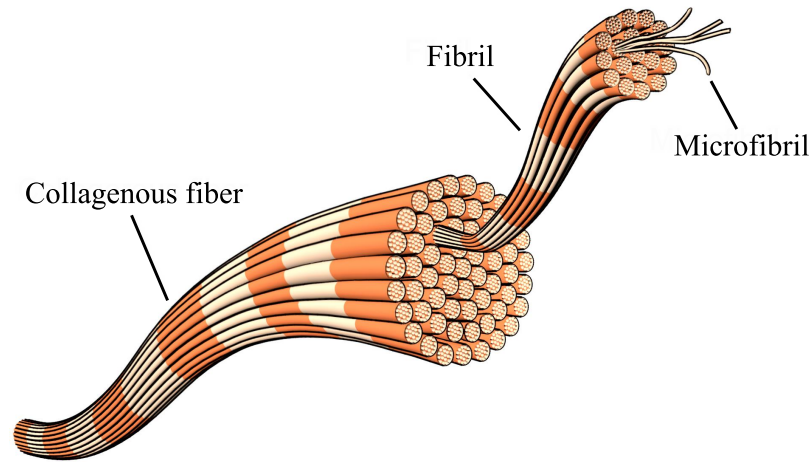


Figure 5.11: Schematic of collagen structure.

The increased density of collagen is a significant factor for diagnosing breast cancer. Individual collagen fibers are bundles of collagen fibrils as shown in Fig. 5.11 [153]. Since the highly oriented structure of collagen fibrils plays a role as the crystal lattice generates electric dipole moments under mechanical pressure, collagen has the piezoelectric effect like crystalline materials [154, 155]. From the observation that high collagen density is found in cancerous breast tissue, it has been systematically investigated whether the elec-

tromechanical coupling factor can be used as an additional criterion to diagnose breast cancer using a portable diagnostic tool.

5.3.1 Portable Diagnostic Tool

Figure 5.12 shows the schematic of the portable diagnostic tool which can phenotype mechanical and electrical property of breast tissue simultaneously. Linear piezoelectric actuator (SLC2490, SmarAct, Germany) with sub-nanometer resolution sensor drives the indenter for mechanical indentation, while MEMS-based biochip in a disposable package measures compression force of indentation and voltage across the tissue sample. 3D-printed structural parts of the package hold the biochip and printed circuit board (PCB), and tissue sample tight for stable measurement.

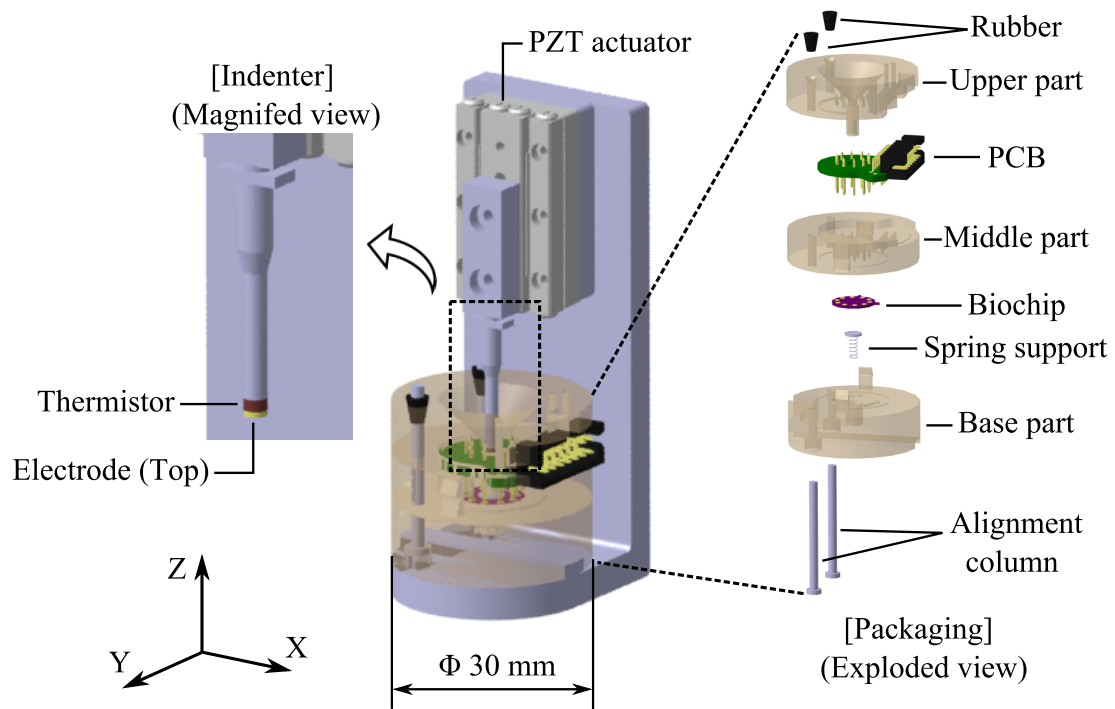


Figure 5.12: Schematic of the portable diagnostic tool.

The biochip consists of a microheater, the electrode (bottom), and a piezoresistive sensing layer. The microheater on the biochip generates the appropriate amount of heat to control the temperature of the tissue sample with the feedback signal from the thermistor at

the tip of the indenter. The electrode (bottom) on the biochip and the electrode (top) at the tip of the indenter allow electric current to flow through the tissue sample located in between these two electrodes. Germanium based piezoresistive sensing layer serves as a force sensor.

5.3.2 Piezoelectric Model

The general constitutive equation for piezoelectric material at constant temperature is given by [156]:

$$\boldsymbol{\epsilon} = \mathbf{S}_E \boldsymbol{\sigma} + \mathbf{d} \mathbf{E} \quad (5.4)$$

$$\mathbf{D} = \mathbf{d}^T \boldsymbol{\sigma} + \mathbf{K}_\sigma \mathbf{E}$$

where, $\boldsymbol{\epsilon}$ is the 6×1 strain vector, \mathbf{S}_E [m^2/N] is the 6×6 elastic compliance tensor at zero electric field, $\boldsymbol{\sigma}$ [N/m^2] is the 6×1 stress vector, \mathbf{d} [m/V or $C(\text{Coulomb})/m$] is the 6×3 piezoelectric modulus tensor, \mathbf{E} [V/m] is the 3×1 electric vector field vector, \mathbf{D} [C/m^2] is the 3×1 electric displacement vector, and \mathbf{K}_σ [$F(\text{Farad})/m$] is the 3×3 dielectric tensor at zero stress.

Two assumptions are made to simplify the model into a one-dimensional case and to allow to design the portable diagnostic tool according to the assumptions: 1) the tissue sample and the tube which holds the sample are perfectly cylindrical in shape and 2) the circumferential boundary of the tissue sample fits tightly inside the tube so that the tissue sample deforms only in the longitudinal direction (i.e. along the Z-axis as shown in Fig. 5.12) without changing its cross-sectional area while being indented. Under these assumptions, the variables \mathbf{D} and \mathbf{E} can be replaced by \mathbf{i} (current vector) and \mathbf{V} (voltage vector), respectively, when the model is represented in the Laplace domain. Considering the model only in Z-direction, which is parallel to the direction of indentation and current path through

the tissue sample, an equation with scalar variables along the Z-axis is obtained as:

$$\begin{bmatrix} \epsilon_z \\ i_z \end{bmatrix} = \begin{bmatrix} (S_E)_z & \frac{d_z}{t} \\ Ad_z s & \frac{A(K_\sigma)_z s}{t} \end{bmatrix} \begin{bmatrix} \sigma_z \\ V_z \end{bmatrix} \quad (5.5)$$

where t and A are the thickness and the cross-sectional area of the tissue sample, respectively, while s is the complex Laplace variable and the subscript, z , represents a parameter along the Z-axis.

The electromechanical coupling factor, k_z , is an indicator of the effectiveness of energy conversion from electrical to mechanical energy along the Z-axis, and is defined as [156]:

$$k_z = \sqrt{\frac{d_z^2}{(S_E)_z (K_\sigma)_z}} = \sqrt{1 - \frac{(S_D)_z}{(S_E)_z}} \quad (5.6)$$

where $(S_D)_z$ is the compliance at zero electric displacement along the Z-axis.

Based on the piezoelectric model, k_z can be obtained by comparing the compliance values of the sample tissue at electrically shorted ($V_z = 0$) and opened ($i_z = 0$) condition along the Z-axis as shown in Fig. 5.13, instead of identifying parameters of d , S_E , and K_σ .

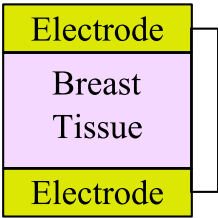
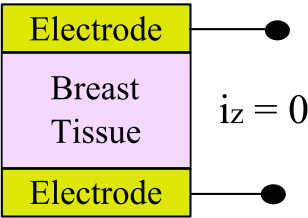
Compliance of breast tissue	
Short Circuit	Open Circuit
 <p>Electrode</p> <p>Breast Tissue</p> <p>Electrode</p> <p>$V_z = 0$</p>	 <p>Electrode</p> <p>Breast Tissue</p> <p>Electrode</p> <p>$i_z = 0$</p>
S_E	$(1 - k_z^2) S_E = S_D$

Figure 5.13: Compliance of breast tissue for two different electrical circuits for obtaining the electromechanical coupling factor (k_z) of the tissue along the Z-axis using tissue indentation tests.

5.3.3 Breast Tissue Sample Preparation

Invasive ductal carcinoma (IDC) and normal breast tissue specimens were carefully selected and extracted from Rutgers Cancer Institute of New Jersey Biospecimen Repository Shared Resource. Even though the specimens from a biobank went through preparation and preservation, the previous efforts showed the same trend of mechanical characteristics when compared with studies on fresh tissues from biopsy [30, 157]. Therefore, banked human breast tissues which are easily accessible over fresh tissues were chosen to prototype and experiment with the new devices. Due to the inherent limitation of biopsy for achieving aligned tissue samples from different persons, the orientation of the sampled tissues is not consistent. Figure 5.14 describes breast tissue sample preparation process for staining and indentation experiment. Five consecutive 4-5 μm sections were taken from each tissue block. The top sections were reserved for immunohistochemical (IHC) staining and special staining, while the last section was stained with hematoxylin and eosin (H&E). These H&E sections were examined under a microscope by a certified pathologist to identify optimum sampling regions for breast cancer and normal breast glandular structure, and subsequently used to guide the extraction of a cylinder of 1.5 mm diameter for experimentation. The tissue block was sectioned once more and stained H&E to confirm that the sampling regions contain desired tissue component. Five specimens each of normal and IDC were prepared and the samples were kept hydrated with phosphate-buffered saline (PBS) at room temperature ($23^{\circ}C \pm 2^{\circ}C$) for 2 hours before pre-conditioning.

5.3.4 Histological Staining Protocols

Several histological staining techniques were selected to visualize key relevant molecules contributing to the change of supportive structure of the breast tissue and surrounding stroma. The normal breast glandular structure is comprised of two-layered breast lobules and ducts. This parenchyma is surrounded by mesenchymal-stroma that provides mechanical support and a tightly controlled biochemical micro-environment [3, 7]. Cancer not only

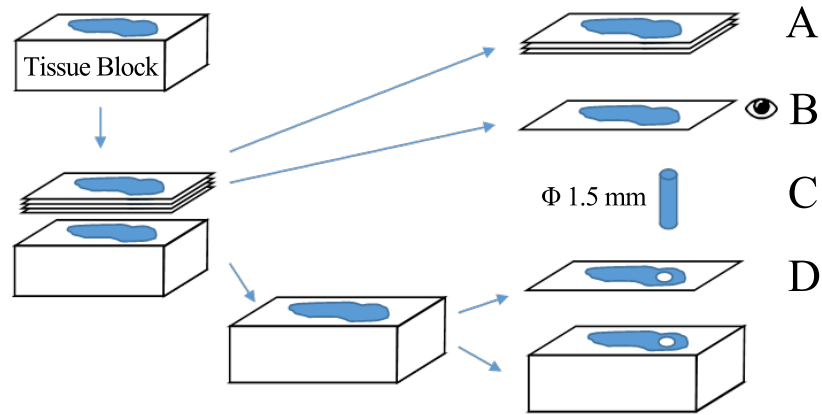


Figure 5.14: Breast tissue sample preparation. (Legend A: Adjacent sections for IHC staining and special staining. Legend B: H&E stained "before/pre" section. Legend C: Cylinder sample to be indented. Legend D: H&E stained "after/post" section.

affects the breast parenchyma cells, but also significantly alters the mesenchymal homeostat and the resulting fibrous mesenchymal reaction often creates the stiff stromal environment that facilitates cancer progression and metastasis. Signs of the so-called desmoplastic change often include an abundance of myofibroblasts and anisotropic collagen, especially type-I collagen, as well as an increase of TGF- β signaling [2]. To visualize the marker proteins in such a molecular microenvironment, Masson's trichrome was selected to show collagen, smooth-muscle actin (SMA) and fibronectin [6]. SMA is normally seen on myoepithelial cells that form the outer layer of breast parenchyma. In invasive carcinoma, on the other hand, the myoepithelial cells are often absent, and SMA visualizes myofibroblasts in the desmoplastic stroma. Fibronectin is secreted in cells in an inactive form and binds extracellular matrix through integrin on the cell surface when folded and assumed dimer formation. It is also upregulated during desmoplasia or fibrotic response.

- H&E staining Protocol

H&E staining was conducted on TISSUE-TEK DRS 2000 (Sakura Finetek USA, Inc., CA, USA) with the Richard-Allan histology signature series stains following the recommended protocol: deparaffinize and rehydrate; hematoxylin solution 3-4 minutes, clarifier solution 1 minute, blueing reagent 1 minute, with rinsing in between;

95% alcohol; Eosin-Y solution 1.5-2 minutes; alcohol and xylene before coverslip.

- General IHC Protocol

All IHC are performed using Ventana Discovery XT automated IHC/ISH slide staining system. Slides are cut at 4-5 μm . Deparaffinization and antigen retrieval are performed using CC1 (Cell Conditioning I, Ventana Medical Systems, Cat #950-124). All primary antibodies are incubated at 37°C for 1 hour. Universal Secondary Antibody (Ventana Medical Systems, Cat #760-4205) is incubated for 12 minutes followed by chromogenic detection kit DAB Map (Ventana Medical Systems, Cat #760-124) or RedMap (Ventana Medical Systems, Cat #760-123). Slides are counterstained with Hematoxylin, then dehydrated and cleared before coverslipping from xylene.

- Trichrome Stain

Deparaffinized specimens were hydrated to deionized water and mordant in pre-heated Bouin's solution at 56°C or overnight at room temperature. After mordanting, wash in running water until yellow color disappears from sections. Staining steps include Working Weigert's Iron Hematoxylin solution for 5-10 minutes, Biebrich Scarlet-Acid Fuchsin Solution for 5 minutes, Working Phosphotungstic / Phosphomolybdic Acid Solution for 5 minutes, Aniline Blue Solution for 5 minutes, 1% Acetic Acid for 2 minutes, with rinsing in between. The slides were finally rinsed in running water, then dehydrated, cleared, mounted and coverslipped.

- SMA-Redmap

Paraffin slides were cut at 4-5 μm . Deparaffinization and antigen retrieval are performed using CC1 (Cell Conditioning Solution, Ventana Medical Systems, Cat #950-124). Anti-SMA (Ventana Medical Systems, Cat #760-2833, mouse monoclonal antibody, [Available Online] <http://ventana.com/product/9?type=4>) is applied and slides are incubated at 37°C for 1 hour. Universal Secondary antibody (Ventana

Medical Systems, Cat #760-4205) is incubated for 12 minutes followed by RedMap detection kit (Ventana Medical Systems, Cat #760-123).

- Fibronectin-DABmap

Paraffin slides were cut at 4-5 μm . Deparaffinization and antigen retrieval are performed using CC1 (Cell Conditioning Solution, Ventana Medical Systems, Cat #950-124). Anti-Fibronectin (Millipore, Cat #AB2033, rabbit polyclonal antibody, [Available Online] <https://www.emdmillipore.com>) is applied at 1:1500 and slides are incubated at 37°C for 1 hour. Universal Secondary antibody (Ventana Medical Systems, Cat #760-4205) is incubated for 12 minutes followed by chromogenic detection kit DABMap (Ventana Medical Systems, Cat #760-124).

5.3.5 Pre-conditioning

Generally, preconditioning of biological specimen is required for obtaining repeatable result during mechanical loading experiment, since internal structure of the specimen changes with repeated loading until it reaches a steady state for the given routine [158]. When any loading condition such as the upper/lower strain limit or strain rate changes, the specimen should be preconditioned again [158]. All breast tissue samples were preconditioned 15 times in compression with a maximum strain of 0.2 and strain rate of 0.01/s. These parameters were the same during the actual indentation experiments.

5.3.6 Experiments and Results

By digitally aligning whole slide images of stained sections, it is able to accurately identify tissue structure and molecular marker on the samples that underwent the indentation experiments. Histological and immunohistological staining results of each normal and IDC sample are shown in Fig. 5.15. The normal specimen images confirmed accurate sampling of normal breast tissue lobules that are surrounded by fibrotic stroma, in which collagen-fibronectin are distributed in a similar pattern, as visualized with Trichrome and Fibronectin

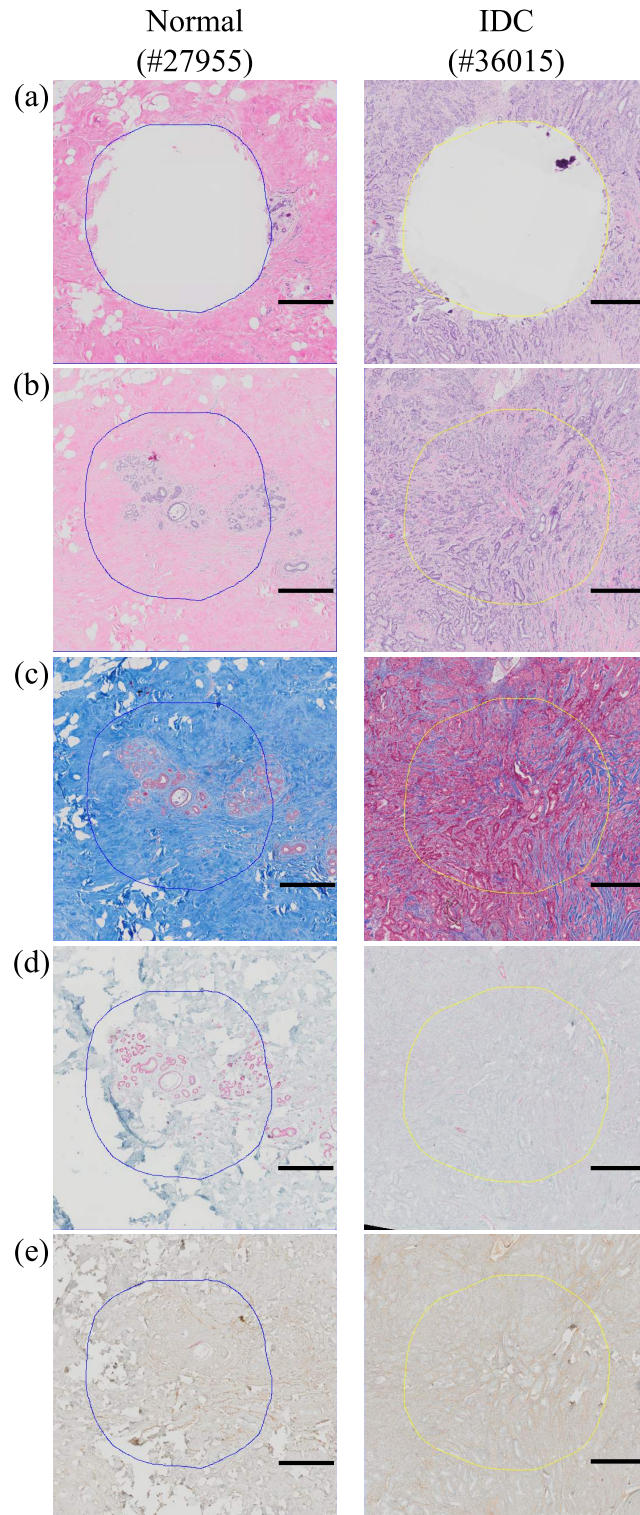


Figure 5.15: Example histological and immunohistological images of normal (#27955) and IDC (#36015) breast tissue: (a) H&E after sampling (b) H&E before sampling (c) Trichrome, (d) SMA, and (e) Fibronectin. Scale bar on each image indicates 500 μm .

stains. SMA staining highlights the present myoepithelial layer. The cancer specimens, on the other hand, show loss of lobular architecture. Trichrome staining shows increased collagen deposition and uneven pattern of fibronectin staining accompanying infiltrating malignant glands. The desmoplastic stroma also displays SMA expression in a haphazard pattern. Figure 5.16 shows the overall experimental setup for measuring responses of the

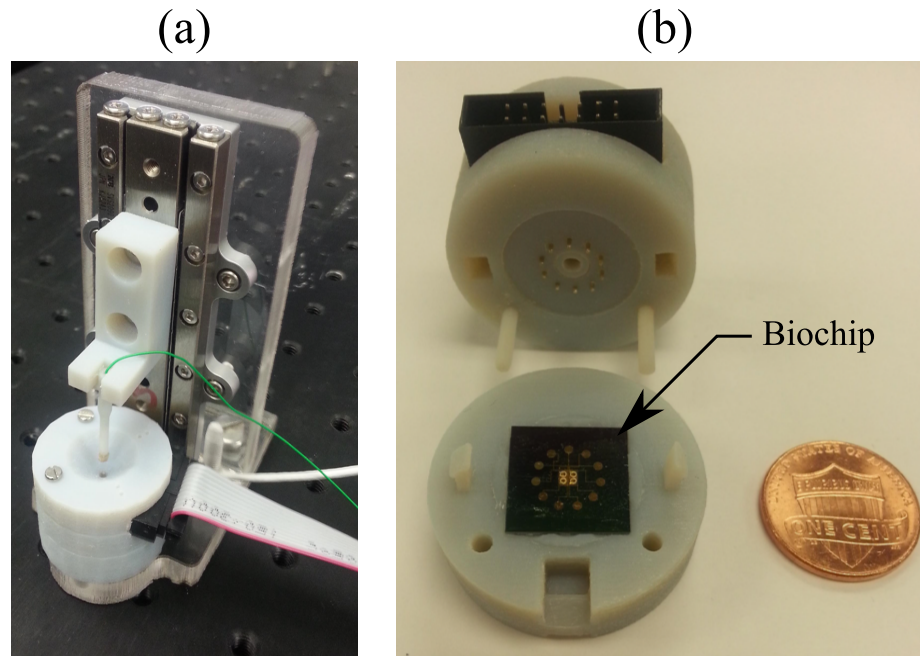


Figure 5.16: Experimental setup: (a) Overall view of the diagnostic tool and (b) Fabricated biochip in the package.

tissues and the biochip in the package. 16 bits data acquisition (DAQ) card (Model 626, Sensoray, USA) was used for recording data. Analog signal amplifier and low pass filter were implemented for conditioning signals from the biochip. The tissue sample was placed at the center of the biochip and cylindrical tube of 3D-printed structure allowed the tissue to deform in the Z-axis only. For the indentation experiment, the maximum strain of 0.2 and strain rate of 0.01/s were applied. Using two electrodes, which are the electrode on the biochip and the electrode at the tip of the indenter, electrical circuit through the tissue can be opened or shorted to enable the measurement of S_D and S_E .

Stress-strain curves of the tissues under compression with electrically opened and shorted

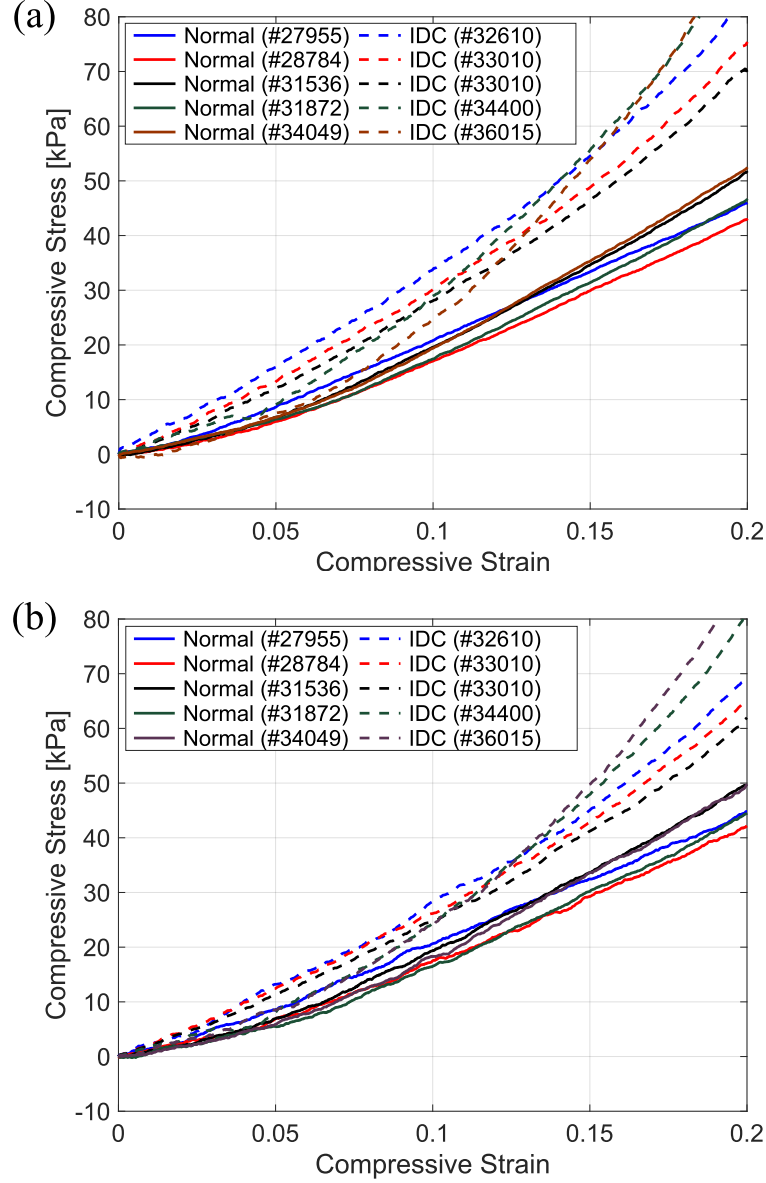


Figure 5.17: Stress-strain curves of the breast tissues under compression 25°C: (a) With electrically opened and (b) With electrically shorted.

cases are shown in Fig. 5.17. The stress of the tissue samples in IDC group tends to increase drastically compared to the normal tissues in both open and short circuit cases as the induced strain gets higher. Using the stress-strain data set, tangent stiffness and electromechanical coupling factor of the tissue are calculated at every compressive strain of 0.05 and plotted as shown in. Fig. 5.18(a) and (b), respectively. To reduce noise amplification effect during calculation of tangent stiffness, the first order central differentiation method with

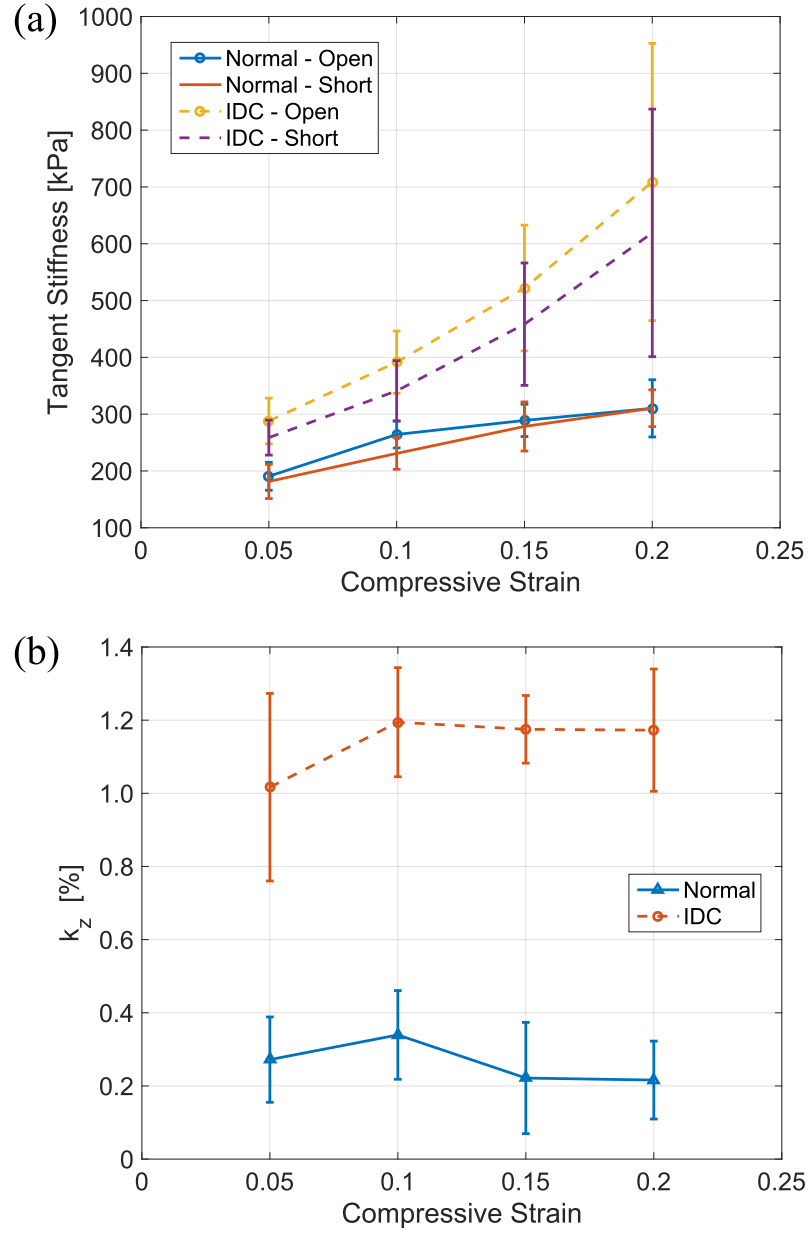


Figure 5.18: Experimental result of breast tissue signatures in Z-axis at 25°C: (a) Tangent stiffness and (b) Electromechanical coupling factor.

eleven data points are used except for the last point of data at the maximum strain of 0.2 in which backward method is applied.

The entire experimental results in tangent stiffness and electromechanical factor of the breast tissue samples at 25-45°C of the range are shown in Table 5.1 for the comparison between normal and IDC group. Regarding with the tangent stiffness, one can observe two

Table 5.1: Experimental results

Strain	Temp.	TS (OC) [kPa]		TS (SC) [kPa]		k_z [%]	
		Normal	IDC	Normal	IDC	Normal	IDC
0.05	25°C	190.7±24.6	288.0±40.2	181.5±30.1	258.9±30.7	0.27±0.12	1.02±0.26
	30°C	188.8±27.4	271.2±51.3	183.1±34.2	249.1±32.6	0.20 ±0.08	1.12±0.32
	35°C	187.2±16.1	287.0±31.2	189.0±29.1	260.1±39.1	0.29 ±0.09	1.06±0.27
	40°C	190.0±20.4	293.0±30.8	177.8±33.1	255.4±29.2	0.24 ±0.11	1.08±0.20
	45°C	189.2±17.4	277.0±34.8	180.3±31.0	261.1±25.9	0.30 ±0.17	1.07±0.28
0.10	25°C	264.2±23.6	391.6±54.8	230.9±28.0	341.0±53.1	0.34±0.12	1.19±0.15
	30°C	258.2±25.1	393.1±55.7	240.2±25.5	333.3±50.9	0.30±0.18	1.02±0.20
	35°C	255.1±19.2	380.9±48.1	226.2±20.5	322.0±39.8	0.37±0.17	1.13±0.16
	40°C	260.6±27.0	399.2±60.7	232.2±22.3	351.0±49.6	0.36±0.15	1.27±0.19
	45°C	248.9±19.9	379.0±44.1	241.9±22.0	334.0±44.0	0.36±0.13	1.26±0.19
0.15	25°C	289.0±28.6	522.0±110.7	278.3±43.2	458.4±107.7	0.22±0.15	1.18±0.09
	30°C	280.2±30.7	502.0±119.1	274.1±44.3	452.1±111.3	0.29±0.16	1.14±0.15
	35°C	283.2±27.7	519.0±103.1	280.0±44.5	460.5±100.1	0.17±0.12	1.17±0.14
	40°C	276.8±22.0	509.0±100.2	269.9±38.8	448.5±113.6	0.25±0.19	1.26±0.17
	45°C	278.0±33.1	512.0±101.0	274.8±36.9	466.4±102.3	0.26±0.17	1.16±0.08
0.20	25°C	310.2±50.4	708.6±244.0	310.4±32.4	619.1±217.9	0.22±0.11	1.17±0.17
	30°C	300.9±58.2	725.0±206.2	298.8±40.1	611.3±199.5	0.23±0.12	1.08±0.15
	35°C	299.2±44.1	695.4±212.2	313.4±30.3	623.3±200.2	0.23±0.11	1.26±0.17
	40°C	301.7±45.9	703.2±201.3	300.4±33.3	608.9±211.0	0.27±0.09	1.16±0.26
	45°C	308.2±39.4	700.9±198.9	311.4±29.1	620.2±205.3	0.28±0.12	1.17±0.14

TS : Tangent Stiffness, OC: Open Circuit, SC: Short Circuit.

Table 5.2: p -value of the two-sample t -test

Strain	Temp.	p -value from TS (OC)	p -value from TS (SC)	p -value from k_z
0.05	25°C	0.0108	0.0155	0.0039
	30°C	0.0140	0.0122	0.0026
	35°C	0.0116	0.0136	0.0034
	40°C	0.0133	0.0148	0.0019
	45°C	0.0156	0.0139	0.0033
0.10	25°C	0.0100	0.0135	0.0022
	30°C	0.0111	0.0120	0.0019
	35°C	0.0096	0.0109	0.0021
	40°C	0.0087	0.0140	0.0008
	45°C	0.0123	0.0133	0.0015
0.15	25°C	0.0082	0.0102	0.0001
	30°C	0.0098	0.0100	0.0017
	35°C	0.0078	0.0083	0.0002
	40°C	0.0101	0.0099	0.0010
	45°C	0.0079	0.0093	0.0008
0.20	25°C	0.0086	0.0096	0.0006
	30°C	0.0087	0.0099	0.0015
	35°C	0.0068	0.0085	0.0004
	40°C	0.0088	0.0089	0.0009
	45°C	0.0078	0.0093	0.0017

TS : Tangent Stiffness, OC: Open Circuit, SC: Short Circuit.

features which are consistent with previous researches on mechanical characterization of breast tissue [62, 77–79] : 1) much bigger difference between normal and IDC samples at higher strain level and 2) smaller temperature effect at the given range than the variation between samples. On the other hand, resources about electromechanical coupling factor for breast cancer specimen are extremely limited. Moreover, a consensus even for the study of bone, which one of the most active areas of research using human tissues, is required since there are inconsistent results among the piezoelectric constants measured by different research groups [159–163].

Higher stiffness in the IDC group can be found on the stiffness plot, especially at higher

strain levels. This result is consistent with the observations in previous research as one of the well-known mechanical signatures of breast cancer [71]. Compared to the stiffness result, electromechanical coupling factor shows a clear distinction between normal and IDC group without overlapping data within one standard deviation for the entire strain range. The result of the two-sample t -test shows that there is a significant difference in electromechanical coupling factor between the normal and IDC group and it can distinguish normal from IDC sample more effectively than mechanical stiffness. While tangent stiffness falls within p -value of 0.02 for both open and short circuit cases for the entire temperature range, p -value of electromechanical coupling factor has one or two orders of smaller magnitude as shown in Table 5.2.

An electromechanical coupling factor (or a piezoelectric constant) generated by collagen in human tissues is known as a parameter that varies with moisture content, pH, frequency of input stress, and orientation of the sample [153, 164], while mechanical stiffness (or elastic modulus) of human soft tissue is affected by strain rate, strain level, shape of indenter [98, 158]. All samples used in the experiment were kept in the same conditions except orientation of each sample which is an inherent limitation of the current biopsy procedure. However, the orientation of breast tissues seems not to affect much on electromechanical coupling factor based on two observations: 1) increased, but unevenly deposited collagen on the staining image and 2) small enough variation on the experimental result among arbitrarily oriented samples. Though the confinement and different orientation of samples might be critical to reach a significantly better diagnostic result, the preliminary result obtained by a simplified model under two assumptions has shown feasibility of the approach without a comprehensive consideration of those factors. There are three reasons for explaining the result: 1) Since only a small set of samples were investigated, the orientation of samples might be biased even though they were blindly sampled. 2) Collagen is deposited without directionality during breast cancer progression. 3) The restriction on lateral expansion during the experiment generates a dominant electromechanical coupling

effect. Although the validity of the measured parameters and finding the optimal experimental procedure still needs to be investigated, the results show that electromechanical coupling factor measured by the portable diagnostic tool can differentiate cancerous breast tissue from normal breast tissue under the given experimental conditions.

5.4 Conclusion

The novelty of this work is the design and fabrication of a complete system for measurement of multiple tissue parameters, which can potentially provide a deterministic and quantitative information of the tissue characteristics, includes mechanical, electrical, and thermal characteristic of the normal tissue as well as the onset and disease progression of the tissue. This device for cancer diagnosis comprises of a disposable single-use components as well as a base platform, which can be used in several studies. The device could delineate the normal and IDC breast tissues by measuring the electro-thermo-mechanical changes as well as electromechanical coupling factor of the breast tissue samples as biomarkers for breast cancer.

Higher mechanical stiffness in cancerous breast tissue serves as a representative biomarker. In practice, however, a single parameter for diagnostic decision may not yield desirable sensitivity and specificity that causes inaccurate diagnostic results such as false negatives or false positives due to variations in the characteristics of the biological samples. Finding a new biomarker to differentiate cancerous tissue from normal tissue and using it as additional criteria can lead to more accurate screening at an early stage. Though the current experimental setup may play only a subsidiary role in a clinical setting as one of the diagnostic criteria, one of the major purposes of investigating the physical property of human breast tissue is to visualize regions of interest by capturing the signature for clinical use. It is envisioned that the technique for measuring the electromechanical properties of breast tissue will be implemented on an independent imaging system or combined with existing imaging techniques such as elastography and electrical impedance tomography (EIT)

to enhance their performance if a satisfactory level of sensitivity for imaging is acquired. In this scenario, the sensitivity of the measurement is as important as measuring absolute values to visualize a targeted region clearly and differences among patients would be compensated by similar methods with other imaging systems such as modulating several input parameters to obtain a customized result.

The design of a portable diagnostic tool for breast cancer and electromechanical coupling factor as a biomarker were demonstrated along with preliminary experimental results. Although experiments with more samples and elaborate protocol are required to verify its practical effectiveness, the preliminary work shows the feasibility of using electromechanical coupling factor as a biomarker for breast cancer diagnosis. In the future work, large number of samples would be investigated using this tool. The main focus is on building a portable automated device which can serve as an indicator to measure the false positive or negative in breast cancer and help the physician to determine the stage of cancer. The tool will be improved to be capable of measuring electromechanical coupling factor in multiple directions at the same time and optimize the experimental protocols by investigating various factors such as orientation and moisture content of the sample. A larger number of samples including fresh tissues as well as normal and cancerous tissue from the same individual will be investigated to verify its feasibility of clinical use. Furthermore, the scope of the study will be expanded to cancerous tissue types under study and exploit the use of machine learning techniques to verify diagnostic accuracy of this new tool.

CHAPTER 6

TOWARD *IN SITU* AND *IN VIVO* BREAST CANCER DIAGNOSIS

Flexible sensors using functional materials have been extensively studied due to their significant potential in biomedical applications. Multi-walled carbon nanotubes (MWCNTs) that have excellent electrical conductivity enables polydimethylsiloxane (PDMS), a biocompatible silicone, to become conductive and piezoresistive as a nano-filler material in the polymer. Dispersion methods of MWCNT in PDMS and characterization of MWCNT/PDMS elastomers are analyzed to establish an optimal fabrication process. The fabricated MWCNT/PDMS-based flexible sensors have been implemented for strain sensing within a needle for *in situ* tissue characterization. Since the developed piezoresistive type of sensors are highly flexible, responsive, easy to scale, cost-effective, simply packaged, and biocompatible, they have numerous applications in the biomedical field.

6.1 Introduction

Recent progress in flexible and stretchable sensors has attracted intensive attention for various biomedical applications such as electronic skins and wearable electronic devices [165, 166]. Polydimethylsiloxane (PDMS) is the most commonly used material for a flexible sensor in those biomedical applications as a substrate due to its biocompatibility, cost-effectiveness, flexibility, thermal stability, low permeability to water, and micropatterning capability [167–170]. Although the low electrical conductivity of PDMS is important for its use in certain applications as a flexible substrate with excellent electrical insulation, this property becomes a challenge to be overcome for applications requiring a conductive elastomer as an active component. Additionally, packaging of PDMS-based sensors has been a significant challenge since it is difficult to solder on PDMS itself or on contact pads made of thin metal film deposited on PDMS surface [171]. Gluing wires using conductive epoxy

or clamping contacts pads are the most common ways to generate an electrical pathway to external circuits for PDMS-based sensors [17, 75, 172, 173].

Several researchers have developed polymer-based conductive elastomer by blending various nanomaterials for such flexible electronics applications [174–178]. Multi-walled carbon nanotube (MWCNT) is one of the effective filler materials to increase electrical conductivity of polymers or epoxy resins since it is less expensive compared to other types of carbon nanotubes while maintaining the characteristics of high electrical conductivity [179]. However, production processes using MWCNTs often produce mixtures of solid morphologies that are entangled or self-associate into aggregates due to the van der Waals force among them and this deteriorates electrical conductivity of the mixtures significantly [180]. Therefore, producing homogeneous MWCNT nanocomposite materials in viscoelastic polymer solutions is essential in the fabrication of a flexible sensor using MWCNTs. Several methods such as shear mixing (simple stirring [181, 182], three-roll milling [179, 183, 184], dissolver disk [185], planetary mixer [186]), dispersion in liquids [176, 180], ultrasonication [187–189] and a combination of two of these methods [166, 190] have been suggested to promote the dispersion of MWCNTs. However, the effectiveness of each method varies due to the processing conditions and characteristics of MWCNTs such as its dimension, purity, and functionalization.

MWCNT/PDMS mixtures have been used as biocompatible conductive elastomers for developing flexible sensors targeting various medical applications: 1) biocompatible electrodes for measuring biosignals such as electroencephalography (EEG), electrocardiogram (ECG), or electromyography (EMG) [191–193], 2) wearable strain sensors for motion analysis (capacitive type [167] and piezoresistive type [166]), 3) a wearable pressure sensor for monitoring human breathing [194], and 4) a tactile sensor for human-robot interaction [184]. Sensors using the piezoresistivity of MWCNT/PDMS elastomers transform mechanical strain into an electrical resistance change and are widely used for non-medical applications as well due to their advantages of simple read-out circuitry and high sensitivity

to both mechanical deformation and pressure [195].

The aim of this chapter is to develop a MWCNT/PDMS-based flexible sensor and implement the sensor for *in situ* mechanical characterization of soft tissues with a sensor that fits in a biopsy needle. An optimal dispersion condition of MWCNTs and encapsulation of MWCNT/PDMS elastomer with pure PDMS are also addressed not only to increase the sensitivity of sensor but also to protect the sensor from mechanical and electrical disturbance.

6.2 MWCNT/PDMS-based Flexible Sensor

6.2.1 Dispersion of MWCNTs

High aspect ratio (length/diameter) MWCNTs (Purity > 95 %, Outside Diameter (OD) < 7 nm, Length: 10–30 μm , US Research Nanomaterials, Inc., Houston, TX, USA) were chosen for this study because the aspect ratio of MWCNTs is one of the important parameters that determine the electrical characteristics of MWCNTs and higher aspect ratio yields better electrical conductivity [190]. In addition, it is known that applying excessive mechanical forces to MWCNT mixtures during the dispersion process deteriorates the electrical conductivity [166, 179]. Therefore, two dispersion methods, shear mixing and ultrasonication in isopropyl alcohol (IPA), were investigated to find an optimal dispersion condition in PDMS (Sylgard 184, Dow Corning Company, Midland, MI, USA). IPA is used as a suitable organic solvent to disperse MWCNTs because both MWCNTs and PDMS are partially soluble in IPA and IPA promotes interaction between the hydrophobic MWCNTs and hydrophilic hydroxyl groups [196]. Other dispersion methods were excluded due to either causing too much loss of the materials during the process or requiring customized tools.

- Shear Mixing Protocol: (a) put PDMS elastomer base on a Petri dish and MWCNTs in 2-10 wt%% of the final mixture including the weight of PDMS curing agent to be

added later, (b) mix them vigorously using a scraper with shearing for several minutes, (c) spread the mixture on a thin non-conductive mold, (d) measure resistance values at multiple points using an ohmmeter (or impedance analyzer) with fixed-distance probes, (d) if the discrepancy among the measured resistance values is less than 5 %, add PDMS curing agent (base:curing agent = 10:1 in weight) and mix them again for another 5 minutes using a scraper, otherwise repeat this process from (b), and (e) degas the mixture using a vacuum pump (TA350, Kozyvacu, Mercer Island, WA, USA) which has the ultimate vacuum of 5 [Pa] for 1 hour.

- Ultrasonication Protocol: (a) prepare a bottle with IPA and MWCNTs (IPA:MWCNT = 30:1 in weight), (b) put the bottle in an ultrasonicator (Q700, Qsonica, Newtown, CT, USA) and operate with 100-120 [W] power for 5 minutes with water circulation, (c) rest 1 minute so as not to heat the mixture excessively, (d) repeat (b)-(c) 5 more cycles (totally 30 minutes of sonication), (e) put PDMS elastomer base into the bottle, (f) repeat (b)-(d), (g) evaporate IPA thoroughly over 12 hours or more (depends on the initial amount of IPA) using a hotplate and magnetic stirrer (HS-H280-Pro, SCILOGEX, Rocky Hill, CT, USA) at 60°C and 300 *rpm* (if the evaporating temperature is too high, over 70°C, cracked or rough surfaces will occur [166]), (h) put PDMS curing agent (base:curing agent = 10:1 in weight), repeat (b)-(d), and (i) degas the mixture using a vacuum pump for 1 hour.

After curing the MWCNT/PDMS mixtures in the shape of a thin film at 80°C for 1 hour using an air oven (ProJet Finisher XL 1-A, 3D Systems Inc., Rock Hill, SC, USA), cross-sections of the elastomers were investigated to evaluate the effectiveness of dispersion methods through a scanning electron microscopy (SEM) machine (S-4700 FE-SEM, Hitachi, Tokyo, Japan). One can intuitively expect that a MWCNT/PDMS elastomer with higher MWCNT concentration would create a more electrically conductive network and this was observed through SEM images as well. As shown in Fig. 6.1, the MWCNT/PDMS elastomer with 10 wt% of MWCNT had noticeably more MWCNTs in both shear mixing

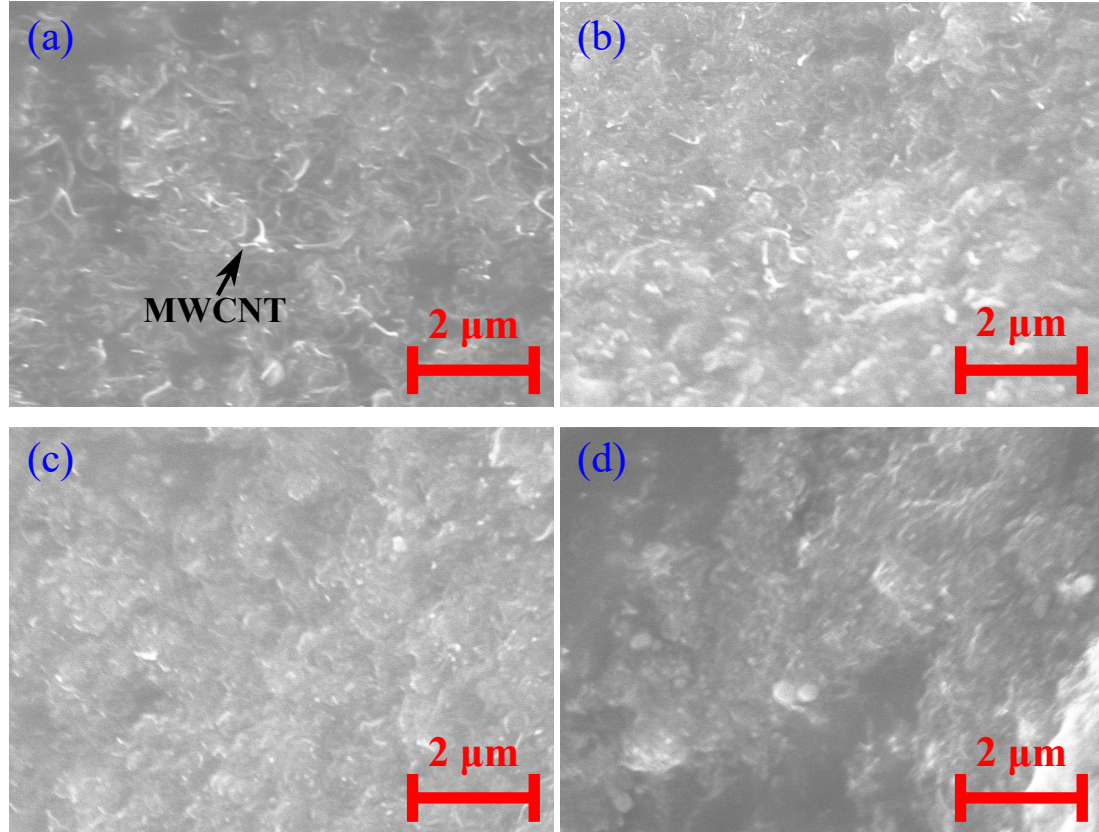


Figure 6.1: SEM images of the MWCNT/PDMS elastomers fabricated by: (a) The shear mixing protocol with 10 wt% of MWCNT, (b) The shear mixing protocol with 5 wt% of MWCNT, (c) The IPA dispersion protocol with 10 wt% of MWCNT, and (d) The IPA dispersion protocol with 5 wt% of MWCNT.

and IPA dispersion protocols, while the shear mixing protocol showed better dispersion results for the 5 wt% and 10 wt% of MWCNT concentration. In addition to the surface investigation, the MWCNT/PDMS elastomers manufactured by the IPA dispersion protocol had 1-2 order of magnitude lower electrical conductivity and a larger deviation among the samples than the MWCNT/PDMS elastomers fabricated by the shear mixing protocol.

6.2.2 Characterization of MWCNT/PDMS Elastomer

Since the shear mixing protocol has shown its benefits on the effectiveness of MWCNT dispersion and the processing time (3 hours vs 16 hours or more), the dispersion of MWCNTs in PDMS for the sensor fabrication will follow the shear mixing protocol, though

this requires a labor intensive mixing process. The mechanical and electrical properties of MWCNT/PDMS elastomers vary with the MWCNT concentration. All samples for the characterization were fabricated through the shear mixing protocol with 2-10 wt% MWCNT concentration. It was difficult to handle and mold MWCNT/PDMS mixtures with over 10 wt% MWCNT concentration due to the increased viscosity of the mixtures. While the maximum elongation was recorded at break with an effective length of 15 mm, the electrical conductivity of the fabricated MWCNT/PDMS elastomer, σ , was calculated by measuring the resistance and its dimensions as:

$$\sigma = \frac{1}{\rho} = \frac{L}{RA} = \frac{L}{RWH} \quad (6.1)$$

where, ρ , R , A , L , W , and H is the resistivity, measured resistance, cross-sectional area, length, width, and height of the material, respectively.

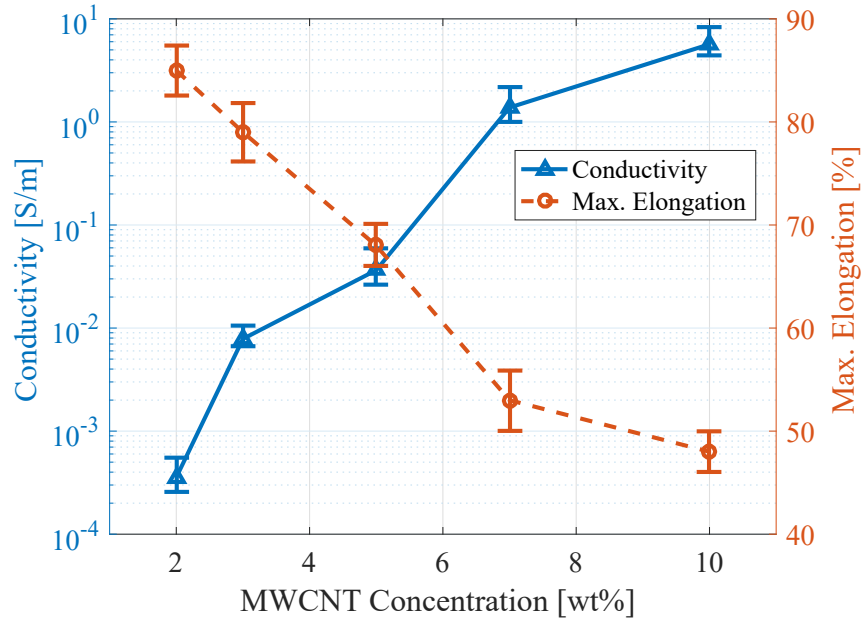


Figure 6.2: Electrical and mechanical characteristics of MWCNT/PDMS elastomers in the dimension of 1(W)×25(L)×0.3(H) mm (effective length for the elongation test: 15 mm) without pure PDMS encapsulation.

Fig. 6.2 shows the characteristics of MWCNT/PDMS elastomers in terms of the electri-

cal conductivity and the stretchability using 5 samples for each batch. The MWCNT/PDMS elastomers have dimensions of $1(W) \times 25(L) \times 0.3(H)$ mm. As more MWCNTs are included, the MWCNT/PDMS elastomer gets harder and less stretchable, though it becomes more electrically conductive. One can find an optimal MWCNT concentration for the physical environment or requirements of a target application.

6.2.3 Sensor Fabrication

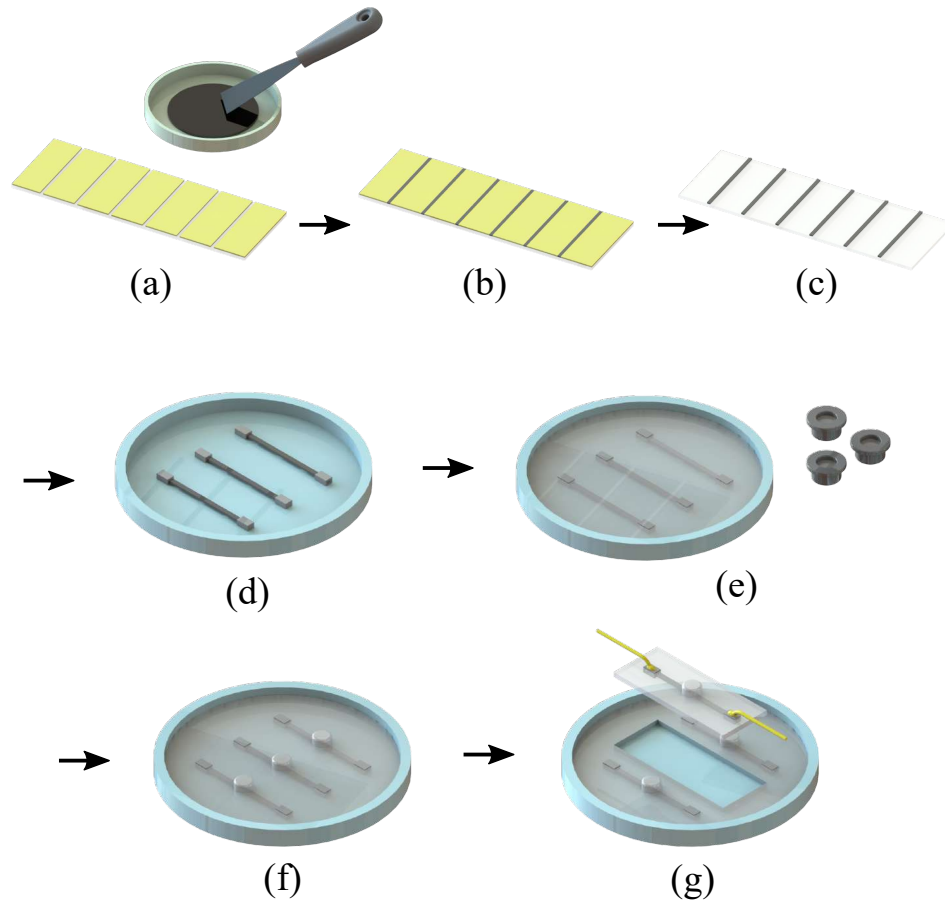


Figure 6.3: MWCNT/PDMS-based flexible sensor fabrication process.

The MWCNT/PDMS-based flexible sensor fabrication process is as follows (see Fig. 6.3): (a) prepare MWCNT/PDMS mixture following the shear mixing protocol and a standard glass slide ($W \times L \times H = 25 \times 75 \times 1$ mm, 12-550D, Fisher Scientific, Pittsburgh, PA, USA) masked with tapes, (b) apply the MWCNT/PDMS mixture to the slide and scrape

out excessive materials, then put the slide into an oven at 80°C for 1 hour of curing, (c) strip the masking tapes from the slide and carefully take the MWCNT/PDMS mixtures off, (d) clamp both ends of the mixtures with solderable connectors and place them on a dish, (e) pour pure PDMS mixture (PDMS base:curing agent = 10:1 in weight) into both the dish up to slightly below the top surface of the connectors and small cylindrical shape of molds, then degas in a vacuum chamber for 1 hour followed by oven curing at 80°C for 1 hour, (f) bond the small contact pads from the molds into the middle of the MWCNT/PDMS elastomers, and (g) solder wires to the top surfaces of the connectors and carefully cut the fabricated sensor out.

Pure PDMS encapsulation keeps the active MWCNT/PDMS component intact and acts as an electric insulator. Since pure PDMS stretches better than a MWCNT/PDMS elastomer, this also slightly increases the stretchability of the sensor. Although it depends on the dimension and MWCNT concentration, around a 5 % increment in the maximum elongation was obtained for sensors with the dimension of 1(W)×25(L)×0.3(H) mm and 10 wt% of MWCNT concentration.

Using the shear mixing dispersion recipe and the fabrication process, two different scales of MWCNT/PDMS-based flexible sensors were fabricated for two different applications, tactile sensing for dexterous grasping of robotic hand and *in situ* tissue characterization through a biopsy needle. The size of the active MWCNT/PDMS component can be easily scaled by modifying the gap between masking tapes, using different masking tapes to adjust the thickness, or cutting out the elastomer for shaping.

6.2.4 Strain Sensor in a Mock-up Needle for *In Situ* Tissue Characterization

Mechanical characterization of human tissues is an important biomarker for disease diagnosis [18, 76, 197–199]. However, inherent discrepancy in mechanical characteristics between *ex vivo* and *in vivo* tissues requires a new tool capable of measuring tissue properties *in situ*. Additionally, once a real-time measurement unit for tissue characterization

is equipped in a biopsy needle, this would help increase the accuracy of biopsy since an operator can reduce unnecessary trials based on the instantaneous information from the measurement unit.

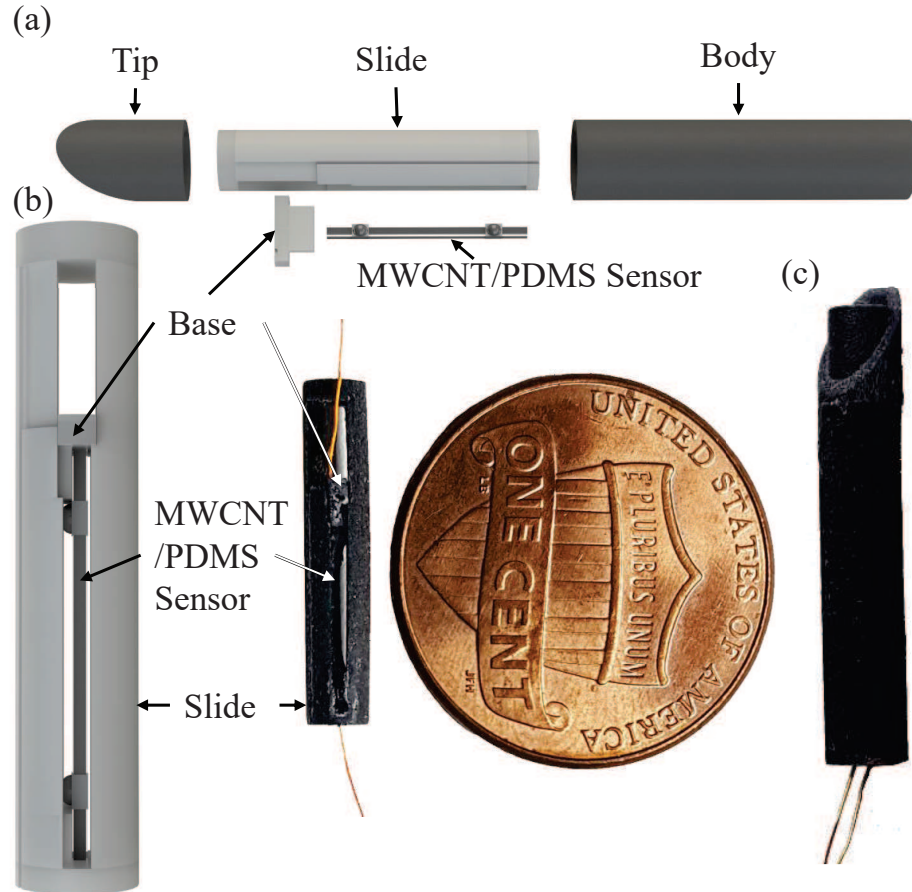


Figure 6.4: Proof-of-concept mock-up needle sensorized with the MWCNT/PDMS-based flexible sensor: (a) Exploded view of apparatus (b) Assembled sensor base and slide as up-scaled rendering (left) and to-scale picture (right), and (c) Fully assembled to-scale sensor apparatus.

A prototype sensor apparatus, shown in Fig. 6.4, was developed to determine the feasibility of incorporating this MWCNT/PDMS-based flexible sensor into a biopsy needle for *in situ* tissue characterization. The MWCNT/PDMS-based flexible sensor was fabricated on a small scale ($0.5(W) \times 7(L) \times 0.1(H)$ mm for the active MWCNT/PDMS component) than the one for the robot hand application without the contact pads in the fabrication process (Fig. 6.3(f)). This apparatus consists of a mock-up needle, base, and slide which were

3D-printed by Multijet MJP 5600 (3D Systems Inc., Rock Hill, SC, USA). The base is fixed in grooves on the inside of the needle and glued to one end of the MWCNT/PDMS-based flexible sensor. The other end of the sensor attaches inside the top part of the slide. The base crosses in between the two walls of the slide which come together again as a platform beneath the base. The wire from the base of the sensor is routed between the slide and inner needle wall through a channel in the slide. The slide serves to transfer compression force from below the base to a tension force stretching the sensor from above the base. When the needle is pushed into a substance, the tissue will create a reactionary force against the platform at the bottom of the slide which will be able to move the slide upward and thus stretch the sensor. The force applied to the sensor will determine how far the sensor is stretched and thus how much the electrical resistance changes. The slide allows for 30 % elongation of the sensor, within the previously determined largest strain without breaking.

For calibration of the sensor, the slider was pushed by a linear motor from one end to another for 2 *mm* displacement at 2 *mm/s* speed. Intuitively, the sensor output should be calibrated with applied force for the target application. Since the current prototype needs to be improved with its design in tolerances among parts to reduce friction of the slider, however, the sensor output was calibrated with its strain instead as shown in Fig. 6.5. The sensor showed a linear and fast enough response for real-time applications.

6.3 Conclusion

A MWCNT/PDMS-based flexible sensor has been developed and implemented on strain sensing in a needle for *in situ* tissue characterization to verify its capability. Fabricated MWCNT/PDMS elastomers have been shown to have piezoresistivity which is sensitive to mechanical strain and a highly flexible structure which allows 40-50 % strain, maximizing the sensitivity of the sensors. Pure PDMS encapsulation not only keeps the sensor intact, protecting the MWCNT/PDMS elastomer from physical damages and electrical noises, but also compensates for degradation of stretchability from adding MWCNTs. Since the devel-

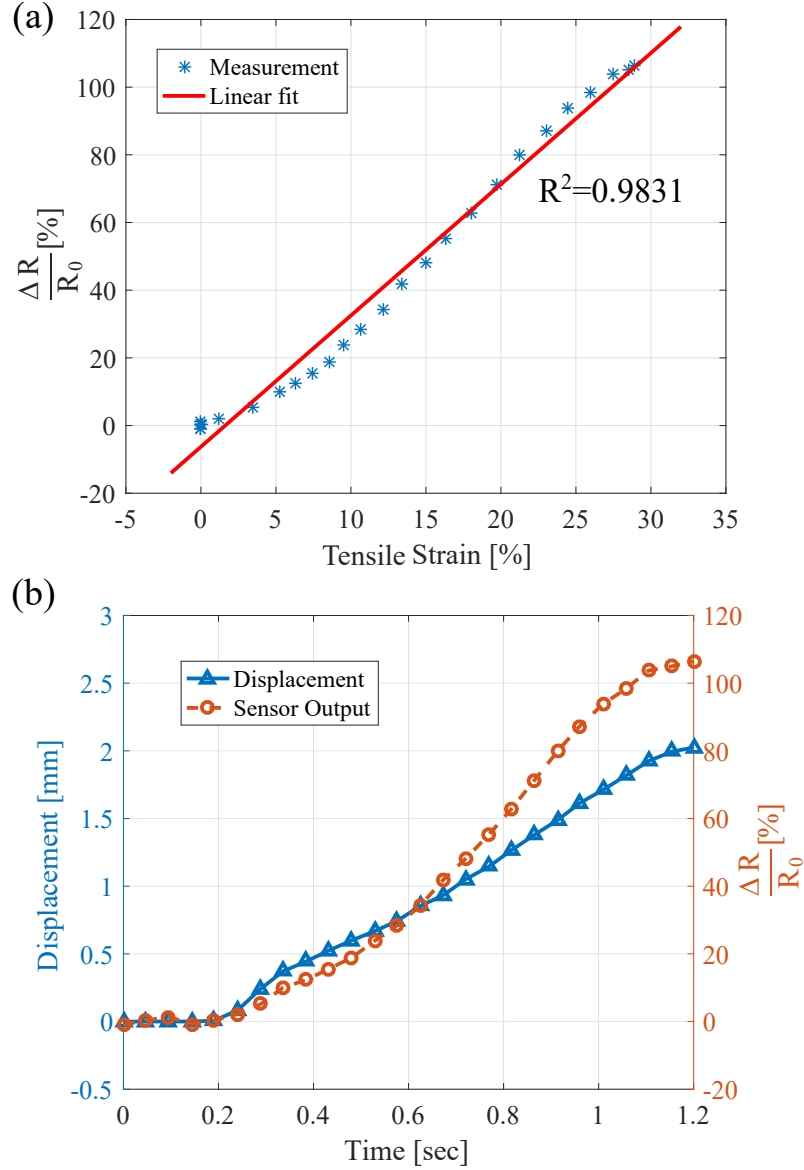


Figure 6.5: Calibration result of the MWCNT/PDMS-based flexible sensor in the mock-up needle.

oped sensors are highly flexible, responsive, easy to scale, cost-effective, simply packaged, and biocompatible, they have a significant potential to be used for many other biomedical applications such as wearable electronics and biosignal monitoring for healthcare.

Based upon the prototype, it is envisioned to be able to incorporate this sensor in an actual biopsy needle using laser micro-machining techniques. In future work, the tissue characterization force sensor apparatus will be miniaturized further and adapted for use

inside of a metal biopsy needle (18G, OD: 1.27 *mm*) with reduced friction rather than the current printed needle replica (3 *mm* inner diameter). The slide must be replaced to the home configuration by pushing on the slide from the back of the needle which will be replaced with a more deployable mechanism.

CHAPTER 7

CONCLUSION AND FUTURE WORK

7.1 Conclusion

The dissertation describes the multi-parameter characterization of human breast tissue specimens with the intent of establishing quantitative biomarkers for cancer progression. Due to variability in the tissue properties across subjects, it is difficult to conclusively attribute signatures to the onset and progression of cancer in the tissue specimens, however, this dissertation presents extensive works that have been carried out towards achieving the goal, accurate cancer diagnosis at the micro-scale using MEMS and robotics. Based on the research work done and experimental results obtained in this dissertation, the following conclusions can be made:

- In the *ex vivo* experiments, cancerous breast tissues were found to be less stiff than normal breast tissues for both tissue types of epithelial and stromal at the micro-scale ($8\ \mu m$ thickness) [17, 75], while it was opposite at a larger scale (over $2\ mm$) which has been widely observed in clinics by palpation. Moreover, cancerous breast tissues were found to have lower electrical/thermal conductivity and higher electromechanical coupling factor than normal breast tissues [168, 198].
- Breast tissue specimens obtained from biopsies are highly heterogeneous in their composition. Therefore, accurate multi-parameter characterization should incorporate with property map acquisitions, instead of point-wise random sampling in the annotated areas of a tissue specimen, and machine learning approach for multi-parameter tissue characterization can provide a greater degree of certainty in the classification results with enough number of datasets collected [197].

- Obtaining representative tissue samples for quantifying physical property alterations in cancerous tissue compared to normal tissue is quite challenging. As observed in the experimental results, tissue elasticity, electrical resistivity, thermal conductivity, and electromechanical coupling factor are patient-specific functions of the individual subject from whom the biopsies were taken and the properties are claimed as biomarkers in the dissertation based on the *ex vivo* experiments and the statistical analysis with small sample sizes.
- A highly flexible and biocompatible sensor using MWCNT, a functional material has shown its feasibility to be implemented in a biopsy needle for *in situ* tissue characterization [200]. A robotic system with MEMS-based sensing technology has great potential for the progression from *ex vivo* tissue characterization studies to *in situ* and *in vivo* diagnosis research.

7.2 Contributions

The contributions presented in this dissertation can be summarized as follows:

- *Development of tissue characterization systems at different scales:* A microscope compatible positioning system for microindentation and a portable cancer diagnostic tool have been developed and demonstrated their capability that overcomes some of the shortcomings of using conventional micropositioning systems by achieving the following features at the same time: 1) Compatibility with an inverted microscope, 2) 4-DOF motion ($XY\theta$ for the planar stage and X for the indenter) 3) Larger range of motion (over 60 mm in each direction, $\pm 10^\circ$), and 4) Sub-micro resolution and accuracy [136, 143]. In addition to the micropositioning system, the portable diagnostic tool has been designed to cover the various size of tissue specimens from microns to millimeters for the compatibility with conventional pathological analysis and biopsy which make the verification of the systems and the implementation to

current medical procedures easier.

- *Multi-parameter characterization of biological tissues:* Using multi-parameter characterization, it was shown possible to account for the inherent variability of biological tissues through machine learning algorithms, which can improve classification accuracy significantly for breast cancer diagnosis [17, 168, 198]. The experimental and computational strategies presented in this dissertation could have a significant impact on high-throughput quantitative studies of biomaterials, which could elucidate various tissue-related disease mechanisms that are phenotyped by their physical signatures [201]. This will also help understand the mechanisms of disease progression at the tissue and cellular level in the basic science fields.
- *Engineering approach to healthcare:* The challenge is to convert existing medical problems into a useful, versatile, and systematic process that repeatedly delivers results. As an efficient strategy for implementing engineering approaches to cancer diagnosis, the results reported in this dissertation can suggest a more quantitative framework in medical fields including pathology and oncology.

7.3 Future Work

The possible directions for future work in this area are:

- *Integrated framework for an automated diagnostic system:* In this dissertation, the various engineering techniques in MEMS and robotics for breast cancer diagnosis were proposed to in a piecemeal manner as a problem-oriented approach. Future work might be directed towards developing an integrated framework that consists of novel hardware systems for more accurate diagnosis, sophisticated diagnostic algorithms based on a clinical database, and easy-to-use interfaces for both medical professionals and users.

- *Clinical verification:* Future work might be directed towards the development of elaborate protocols for clinical verification such as patient-specific characterization by comparing normal and cancerous tissue specimens from a single patient, statistical analysis with a larger number of datasets such as sensitivity, specificity, accuracy, precision, repeatability, reproducibility, and limit of detection to validate the clinical effectiveness of the system.
- *In vivo tissue characterization for cancer diagnosis:* Although the *ex vivo* studies help us finding a certain biomarker for diagnosing a disease in a safer way, thorough *in vivo* verification should be followed to confirm the effectiveness of the biomarker to be used in clinics. Additional *in vivo* verification process for the biomarkers proposed in this dissertation will be investigated especially for the electromechanical coupling factor, which has not been reported anywhere else as a biomarker for breast cancer to the best of my knowledge.

Appendices

APPENDIX A

NOMENCLATURE FOR CHAPTER 3

NOMENCLATURE

$\{W\}$	World frame (or fixed frame)
O	Origin of $\{B\}$
P	Idealized point of contact of PZT ₂ with the stage
Q	Idealized point of contact of PZT ₁ with the stage
M	Midpoint of \overline{PQ}
A	CoR of the stage
C	CoM of the stage
Ω	$O, P, Q, M, A,$ and C
$\mathbf{\Omega}^W$	Position vector of Ω in $\{W\}$ ($[x_{\Omega}^W, y_{\Omega}^W, z_{\Omega}^W]^T$)
$\dot{\mathbf{\Omega}}^W$	Velocity vector of Ω in $\{W\}$ ($[\dot{x}_{\Omega}^W, \dot{y}_{\Omega}^W, \dot{z}_{\Omega}^W]^T$)
$\mathbf{\Omega}^B$	Position vector of Ω in $\{B\}$ ($[x_{\Omega}^B, y_{\Omega}^B, z_{\Omega}^B]^T$)
$\{B\}$	Body frame (or moving frame)
$\dot{\mathbf{\Omega}}^B$	Velocity vector of Ω in $\{B\}$ ($[\dot{x}_{\Omega}^B, \dot{y}_{\Omega}^B, \dot{z}_{\Omega}^B]^T$)
α	Angle of $\angle QPO$
u_1	Linear input velocity by PZT ₁ along the x^W -axis

u_2	Linear input velocity by PZT ₂ along the y^W -axis
\mathbf{u}_1^W	Velocity input vector by PZT ₁ in $\{W\}$
\mathbf{u}_2^W	Velocity input vector by PZT ₂ in $\{W\}$
D_x	x-coordinate of the geometric center of the stage in $\{W\}$
D_y	y-coordinate of the geometric center of the stage in $\{W\}$
I_C	Moment of inertia of the stage at the CoM
m	Mass of the stage
θ	Orientation of the stage
\mathbf{d}^W	Moment arm vector in $\{W\}$
\mathbf{v}_C^W	Velocity vector of the CoM in $\{W\}$
\mathbf{L}	Angular momentum vector of the stage in $\{W\}$
C_x	x-coordinate of the CoM of the stage in $\{B\}$
C_y	y-coordinate of the CoM of the stage in $\{B\}$
\mathbf{g}_i	Vector field of the stage ($i = 1, 2$)
\mathbf{g}_j	Vector field by the Lie Bracket ($j = 3, 4, 5$)
G_k	Distribution of vector fields ($k = 1, 2, 3$)
H	Non-zero denominator of the vector fields of the stage
\mathbf{u}_{xxx}	Input vector for each control step ($xxx = rot, sld, trl$)
$\dot{\theta}$	Angular velocity of the stage
k_{xxx}	Control gain for each control step ($xxx = rot, sld, trl$)

s_k	Sliding surface for each control step ($k = 1, 2, 3$)
\dot{s}_k	Time derivative of s_k ($k = 1, 2, 3$)
V_k	Lyapunov function for each control step ($k = 1, 2, 3$)
\dot{V}_k	Time derivative of V_k ($k = 1, 2, 3$)
J_c	Ratio of \dot{y}_O^W to \dot{x}_O^W under the constraint of $\dot{\theta} = 0$
J_d	Value of J_c at the desired position and orientation
y	Sliding line in XY plane
a	Slope of the sliding line
x_d	Desired x-coordinate position of the stage in $\{W\}$
S_θ	$\sin\theta$
y_d	Desired y-coordinate position of the stage in $\{W\}$
θ_d	Desired orientation of the stage
\mathbf{X}	State vector of the stage
$\dot{\mathbf{X}}$	Time derivative of \mathbf{X}
e_x	Position tracking error along the x^W axis
e_y	Position tracking error along the y^W axis
e_θ	Orientation tracking error
C_θ	$\cos\theta$
T_θ	$\tan\theta$
\mathbf{R}_B^W	Rotation transformation matrix from $\{B\}$ to $\{W\}$

$\dot{\mathbf{R}}_B^W$ Time derivative of \mathbf{R}_B^W

APPENDIX B

USE OF COPYRIGHTED MATERIALS AND PERMISSIONS

1. © 2019 IEEE. Reprinted, with permission, from **Kihan Park**, Phillip Tran, Nancy Deaton, and Jaydev P. Desai, "Multi-walled Carbon Nanotube (MWCNT)/PDMS-based Flexible Sensor for Medical Applications", *IEEE International Symposium on Medical Robotics (ISMR 2019)*, Apr. 2019.
2. © 2018 IEEE. Reprinted, with permission, from **Kihan Park**, Wenjin Chen, Marina A. Chekmareva, David J. Foran, and Jaydev P. Desai, "Electromechanical Coupling Factor of Breast Tissue as a Biomarker for Breast Cancer", *IEEE Transactions on Biomedical Engineering*, Jan. 2018.
3. © 2017 IEEE. Reprinted, with permission, from **Kihan Park** and Jaydev P. Desai, "Machine Learning Approach for Breast Cancer Localization", *International Conference on Manipulation, Automation and Robotics at Small Scales (MARSS 2017)*, Jul. 2017.
4. © 2016 IEEE. Reprinted, with permission, from **Kihan Park** and Jaydev P. Desai, "Micropositioning and Control of an Underactuated Platform for Microscopic Applications", *IEEE/ASME Transactions on Mechatronics*, Dec. 2016.
5. © 2016 IEEE. Reprinted, with permission, from Hardik J. Pandya, **Kihan Park**, Wenjin Chen, Lauri A. Goodell, David J. Foran, and Jaydev P. Desai, "Towards a Portable Cancer Diagnostic Tool Using a Disposable MEMS-based Biochip", *IEEE Transactions on Biomedical Engineering*, Jul. 2016.
6. © Royal Society of Chemistry 2015. Reproduced with permission from Hardik J. Pandya, **Kihan Park**, Wenjin Chen, Marina A. Chekmareva, David J. Foran and Jaydev P. Desai, "Simultaneous MEMS-Based Electro-Mechanical Phenotyping of Breast Cancer", *Lab on a Chip*, Sep. 2015.
7. © 2015 IEEE. Reprinted, with permission, from Carolyn M. Davis, **Kihan Park**, and Jaydev P. Desai, "Design and Analysis of a Under-actuated XY-theta Stage for Automated Tissue Indentation", *IEEE/RSJ International Conference on Intelligent Robots and Systems (IROS 2015)*, Sep. 2015.
8. © Copyright 2015 IOP Publishing. Reprinted, with permission, from Hardik J. Pandya, **Kihan Park**, and Jaydev P. Desai, "Design and Fabrication of a Flexible MEMS-Based Electro-Mechanical Sensor Array for Breast Cancer Diagnosis", *Journal of Micromechanics and Microengineering*, Jun. 2015.

REFERENCES

- [1] American Cancer Society, “Cancer Facts & Figures 2019,” *Atlanta: American Cancer Society*, 2019.
- [2] S Busch, A Acar, Y Magnusson, P Gregersson, L. Rydén, and G Landberg, “TGF- β Receptor Type-2 Expression in Cancer-associated Fibroblasts Regulates Breast Cancer Cell Growth and Survival and is a Prognostic Marker in Pre-menopausal Breast Cancer,” *Oncogene*, vol. 34, no. 1, pp. 27–38, 2015.
- [3] J. Alexander and E. Cukierman, “Stromal Dynamic Reciprocity in Cancer: Intricacies of Fibroblastic-ECM Interactions,” *Current Opinion in Cell Biology*, vol. 42, pp. 80–93, 2016.
- [4] P. P. Provenzano, K. W. Eliceiri, J. M. Campbell, D. R. Inman, J. G. White, and P. J. Keely, “Collagen Reorganization at the Tumor-stromal Interface Facilitates Local Invasion,” *BMC Medicine*, vol. 4, no. 1, pp. 1–16, 2006.
- [5] M. W. Conklin, J. C. Eickhoff, K. M. Riching, C. A. Pehlke, K. W. Eliceiri, P. P. Provenzano, A. Friedl, and P. J. Keely, “Aligned Collagen Is a Prognostic Signature for Survival in Human Breast Carcinoma,” *The American Journal of Pathology*, vol. 178, no. 3, pp. 1221–1232, 2011.
- [6] D. C. Zaha, “Significance of Immunohistochemistry in Breast Cancer,” *World Journal of Clinical Oncology*, vol. 5, no. 3, pp. 382–392, 2014.
- [7] J. Insua-Rodríguez and T. Oskarsson, “The Extracellular Matrix in Breast Cancer,” *Advanced Drug Delivery Reviews*, vol. 97, pp. 41–55, 2016.
- [8] D. A. Berry, K. A. Cronin, S. K. Plevritis, D. G. Fryback, L. Clarke, M. Zelen, J. S. Mandelblatt, A. Y. Yakovlev, J. D. F. Habbema, and E. J. Feuer, “Effect of Screening and Adjuvant Therapy on Mortality from Breast Cancer,” *New England Journal of Medicine*, vol. 353, no. 17, pp. 1784–1792, 2005.
- [9] M. S. O’Malley, S. W. Fletcher, U. P.S. T. Force, *et al.*, “Screening for Breast Cancer with Breast Self-examination,” *JAMA*, vol. 257, no. 16, pp. 2197–203, 1987.
- [10] L. H. Baker, “Breast Cancer Detection Demonstration Project: Five-year Summary Report,” *CA: A Cancer Journal for Clinicians*, vol. 32, no. 4, pp. 194–225, 1982.
- [11] H. F. Dvorak, “Tumors: Wounds That Do Not Heal,” *New England Journal of Medicine*, vol. 315, no. 26, pp. 1650–1659, 1986.

- [12] S. Alowami, S. Troup, S. Al-Haddad, I. Kirkpatrick, and P. H. Watson, “Mammographic density is related to stroma and stromal proteoglycan expression,” *Breast Cancer Research*, vol. 5, no. 5, R129–R135, 2003.
- [13] D. T. Butcher, T. Alliston, and V. M. Weaver, “A Tense Situation: Forcing Tumour Progression,” *Nature Reviews Cancer*, vol. 9, no. 2, pp. 108–122, 2009.
- [14] K. R. Levental, H. Yu, L. Kass, J. N. Lakins, M. Egeblad, J. T. Erler, S. F. Fong, K. Csiszar, A. Giaccia, W. Weninger, *et al.*, “Matrix Crosslinking Forces Tumor Progression by Enhancing Integrin Signaling,” *Cell*, vol. 139, no. 5, pp. 891–906, 2009.
- [15] D. Needham, “Possible Role of Cell Cycle-dependent Morphology, Geometry, and Mechanical Properties in Tumor Cell Metastasis,” *Cell Biophysics*, vol. 18, no. 2, pp. 99–121, 1991.
- [16] J. Swift, I. L. Ivanovska, A. Buxboim, T. Harada, P. D. P. Dingal, J. Pinter, J. D. Pajerowski, K. R. Spinler, J.-W. Shin, M. Tewari, *et al.*, “Nuclear Lamin-A Scales with Tissue Stiffness and Enhances Matrix-directed Differentiation,” *Science*, vol. 341, no. 6149, 1240104:1–16, 2013.
- [17] H. J. Pandya, K. Park, W. Chen, M. A. Chekmareva, D. J. Foran, and J. P. Desai, “Simultaneous MEMS-based Electro-mechanical Phenotyping of Breast Cancer,” *Lab on a Chip*, vol. 15, no. 18, pp. 3695–3706, 2015.
- [18] M. Plodinec, M. Loparic, C. A. Monnier, E. C. Obermann, R. Zanetti-Dallenbach, P. Oertle, J. T. Hyotyla, U. Aebi, M. Bentires-Alj, R. Y. Lim, *et al.*, “The Nanomechanical Signature of Breast Cancer,” *Nature Nanotechnology*, vol. 7, no. 11, pp. 757–765, 2012.
- [19] S. Suresh, “Biomechanics and Biophysics of Cancer Cells,” *Acta Materialia*, vol. 55, no. 12, pp. 3989–4014, 2007.
- [20] S. Kumar and V. M. Weaver, “Mechanics, Malignancy, and Metastasis: The Force Journey of a Tumor Cell,” *Cancer and Metastasis Reviews*, vol. 28, no. 1-2, pp. 113–127, 2009.
- [21] D. Allred, J. M. Harvey, M. Berardo, and G. M. Clark, “Prognostic and Predictive Factors in Breast Cancer by Immunohistochemical Analysis,” *Modern Pathology: an Official Journal of the United States and Canadian Academy of Pathology, Inc.*, vol. 11, no. 2, pp. 155–168, 1998.
- [22] M. D. Holmes, W. Y. Chen, D. Feskanich, C. H. Kroenke, and G. A. Colditz, “Physical Activity and Survival after Breast Cancer Diagnosis,” *JAMA*, vol. 293, no. 20, pp. 2479–2486, 2005.

- [23] S. E. Cross, Y.-S. Jin, J. Rao, and J. K. Gimzewski, “Nanomechanical Analysis of Cells from Cancer Patients,” *Nature Nanotechnology*, vol. 2, no. 12, p. 780, 2007.
- [24] J. Wegener, C. R. Keese, and I. Giaever, “Electric Cell-substrate Impedance Sensing (ECIS) as a Noninvasive Means to Monitor the Kinetics of Cell Spreading to Artificial Surfaces,” *Experimental Cell Research*, vol. 259, no. 1, pp. 158–166, 2000.
- [25] D. L. Polla, A. G. Erdman, W. P. Robbins, D. T. Markus, J. Diaz-Diaz, R. Rizq, Y. Nam, H. T. Brickner, A. Wang, and P. Krulevitch, “Microdevices in Medicine,” *Annual Review of Biomedical Engineering*, vol. 2, no. 1, pp. 551–576, 2000.
- [26] C. Prodan, F. Mayo, J. Claycomb, J. Miller Jr, and M. Benedik, “Low-frequency, Low-field Dielectric Spectroscopy of Living Cell Suspensions,” *Journal of applied physics*, vol. 95, no. 7, pp. 3754–3756, 2004.
- [27] T. R. Gowrishankar and J. C. Weaver, “An Approach to Electrical Modeling of Single and Multiple Cells,” *Proceedings of the National Academy of Sciences*, vol. 100, no. 6, pp. 3203–3208, 2003.
- [28] H. J. Pandya, R. Roy, K. Park, and J. P. Desai, “Microscale Sensors for Breast Cancer Diagnosis,” in *Encyclopedia of Medical Robotics – Volume 2: Micro and Nano Robotics in Medicine*, World Scientific, 2018, ch. 13, pp. 275–310.
- [29] R. Roy, “Mechanical Characterization of Normal and Cancerous Breast Tissue Specimens Using Atomic Force Microscopy,” PhD thesis, University of Maryland, College Park, 2014.
- [30] H. J. Pandya, R. Roy, W. Chen, M. A. Chekmareva, D. J. Foran, and J. P. Desai, “Accurate Characterization of Benign and Cancerous Breast Tissues: Aspecific Patient Studies Using Piezoresistive Microcantilevers,” *Biosensors and Bioelectronics*, vol. 63, pp. 414–424, 2015.
- [31] M. Lekka, D. Gil, K. Pogoda, J. Dulińska-Litewka, R. Jach, J. Gostek, O. Klymenko, S. Prauzner-Bechcicki, Z. Stachura, J. Wiltowska-Zuber, *et al.*, “Cancer Cell detection in Tissue Sections Using AFM,” *Archives of Biochemistry and Biophysics*, vol. 518, no. 2, pp. 151–156, 2012.
- [32] J. K. Gimzewski, C. Gerber, E. Meyer, and R. Schlittler, “Observation of a Chemical Reaction Using a Micromechanical Sensor,” *Chemical Physics Letters*, vol. 217, no. 5-6, pp. 589–594, 1994.
- [33] T. Thundat, R. J. Warmack, G. Chen, and D. Allison, “Thermal and Ambient-induced Deflections of Scanning Force Microscope Cantilevers,” *Applied Physics Letters*, vol. 64, no. 21, pp. 2894–2896, 1994.

- [34] M. K. Ghatkesar, H.-P. Lang, C. Gerber, M. Hegner, and T. Braun, “Comprehensive Characterization of Molecular Interactions Based on Nanomechanics,” *PloS one*, vol. 3, no. 11, e3610, 2008.
- [35] N. Backmann, C. Zahnd, F. Huber, A. Bietsch, A. Plückthun, H.-P. Lang, H.-J. Güntherodt, M. Hegner, and C. Gerber, “A Label-free Immunosensor Array Using Single-chain Antibody Fragments,” *Proceedings of the National Academy of Sciences*, vol. 102, no. 41, pp. 14 587–14 592, 2005.
- [36] J Fritz, M. Baller, H. Lang, H Rothuizen, P Vettiger, E Meyer, H.-J. Güntherodt, C. Gerber, and J. Gimzewski, “Translating Biomolecular Recognition into Nanomechanics,” *Science*, vol. 288, no. 5464, pp. 316–318, 2000.
- [37] U. Lang, P. Rust, and J. Dual, “Towards Fully Polymeric MEMS: Fabrication and Testing of PEDOT/PSS Strain Gauges,” *Microelectronic Engineering*, vol. 85, no. 5-6, pp. 1050–1053, 2008.
- [38] N. Liu, G. Fang, J. Wan, H. Zhou, H. Long, and X. Zhao, “Electrospun PEDOT:PSS–PVA nanofiber Based Ultrahigh-strain Sensors with Controllable Electrical Conductivity,” *Journal of Materials Chemistry*, vol. 21, no. 47, pp. 18 962–18 966, 2011.
- [39] A. Mata, A. J. Fleischman, and S. Roy, “Characterization of Polydimethylsiloxane (PDMS) Properties for Biomedical Micro/nanosystems,” *Biomedical Microdevices*, vol. 7, no. 4, pp. 281–293, 2005.
- [40] T Adrega and S. Lacour, “Stretchable Gold Conductors Embedded in PDMS and Patterned by Photolithography: Fabrication and Electromechanical Characterization,” *Journal of Micromechanics and Microengineering*, vol. 20, no. 5, p. 055 025, 2010.
- [41] Physik Instrumente, *2014 Complete Precision Positioning Catalog PI & PI miCos*, 2014. [Online]. Available: <http://www.pi-usa.us/pdf/index.php>.
- [42] ThorLabs Inc., *Complete Product Selection Online*, 2014. [Online]. Available: <http://www.thorlabs.com/navigation.cfm>.
- [43] Zaber Technologies Inc., *Zaber Technologies: Simplifying Motion Control 2014 Catalogue*, 2014. [Online]. Available: <http://www.zaber.com/documents/ZaberCatalog.pdf>.
- [44] Mad City Labs Inc., *Nanopositioning Systems: Product Catalog 700-N*, 2012. [Online]. Available: <http://www.madcitylabs.com/catalog.pdf>.

- [45] Newport Corporation, *Motion Control: Precision Motion - Guaranteed*, 2014. [Online]. Available: <http://www.newport.com/Motion-Control/5680969/1033/section.aspx>.
- [46] SmarAct GmbH, *SmarAct 2014 Catalog*, 2014. [Online]. Available: <http://www.smaract.de/index.php/catalog>.
- [47] Olympus Corporation of the Americas, *Inverted Microscopes*, 2014. [Online]. Available: <http://www.olympusamerica.com>.
- [48] Nikon Instruments Inc., *Complete Product Selection Online*, 2014. [Online]. Available: <http://www.nikoninstruments.com/Products/>.
- [49] P. P. Rosen, “Rosen’s Breast Pathology,” in Third. Lippincott Williams & Wilkins, 2008.
- [50] N. Sclater, “Mechanisms and Mechanical Devices Sourcebook,” in Fifth. McGraw-Hill, 2011.
- [51] J. R. Brauer, “Magnetic Actuators and Sensors,” in Second. Wiley-IEEE Press, 2014.
- [52] M. Ho and J. Desai, “Characterization of SMA Actuator for Applications in Robotic Neurosurgery,” in *Engineering in Medicine and Biology Society, 2009. EMBC 2009. Annual International Conference of the IEEE*, 2009, pp. 6856–6859.
- [53] J. M. Jani, M. Leary, A. Subic, and M. A. Gibson, “A Review of Shape Memory Alloy Research, Applications and Opportunities,” *Materials & Design*, vol. 56, pp. 1078–1113, 2014, ISSN: 0261-3069.
- [54] L. Cross and W. Heywang, “Introduction,” in *Piezoelectricity: Evolution and Future of a Technology*, W. Heywang, K. Lubitz, and W. Wersing, Eds., Germany: Springer, 2008.
- [55] K. Uchino, “Piezoelectric Motors and Transformers,” in *Piezoelectricity: Evolution and Future of a Technology*, W. Heywang, K. Lubitz, and W. Wersing, Eds., Germany: Springer, 2008.
- [56] S. Arnold, P. Pertsch, and K. Spanner, “Piezoelectric Positioning,” in *Piezoelectricity: Evolution and Future of a Technology*, Springer, 2008.
- [57] R. Yang, M. Jouaneh, and R. Schweizer, “Design and Characterization of a Low-profile Micropositioning Stage,” *Precision Engineering*, vol. 18, no. 1, pp. 20–29, 1996.

- [58] J. W. Ryu, D.-G. Gweon, and K. S. Moon, "Optimal Design of a Flexure Hinge Based XY ϕ Wafer Stage," *Precision Engineering*, vol. 21, no. 1, pp. 18–28, 1997.
- [59] W. Cai, G. Shang, Y. Zhou, P. Xu, and J. Yao, "An Alternative Flat Scanner and Micropositioning Method for Scanning Probe Microscope," *Review of Scientific Instruments*, vol. 81, p. 123 701, 2010.
- [60] N. Tan, C. Clevy, G. Laurent, P. Sandoz, and N. Chaillet, "Characterization and Compensation of XY Micropositioning Robots Using Vision and Pseudo-periodic Encoded Patterns," in *Robotics and Automation (ICRA), 2014 IEEE International Conference on*, 2014, pp. 2819–2824.
- [61] P. Lu, V. M. Weaver, and Z. Werb, "The Extracellular Matrix: A Dynamic Niche in Cancer Progression," *Journal of Cell Biology*, vol. 196, no. 4, pp. 395–406, 2012.
- [62] A. Samani, J. Zubovits, and D. Plewes, "Elastic Moduli of Normal and Pathological Human Breast Tissues: An Inversion-technique-based Investigation of 169 Samples," *Physics in Medicine and Biology*, vol. 52, no. 6, p. 1565, 2007.
- [63] N. F. Boyd, G. S. Dite, J. Stone, A. Gunasekara, D. R. English, M. R. McCredie, G. G. Giles, D. Trichler, A. Chiarelli, M. J. Yaffe, *et al.*, "Heritability of Mammographic Density, a Risk Factor for Breast Cancer," *New England Journal of Medicine*, vol. 347, no. 12, pp. 886–894, 2002.
- [64] G. Smolyakov, B. Thiebot, C. Campillo, S. Labdi, C. Severac, J. Pelta, and É. Dague, "Elasticity, Adhesion, and Tether Extrusion on Breast Cancer Cells Provide a Signature of Their Invasive Potential," *ACS Applied Materials & Interfaces*, vol. 8, no. 41, pp. 27 426–27 431, 2016.
- [65] A. Ansardamavandi, M. Tafazzoli-Shadpour, R. Omidvar, and I. Jahanzad, "Quantification of Effects of Cancer on Elastic Properties of Breast Tissue by Atomic Force Microscopy," *Journal of the Mechanical Behavior of Biomedical Materials*, vol. 60, pp. 234–242, 2016.
- [66] S. Kaushik, M. W. Pickup, and V. M. Weaver, "From Transformation to Metastasis: Deconstructing the Extracellular Matrix in Breast Cancer," *Cancer and Metastasis Reviews*, vol. 35, no. 4, pp. 655–667, 2016.
- [67] M. E. Gonzalez, E. Martin, C. Arellano-Gracia, A. Lama, and C. G. Kleer, "Mesenchymal Stem Cell-derived Collagen I Plays a Role in Organizing Breast Cancer Cell Migration and Metastasis," in *American Association for Cancer Research (AACR) 107th Annual Meeting*, vol. 76, 2016.
- [68] E. Alzurqa, A. Almaqtari, B. S. Aldin, M. Hamoud, S. Othman, and S. Nasr, "New Improved Electrical Impedance Spectroscopy System for Early Breast Cancer De-

tection,” *Imperial Journal of Interdisciplinary Research*, vol. 2, no. 4, pp. 732–738, 2016.

- [69] A. Calzado-Martin, M. Encinar, J. Tamayo, M. Calleja, and A. San Paulo, “Effect of Actin Organization on the Stiffness of Living Breast Cancer Cells Revealed by Peak-force Modulation Atomic Force Microscopy,” *ACS Nano*, vol. 10, no. 3, pp. 3365–3374, 2016.
- [70] T. Anh-Nguyen, B. Tiberius, U. Pliquet, and G. A. Urban, “An Impedance Biosensor for Monitoring Cancer Cell Attachment, Spreading and Drug-induced Apoptosis,” *Sensors and Actuators A: Physical*, vol. 241, pp. 231–237, 2016.
- [71] T. A. Krouskop, T. M. Wheeler, F. Kallel, B. S. Garra, and T. Hall, “Elastic Moduli of Breast and Prostate Tissues Under Compression,” *Ultrasonic Imaging*, vol. 20, no. 4, pp. 260–274, 1998.
- [72] H. J. Pandya, W. Chen, L. A. Goodell, D. J. Foran, and J. P. Desai, “Mechanical Phenotyping of Breast Cancer Using MEMS: A Method to Demarcate Benign and Cancerous Breast Tissue,” *Lab on a Chip*, vol. 14, no. 23, pp. 4523–4532, 2014.
- [73] J. Jossinet and M. Schmitt, “A Review of Parameters for the Bioelectrical Characterization of Breast Tissue,” *Annals of the New York Academy of Sciences*, vol. 873, no. 1, pp. 30–41, 1999.
- [74] R. Roy and J. P. Desai, “Determination of Mechanical Properties of Spatially Heterogeneous Breast Tissue Specimens Using Contact Mode Atomic Force Microscopy (AFM),” *Annals of Biomedical Engineering*, vol. 42, no. 9, pp. 1806–1822, 2014.
- [75] H. J. Pandya, K. Park, and J. P. Desai, “Design and Fabrication of a Flexible MEMS-based Electro-mechanical Sensor Array for Breast Cancer Diagnosis,” *Journal of Micromechanics and Microengineering*, vol. 25, no. 7, 075025 (13 pp), 2015.
- [76] H. J. Pandya, K. Park, W. Chen, L. A. Goodell, D. J. Foran, and J. P. Desai, “Towards a Portable Cancer Diagnostic Tool Using a Disposable MEMS-based Biochip,” *IEEE Transactions on Biomedical Engineering*, vol. 63, no. 7, pp. 1347–1353, 2016.
- [77] E Sapin-de Brosses, J. Gennisson, M Pernot, M Fink, and M Tanter, “Temperature Dependence of the Shear Modulus of Soft Tissues Assessed by Ultrasound,” *Physics in Medicine and Biology*, vol. 55, no. 6, p. 1701, 2010.
- [78] P. Wellman, R. D. Howe, E. Dalton, and K. A. Kern, “Breast Tissue Stiffness in Compression Is Correlated to Histological Diagnosis,” *Harvard BioRobotics Laboratory Technical Report*, pp. 1–15, 1999.

- [79] A. Samani, J. Bishop, C. Luginbuhl, and D. B. Plewes, “Measuring the Elastic Modulus of ex vivo Small Tissue Samples,” *Physics in Medicine and Biology*, vol. 48, no. 14, p. 2183, 2003.
- [80] M. Jordan and T. Mitchell, “Machine Learning: Trends, Perspectives, and Prospects,” *Science*, vol. 349, no. 6245, pp. 255–260, 2015.
- [81] H.-L. Chen, B. Yang, J. Liu, and D.-Y. Liu, “A Support Vector Machine Classifier with Rough Set-based Feature Selection for Breast Cancer Diagnosis,” *Expert Systems with Applications*, vol. 38, no. 7, pp. 9014–9022, 2011.
- [82] H. A. Abbass, “An Evolutionary Artificial Neural Networks Approach for Breast Cancer Diagnosis,” *Artificial Intelligence in Medicine*, vol. 25, no. 3, pp. 265–281, 2002.
- [83] J. A. Cruz and D. S. Wishart, “Applications of Machine Learning in Cancer Prediction and Prognosis,” *Cancer Informatics*, vol. 2, 2006.
- [84] K. Polat and S. Güneş, “Breast Cancer Diagnosis Using Least Square Support Vector Machine,” *Digital Signal Processing*, vol. 17, no. 4, pp. 694–701, 2007.
- [85] K. A. Nichols and A. M. Okamura, “Autonomous Robotic Palpation: Machine Learning Techniques to Identify Hard Inclusions in Soft Tissues,” in *Robotics and Automation (ICRA), 2013 IEEE International Conference on*, IEEE, 2013, pp. 4384–4389.
- [86] L. Ghenim, H. Kaji, Y. Hoshino, T. Ishibashi, V. Haguët, X. Gidrol, and M. Nishizawa, “Monitoring Impedance Changes Associated with Motility and Mitosis of a Single Cell,” *Lab on a Chip*, vol. 10, no. 19, pp. 2546–2550, 2010.
- [87] D. Allred, S. Mohsin, and S. Fuqua, “Histological and Biological Evolution of Human Premalignant Breast Disease,” *Endocrine-related Cancer*, vol. 8, no. 1, pp. 47–61, 2001.
- [88] X.-J. Ma, R. Salunga, J. T. Tuggle, J. Gaudet, E. Enright, P. McQuary, T. Payette, M. Pistone, K. Stecker, B. M. Zhang, *et al.*, “Gene Expression Profiles of Human Breast Cancer Progression,” *Proceedings of the National Academy of Sciences*, vol. 100, no. 10, pp. 5974–5979, 2003.
- [89] S. B. Edge and C. C. Compton, “The American Joint Committee on Cancer: The 7th Edition of the AJCC Cancer Staging Manual and the Future of TNM,” *Annals of Surgical Oncology*, vol. 17, no. 6, pp. 1471–1474, 2010.

- [90] M. Lacroix, R.-A. Toillon, and G. Leclercq, "Stable 'Portrait' of Breast Tumors During Progression: Data from Biology, Pathology and Genetics," *Endocrine-related Cancer*, vol. 11, no. 3, pp. 497–522, 2004.
- [91] U. Lang, N. Naujoks, and J. Dual, "Mechanical Characterization of PEDOT:PSS Thin Films," *Synthetic Metals*, vol. 159, no. 5-6, pp. 473–479, 2009.
- [92] T. Tsutsui and K. Fujita, "The Shift from "Hard" to "Soft" Electronics," *Advanced Materials*, vol. 14, no. 13-14, pp. 949–952, 2002.
- [93] G. Latessa, F. Brunetti, A. Reale, G. Saggio, and A. Di Carlo, "Piezoresistive Behaviour of Flexible PEDOT:PSS Based Sensors," *Sensors and Actuators B: Chemical*, vol. 139, no. 2, pp. 304–309, 2009.
- [94] J. L. Hutter and J. Bechhoefer, "Calibration of Atomic-force Microscope Tips," *Review of Scientific Instruments*, vol. 64, no. 7, pp. 1868–1873, 1993.
- [95] D. Rudoy, S. G. Yuen, R. D. Howe, and P. J. Wolfe, "Bayesian Change-point Analysis for Atomic Force Microscopy and Soft Material Indentation," *Journal of the Royal Statistical Society: Series C (Applied Statistics)*, vol. 59, no. 4, pp. 573–593, 2010.
- [96] A. Pillarisetti, J. P. Desai, H. Ladjal, A. Schiffmacher, A. Ferreira, and C. L. Keefer, "Mechanical Phenotyping of Mouse Embryonic Stem Cells: Increase in Stiffness with Differentiation," *Cellular Reprogramming (Formerly "Cloning and Stem Cells")*, vol. 13, no. 4, pp. 371–380, 2011.
- [97] K. D. Costa, A. J. Sim, and F. C. Yin, "Non-Hertzian Approach to Analyzing Mechanical Properties of Endothelial Cells Probed by Atomic Force Microscopy," *Journal of biomechanical engineering*, vol. 128, no. 2, pp. 176–184, 2006.
- [98] M. Zhang, Y. Zheng, and A. Mak, "Estimating the Effective Young's Modulus of Soft Tissues from Indentation Tests - Nonlinear Finite Element Analysis of Effects of Friction and Large Deformation," *Medical Engineering Physics*, vol. 19, no. 6, pp. 512–517, 1997.
- [99] P. J. Cumpson, C. A. Clifford, and J. Hedley, "Quantitative Analytical Atomic Force Microscopy: A Cantilever Reference Device for Easy and Accurate AFM Spring-constant Calibration," *Measurement Science and Technology*, vol. 15, no. 7, p. 1337, 2004.
- [100] T. A. Hope and S. E. Iles, "Technology Review: The Use of Electrical Impedance Scanning in the Detection of Breast Cancer," *Breast Cancer Research*, vol. 6, no. 2, p. 69, 2004.

- [101] M. Cristofanilli, A. Gonzalez-Angulo, N. Sneige, S.-W. Kau, K. Broglio, R. L. Theriault, V. Valero, A. U. Buzdar, H. Kuerer, T. A. Buccholz, *et al.*, “Invasive Lobular Carcinoma Classic Type: Response to Primary Chemotherapy and Survival Outcomes,” *Journal of Clinical Oncology*, vol. 23, no. 1, pp. 41–48, 2004.
- [102] T. J. Yeatman, A. B. Cantor, T. J. Smith, S. K. Smith, D. S. Reintgen, M. S. Miller, N. N. Ku, P. A. Baekey, and C. E. Cox, “Tumor Biology of Infiltrating Lobular Carcinoma. Implications for Management,” *Annals of Surgery*, vol. 222, no. 4, p. 549, 1995.
- [103] H. Zhao, A. Langerød, Y. Ji, K. W. Nowels, J. M. Nesland, R. Tibshirani, I. K. Bukholm, R. Karesen, D. Botstein, A.-L. Børresen-Dale, *et al.*, “Different Gene Expression Patterns in Invasive Lobular and Ductal Carcinomas of the Breast,” *Molecular Biology of the Cell*, vol. 15, no. 6, pp. 2523–2536, 2004.
- [104] Y. Sun, B. J. Nelson, D. P. Potasek, and E. Enikov, “A Bulk Microfabricated Multi-axis Capacitive Cellular Force Sensor Using Transverse Comb Drives,” *Journal of Micromechanics and Microengineering*, vol. 12, no. 6, pp. 832–840, 2002.
- [105] Y. Sun, S. N. Fry, D. Potasek, D. J. Bell, and B. J. Nelson, “Characterizing Fruit Fly Flight Behavior Using a Microforce Sensor with a New Comb-drive Configuration,” *Journal of Microelectromechanical Systems*, vol. 14, no. 1, pp. 4–11, 2005.
- [106] J Premkumar, B. S. Kumar, M Madhu, M Sivakumar, K. J. Song, and Y. Wong, “Key Factors in Cu Wire Bonding Reliability: Remnant Aluminum and Cu/Al IMC Thickness,” in *2008 10th Electronics Packaging Technology Conference*, IEEE, 2008, pp. 971–975.
- [107] J. Golden, H. Miller, D. Nawrocki, and J. Ross, “Optimization of Bi-layer Lift-off Resist Process,” *CS Mantech Technical Digest*, 2009.
- [108] Microsensors Inc., *MS3110 Universal Capacitive Readout IC*, 2001. [Online]. Available: http://www.ic72.com/pdf_file/m/145347.pdf.
- [109] P. N. Wahjudi, J. H. Oh, S. O. Salman, J. A. Seabold, D. C. Rodger, Y.-C. Tai, and M. E. Thompson, “Improvement of Metal and Tissue Adhesion on Surface-modified Parylene C,” *Journal of Biomedical Materials Research Part A*, vol. 89, no. 1, pp. 206–214, 2009.
- [110] P. Ouyang, R. Tjiptoprodjo, W. Zhang, and G. Yang, “Micro-motion Devices Technology: The State of Arts Review,” *The International Journal of Advanced Manufacturing Technology*, vol. 38, no. 5-6, pp. 463–478, 2008.

- [111] Y. K. Yong, T.-F. Lu, and D. C. Handley, "Review of Circular Flexure Hinge Design Equations and Derivation of Empirical Formulations," *Precision Engineering*, vol. 32, no. 2, pp. 63–70, 2008.
- [112] Y. Li and Q. Xu, "A Novel Piezoactuated XY Stage with Parallel, Decoupled, and Stacked Flexure Structure for Micro-/Nanopositioning," *Industrial Electronics, IEEE Transactions on*, vol. 58, no. 8, pp. 3601–3615, 2011.
- [113] Y. K. Yong, S. S. Aphale, and S. R. Moheimani, "Design, Identification, and Control of a Flexure-based XY Stage for Fast Nanoscale Positioning," *Nanotechnology, IEEE Transactions on*, vol. 8, no. 1, pp. 46–54, 2009.
- [114] Y. Li, J. Huang, and H. Tang, "A Compliant Parallel XY Micromotion Stage with Complete Kinematic Decoupling," *Automation Science and Engineering, IEEE Transactions on*, vol. 9, no. 3, pp. 538–553, 2012.
- [115] S.-K. Kuo, X. Shan, and C.-H. Menq, "Large Travel Ultra Precision x-y- θ Motion Control of a Magnetic-suspension Stage," *Mechatronics, IEEE/ASME Transactions on*, vol. 8, no. 3, pp. 334–341, 2003.
- [116] Q. Xu, "Design, Testing and Precision Control of a Novel Long-stroke Flexure Micropositioning System," *Mechanism and Machine Theory*, vol. 70, pp. 209–224, 2013.
- [117] A. Humphris, M. Miles, and J. Hobbs, "A Mechanical Microscope: High-speed Atomic Force Microscopy," *Applied Physics Letters*, vol. 86, no. 3, pp. 34 106–34 106, 2005.
- [118] Z. Sun, "Research on the Motion Control for the Underactuated Mechanical Systems," in *First International Conference on Information Sciences, Machinery, Materials and Energy*, Atlantis Press, 2015, pp. 1928–1931.
- [119] M. W. Spong, "Underactuated Mechanical Systems," in *Control Problems in Robotics and Automation*, Springer, 1998.
- [120] K. M. Lynch, "Controllability of a Planar Body with Unilateral Thrusters," *Automatic Control, IEEE Transactions on*, vol. 44, no. 6, pp. 1206–1211, 1999.
- [121] H. J. Sussmann, "A Sufficient Condition for Local Controllability," *SIAM Journal on Control and Optimization*, vol. 16, no. 5, pp. 790–802, 1978.
- [122] Q. Li and S. Payandeh, "Modeling and Analysis of Dynamic Multi-agent Planar Manipulation," in *Proceedings of the 2001 IEEE International Symposium on Computational Intelligence in Robotics and Automation*, 2001.

- [123] J. E. Bobrow, S. Dubowsky, and J. Gibson, "Time-optimal Control of Robotic Manipulators Along Specified Paths," *The International Journal of Robotics Research*, vol. 4, no. 3, pp. 3–17, 1985.
- [124] Z. Shiller and S. Dubowsky, "On Computing the Global Time-optimal Motions of Robotic Manipulators in the Presence of Obstacles," *Robotics and Automation, IEEE Transactions on*, vol. 7, no. 6, pp. 785–797, 1991.
- [125] P. Y. Li and R. Horowitz, "Passive Velocity Field Control of Mechanical Manipulators," *Robotics and Automation, IEEE Transactions on*, vol. 15, no. 4, pp. 751–763, 1999.
- [126] R. Ortega, M. W. Spong, F. Gómez-Estern, and G. Blankenstein, "Stabilization of a Class of Underactuated Mechanical Systems via Interconnection and Damping Assignment," *Automatic Control, IEEE Transactions on*, vol. 47, no. 8, pp. 1218–1233, 2002.
- [127] V. Sankaranarayanan and A. D. Mahindrakar, "Control of a Class of Underactuated Mechanical Systems Using Sliding Modes," *Robotics, IEEE Transactions on*, vol. 25, no. 2, pp. 459–467, 2009.
- [128] K. M. Lynch, N. Shiroma, H. Arai, and K. Tanie, "Collision-free Trajectory Planning for a 3-DoF Robot with a Passive Joint," *The International Journal of Robotics Research*, vol. 19, no. 12, pp. 1171–1184, 2000.
- [129] F. Bullo and K. M. Lynch, "Kinematic Controllability for Decoupled Trajectory Planning in Underactuated Mechanical Systems," *Robotics and Automation, IEEE Transactions on*, vol. 17, no. 4, pp. 402–412, 2001.
- [130] T. Narikiyo, J. Sahashi, and K. Misao, "Control of a Class of Underactuated Mechanical Systems," *Nonlinear Analysis: Hybrid Systems*, vol. 2, no. 2, pp. 231–241, 2008.
- [131] Univ. of Cambridge Dept. of Eng., *Young's Modulus - Cost*. [Online]. Available: http://www-materials.eng.cam.ac.uk/mpsite/interactive_charts/stiffness-cost/NS6Chart.html.
- [132] MatWeb Material Property Data, *Alcoa MIC-6 Aluminum Mold Alloy*. [Online]. Available: <http://www.matweb.com>.
- [133] ———, *Graphite, Carbon, C*. [Online]. Available: <http://www.matweb.com>.
- [134] L. Mejia, H. Simas, and D. Martins, "Force Capability in General 3-DoF Planar Mechanisms," *Mechanism and Machine Theory*, vol. 91, pp. 120–134, 2015.

- [135] Q. Yao, J Dong, and P. M. Ferreira, “Design, Analysis, Fabrication and Testing of a Parallel-kinematic Micropositioning XY Stage,” *International Journal of Machine Tools and Manufacture*, vol. 47, no. 6, pp. 946–961, 2007.
- [136] C. M. Davis, K. Park, and J. P. Desai, “Design and Analysis of an Under-actuated XY θ Stage for Automated Tissue Indentation,” in *Intelligent Robots and Systems (IROS), 2015 IEEE/RSJ International Conference on*, IEEE, 2015, pp. 4331–4336.
- [137] R. M. Murray, Z. Li, and S. S. Sastry, *A Mathematical Introduction to Robotic Manipulation*. CRC press, 1994.
- [138] R. Hermann and A. J. Krener, “Nonlinear controllability and observability,” *IEEE Transactions on automatic control*, vol. 22, no. 5, pp. 728–740, 1977.
- [139] R. M. Murray and S. S. Sastry, “Nonholonomic Motion Planning: Steering Using Sinusoids,” *Automatic Control, IEEE Transactions on*, vol. 38, no. 5, pp. 700–716, 1993.
- [140] J.-J. E. Slotine and W. Li, *Applied Nonlinear Control*. Prentice-hall Englewood Cliffs, NJ, 1991.
- [141] R. Long, M. S. Hall, M. Wu, and C.-Y. Hui, “Effects of Gel Thickness on Microscopic Indentation Measurements of Gel Modulus,” *Biophysical Journal*, vol. 101, no. 3, pp. 643–650, 2011.
- [142] L. Wang, *Support Vector Machines: Theory and Applications*. Springer Science & Business Media, 2005, vol. 177.
- [143] K. Park and J. P. Desai, “Micropositioning and Control of an Underactuated Platform for Microscopic Applications,” *IEEE/ASME Transactions on Mechatronics*, vol. 21, no. 6, pp. 2635–2646, 2016.
- [144] J. S. Bae, J. M. Chang, S. H. Lee, S. U. Shin, and W. K. Moon, “Prediction of Invasive Breast Cancer Using Shear-wave Elastography in Patients with Biopsy-confirmed Ductal Carcinoma In Situ,” *European Radiology*, vol. 27, no. 1, pp. 7–15, 2017.
- [145] B. Shin, D. Gopaul, S. Fienberg, and H. J. Kwon, “Application of Eshelby’s Solution to Elastography for Diagnosis of Breast Cancer,” *Ultrasonic Imaging*, vol. 38, no. 2, pp. 115–136, 2016.
- [146] K. Skerl, S. Vinnicombe, K. Thomson, D. McLean, E. Giannotti, and A. Evans, “Anisotropy of Solid Breast Lesions in 2D Shear Wave Elastography Is an Indicator of Malignancy,” *Academic Radiology*, vol. 23, no. 1, pp. 53–61, 2016.

- [147] T. Faes, H. Van der Meij, J. De Munck, and R. Heethaar, "The Electric Resistivity of Human Tissues (100 Hz-10 MHz): A Meta-analysis of Review Studies," *Physiological Measurement*, vol. 20, no. 4, R1, 1999.
- [148] T. Morimoto, S. Kimura, Y. Konishi, K. Komaki, T. Uyama, Y. Monden, D. Y. Kinouchi, and D. T. Iritani, "A Study of the Electrical Bio-impedance of Tumors," *Journal of Investigative Surgery*, vol. 6, no. 1, pp. 25–32, 1993.
- [149] T. Malecka-Massalska, K. Chara, P. Golebiowski, M. Wladysiuk, A. Smolen, A. Kurylcio, B. Zuchora, J. Zubrzycki, G. Orłowska-Kowalik, K. Lupa-Zatwarnicka, *et al.*, "Altered Tissue Electrical Properties in Women with Breast Cancer—Preliminary Observations," *Annals of Agricultural and Environmental Medicine*, vol. 20, no. 3, 2013.
- [150] J. Jossinet, "Variability of Impedivity in Normal and Pathological Breast Tissue," *Medical and Biological Engineering and Computing*, vol. 34, no. 5, pp. 346–350, 1996.
- [151] A. Rowe, "Piezoresistance in Silicon and Its Nanostructures," *Journal of Materials Research*, vol. 29, no. 6, pp. 731–744, 2014.
- [152] D. Shahrjerdi, B. Hekmatshoar, L. Rezaee, and S. Mohajerzadeh, "Low Temperature Stress-induced Crystallization of Germanium on Plastic," *Thin Solid Films*, vol. 427, no. 1-2, pp. 330–334, 2003.
- [153] J. J. Telega and R. Wojnar, "Piezoelectric Effects in Biological Tissues," *Journal of Theoretical and Applied Mechanics*, vol. 40, pp. 723–759, 2002.
- [154] A. A. Marino, R. O. Becker, and S. C. Soderholm, "Origin of the Piezoelectric Effect in Bone," *Calcified Tissue Research*, vol. 8, no. 1, pp. 177–180, 1971.
- [155] E. Fukada and I. Yasuda, "Piezoelectric Effects in Collagen," *Japanese Journal of Applied Physics*, vol. 3, no. 2, pp. 117–121, 1964.
- [156] T. Ikeda, *Fundamentals of Piezoelectricity*. Oxford University Press, 1996.
- [157] R. Roy, W. Chen, L. A. Goodell, J. Hu, D. J. Foran, and J. P. Desai, "Microarray-facilitated Mechanical Characterization of Breast Tissue Pathology Samples Using Contact-mode Atomic Force Microscopy (AFM)," in *Biomedical Robotics and Biomechatronics (BioRob), 2010 3rd IEEE RAS and EMBS International Conference on*, IEEE, 2010, pp. 710–715.
- [158] Y. C. Fung, *Biomechanics: Mechanical Properties of Living Tissues*. Springer-Verlag, New York, 1993.

- [159] C Halperin, S Mutchnik, A Agronin, M Molotskii, P Urenski, M Salai, and G Rosenman, "Piezoelectric Effect in Human Bones Studied in Nanometer Scale," *Nano Letters*, vol. 4, no. 7, pp. 1253–1256, 2004.
- [160] G. Hastings, M. ElMessiery, and S Rakowski, "Mechano-electrical Properties of Bone," *Biomaterials*, vol. 2, no. 4, pp. 225–233, 1981.
- [161] G. Hastings and F. Mahmud, "Electrical Effects in Bone," *Journal of Biomedical Engineering*, vol. 10, no. 6, pp. 515–521, 1988.
- [162] E. Fukada and I. Yasuda, "On the Piezoelectric Effect of Bone," *Journal of the Physical Society of Japan*, vol. 12, no. 10, pp. 1158–1162, 1957.
- [163] S. B. Lang, "Piezoelectricity, Pyroelectricity and Ferroelectricity in Biomaterials: Speculation on Their Biological Significance," *IEEE Transactions on Dielectrics and Electrical Insulation*, vol. 7, no. 4, pp. 466–473, 2000.
- [164] E. H. Frank and A. J. Grodzinsky, "Cartilage Electromechanics - I. Electrokinetic Transduction and the Effects of Electrolyte pH and Ionic Strength," *Journal of Biomechanics*, vol. 20, no. 6, pp. 615–627, 1987.
- [165] S. Jung, J. H. Kim, J. Kim, S. Choi, J. Lee, I. Park, T. Hyeon, and D.-H. Kim, "Reverse-micelle-induced Porous Pressure-sensitive Rubber for Wearable Human-machine Interfaces," *Advanced Materials*, vol. 26, no. 28, pp. 4825–4830, 2014.
- [166] J. H. Kim, J.-Y. Hwang, H. R. Hwang, H. S. Kim, J. H. Lee, J.-W. Seo, U. S. Shin, and S.-H. Lee, "Simple and Cost-effective Method of Highly Conductive and Elastic Carbon Nanotube/polydimethylsiloxane Composite for Wearable Electronics," *Scientific Reports*, vol. 8, no. 1375, pp. 1–11, 2018.
- [167] M. Filippidou, E Tegou, V Tsouti, and S Chatzandroulis, "A Flexible Strain Sensor Made of Graphene Nanoplatelets/ polydimethylsiloxane Nanocomposite," *Micro-electronic Engineering*, vol. 142, pp. 7–11, 2015.
- [168] H. J. Pandya, J. Sheng, and J. P. Desai, "Towards a Tri-axial Flexible Force Sensor for Catheter Contact Force Measurement," in *SENSORS, 2016 IEEE*, IEEE, 2016, pp. 1–3.
- [169] B. Wang, B.-K. Lee, M.-J. Kwak, and D.-W. Lee, "Graphene/polydimethylsiloxane Nanocomposite Strain Sensor," *Review of Scientific Instruments*, vol. 84, no. 10, 105005:1–4, 2013.
- [170] H. J. Pandya, J. Sheng, and J. P. Desai, "MEMS-Based Flexible Force Sensor for Tri-Axial Catheter Contact Force Measurement," *Journal of Microelectromechanical Systems*, vol. 26, no. 1, pp. 264–272, 2017.

- [171] L. Guo and S. P. DeWeerth, "Implementation of Integratable PDMS-based Conformable Microelectrode Arrays Using a Multilayer Wiring Interconnect Technology," in *Engineering in Medicine and Biology Society, 2009. EMBC 2009. Annual International Conference of the IEEE*, IEEE, 2009, pp. 1619–1622.
- [172] S. P. Lacour, C. Tsay, S. Wagner, Z. Yu, and B. Morrison, "Stretchable Microelectrode Arrays for Dynamic Neuronal Recording of In Vitro Mechanically Injured Brain," in *Sensors, 2005 IEEE*, IEEE, 2005, pp. 617–620.
- [173] K. W. Meacham, R. J. Giuly, L. Guo, S. Hochman, and S. P. DeWeerth, "A lithographically patterned, elastic multi-electrode array for surface stimulation of the spinal cord," *Biomedical Microdevices*, vol. 10, no. 2, pp. 259–269, 2008.
- [174] E. Katz and I. Willner, "Biomolecule-functionalized Carbon Nanotubes: Applications in Nanobioelectronics," *ChemPhysChem*, vol. 5, no. 8, pp. 1084–1104, 2004.
- [175] L. Pan, A. Chortos, G. Yu, Y. Wang, S. Isaacson, R. Allen, Y. Shi, R. Dauskardt, and Z. Bao, "An Ultra-sensitive Resistive Pressure Sensor Based on Hollow-sphere Microstructure Induced Elasticity in Conducting Polymer Film," *Nature Communications*, vol. 5, no. 3002, pp. 1–8, 2014.
- [176] J. Pan, S. Liu, Y. Yang, and J. Lu, "A Highly Sensitive Resistive Pressure Sensor Based on a Carbon Nanotube-liquid Crystal-PDMS Composite," *Nanomaterials*, vol. 8, no. 6, pp. 413:1–8, 2018.
- [177] G. Mittal, V. Dhand, K. Y. Rhee, S.-J. Park, and W. R. Lee, "A Review on Carbon Nanotubes and Graphene as Fillers in Reinforced Polymer Nanocomposites," *Journal of Industrial and Engineering Chemistry*, vol. 21, pp. 11–25, 2015.
- [178] M. T. Byrne and Y. K. Gun'ko, "Recent Advances in Research on Carbon Nanotube-polymer Composites," *Advanced materials*, vol. 22, no. 15, pp. 1672–1688, 2010.
- [179] I. D. Rosca and S. V. Hoa, "Highly Conductive Multiwall Carbon Nanotube and Epoxy Composites Produced by Three-roll Milling," *Carbon*, vol. 47, no. 8, pp. 1958–1968, 2009.
- [180] J. Hilding, E. A. Grulke, Z. George Zhang, and F. Lockwood, "Dispersion of Carbon Nanotubes in Liquids," *Journal of Dispersion Science and Technology*, vol. 24, no. 1, pp. 1–41, 2003.
- [181] A. Allaoui, S. Bai, H.-M. Cheng, and J. Bai, "Mechanical and Electrical Properties of a MWNT/epoxy composite," *Composites Science and Technology*, vol. 62, no. 15, pp. 1993–1998, 2002.

- [182] S.-M. Yuen, C.-C. M. Ma, H.-H. Wu, H.-C. Kuan, W.-J. Chen, S.-H. Liao, C.-W. Hsu, and H.-L. Wu, "Preparation and Thermal, Electrical, and Morphological Properties of Multiwalled Carbon Nanotube and Epoxy Composites," *Journal of Applied Polymer Science*, vol. 103, no. 2, pp. 1272–1278, 2007.
- [183] F. H. Gojny, M. H. Wichmann, B. Fiedler, I. A. Kinloch, W. Bauhofer, A. H. Windle, and K. Schulte, "Evaluation and Identification of Electrical and Thermal Conduction Mechanisms in Carbon Nanotube/epoxy Composites," *Polymer*, vol. 47, no. 6, pp. 2036–2045, 2006.
- [184] H. Lee, D. Kwon, H. Cho, I. Park, and J. Kim, "Soft nanocomposite based multi-point, multi-directional strain mapping sensor using anisotropic electrical impedance tomography," *Scientific Reports*, vol. 7, no. 39837, pp. 1–10, 2017.
- [185] J. Z. Kovacs, B. S. Velagala, K. Schulte, and W. Bauhofer, "Two Percolation Thresholds in Carbon Nanotube Epoxy Composites," *Composites Science and Technology*, vol. 67, no. 5, pp. 922–928, 2007.
- [186] N. Hu, Z. Masuda, G. Yamamoto, H. Fukunaga, T. Hashida, and J. Qiu, "Effect of Fabrication Process on Electrical Properties of Polymer/multi-wall Carbon Nanotube Nanocomposites," *Composites Part A: Applied Science and Manufacturing*, vol. 39, no. 5, pp. 893–903, 2008.
- [187] J. Li, P.-S. Wong, and J.-K. Kim, "Hybrid Nanocomposites Containing Carbon Nanotubes and Graphite Nanoplatelets," *Materials Science and Engineering: A*, vol. 483, pp. 660–663, 2008.
- [188] A. S. dos Santos, T. d. O. Leite, C. A. Furtado, C. Welter, L. C. Pardini, and G. G. Silva, "Morphology, Thermal Expansion, and Electrical Conductivity of Multiwalled Carbon Nanotube/epoxy Composites," *Journal of Applied Polymer Science*, vol. 108, no. 2, pp. 979–986, 2008.
- [189] D. Zilli, S. Goyanes, M. Escobar, C. Chilotte, V. Bekeris, A. Cukierman, and G. Rubiolo, "Comparative Analysis of Electric, Magnetic, and Mechanical Properties of Epoxy Matrix Composites with Different Contents of Multiple Walled Carbon Nanotubes," *Polymer Composites*, vol. 28, no. 5, pp. 612–617, 2007.
- [190] J. Li, P. C. Ma, W. S. Chow, C. K. To, B. Z. Tang, and J.-K. Kim, "Correlations between Percolation Threshold, Dispersion State, and Aspect Ratio of Carbon Nanotubes," *Advanced Functional Materials*, vol. 17, no. 16, pp. 3207–3215, 2007.
- [191] H.-C. Jung, J.-H. Moon, D.-H. Baek, J.-H. Lee, Y.-Y. Choi, J.-S. Hong, and S.-H. Lee, "CNT/PDMS Composite Flexible Dry Electrodes for Long-term ECG Monitoring," *IEEE Transactions on Biomedical Engineering*, vol. 59, no. 5, pp. 1472–1479, 2012.

- [192] J. H. Lee, Y. W. Nam, H.-C. Jung, D.-H. Baek, S.-H. Lee, and J. S. Hong, “Shear Induced CNT/PDMS Conducting Thin Film for Electrode Cardiogram (ECG) Electrode,” *BioChip Journal*, vol. 6, no. 1, pp. 91–98, 2012.
- [193] S. M. Lee, H. J. Byeon, J. H. Lee, D. H. Baek, K. H. Lee, J. S. Hong, and S.-H. Lee, “Self-adhesive Epidermal Carbon Nanotube Electronics for Tether-free Long-term Continuous Recording of Biosignals,” *Scientific Reports*, vol. 4, no. 6074, pp. 1–9, 2014.
- [194] J. Park, Y. Lee, J. Hong, M. Ha, Y.-D. Jung, H. Lim, S. Y. Kim, and H. Ko, “Giant Tunneling Piezoresistance of Composite Elastomers with Interlocked Microdome Arrays for Ultrasensitive and Multimodal Electronic Skins,” *ACS Nano*, vol. 8, no. 5, pp. 4689–4697, 2014.
- [195] C. Pang, G.-Y. Lee, T.-i. Kim, S. M. Kim, H. N. Kim, S.-H. Ahn, and K.-Y. Suh, “A Flexible and Highly Sensitive Strain-gauge Sensor Using Reversible Interlocking of Nanofibres,” *Nature Materials*, vol. 11, no. 9, pp. 795–801, 2012.
- [196] J. N. Lee, C. Park, and G. M. Whitesides, “Solvent compatibility of polydimethylsiloxane based microfluidic devices,” *Analytical Chemistry*, vol. 75, no. 23, pp. 6544–6554, 2003.
- [197] K. Park and J. P. Desai, “Machine Learning Approach for Breast Cancer Localization,” in *Manipulation, Automation and Robotics at Small Scales (MARSS), 2017 International Conference on*, IEEE, 2017, pp. 154–159.
- [198] K. Park, W. Chen, M. A. Chekmareva, D. J. Foran, and J. P. Desai, “Electromechanical Coupling Factor of Breast Tissue as a Biomarker for Breast Cancer,” *IEEE Transactions on Biomedical Engineering*, vol. 65, no. 1, pp. 96–103, 2018.
- [199] D. M. Ebenstein, D. Coughlin, J. Chapman, C. Li, and L. A. Pruitt, “Nanomechanical Properties of Calcification, Fibrous Tissue, and Hematoma from Atherosclerotic Plaques,” *Journal of Biomedical Materials Research Part A*, vol. 91, no. 4, pp. 1028–1037, 2009.
- [200] K. Park, P. Tran, N. Deaton, and J. P. Desai, “Multi-walled Carbon Nanotube (MWCNT)/PDMS-based Flexible Sensor for Medical Applications,” in *2019 International Symposium on Medical Robotics (ISMR)*, IEEE, 2019, pp. 1–8.
- [201] K. Park, G. E. Lonsberry, M. Gearing, A. I. Levey, and J. P. Desai, “Viscoelastic Properties of Human Autopsy Brain Tissues as Biomarkers for Alzheimer’s Diseases,” *IEEE Transactions on Biomedical Engineering*, vol. 66, no. 6, pp. 1705–1713, 2019.